UNIVERSITÀ DEGLI STUDI DI NAPOLI
"FEDERICO II"

Dottorato di Ricerca in Fisica

Ciclo XXXV

Coordinatore: Prof. Vincenzo Canale

Cosmological probes and Extended Gravity and Electromagnetism.

Settore Scientifico Disciplinare FIS/05

Dottorando
Giuseppe Sarracino

Tutori
Prof. Salvatore Capozziello
Prof. Alessandro D.A.M. Spallicci

Anni 2019/2022

A Zia Carmela.

Abstract

In this thesis, we have performed analysis regarding some frontiers of astrophysics and cosmology, considering both observational data as well as novel models and frameworks. More specifically, we have studied a correlation involving physical parameters of Gamma-Ray Bursts (GRBs), intending to use these features both to classify GRBs into physical classes as well as for employing them as cosmological tools, to infer parameters like the matter content in the Universe today and the Hubble constant. Indeed, for our investigations on GRBs as cosmological tools, we have performed simulations starting from the best-fit GRB fundamental plane parameters, and we have analyzed real GRBs data together with other more conventional cosmological probes, such as Supernovae type Ia (SNe Ia) and Baryon Acoustic Oscillations (BAO), via a Bayesian approach. We then explore possible extensions both of classical electromagnetism as well as of General Relativity. For the former, we study what the contribution of non-standard electromagnetic effects would be on cosmological observations, in particular on their related redshift, using mock data as well as the aforementioned SNe Ia and BAO data sets, in cosmological models where we do not introduce the still mysterious dark energy. We then study the Earth's magnetosphere and the surrounding solar wind region by considering data from the Magnetospheric Multiscale (MMS) Mission, to find possible evidence of non-standard electromagnetism using data related to the measured current densities in these regions. From the gravitational point of view, instead, we study a particular Extended Theory of Gravity (ETG), known as $f(R)-$Gravity, in the weak, astrophysical, field regime. In particular, we apply it to the stellar structure of non-compact objects, including variable stars.

Keywords: Cosmology; Supernovae Type Ia; Gamma-ray Bursts; Modified Electromagnetism; Extended Gravity; Stellar Structure.

Contents

Specific Publications

1. "The X-ray fundamental plane of the Platinum Sample, the Kilonovae and the SNe Ib/c associated with GRBs" Dainotti M.G., Lenart A., **Sarracino G.**, Nagataki S., Capozziello S., Fraija N., The Astrophysical Journal, 904, 97. arXiv:2010.02092 [astro-ph.HE] (2020)

2. "Einstein, Planck and Vera Rubin: relevant encounters between the cosmological and the quantum worlds" Salucci P., Esposito G., Lambiase G., Battista E., Benetti M., Bini D., Boco L., Sharma G., Bozza V., Buoninfante L., Capolupo A., Capozziello S., Covone G., D'Agostino R., De Laurentis M., De Martino I., De Somma G., Di Grezia E., Di Paolo C., Fatibene L., Gammaldi V., Geralico A., Ingoglia L., Lapi A., Luciano G., Mastrototaro L., Naddeo A., Pantoni L., Petruzziello L., Piedipalumbo E., Pietroni S., Quaranta A., Rota P., **Sarracino G.**, Sorge F., Stabile A., Stornaiolo C., Tedesco A., Valdarnini R., Viaggiu S., Yunge A.A.V.,, Frontiers in Physics, Volume 8, id.579 arXiv:2011.09278 [astro-ph.HE] (2021)

3. "Investigating dark energy by electromagnetic frequency shifts" Spallicci A. D. A. M., **Sarracino G.**, Capozziello S., The European Physical Journal Plus, 137, 2. arXiv:2202.02731 [astro-ph.CO] (2022)

4. "Optical and X-ray GRB Fundamental Planes as cosmological distance indicators" Dainotti M. G., Nielson V., **Sarracino G.**, Rinaldi E., Nagataki S., Capozziello S., Gnedin O. Y., Bargiacchi G, Monthly Notices of the Royal Astronomical Society, 514, 2., pp.1828-1856, arXiv:2203.15538 [astro-ph.CO] (2022)

5. "Gamma-ray bursts, supernovae Ia, and baryon acoustic oscillations: A binned cosmological analysis" Dainotti M. G.,**Sarracino G.**, Capozziello S., Publications of the Astronomical Society of Japan, 74, 5, pp.1095-1113, arXiv:2206.07479 [astro-ph.CO] (2022)

6. "The Gamma-ray Bursts Fundamental Plane correlation as a cosmological tool" Dainotti M. G.; Lenart A., Chraya A., **Sarracino, G.**; Nagataki S., Fraija N.,

Capozziello S., Bogdan M., Monthly Notices of the Royal Astronomical Society, 518, 2, pp. 2201–2240, arXiv:2209.08675 [astro-ph.CO] (2022).

7. "Investigating dark energy by electromagnetic frequency shifts II: the Pantheon+ Sample" **Sarracino G.**, Spallicci A.D.A.M., Capozziello S., The European Physical Journal Plus, 137, 1386 arXiv:2211.11438 [astro-ph.CO] (2022).

8. "Testing the Ampère-Maxwell law on the photon mass and Lorentz-Poincaré symmetry violation with MMS multi-spacecraft data" Spallicci A. D. A. M., **Sarracino G.**, Randriamboarison, O., Helayël-Neto, J. A., to be submitted, arXiv:2205.02487 [astro-ph.HE] (2022).

9. "Stellar Structure in Extended Gravity: The Case of Variable Stars" **Sarracino G.**, Feola P., Capozziello S., to be submitted

List of Figures

List of Tables

Chapter 1

Introduction

General Relativity (GR), is one of the two principal pillars of modern physics, the second being the Quantum Field Theory (QFT). Being first proposed by Einstein in [1], more than one hundred years ago, it quickly became clear that GR was a necessary evolution of Newtonian Gravity, which was thought to be, at that time, the "status quo" of gravitational interactions.

One of the most successful byproducts of this theory has been the birth of modern cosmology, a scientific branch whose aim is to describe our Universe in a mathematical and quantitative way, thus allowing us to answer important questions, remained unsolved since the birth of mankind as we know it, in an objective (as far as possible) fashion, via models, equations, simulations, and observations.

Nowadays, the so-called Λ Cold Dark Matter (ΛCDM) model is considered the standard cosmological model, which is able to schematize and parameterize our Universe with only six free parameters [2]: the baryon density parameter, the dark matter density parameter, the observed angular size of the sound horizon at recombination, the scalar spectral index, the curvature fluctuation amplitude, and finally the reionization optical depth. These parameters are then used to derive, under certain constraints and hypotheses, all the other cosmological ones, thus being able to describe the Universe at least for the vast majority of its lifetime.

The ΛCDM model depicts the Universe as being made up of three major components: a cosmological constant Λ, associated with the so-called dark energy, that should account for 68% of the density inside the Universe [3, 2], a cold (non-relativistic) dark matter, which should account for around the 27% of the cosmic pie [4, 5], and lastly, the remaining 5% is composed of ordinary baryonic ordinary matter, that forms stars and galaxies as we know them. This model is strikingly successful in its predictions in concordance with the cosmological observations, like, for instance, with the observed acceleration of the expansion of the Universe [6], for which the cosmological constant

has been reintroduced after many decades since its first appearance in the cosmological equations, the latter being due to Einstein himself (albeit for different, and later revealed wrong, reasons).

Despite their success, GR and the ΛCDM model present some issues that are at the center of the current attention of the cosmological and astrophysical communities: the most glaring one is the nature itself of dark energy and dark matter. Even after many experiments and theoretical assessments [7, 8, 9, 10], still no positive evidence has been found being able to answer the fundamental question regarding the nature of these mysterious fluids. Thus, we have to recognize that, according to the ΛCDM model, we currently do not know what 95% of our Universe is made up of [11].

Another main theoretical issue concerns GR itself, particularly its link with QFT. Despite being the two pillars on which modern physics is based, up to now their "merging" has not been possible, because very difficult conceptual problems have arisen, that have not allowed the scientific community to link these two theories in a satisfying and complete manner, thus not permitting the birth of the so-called "theory of everything".

Other problems have been found also from the observational point of view: for instance, the famous Hubble Constant (H_0) tension is also a glaring issue that needs to be addressed. Indeed, the so-called late-time measurements related to this quantity, which are linked to the cosmological ladder [12], are not consistent with the early-time results, based on the Cosmic Microwave Background (CMB) radiation [2]. This tension still exists despite many years of painstaking efforts of both teams to increase the precision of their instruments, refine their methodologies, and reduce their systematic errors, thus hinting at a more fundamental issue inside the model itself. We also have to stress that this is not the only tension that exists from an observational point of view (for instance, we recall the $S_8 = \sigma_8\sqrt{\Omega_M/0.3}$ tension [13, 14, 15]).

From an astrophysical point of view, GR has to be tested both in weak and strong gravitational regimes, because, especially in the latter case, both white dwarfs exceeding the Chandrasekhar limit [16, 17] as well as supermassive Neutron Stars (NS) [18, 19] have been observed.

These issues have brought the scientific community to wonder if, as happened in previous instances during the history of physics, there is a more complete paradigm beyond GR (and in general, the current status quo of Physics), able to overcome its limits while still keeping its overwhelming successes. The analysis in this thesis is an investigation of such possibilities, both from an observational and more theoretical point of view, regarding some peculiar cases.

We start our analysis from the observational frontier, using data from the Supernovae type Ia (SNe Ia [20]) and Baryonic Acoustic Oscillations (BAO, [21]), which are widely

used as cosmological probes, to infer cosmological parameters like H_0 and the current matter density component in the universe, Ω_M, considering also a novel, less conventional, probe: the Gamma-Ray Bursts (GRBs).

GRBs are extremely luminous transient objects, whose nature has fascinated the scientific community since they were serendipitously discovered around sixty years ago. These events do not have a preferred position in the sky, being detected in every direction, and usually last from fractions of seconds up to hours in extreme cases. One of their main features is the fact that they easily outshine other cosmological probes that are a part of the cosmic ladder, thus, if used for cosmological applications, they can be used to infer information from redshifts which are way beyond the distances usually linked to the other conventional probes (indeed, the furthest GRB ever detected has been found at $z = 9.4$ [22]).

In order to use the GRBs as cosmological probes, the physics behind them needs to be extremely well understood. Unfortunately for this point of view, contrary to what has been inferred for SNe Ia, whose physical mechanisms, apart from some outliers, are well-known and can be applied to the majority of them, GRBs are way more heterogeneous, with more possible candidates both for the astrophysical objects acting as their progenitors as well as for their emission mechanisms. This is reflected also in their observational properties, especially in their luminosities [23, 24], which may span different orders of magnitude. All these features make GRBs more difficult to be considered as cosmological probes with respect to other astrophysical objects currently utilized in the cosmological ladder.

For this final aim, empirical correlations among observational quantities of GRBs have been found. In our work, we shall focus on the GRB fundamental plane correlation (also known as the 3D Dainotti relation) [24, 25, 26] which is a correlation among the prompt peak luminosity, the luminosity at the end of the plateau emission, and the corresponding end time of the plateau. We shall study this correlation in an extended set of GRBs, which have been divided into different subclasses, according to their morphological features. We shall find if there are differences between these subsets regarding the best-fit parameters of this correlation [24]. We will also find which of these correlations present the smallest related intrinsic scatter by using a Bayesian approach [27], thus being more suitable to be used as a cosmological tool. This investigation shall be performed also by taking into account selection biases and evolutionary effects, by employing the so-called EP statistical method [28]. Lastly, an update regarding the best-fit computations of the most interesting GRB set studied by us shall be presented, providing new evolutionary coefficients as well as reliability checks on the best-fit itself using other methodologies.

Next, we shall employ this correlation for cosmological applications. We will first study [29], via simulations, how many GRBs belonging to two particular samples (defined in different wavelengths) are needed in order to constrain with a certain desired precision on Ω_M. More specifically, we shall study three thresholds reached by SNe Ia [30, 31, 20] on the precision of a particular cosmological parameter, and compare those with our simulations. Once we have found the number of necessary GRBs to achieve such limits, we shall derive, following realistic assumptions regarding present and future GRB observational missions and campaigns, how many years of GRB observations should be necessary to reach the studied precision limits obtained using simulated GRBs. We will see that multiple hypotheses shall be investigated using different baselines for our simulations, as well as further possibilities regarding GRBs data and their relative errors.

After the aforementioned dissemination, we will consider the GRBs set at our disposal for cosmological applications. More specifically [32], after obtaining closed contours for different cosmological parameters employing the SN Ia, BAO, and GRB samples at our disposal, we shall also perform a binned analysis, dividing our samples in order of increasing redshift, with the idea of gathering all GRBs in the last bin, the one corresponding to the highest redshift interval. This has been done to further analyze the total contribution to the derivation of the cosmological parameters brought by the GRBs, exploiting the fact that GRBs are generally detected at much higher redshifts than other, more conventional, probes. Finally, we will study what can be inferred from the GRBs data alone after some caveats regarding their calibration are employed, based on the SNe Ia results [33].

It is important to stress that, up to now, our cosmological tests are focused on the determination of cosmological parameters (and more importantly on their precision) still taking into account the ΛCDM model (or modifications of its exact parameters, to test if they are reproduced by our best-fit computations), the focus being the use of a novel probe like the GRBs. From this point on, instead, we shall concentrate on new hypotheses, moving from the ΛCDM model to new theories.

Indeed, we now begin investigating a novel framework, according to which the effects normally attributed to the unknown dark energy from the ΛCDM model could actually have a completely different nature, that would not imply the existence of this mysterious fluid. Indeed, we wonder if, as Newtonian gravity is an approximation of GR, also classical electromagnetism is an approximation of a broader, more complete electromagnetic theory [34]. Thus, we give an optical origin to the effects normally attributed to dark energy, which is transferred to the redshift of the astrophysical sources [35]. Indeed, we study cosmological models utilizing the SNe Ia and BAO data considered previously, in

which we assume that there is not any dark energy contribution, but every astrophysical source presents a further component to the total redshift due to these non-standard electromagnetic effects. These contributions may be blue or red (so not just red as for the conventional cosmological redshifts), depending on all the non-standard electromagnetic interactions in which the photon is involved during its journey to us. We investigate this hypothesis also for mock redshifts, and we build new Hubble diagrams when general trends are studied. Finally, we also take into account, for this analysis, the novel Pantheon+ sample of SNe Ia [36], which is an update of the Pantheon set [20] that has been employed for all the previously mentioned computations, with the aim of comparing the results achieved by these two sets.

This analysis works whichever the underlying non-standard electromagnetism theory may be, given that, up to this point, only the "a posteriori" effect on the observed redshift is investigated. In general, the first idea of something beyond Maxwellian electromagnetism is the massive photon proposed by de Broglie [37], which was studied also by his scholar Proca [38]. Further possible extensions come from the Standard Model Extension (SME) [39] paradigm, and non-linear Electromagnetism [40, 41].

Moving to a more fundamental level, we also investigate the deviations from non-standard electromagnetic effects using data collected by the Magnetospheric Multiscale (MMS) Mission [42], which is a constellation of four satellites flying in a tetrahedral formation in Earth's magnetosphere as well as in the surrounding solar wind. On these satellites, there are instruments capable of measuring different properties of the medium, like ion density, temperature, and magnetic fields. Using these data, we can compare the particle current density measured directly with the rotational current density that can be derived by the Ampere-Maxwell equation using a particular technique called curlmeter [43], to find if there are deviations between these two current densities. Working under the hypothesis that these deviations are all due to non-standard electromagnetic effects, we are able to derive an estimate for the mass of the photons where these deviations are found, as well as for the value of parameters linked to the SME. We will also explore the regions in which these inconsistencies arise, to investigate if there are preferred physical conditions for such events.

Moving along the extended theories, another possible extension that is on the radar of many scientists concerns GR itself. In this framework, we find what are known as extended theories of Gravity (ETGs) [11], called as such because they are theories in which GR is extended in different possible ways, for instance by introducing in the Einstein-Hilbert action different functions of the Ricci scalar ($f(R)$-Gravity), or by considering further scalar fields. These theories have been studied in many fields related to astrophysics and cosmology [19, 44], with the aim of reproducing the successes of GR while

also overcoming its observational and fundamental limits. For instance, in this paradigm, both dark energy and dark matter could have a geometrical origin instead of a material one [11], also, this is a possible way to give a theoretical explanation to the so-called inflationary paradigm [45], which is the exponentially fast acceleration period in the very early time of the Universe, that has to be introduced in order to describe some observations which, as we will see, cannot be encompassed in the standard cosmology approach, like the asymptotic flatness or the absence of magnetic monopoles [46].

In this analysis, we will present an application of ETGs, in particular $f(R)$-Gravity, to the structure of non-compact objects, more specifically variable stars. We shall derive the modified stellar structure equations [47] and, following [49, 48], we will also find the modified Lane-Emden equations considering the polytropic assumption, which we shall numerically solve in order to derive different physical parameters of the stars, like the mass and the period for a variable object. As we will see, this analysis can be used also to study stars that are very massive [50], that are not easily explained in the GR framework both from the stability point of view of these stellar structures [47] as well as for the issues concerning the stellar formation processes [51, 52].

As it can be noted by the focal points previously stated, which shall be deeply developed in the course of this manuscript, the work proposed and performed in this thesis is concentrated on some of the existent frontiers of astrophysics and cosmology, investigating novel approaches regarding those both from an observational and theoretical point of view.

In Chapter 2 we will briefly introduce GR and the ΛCDM model, then we shall present some of their issues, from the tensions between the cosmological parameters to the structure of compact objects, passing through the link between GR and QFT, the nature of dark matter and dark energy, and the inflationary paradigm.

In Chapter 3 we will present the astrophysical objects which shall be used for cosmological applications in the following chapters, in particular SNe Ia, BAO, and GRBs. Regarding GRBs, a more in-depth description of our current understanding of their emission mechanism and progenitors will be presented, with a focus on some of the empirical correlations found between some physical features of the detected GRB light curves. Then, we will present the main results reached in [24], where a particular correlation, known as the fundamental plane relation for GRBs, has been used for different GRBs subsets, to see if it may be used as a discriminator among different classes and to find the morphological subsets whose best-fit planes present the smallest intrinsic scatters, thus revealing to be more suitable as cosmological tools. Finally, we will present an updated study of the evolutionary coefficients involved in the correction for the selection biases and evolutionary effects, performed in [33] as well as different reliability checks on the

fundamental plane related to a class particularly promising for cosmological applications, performed using other statistical methods.

In Chapter 4, the main cosmological results involving GRBs are presented. We first introduce the methodology used to apply our data set (composed of SNe Ia, BAO, and GRBs) for cosmological computations. Then, the main results of [29] are shown, in which simulations have been performed on GRBs, in order to estimate how many of them, lying on the best-fit fundamental plane of particular samples and sets, are needed in order to compute cosmological parameters (more specifically Ω_M), with a certain desired precision, the idea being to trace the "future history" of GRBs as cosmological tools, and see if and how they will be as competitive as the nowadays SNe Ia sets for these applications, considering three particular thresholds reached by SNe Ia cosmology in the past years. We then present the cosmological results obtained using the real data sets themselves, considering GRBs together with SNe Ia and BAO, which have been obtained in [29, 32, 33]. These computations have been performed by considering different combinations of these three probes, taking the SNe Ia results as reference points, to understand how much the precision on the cosmological results improves by adding more probes. For this aim, we have also focused our computations on a binned analysis, dividing our set into five different bins, and on all the results obtained for Ω_M and H_0 for each bin in which we have divided our samples. We will also show a Hubble diagram involving the GRBs used in our cosmological studies, and a calibration test performed on GRBs having the same redshift range of the considered SNe Ia set.

In Chapter 5, we shift our focus to non-standard electromagnetism and its cosmological and astrophysical implications. After an introduction, in which we describe what are some of the possible theories going beyond Maxwellian electromagnetism, focusing in particular on the messengers of this interaction (the photons), we shall provide an estimate on the shift in frequency due to these effects for astrophysical observations [39]. This frequency shift has implications also on the observed redshift of astrophysical sources, for which we find a second contribution that is not cosmological, but purely optical [34], and can be linked to any non-standard electromagnetic paradigm. We then describe the analysis performed in [35], where this new shift has been studied using mock data as well as real measurements based on SNe Ia and BAO, the former being represented by the Pantheon sample [20]. In particular, the best-fit parameters for these shifts have been found for cosmological models without any dark energy contributions, thus giving to these non-standard shifts the effects normally attributed to the acceleration provoked by this mysterious fluid. We have studied both an individualistic approach, in which the derivation of the non-standard shift for a particular data point is independent of all the others belonging to the data set, with the idea that these shifts depend not only on

the distance from us but also on other factors, like the environment of the host galaxy, as well as a collective approach, in which this shift (more specifically, a parameter related to the shift and the distance itself) is treated as a cosmological quantity valid for every data point so that a new Hubble diagram can be built. Finally, we have performed the same analysis also considering the Pantheon+ sample [36] of SNe Ia, performed in [53], computing the same cases previously mentioned and comparing each of them with the corresponding results obtained considering the Pantheon set.

We then focus on a more fundamental issue regarding non-standard electromagnetism. After a brief introduction regarding past experiments looking for an upper limit on the photon mass, we shall describe the analysis performed in [54], where we employ almost 6 years of data collected by MMS to find traces of possible deviations of the measured particle current density with the rotational current density derived using the curlmeter technique, a method which employs the distances between spacecraft and the measured magnetic fields, with the assumption that these discrepancies could be due to non-standard electromagnetic effects. Considering the Parker model for the data points inside the solar wind [55], an estimate on the vector potential can be given, thus deriving the value of the estimated photon mass for the de Broglie-Proca (dBP) massive photon electromagnetism in cases in which inconsistencies are found (or an upper limit for the consistencies cases) as well as for the SME parameters.

In Chapter 6, we focus on another possible extension, related directly to GR. Indeed, we shall apply $f(R)-$Gravity to the stellar structure of non-compact objects, like main sequence stars or Classical Cepheids, thus shifting from the cosmological issues treated in the previous chapters to an astrophysical one, keeping in mind that any theory has to be consistent at every scale, and for every observational evidence. First, we shall derive the field equations for $f(R)-$Gravity starting from a variational principle. Then, under some approximations, we will derive the Newtonian limit of these field equations, which has to be applied to the case in our study. We then derive a general form for the stellar structure equation system in $f(R)-$Gravity. Using the polytropic assumption, that links the pressure and the density inside the star without involving other physical features like the temperature, we can derive the modified Lane-Emden equations for $f(R)-$Gravity, which may have two different forms [Sarracino et al. 2023, in preparation]. We numerically solve both of them following [49, 48], comparing GR with $f(R)-$Gravity. Finally, under certain assumptions and fixed free parameters, we derive different physical quantities of the stars, like the mass, radius, luminosity, and period of variable stars.

in Chapter 7 conclusions are drawn, and a general discussion about our results is shown, as well as future possible outlooks for our work.

Chapter 2

Open Issues in Cosmology and General Relativity

In this chapter, a brief description of General Relativity (GR) and the ΛCDM model is shown, given that both these theories are the fundamental baseline of all the analysis performed through this thesis. Then, some reasons are shown, theoretical as well as observational, for which one could imagine extending these theories, confirming their major successes, and overcoming their limits.

2.1 General Relativity and the ΛCDM model

We begin by briefly introducing GR and one of its most successful products: the standard cosmological ΛCDM model, as well as fundamental notions that will be used throughout the thesis. GR has been introduced by Einstein in [1], and it is based on the hypothesis that space and time are one single space-time structure which, in the limit of massive contributions, collapses into the Minkowskian space-time metric. This theory is based on four main theoretical pillars [11]:

- The *Principle of Relativity* is the requirement that all observers must be equally valid for describing physics. In particular, inertial frames (which do not exist globally) are not preferred a priori. This postulate addresses the main shortcoming of Special Relativity, formulated in 1905 by Einstein himself [56], being based on preferred inertial frames and Lorentz boosts between them.

- The *Equivalence Principle* requires acceleration effects to be locally indistinguishable from gravitational phenomena (roughly speaking, it states the equivalence between the inertial and gravitational masses). This Principle has actually three different formulations: the Weak Equivalence Principle, the Einstein Equivalence

Principle, and the Strong Equivalence Principle, stressing that the latter is speculated to be coherent only with GR [46].

- The *Principle of General Covariance* requires that the field equations must be "generally covariant" tensor equations, whose form has to be the same in all coordinate systems, and states that all coordinate systems are equivalent in the description of physics [57].
- The *Principle of Causality* requires that each point in space-time must admit a notion of past, present, and future, which has to be the same for all the physical observers.

In GR, gravitational interactions are described through the curvature of a metric tensor field $g_{\mu\nu}$ related to the interval $ds^2 = g_{\mu\nu}dx^\mu dx^\nu$ of a four-dimensional space-time manifold (for the metric, we will use the signature (-,+,+,+) and consider c=1).

Once the metric tensor is specified, the curvature of the space-time is given by the Riemann tensor (using the usual Greek letters for the indexes spamming from 1 to 4):

$$R^\nu_{\alpha\beta\mu} = \Gamma^\nu_{\alpha\mu,\beta} - \Gamma^\nu_{\beta\mu,\alpha} + \Gamma^\sigma_{\alpha\beta}\Gamma^\nu_{\sigma\mu} - \Gamma^\sigma_{\mu\beta}\Gamma^\nu_{\sigma\alpha} \tag{2.1}$$

where the commas denote partial derivation. Its contraction

$$R_{\alpha\mu} = R^\beta_{\alpha\beta\mu} \tag{2.2}$$

is known as the Ricci tensor, while

$$R = R^\mu_\mu = g^{\mu\nu}R_{\mu\nu} \tag{2.3}$$

is defined as the Ricci scalar, and is the scalar curvature of the tensor $g_{\mu\nu}$. Considering matter as a perfect fluid (which is a fluid that can be completely characterized by its rest frame mass density and isotropic pressure) the matter stress-energy tensor can be written as

$$T^{(m)}_{\mu\nu} = (P + \rho)u_\mu u_\nu + P g_{\mu\nu} \tag{2.4}$$

where u^μ is the four-dimensional velocity of the particles of the fluid, while P and ρ are the pressure and energy density of the fluid, respectively. The continuity equation requires $T^{(m)}_{\mu\nu}$ to be covariantly constant, which means that it has to satisfy the conservation law

$$\nabla^\mu T^{(m)}_{\mu\nu} = 0, \tag{2.5}$$

where ∇_α denotes the covariant derivative operator of the metric $g_{\mu\nu}$. Because of this

relation, and the fact that $\nabla^\mu R_{\mu\nu}$ does not vanish except for the special case $R = 0$, Einstein and Hilbert concluded heuristically that the equations for the dynamics of gravity are given by [46]

$$G_{\mu\nu} = \kappa T^{(m)}_{\mu\nu}, \tag{2.6}$$

where $\kappa = 8\pi G$ (G is the gravitational constant), and

$$G_{\mu\nu} = R_{\mu\nu} - \frac{1}{2} g_{\mu\nu} R \tag{2.7}$$

is known as the Einstein tensor of $g_{\mu\nu}$, which satisfies the conservation law

$$\nabla^\mu G_{\mu\nu} = 0. \tag{2.8}$$

It is possible to obtain the same result from computations based on the variational principle [46]: in particular, Einstein and Hilbert derived the equations also from the variation of the action given by a Lagrangian which consists of two terms: the first one is the "matter" Lagrangian density $\mathcal{L}^m$, whose variational derivative is

$$T^{(m)}_{\mu\nu} = -\frac{2}{\sqrt{-g}} \frac{\delta(\sqrt{-g}\mathcal{L}^m)}{\delta g^{\mu\nu}}, \tag{2.9}$$

where g is the determinant of the metric tensor, while the second term is the *Hilbert-Einstein Lagrangian*:

$$\sqrt{-g}\mathcal{L}_{HE} = \sqrt{-g}R. \tag{2.10}$$

The choice of Hilbert and Einstein was rather arbitrary, as it became clear a few years later, but it was certainly the simplest from both the mathematical and physical points of view. Indeed, as we shall see in the following, other choices are possible.

One of the most natural applications of GR is modern cosmology. Assuming the cosmological principle, according to which the Universe is both homogeneous and isotropic beyond a certain scale, and starting from the Friedmann-Lemaitre-Robertson-Walker metric (reintroducing c) [58, 59, 60]:

$$ds^2 = c^2 dt^2 - a^2(t)\left[\frac{dr^2}{1 - kr^2} + r^2\Omega^2\right], \tag{2.11}$$

where Ω is the angular part of the metric, $a(t)$ is the scale factor and k can be equal to $-1, 0, 1$ depending on the curvature of the universe, it is possible to derive the Friedman cosmological equations [46, 61]:

$$\left(\frac{\dot{a}}{a}\right)^2 + \frac{kc^2}{a^2} = \frac{8\pi G\rho}{3} + \frac{\Lambda c^2}{3}, \tag{2.12}$$

$$\frac{\ddot{a}}{a} = -\frac{4\pi G}{3}\left(\rho + \frac{3p}{c^2}\right) + \frac{\Lambda c^2}{3}, \tag{2.13}$$

where G is the gravitational constant, ρ is the density, p is the pressure, and Λ is the so-called cosmological constant, nowadays associated with dark energy. These two equations are the base of the standard cosmological paradigm. It is possible to write the scale factor appearing in the previous equations as a function of the redshift z of the astrophysical sources as follows [46]

$$a = \frac{1}{(1+z)}. \tag{2.14}$$

This allows us to write the cosmological distances as a function of the redshift [62]. It is possible to rewrite Eq. (2.12) in terms of densities in the following way [63]

$$\frac{H^2(z)}{H_0^2} = \Omega_r(1+z)^4 + \Omega_M(1+z)^3 + \Omega_k(1+z)^2 + \Omega_\Lambda, \tag{2.15}$$

where $H(z) = \dot{a}/a$ is the Hubble Parameter, H_0 is the Hubble Constant, Ω_R is the energy density associated with the radiation in the Universe, Ω_M is the matter density content (in which also dark matter is taken into account), Ω_k is the density associated to the curvature, and Ω_Λ is the density associated with the cosmological constant, and so with dark energy. All these quantities but $H(z)$ are computed in the present era. Defining the function $E(z)$ as

$$E(z) = \frac{H(z)}{H_0} = \sqrt{\Omega_r(1+z)^4 + \Omega_M(1+z)^3 + \Omega_k(1+z)^2 + \Omega_\Lambda}\,, \tag{2.16}$$

we can now write all the possible definitions of distances in cosmology as a function of $E(z)$. Indeed, from a cosmological point of view, different distances from the same astrophysical source can be defined with different meanings and applications [62]. Particularly, we shall see that the most used distance in our analysis regarding cosmological computations, which shall be presented in the next chapters, is the so-called luminosity distance $d_L(z)$, which is a cosmological distance that is linked to the flux of photons received by a particular source. It is defined as

$$d_L(z) = (1+z)d_M(z)\,, \tag{2.17}$$

where $d_M(z)$ is the transverse comoving distance

$$d_{\rm M}(z) = \frac{c}{H_0}\int_0^z \frac{dz'}{E(z')}\,, \tag{2.18}$$

for $\Omega_K = 0$ (flat universe),

$$d_{\rm M}(z) = \frac{c}{H_0\sqrt{\Omega_K}} \sinh\left(\frac{H_0\sqrt{\Omega_K}}{c}\int_0^z \frac{dz'}{E(z')}\right) , \tag{2.19}$$

for $\Omega_K > 0$ (open universe), and

$$d_{\rm M}(z) = \frac{c}{H_0\sqrt{|\Omega_K|}} \sin\left(\frac{H_0\sqrt{|\Omega_K|}}{c}\int_0^z \frac{dz'}{E(z')}\right) , \tag{2.20}$$

for $\Omega_K < 0$ (closed universe). The luminosity distance is important for observational cosmology because it is linked to the so-called "standard candles", which are astrophysical objects whose intrinsic luminosity can be derived via their physical mechanism, generally correlated with other quantities which are independent of their distance from us, and so can be used to measure the distance itself via the definition of $d_L(z)$. Another very important cosmological distance is the angular diameter one, defined as

$$d_A(z) = \frac{d_M(z)}{(1+z)} , \tag{2.21}$$

which is linked to the "standard rulers" (i. e., objects whose geometrical features can be deduced in some other ways and that can be used to derive the distance from us) of the Universe, like $d_L(z)$ is to the standard candles. Finally, we also have defined the light-travel distance, which is the actual length traveled by the photon in an expanding universe

$$r = \frac{c}{H_0}\int_0^z \frac{dz'}{(1+z')E(z')} . \tag{2.22}$$

A comparison between 3 different cosmological distances (luminosity, angular diameter, and comoving distances) and their evolution with the redshift is shown in Figure 2.1. We note how at low redshift these quantities are actually very similar between one to the other, while at high redshifts, the luminosity distance, given the same redshift, is always higher with respect to the angular diameter (which decreases with the redshift after a certain threshold) and comoving ones.

Another relation that exists between the different cosmological densities is the so-called cosmic triangle equation, which can be derived directly from Eq. (2.12). Neglecting the radiation density, this formula reads as

$$\Omega_M + \Omega_\Lambda + \Omega_k = 1 , \tag{2.23}$$

thus we can link the density of matter in the Universe with the others related to dark energy and curvature.

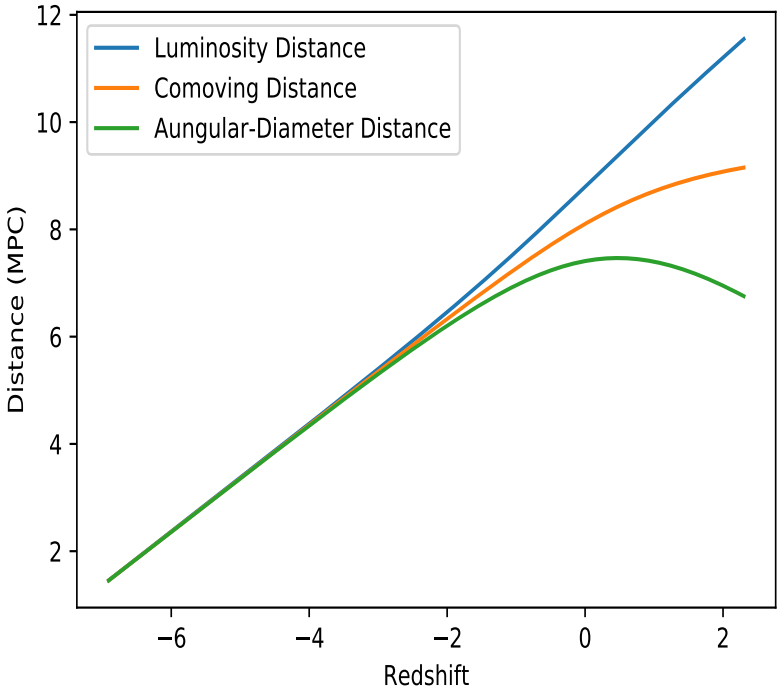

Figure 2.1: Cosmological distances and their evolution with the redshift. Both axes are on a logarithmic scale.

From a historical point of view, dark matter has been introduced by the astronomer Zwicky, as a concept to explain the missing mass in a cluster of Galaxies [64] that should have been measured due to the virial theorem. Introducing this dark matter component is also mandatory to explain the rotation curves of the galaxies, which otherwise would not be well fitted by Newtonian computations (that should work at these scales) [65, 66] if one were to consider only the baryonic mass of the galaxies. Instead, the cosmological constant, subsequently linked to the dark energy, was first introduced by Einstein himself, to maintain a stationary universe as a solution for his equations [67]. Later, observations showed that our Universe is not stationary, so for a period (up to the end of the last century), this constant has been often dropped from the cosmological equations[1]. Without this parameter, from the Friedman equations, one would expect a decelerated expansion of the Universe, but in [6] observations related to the Supernovae Type Ia (SNe Ia)[2], proved a mismatch between the known redshift of these astrophysical objects with their measured luminosity distances for a universe in a decelerated expansion. To solve this issue, the cosmological constant has been reintroduced in the equations, this time associated with a dark fluid with negative pressure, that would be able to fit the accelerated expansion of our Universe that the aforementioned observations imply. This result has been confirmed also by the detection of temperature anisotropies of the cosmic microwave background (CMB) radiation, firstly detected by balloon-born experiments such as BOOMERANG [70] and MAXIMA [71].

From an observational point of view, the paradigm that best explains the cosmological observations using the previous equations is the so-called ΛCDM model. According to this model, the Universe is made up of the three following components: ordinary matter (5%), dark matter (27% [4, 5]), and dark energy (68% [3, 2]). This model is based on six free parameters: the baryon density parameter; dark matter density parameter; the observed angular size of the sound horizon at recombination scalar spectral index; curvature fluctuation amplitude; and reionization optical depth [2]. This is also the smallest possible number of parameters able to present an acceptable fit for the observations, while other cosmological quantities, like H_0, are either derived or fixed.

The cosmological parameters of the ΛCDM model can be measured in a variety of ways. One of these is through the data gathered from the Cosmic Microwave Background (CMB) radiation [2], thus linked to the early time Universe. Indeed, studying the power

[1] Einstein himself later referred to the cosmological constant as his "biggest blunder".

[2] SNe Ia are very luminous explosions happening in binary systems, where one of the two stars is a white dwarf, due to the overflow of matter into the white dwarf coming from the surface of its companion, that would bring it to surpass the Chandrasekhar Mass limit [16]. Because the physical mechanism which causes the explosion is intrinsically the same for every phenomenon, the luminosities associated with them can be standardized [68, 69] (a more detailed description of this object will be shown in the following chapter).

spectrum of the CMB originated at the recombination epoch allows us to derive directly some cosmological parameters. It is important to stress that, given their nature, these measurements are model dependent: observations of the early Universe, up to $z \sim 1100$, are translated in terms of parameters defined for $z = 0$ [72].

Other methods used to measure, directly and indirectly, the cosmological parameters are via different cosmological probes. Many of those probes are used as "standard candles", as the SNe Ia mentioned previously. These standard candles are employed in a specific pattern depending on the magnitude of the distance itself, as a part of the so-called "cosmological ladder", in which each step is calibrated on the previous. The first step is represented by the stellar parallax [73][3]; the second step, instead, by the primary distance indicators, like the Cepheids[4] [6, 12], or the tip of the red giant branch (TRGB) [5][75]. The third step is represented by probes like SNe Ia, which use the primary distance indicator as an anchor in regions of the universe where both are detected, and which can explore relatively high redshift regions due to their higher luminosities.

Another possible way to derive cosmological parameters from observations uses the Baryon Acoustic Oscillations (BAO)[6][21, 76], or the weak lensing[7][77, 78]. Also, other possible cosmological distance indicators have been used in the literature, some of which will be presented in more detail in chapter 4.

Both GR and the ΛCDM model have been very successful in their predictions, as many observational tests have proven. A couple of examples are the recent detection of gravitational waves (GWs) [79], or both the direct and indirect measurements of cosmological parameters via different methods and probes. For a comprehensive summary of the accuracy reached by the parameter-fitting in the ΛCDM model, as well as for possible outlooks related to tensions we are going to describe, see [13, 80, 81, 82, 83]. As we will state again also in the following discussions, this is an important point to keep in mind while thinking about the shortcomings of these theories and how to surpass them.

[3]The stellar parallax is the apparent shift of a nearby star with the background due to the Earth's revolution around the Sun. Because of its nature, it may be used only for objects in our Galaxy, and, thanks to the Gaia mission, in the Magellanic clouds

[4]Cepheids are variable stars which can be found in a particular position of the H-R diagram, pulsing in a periodic manner. A specific relation between their luminosities and variation periods can be found [74]

[5]The TRGB is a specific stellar evolutionary phase, represented by the point at which its red giant phase ends.

[6]BAO are fluctuations in the density of the visible baryonic matter of the Universe, caused by acoustic density waves in the primordial plasma of the early Universe. As previously mentioned, they can be used as "standard rulers"

[7]The weak lensing is a particular lensing phenomenon in which the light deflection due to gravitational fields is impossible to detect in a single background source.

2.2 Cosmological Issues

After the introduction of GR and the ΛCDM model, and some examples of their successes, let us now discuss some "hot-topic issues" regarding these theories, that need to be addressed in order to have a complete and satisfactory view of our Universe [11, 7]. In this section, we will present some of these problems, while, in the next chapters, we will show some tools that have the ultimate aim of trying to overcome them, both from an observational and theoretical point of view. We will anticipate that some of these issues can be addressed, at least theoretically, using the Extended Theories of Gravity (ETGs), which will be treated more extensively in Chapter 6.

2.2.1 General Relativity and Quantum Gravity

GR and the Quantum Field Theory (QFT) are the pillars upon which modern physics is based. The former has been very successful in describing gravitational systems at large-enough scales, while the latter excels in the description of physical processes at high energy regimes or very small scales, where a classical paradigm breaks down. However, in their current state of the art, the two theories do not consider the regimes in which the other excels: GR is a classical theory that does not take into account the quantum nature of matter, while QFT assumes that space-time is flat, and even its extensions, such as QFT in curved space-time, consider space-time as a rigid arena inhabited by quantum fields [11] and, so, not as a variable itself, as is the case for GR.

Even if experiments related to gravity at scales at which quantum effects become important are improbable also in future experiments (the Planck scale under which these phenomena would become relevant is 10^{-33} cm [11]), it would still be interesting to find a theory being able to describe all scales of the known Universe in a comprehensive way (the so-called "theory of everything"). Also, some fundamental issues are linked to the Planck scale itself, the most relevant being the Big Bang scenario, according to which the Universe inevitably goes through an era in which its dimensions are smaller than the Planck scale (Planck era) [46], that, incidentally, is currently also the most obscure period of the history of our Universe. This particular issue is the reason why formulating a "quantum cosmology" paradigm is a necessary step to understanding the initial conditions of the Universe and having a complete picture of it since its birth.

From a quantum mechanical point of view, the Universe should be described by a wave function, which assigns a certain probability to obtain a particular configuration of space-time and matter variables. From this theoretical line of research seems that the Universe can enucleate from the "void" [46], i.e. a configuration without a classical space-time. The wave function can be used to calculate the probability of this phenomenon.

The main issue with this approach is the unification of gravity with other natural forces. In this regard, many efforts have been performed by the scientific community in the past decades. In the quantum approach, the states of a physical system are represented by a vector in a Hilbert space $\mathcal{H}$, while the physical fields are represented by linear operators defined on domains of $\mathcal{H}$. The fundamental, conceptual issue is that GR describes simultaneously the gravitational degrees of freedom and the background space-time in which these are defined. This means that, in order to define the concepts upon which GR is based, it is mandatory to solve the field equations that can give a certain space-time as a solution. This problem becomes complex in Quantum Gravity: because of the Uncertainty Principle, particles do not have a definitive trajectory: the temporal evolution provides a probability amplitude $\psi(x,t)$; so, the evolution of an initial state does not give a specific space-time, which means that we cannot define basic concepts of GR, without which cannot be defined, like causality relation, a specific time and so on.

Because of the difficulties of building a complete theory unifying interactions and particles, during the last decades, the two aforementioned pillars of modern physics have been critically re-analyzed by the scientific community. For instance, regarding GR, it is assumed that the geometry (i.e. the Ricci tensor or the Ricci scalar) interacts directly with quantum matter fields, which back-react on it. This interaction necessarily modifies the standard gravitational theory, that is, the Hilbert-Einstein Lagrangian of gravity is modified by adding effective fields to the Ricci scalar, this is one of the first examples of an ETG theory.

To try to overcome the previously mentioned problems, two approaches have been used, which have given different answers [11]: the canonical approach, which is based on the Hamiltonian formulation of GR, and aims at using the canonical quantization procedure [84, 85], and the covariant approach [11, 86] which tries to use the same procedures and concepts of QFT by splitting the metric tensor and using a perturbative approach. Both methods have achieved some interesting results during the past years, but they also present some issues that did not, up to now, allow them to solve definitely this fundamental issue.

Of course, Quantum Gravity, as with any other physical theory, has to be confirmed by experiments (or, in this case, observations). Two possible tests for this kind of theory are [11]:

- The evaporation of black holes (BH): a key observation would be the final evaporation phase of a BH. To this end, it would be useful to observe the signatures of primordial BH. These objects are forming not at the end of stellar collapse, like for the ordinary stellar-mass BH, nor as a merging mechanism as the supermassive BHs in the core of the galaxies. Instead, they can originate from strong density

perturbations in the early Universe. In the context of inflation, their initial mass can be as small as 1 g. Primordial BH with initial masses of about 5×10^{14} g would evaporate at the present age of the Universe. Up to now, no such object has been observed yet [87], also given the extreme conditions that should be studied to achieve such an observation.

- Cosmology: quantum aspects of the gravitational field may be detected in the anisotropy spectrum of the CMB. Future experiments may be able to observe the contribution of the gravitons generated in the early Universe [45].

2.2.2 The Inflationary Paradigm

Having briefly explained why it is necessary to introduce Quantum Gravity to explain the initial conditions of the Universe, let us now take into account other observational issues related to the ΛCDM model. Indeed, several observations cannot be explained by this model by itself, which have bought a new paradigm describing the early times of the Universe's expansion. The issues are summarized as follows [46]:

- Homogeneity: photons that cannot be casually connected if the expansion of the Universe is due just the ΛCDM model show the same temperature, thus proving a physical connection between them.

- Asymptotic Flatness: observations show that the Universe is very close to being spatially flat [88] (even if some evidence for a closed universe has been found [89]), but any small departure from the flatness in the early times of the Universe's history would have been amplified by the dynamical evolution of the Universe itself, thus arriving to a "fine-tuning" issue.

- The absence of magnetic monopoles: magnetic monopoles are naturally predicted by many grand unified theories [90], and yet they have never been observed.

- Formation of Structures: high scale structures, bigger than 50 Mpc, have been built during the expansion of the Universe. These regions should not be causally connected.

These problems have brought to the so-called inflationary paradigm, according to which, during the early epochs of the Universe, there has been an exponential accelerated phase, during which the Universe itself has expanded by a factor of approximately e^{60} in a very brief time interval [46]. This expansion can address all the problems mentioned above. For instance, according to this idea, we do not see magnetic monopoles because we can casually see just a small fraction of the Universe that has exponentially expanded

in the early times, so they could exist in a place that we cannot reach, while the casual connection of large structures can be explained by the fact that they started to form when their components could be causally connected.

While the ΛCDM model is well defined, there is not yet a unique theory for the Inflationary Paradigm (which, itself, is beyond the standard cosmological model). Indeed, two main classes of Inflationary models exist: the first consists of a description of gravity where the Einstein GR equations are used, and a scalar field (or more scalar fields) are employed as a source term for the inflation, while in the second both the equations and the source term are modified. The latter framework seems to work better than the former because eliminates a great number of problems connected to the choice of the particular gravitational theory [46]. The ETGs fall in the latter framework. Indeed, the inflationary scenarios related to ETGs seem to be concordant with the CMB observations [91, 92, 93, 94]. This is because it is possible to demonstrate that the higher order and non-minimally coupled terms in an ETG can always be associated with additional scalar fields via a conformal transformation [95]. This association can be useful also because they allow considering multiple inflationary events to produce structures at different scales [91, 96], with the idea of different inflationary epochs which are associated with different scalar fields.

Lastly, inflationary models based on ETGs could solve the "Graceful exit problem" [97], which consists of the theoretical explanation of the end of the inflationary phase and the beginning of the ordinary acceleration phase of the Universe [98].

2.2.3 Dark Matter and Dark Energy

As previously mentioned, according to the ΛCDM model, up to 95% of the Universe is composed of either dark matter or dark energy, which have been introduced to match the observations to the standard cosmological model and GR [64, 66, 6]. The main issue regarding these physical quantities is that their nature remains completely unknown. Related to dark matter, a plethora of very precise, fine-tuned experiments have been performed (and are still being performed) [8, 9, 10], from many collaborations and faculties, like the GSSI and CERN, but, up to now, only null results have been found regarding the nature of this quantity. A similar situation applies to dark energy. As we have seen, dark energy, for the ΛCDM model, is parameterized by a constant density, Ω_Λ, introduced to explain the accelerated expansion of the Universe, but, again, its nature is still a complete mystery. One of the most pressing matters regarding this constant is its value: there is, indeed, an enormous discrepancy between the value measured by cosmological observations with respect to the same quantity computed by particle physics as the zero-point energy in the vacuum [11] (a striking difference that can be as high as 120 orders of

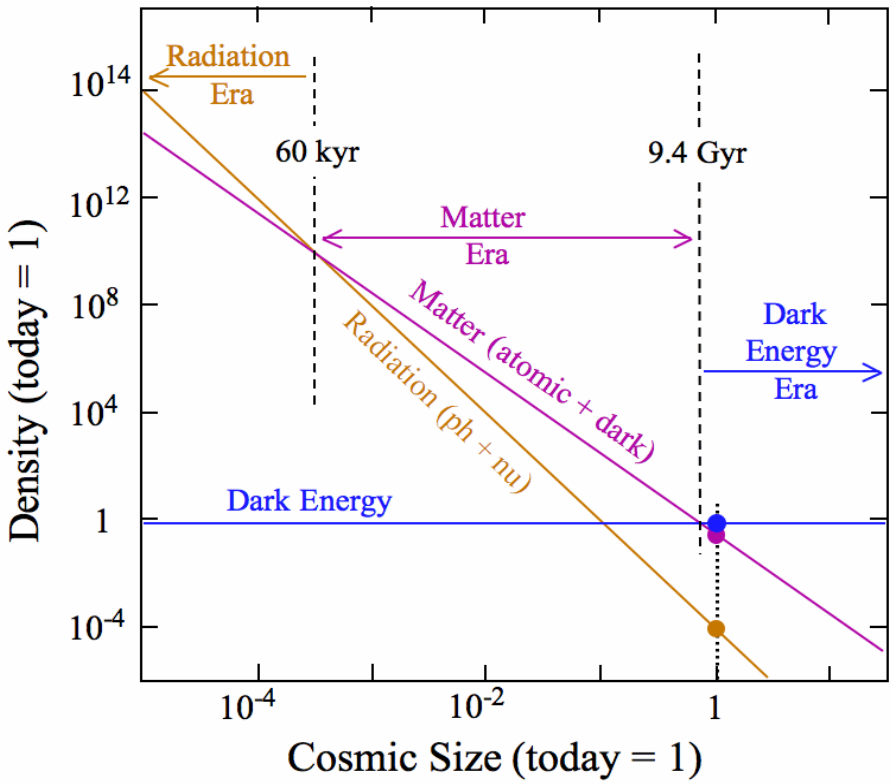

Figure 2.2: The evolution of the densities composing the universe with the time. Both axes are on a logarithmic scale.

magnitude). Also, according to the ΛCDM model, it seems that we live in a very special epoch, where the dark energy density is of the same order of magnitude with respect to the matter density, which is arguably a highly odd coincidence, given that latter evolves with the cosmological time while the former should remain fixed: this issue is known as the coincidence problem [99].

To understand this conceptual problem, we consider the densities evolution in the Universe with the time shown in Figure 2.2 [8]. In particular, we note how peculiar the concordance in order of magnitude of Ω_M and Ω_Λ (that acts like a constant as described by the ΛCDM model) is in our current time, given the evolution of Ω_M and Ω_K. We also note that this coincidence should not be verified in any other cosmological epoch given this evolution.

The dark energy constant is associated with an equation of state of the type $w = -1$ [7]. There exist also models in which the dark energy is not simply a constant [100, 101], but it is represented by a scalar field ϕ rolling slowly down a flat section of a potential $V(\phi)$ and giving rise to the models known as quintessence [102]. One of the main issues of this kind of theory is still the coincidence problem: even if the scalar field

[8] figure taken from https://physics.stackexchange.com/questions/233801

is evolving with time like the other densities, there is no reason, according to our current understanding, about why the dark fluid and the matter density are of the same order of magnitude in the current epoch. Also, the scalar field related to these models has an unknown nature itself.

Other possible schematizations of dark energy have been introduced in the past years [103], like models in which interactions between dark energy and dark matter are taken into account [104]. There are also hypotheses according to which only one cosmological fluid exists, that acts like dark energy at low densities and dark matter at high ones. For this class of theories, the coincidence problem is naturally solved, because this framework addresses the transition from a matter-dominated era to a dark energy-dominated epoch [105].

In summary, for the ΛCDM model, 95% of the Universe is still unknown, many models and schematizations exist trying to provide a comprehensive physical origin to these mysterious quantities, but still, no experimental evidence has been found. Also, all these hypotheses can bring different cosmological models that are able to explain the accelerated expansion of the Universe; thus, there exists a degeneracy between those, that cannot allow us to discriminate among them.

There are other possibilities to explain the effects normally attributed to dark energy and dark matter, that would imply going beyond GR and the ΛCDM model, as well as a change of perspective on the problem itself: one of those regards the possibility of introducing non-standard electromagnetic effects due to possible extensions of the Maxwellian theory [35], which will be extensively detailed in chapter 5, the other is considering, again, the ETGs: indeed, for this second approach, the observed acceleration is not the manifestation of yet another ingredient of the cosmic pie, but rather the first signal of a breakdown, in the infrared limit, of the laws of gravitation as we understand them [106]. Indeed, for this framework, we are considering the idea that the acceleration originates from a "geometrical" source, rather than a material one [107]. For instance, a cosmological constant may be recovered as a consequence of a non-vanishing torsion field, able to match the observations [108]. SNe Ia data could also be efficiently fitted by including in the gravitational sector higher order curvature invariants [109]. In the literature, there are many other theoretical frameworks using ETGs that attempt to go beyond the dark universe described by the ΛCDM model, naturally providing a cosmological component with negative pressure originating from the geometry of the universe. Given the abundance of these models, an issue regarding the degeneracy of these, as the one mentioned above related to the nature of dark energy, still exists. This is because there exists only a limited number of cosmological tests to discriminate between these models [91]. We expect that this issue, with time and the certain future improvement of the

detectors and experimental apparatuses, should be overcome by the scientific community.

The important point is that the ETGs have to be as successful as GR in the appropriate energy scales, while also overcoming its limits. This means that, in the weak field limit, they have to be able to reproduce the same results obtained in GR, while also improving them if possible. Indeed, even the weak limit is a matter of debate concerning the ETGs: in fact, some of them do not reproduce exactly the Einsteinian results in their Newtonian limit but, in some sense, generalize them. For instance, the ETG with Lagrangian $(R + \alpha R^2)$ gives rise to Yukawa-like corrections to the Newtonian potential with potentially interesting physical consequences, as we shall see in chapter 6. In general, this allows for test beds also at astrophysical scales with weak fields for both GR and ETGs, which could be used to confirm or rule out all these possible theories.

2.2.4 Tensions in the Standard Cosmological Model

As previously mentioned, the ΛCDM model has been very successful in the fit of cosmological parameters, and yet very famous tensions (incompatibilities within the given errors) exist between different measurements which are the object of a very intense discussion in the scientific community [13]. Certainly, the most famous one in cosmology is related to the Hubble Constant, H_0, between the early time measurements using the CMB compared with the late observations deduced using the cosmological ladder. Considering the latest results, the CMB measurements, performed by the Planck collaboration [2], found $H_0 = 67.4 \pm 0.5$ km/(s Mpc), while the latest results presented by the SH0ES collaboration, using the cosmic ladder method, give us $H_0 = 73.04 \pm 1.04$ km/(s Mpc). We are looking at a 5σ tension between these two measurements [12], which in principle should instead present the same result. An interesting fact is that these two values represent two sets, each composed of many measurements: indeed, all the early time estimations of H_0 agree with each other, and the same is true for the late-time deductions [13]. Thus, the tension is between early and late type measurements of this quantity. It is also important to note that the late-time estimates are independent of the ΛCDM model itself, while the observations concerning the CMB are model dependent. One late-time measurement, the cosmic ladder approach, has already been defined previously, but it is important to note again that SNe Ia, Classical Cepheids, and the stellar parallax are not the only astrophysical objects that can be used for estimating H_0 using cosmological probes, as we will see in more detail in the next chapters. Indeed, there have been various attempts in obtaining new values via the cosmic ladder by changing the calibration processes between different steps of the ladder (an example is considering Classical Cepheids that are not in our galaxy but in the Large Magellanic Cloud [110]) or using new probes, like Near Infrared SNe Ia [111]. For a comprehensive review of all the re-

cent measurements obtained using late-time probes, see [13]. The issue is that even if all these measurements are averaged in different combinations, they present a tension between 4.5σ and 6.3σ concerning the Planck results [112, 113]. Considering that we are dealing with measurements, possible systematic effects could be the reason for this tension, but both the Planck and SH0ES teams are being very scrupulous in addressing them, finding that possible systematic effects are not enough for explaining the tension [12], also, only calibration errors would not explain why also other collaborations using different probes find a similar tension. The alternative would be that new physics, beyond the ΛCDM model, is responsible for this tension, which would mean that finding a possible explanation for the tension becomes crucial also at the fundamental level.

In Figure 2.3 a comprehensive collection of results involving H_0 during the years is presented [114], from which we can appreciate the glaring difference between early, indirect type measurements with late direct observations, obtained with different probes.

In recent years, non-parametric models have also been used, which would be able to derive the cosmological parameters directly from the data, without assuming cosmological models a priori [13]. Some examples use cosmography [116, 117], while others use machine learning approaches [118].

As previously mentioned, other possible probes can be used to derive cosmological parameters [119]. The important point is that a plethora of measurements exists in the literature, which falls into one of the two main groups of results from the H_0 tension [13].

A new window on these measurements has been opened by the GW observations, which in principle can be used as standard sirens, i.e., propagating waves whose features are known from the physics behind their origin, which can be inferred independently from their distance, and thus used to derive the distance itself. The first results on the estimation of H_0 using GW show important uncertainties, not competitive with the more conventional measurements, that cannot allow discriminating on which side of the tension these observations may belong (or if they actually fill the gap) [120, 121]. Nevertheless, given that we are only at the dawn of the GW era, significant improvements are expected from this approach in the near future, when new generations of GW instruments will be operational [13].

It is important to stress that, although the H_0 tension is certainly the most famous related to cosmological data, it is not the only tension existing between the results provided by the ΛCDM model and late-time measurements. Indeed, another example is the so-called $S_8 = \sigma_8\sqrt{\Omega_M/0.3}$ tension, where S_8 is a parameter indicating the strength with which matter is clustered in the Universe. Indeed, there is a discrepancy at $2-3\sigma$ level [13] between the measurements given by the Planck data and late time probes, such as weak gravitational lens and cluster of galaxies [14, 15]. In particular, the S_8 mea-

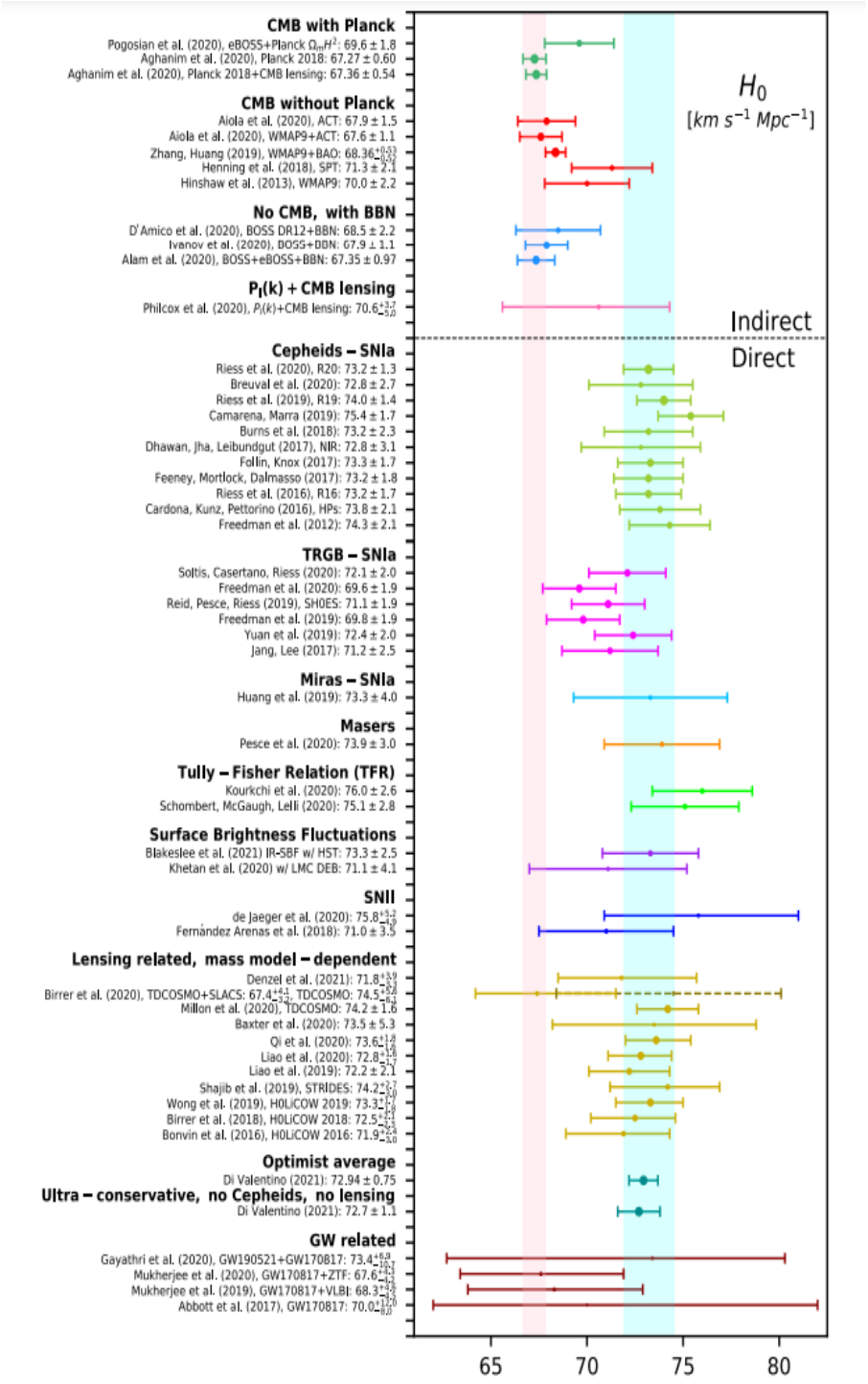

Figure 2.3: In this plot we find various measurements of H_0 with precision at 1 σ level, obtained by different missions and groups, performed up to 2021. The cyan band corresponds to the second to last measurement of the SH0ES team [115] ($H_0 = 73.2 \pm 1.3$ km/(s Mpc)), while the light pink vertical band corresponds to the Planck Collaboration results [2]. Credits for the figure to [114].

surements from CMB data are systematically larger than the late-time measurements. Systematic effects can still play a role in the measurements, as usual, but the fact that we find a tension similar to that related to H_0 from different collaborations even for measurements of different quantities may hint that more fundamental issues are at hand.

Other measurements are also challenging the ΛCDM model, like the previously mentioned possibility, inferred by recent observations, that the Universe is actually closed [89], as well as the so-called "Axis of Evil", which is an apparent correlation between the plane of the Solar System and aspects of CMB, that seems to give us a preferred position in the Universe, which should not be possible considering the Cosmological Principle [122] (the Solar System is only one of the billions of similar systems, why would it have a preferred position in the Universe?). In summary, even if unknown systematic effects, as well as selection biases, are still possible, the scientific community has to understand if they are the sole reason for these tensions or if new physics is at hand, which could modify the ΛCDM model that is, up to now, the most widely accepted model regarding our Universe.

It should also be noted, again, that the ΛCDM model, even considering the issues discussed in the previous sections, is still an extremely successful model able to fit the majority of the cosmological data and to describe with precision a great part of our Universe with a small number of free parameters, which would mean that any alternative theoretical approach must (to the very least) be able to reproduce its results. This consideration may hint at the possibility that the ΛCDM model is actually a very valid approximation to a more complete cosmological model yet to be found (like what is Newtonian gravity with respect to GR). We will see a similar assumption on Maxwell's electromagnetism in chapter 5 and on GR (the ETG framework previously introduced) in chapter 6.

Regarding this point, many possibilities have been proposed by the scientific community in the past decades, some of which, like quintessence models, have already been cited. As we will see, ETG models have also been used for cosmological applications [123, 44].

2.3 Astrophysical Issues

Up to now, issues related to the cosmological point of view have been presented: from the initial conditions of our Universe, to the inflationary Paradigm, to the "mandatory" presence of dark constituents of unknown nature, and finally to the tensions in the cosmological parameters measured by different probes. We now change our perspective and look at some astrophysical observations which may suggest the possibility of theories going beyond GR also to these scales.

Conceptually speaking, the idea of looking for tests-bed hinting at new theoretical discoveries would suggest testing GR in strong gravitational field regimes, where the extreme environment could cause a breakdown of this theory in favor of alternative (or more complete) frameworks, like ETGs. These regions are found near very compact and dense astrophysical objects, like Neutron Stars (NS), or BH.

In general, these kinds of tests are very difficult for two main reasons [124]: the first one is that phenomena occurring in strong gravitational fields are complex, extreme, and often explosive, making it very difficult to find observable properties that depend cleanly on the gravitational field and that allow for quantitative tests of gravitational theories, while the second one is that there is not a general theoretical framework within which quantify deviations from GR predictions in the strong-field regime.

Nevertheless, during the past few years, an incredible improvement in these kinds of observations has been achieved, thanks to the effort of the scientific community: we can think of, again, the birth of GW astronomy. Indeed, the famous event GW170817 [125], which signed the dawn of the GW era, was due to the inspiraling of two NS, which would mean that GW can shed light on the exact extreme events that would be able to test GR by studying phenomena happening near compact objects; indeed, even the observations of GW one century after Einstein's prediction represent, by itself, a beautiful confirmation of GR.

All the historical GR tests have been performed in the Solar System [124], which means that the strongest gravitational field tested by these experiments is found on the surface of the Sun, which corresponds to a gravitational redshift equal to

$$z_{\odot} \approx \frac{GM_{\odot}}{R_{\odot}c^2} \approx 2 \times 10^{-6}, \tag{2.24}$$

and to a space-time curvature defined as

$$\frac{GM_{\odot}}{R_{\odot}^3 c^2} \approx 4 \times 10^{-28} cm^{-2}. \tag{2.25}$$

Of course, these quantities are significantly smaller than what can be found in strong gravitational regimes, like in the vicinity of NS and BH, where we find a gravitational redshift of ≈ 1 and a space-time curvature of $\approx 2 \times 10^{-13}$. With the aforementioned solar system tests, a deviation of GR's prediction using parameterized post-Newtonian (PPN) parameters has been found to be of order $\approx 10^{-5}$ [126]. This would imply that strong field tests could find way more significant deviations from the GR predictions. Related to these regions, we have to note that GR would imply an infinite curvature and matter density in the integration, forward in time, of the Oppenheimer-Snyder equations, which

describe the collapse of a cloud of dust [127, 124]. Clearly, this solution is non-physical and has to be complemented in some other way.

As we already mentioned, the strongest gravitational fields around astrophysical systems can be found near NS and BH in X-ray binaries. Large gravitational potentials, but smaller curvatures can be found around the horizons of intermediate-mass BH (whose existence is still being under investigation, with the closest observational proof being the GW signal GW190521, to which it has been associated a merging of two intermediate-mass BH into a 150 $M_\odot$ one [128]) and in active galactic nuclei. Weaker gravitational fields exist near the surfaces of white dwarfs, main-sequence stars, or at the distances of the various planets in our solar system. Finally, even weaker gravitational fields are probed by observations of the trajectories of the stars close to the black hole in the center of our galaxy (Sgr A*), and by studies of the rotational curve of the Milky Way and other galaxies [124]. A comprehensive map of the gravitational parameters expected by these objects is represented in Figure 2.4. From this figure, we may note that only a limited part of this parameter space can be accessible to experiments. Indeed, the region corresponding to the condition $\epsilon > 1$ symbolizes distances from a gravitating object that are smaller than their event horizon radius and are, therefore, inaccessible to observers. Also, the dark energy itself may influence these tests, especially below the green line visualized in Figure 2.4. Finally, the ability to perform a quantitative test of a gravitational theory also relies on an independent measurement of the mass that generates the gravitational field itself. This is not always possible, especially in various cosmological settings, where gravitational phenomena are used mostly to infer the presence of dark matter and not to test GR. This kind of system is found under the purple line in Figure 2.4.

We also have to note that supermassive NS have been observed in recent years, which would require a very stiff equation of state in GR [129], as well as white dwarfs exceeding the Chandrasekhar's limit [16, 17]. These observations are not easily explained by GR formalism, thus ETG studies have been performed both related to white dwarfs [130] as well as NS [131, 133, 19, 132]. For instance, regarding the NS, it has been found that ETGs are able to insert supermassive NS in their theoretical framework without hypothesizing exotic equations of state, because, considering the same equation of state and initial conditions, they may model, using the mass-radius relation, NS more massive than the GR counterpart. For a comprehensive review of compact objects in ETG theories, see [134].

As we have seen, the extreme regions with very high gravitational fields are the most interesting to test GR and ETGs, but even so, it is necessary to test ETGs also in the weak field regimes, to see if they are able to reproduce the GR results or to quantify if, and how, they are expected to change in the extended formalism (as previously mentioned, the ETG

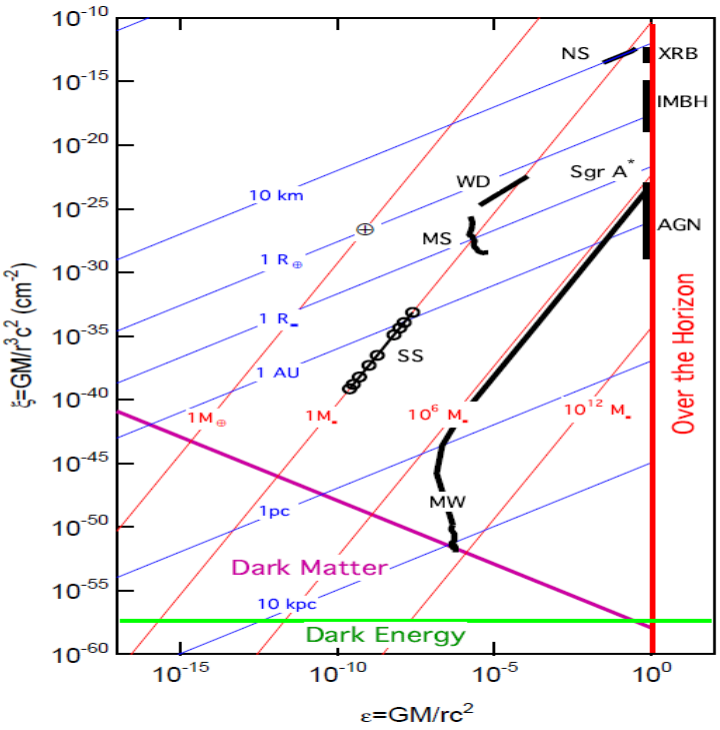

Figure 2.4: A parameter space for quantifying the strength of a gravitational field. The x-axis measures the potential, while the y-axis measures the space-time curvature of the gravitational field at a radius r away from a central object of mass M. These two parameters provide two different quantitative measures of the strength of the gravitational fields. Credits for the figure to [124].

weak field limits is a very debated theoretical point of this paradigm, because some of these limits do not reproduce exactly the results given by GR).

From the observational point of view, moving to the weak gravitational regimes, we note that non-compact stars have been detected, whose inferred mass is not easily explained by the GR (Newtonian) formalism. Up to now, the most massive star has been found in the NGC 2070 star cluster, where a Wolf-Rayet object with an estimated mass of $315M_{\odot}$ has been detected [50] (even if other, new, estimates provide a mass of around $222M_{\odot}$ [135]). This is not the only case of a very massive star [136]. The existence of these very massive stars presents theoretical challenges both from a stability point of view [47] as well as for their birth from interstellar gas [51], and for other observations-derived limits on the stellar mass itself [137]. This is a possible test bed for ETGs in a weak gravitational environment: indeed, as it will be detailed in chapter 6, ETGs, more specifically $f(R)$-Gravity, have been applied to the stellar structure of non-compact objects [49, 48, 138], as well as for their origin from interstellar clouds [52], giving rise to theoretical solutions in the ETG framework which are able to naturally include stellar objects more massive than the structures foreseen by GR in the same initial condition, as well as helping the star formation under the same initial conditions for the interstellar clouds.

Scalar-tensor theories have been used related to different astrophysical distance indicators such as Classical Cepheids [139, 140]. Other tests in the weak gravitational field limit have been performed regarding the two-body problem [141], and the orbit of the so-called S stars around Sgr A*, which we recall is the supermassive black hole at the center of our galaxy [142, 143, 144]. These are only a few examples of the possible tests that can be performed on ETGs in the weak limit, where they are expected to at least reproduce GR results or to even present better fits to the real data due to their generalizations. As previously mentioned, we shall see in more detail a further example of stellar structure in $f(R)$-Gravity for non-compact objects in chapter 6.

Chapter 3

Physics behind the Cosmological Probes

In this chapter, we focus on the physics behind the cosmological probes studied in the following chapters of this thesis. In particular, we focus on SNe Ia, GRBs, and BAO, giving more space to the GRBs.

3.1 SNe Ia

SNe Ia are a particular type of SN. In general, the SNe are very luminous and explosive events associated with stars. A classification of these phenomena based on their detected spectra has been performed in the past decades by the scientific community: in particular, type II SNe present strong hydrogen lines, while Type I do not show them. These two macro-classes have, in turn, been divided into subclasses, always using spectroscopic features. For instance, the type I class is further divided into type Ia (showing silicon lines), type Ib (showing helium lines), and type Ic (without helium nor silicon lines). This classification is still evolving nowadays, with new definitions of subclasses, because of the presence of abnormal SNe showing intermediate features among the previously mentioned features [145, 146].

From a more physical point of view, the classification is drastically different: indeed, while SNe Ia are linked to the explosion of white dwarfs in binary systems exceeding the Chandrasekhar limit because of the injection of mass of the companion star, all the other SNe are believed to be due to core-collapse explosions of very massive stars at the end of their lifetimes. The differences in their spectroscopic lines are a consequence of the nature of the progenitor stars and their evolutionary history. This conclusion is also confirmed by the fact that core-collapse SNe are found in star-forming regions and galaxies, indicating the brief lifetime of their progenitors.

SNe Ia are, instead, given their nature, found in every type of galaxy, meaning that their progenitors can also have long lifespans (as is the case for less massive stars and

white dwarfs). The particular, historical model which agrees well with the majority of SNe Ia observations is the so-called single-degenerate Chandrasekhar-mass explosion model [147], in which the white dwarf accretes mass in a binary system, stealing it from its companion, that is a less evolved star (for instance, a red giant, which is way less dense than a white dwarf, especially in the external regions). In principle, spectroscopic differences may be found also between different SNe Ia depending on the white dwarfs acting as a progenitor (in particular, on the elements of which are composed), but it has been found that the main candidates for the SNe Ia explosion are the carbon-oxygen white dwarfs [148].

After the explosion due to the white dwarf surpassing its stability limit, the burning front moves subsonically, producing heavy elements like iron. The SNe Ia light curves are well-fitted by the deflagration model shown in [149]. SNe Ia light curves are primarily powered by the β-decay of the radioactive ^{56}Ni produced during the explosion [150].

The mechanism behind the explosion of SNe Ia is, in general, well understood. In particular, according to its nature, the luminosity should be approximately the same for every SNe Ia: indeed, they show an absolute magnitude which is around $\mathrm{M} \simeq -19$[151], but both super-luminous [152], as well as sub-luminous [153], SNe Ia have been observed, suggesting the possibility of more complex physical mechanisms, linked to the primary phenomena previously explained, like a delayed detonation scenario for the super-luminous SNe Ia [154], or a double degenerate model in which a merging of two white dwarfs causes the explosion, instead of the so-called single degenerate scenario in which the inflow of matter comes from a non-compact, less evolved star.

Even with these caveats, their nearly uniform luminosity has suggested the scientific community to use them as standard candles. Indeed, SNe Ia are standardizable in the sense that, even if their light curves are not exactly uniform for every SNe Ia, they obey a phenomenological correlation, known as the Phillips relation [68], between the peak magnitude of the light curve itself and luminosity decline rate in each SN Ia. This relation can be parameterized by a stretch factor [155]: in fact, different light curves with different luminosities can be incorporated by one single template once this stretch factor has been applied.

The role of SNe Ia in cosmological measurements has been of fundamental importance [156]. Historically speaking, progress on their actual use as cosmological probes has been performed since the advent of CCD images in the 1990s [157], after which, two main teams have been working on the distance measurements of high-z SNe Ia: the Supernova Cosmology Project (SCP) and the High-z team (HZT). These measurements have also been used to infer the best-fit parameters of cosmological values, like Ω_M and Ω_Λ. These observations showed SNe Ia at high-z that were fainter in a flat,

matter-dominated universe with $\Omega_M = 1$ than their lower redshift counterparts. This fact has brought to the reintroduction of dark energy and to the currently accepted best-fit parameters of $\Omega_M \sim 0.3$ and $\Omega_\Lambda \sim 0.7$, which implies an accelerated expansion of our Universe, as anticipated in the previous chapter.

Since then, SNe Ia have been a cardinal part of the distance ladder, and have been used in many works in the literature regarding the measurements of cosmological parameters. This has brought the scientific community to create more and more complete SNe Ia catalogs, where careful analysis has been performed on the light curves and redshift estimations. One of the most recent catalogs is the so-called Pantheon sample [20], composed of 1048 SNe Ia collected from many observational campaigns, which are CfA1-CfA4 [158, 159, 160, 161, 162], CSP [163], LOSS [164], ESSENCE [165], SNLS [166], SDSS [167], PS1 [168], SCP [169], GOODS [170] and finally CANDELS/CLASH [171, 172]. The redshift interval of the Pantheon sample goes from $z = 0.01$ up to $z = 2.26$. This is also the SNe Ia sample that has been used for the cosmological application that will be presented in the following chapters, in which we will show also how we have treated the information provided by this sample for our cosmological computations. Very recently, an update of this sample, called Pantheon+ [36], has been used for the new estimate of H_0 of the SH0ES program [12, 173]. This is an extension of the Pantheon set, and it is composed of 1701 light curves taken from 1550 SNe Ia, with the new additions being especially in the low redshift regions, to further increase the reliability of the calibration procedure on the Classical Cepheids.

3.2 Gamma-Ray Bursts: introduction

As we will see in the next section, one of the studies performed in this thesis has been focused on applying GRBs as cosmological tools together with other probes. In this section, we shall describe the phenomenology and the physics behind these astrophysical objects.

GRBs are incredibly luminous explosions, in fact, the most luminous transient phenomena in the Universe after the Big Bang (Indeed, the most luminous GRBs are 11 orders of magnitude more luminous than the typical SN Ia). They are irregular pulses of radiation lasting typically less than one minute with a non-thermal (broken power-law) spectrum peaking at $\sim 10 - 10^4$ keV [23]. Their nature is clearly intergalactic, as it was noted because of the observations not having a preferred plane coincident with our galaxy disk, but being homogeneously distributed in all the sky. Indeed, the furthest GRB ever detected has a redshift equal to $z = 9.4$ [22], much beyond the limit reached by SNe Ia.

GRBs' emission is usually divided into two phases, a prompt main emission followed

by what is called the afterglow phase. Different observational campaigns and satellites have been used in the past decades to detect observations in the high-energy spectrum, allowing us to shed light on the phenomena involved in GRBs emission. One of the most important instruments from this point of view is the Neil Gehrels Swift Observatory (hereafter Swift) [174], launched in 2004, thanks to which many observational features, that will be presented in the following paragraphs, have been revealed.

Observationally speaking, the prompt emission duration is described by a histogram in the time duration presenting two peaks, the first around 0.3 s, while the second at 30 s, with a gap around 2 s [23]. This fact has led to the first, macro-classification of GRBs into two main classes, the Short GRBs and Long GRBs, depending on the duration of the prompt emission: indeed, if this duration is less than 2 s, we are talking about a Short GRB, while, for the opposite case, of a Long GRB [175, 176]. To be more precise, the parameter measured is known as T_{90}, which is the time over which a burst emits from 5% to 95% of its total measured counts in the prompt emission. The different prompt duration has suggested to the scientific community that there are two, main, different physical mechanisms acting as the engine of these objects, which is also confirmed by the fact that, usually, Short GRBs are harder (present a more relevant high-energy component with respect to the total detected energy) than the Long GRBs.

GRBs prompt light curves have been compared to snowflakes: indeed, it is very hard to observe two GRBs with very similar prompt light curves [177], but there are some features in common, like the presence of asymmetric pulses given by sharp rises and shallower decays [23], and the duration themselves.

From a spectral point of view, the prompt emission is usually well described by the so-called Band Spectrum [178, 179], which is characterized by two decay phases divided by the so-called knee of the spectrum. The energies characterizing the prompt emission are typically very high: indeed, it is often detected from the hard X-ray band up to 100 MeV γ-rays, with sometimes also an optical component [24].

The second part of the total GRB emission is called afterglow: it is the long-lasting energy emission following the main explosion, usually detected in different wavelengths (X-rays, optical, and sometimes radio). Generally, the time evolution of the afterglow is divided into five main components [23]:

- A very steep decay phase right after the prompt emission.
- A very shallow decay phase called the plateau, in which the flux remains almost constant.
- The normal decay phase.
- A late steepening of the decay phase.

- flaring activity which may happen through the entire afterglow emission.

Each of these phases is divided by "breaking points" in time. This is the main scheme that can describe fairly well the majority of the afterglow light curves, but there are some exceptions: for instance, in [180] a particular Short GRB has been studied whose afterglow cannot be described by the summary presented above, showing a very steep decay phase after the plateau.

As we will discuss, the second break in the afterglow light curves is attributed to the so-called jet break, due to the relativistic and collimated nature of GRBs' ejecta. Given this assumption, the break should be achromatic, as it is indeed the case for the majority of the GRBs [181], and yet, even for this feature, exceptions have been observed, where a relationship between the position of this break and the spectral band has been noted [182]. Just from the description above, we notice how the observations suggest that GRBs are way more varied in their phenomenology than SNe Ia, both photometrically and spectroscopically.

A very important observation related to the GRBs involves the electromagnetic counterpart of the gravitational wave event GW170817 [183]: indeed, the X-ray counterpart has been identified with a Short GRB, while the softer side to a Kilonova (KN) [184], which is an explosive event following the coalescence of two compact objects, thus presenting an evident link between a Short GRB with its progenitor as well as with a gravitational wave event. On the link between KNe and GRBs, we shall return in the next sections.

Another association suggested by the observations is between the Long GRBs and core-collapse SNe [185]. All these facts have led the scientific community to understand that high-energy processes, such as synchrotron radiation and inverse Compton scattering, must be at hand to describe the emission due to GRBs. Indeed, the main model of GRBs describes them as a central engine expelling ejecta moving at relativistic speed in a collimated beam. This ejecta creates a shock front with the interstellar medium which is responsible for the energetic processes detected during the afterglow. This external shock scenario [186], is able to describe the five components afterglow light curve described above, while to explain the observation in [180], internal shocks in the ejecta itself must be taken into account [23], which may be due to the reverse shock formed at the front with the interstellar medium moving backward in the ejecta itself, as well as because of the formation of internal shock fronts. A long-lasting activity of the central engine itself during the afterglow phase may also be considered for these internal plateau scenarios. In general, the difference between the internal and external plateau can be derived from the value of the temporal power-law (PL) decay index of the plateau, α_i [24]: a very steep decay indicates the possible internal origin of the plateau [187, 188].

The second break in the light curve mentioned above is believed to be due to the collimated form of the emission and its relativistic velocity: indeed, due to the relativistic nature of the jet, in the first phases of the emission, the related relativistic angle is smaller than the collimation one, so that all the radiation can be seen by an external observer. Due to the shock front slowing down, then, the magnitude of the relativistic angle reaches and surpasses the collimation limit. After this event, only a part of the full radiation budget can be detected, and the break in the light curve happens. The chromatic behavior observed for some GRBs of this break may be explained by the different possible emission sites (In particular the reverse shock and the long-lasting energy injection from the central engine itself) [23].

All these observational facts have led the scientific community to two main possible astrophysical phenomena, that may lead to the explosion of GRBs, which are either the coalescence of two compact objects [189] or the explosion of very massive stars [190]. These models have found evidence in the observations mentioned above. Usually, Long GRBs are associated with the core-collapse models, while Short GRBs to the merging, but there have been some exceptions: for instance, there have been observed Long GRBs with no-SNe associations, even in situations where the SN should have been clearly detected, like the nearby $z = 0.09$ SN-less GRB 060505, and GRB 060614A, with $z = 0.125$ [24], which could mean that the associations Long GRBs-Collapse of very massive star/ Short GRBs-Merging of two compact objects may not be perfect, and some outliers can be found.

Related to this point, a classification scheme has been proposed based on the progenitors themselves [191]: Type I GRBs are related to the merging of compact objects, while Type II GRBs are associated with the collapse of massive stars. This classification is linked to observational evidence going beyond the prompt duration itself.

In particular, type I GRBs have the following principal features [186, 191, 24]:

- Prompt duration ≤ 2 s.
- No SN association.
- Detected in elliptical or early-type galaxies, where generally no massive stars are found, and with low star formation rates (SFRs).
- They received a "natal kick" so that they are pushed away from their original birth site.

Meanwhile, type II GRBs may be identified by:

- Prompt duration ≥ 2 s, also considering the $(1 + z)$ factor due to the cosmological distance.

- Clear SNe association.
- Detected in galaxies with high star formation rates.
- They explode in the same location where the progenitor stars are formed.
- A stratified stellar-wind-type medium [192, 193].

Regarding the central engine powering GRBs, there are again two main models that are widely accepted by the scientific community: either the central engine is a hyper-accreting BH, or a fast rotating highly magnetized neutron star, known as a magnetar [23]. Indeed, from the observations, the central engine has to be able to launch an extremely energetic jet far surpassing the Eddington Luminosity limit. Also, they should be intermittent and be able to reactivate at later times, to explain the flaring activity detected during the afterglow emission. These two models satisfy all these features.

It is possible to distinguish between the two central engine models from the phenomenological features [194, 195]. A summary of the differences between these models is as follows [23]

- The magnetar model has an upper energy limit of around 10^{52} erg, while this limit does not exist in the accreting BH model. The problem to discern between the two models using this feature is the collimated nature of GRBs emission because it would not be possible to detect directly the total energy of an off-axis jet.
- The requirements regarding the rotation rate are more severe for the hyper-accreting BH model.
- A steep decline of the X-ray light curve at the end of the prompt phase can be explained more easily by the hyper-accreting BH model.
- The combination of a flat X-ray light curve (which would require a constant accretion rate) and a subsequent very rapid drop is more understandable in the magnetar framework.
- X-ray flares are easier to schematize using the magnetar model.

It is also necessary to note that other alternatives have been proposed by the scientific community, both regarding the central engine and the progenitors of GRBs [23]. Also, differently from the SNe Ia case, these physical central engines do not impose a strictly defined morphology, given that they have to encompass events that may be very different from one to the other.

As it may be noted from the introduction above, the physics behind GRBs is way more heterogeneous than what can be hypothesized for SNe Ia. Indeed, many more GRBs subclasses have been defined in the past years [24], going beyond the macro-classes previously described: in fact, we find the X-ray flashes (XRFs) with unusually soft spectra and greater fluence in the X-ray band (2-30 keV) than in the γ-ray band (30-400 keV), the Ultra-long GRBs (ULGRBs) with a very long prompt duration [196, 197], GRBs that show a detectable association with SNe Ia [185]. We may also find GRBs that present features between the Long and Short GRBs, called Short GRBs with extended emission (SEE) [198]. We will show how these and other subclasses have been studied in [24], for now, we note that, in general, they are not even mutually excluding, so a single GRB may belong to different subclasses.

3.3 Gamma-Ray Burst correlations

Even considering the complexity of the astrophysical processes that may lay behind GRBs, in the last years, the scientific community has noticed different important correlations between physical parameters involving both prompt and afterglow GRB features. In this section, we shall briefly present some of these and then go into more detail about a particular fundamental plane correlation, that has been used by us both as a discriminator between classes as well as a possible cosmological tool, as we will see.

One of the first correlations discovered is the so-called Amati relation [23], between the photon energy at the peak of the prompt spectrum in the rest frame of the GRB, $E_{p,z}$, and the isotropic gamma-ray energy spectrally extrapolated to a standard energy band in the GRB rest frame $E_{\gamma,iso}$ [199]. This relation is found for Long GRBs with known redshifts and has also been used for cosmological computations [200, 201], as we will see. Even if it has been suggested that this correlation is due to selection biases [202], counter-arguments show that these effects cannot completely delete the relation [203], but they may still increase the intrinsic scatter on the correlation itself [23], which, as we shall see, is a parameter of utmost importance for possible cosmological applications.

Another correlation regarding only prompt phase variables has been discovered between $E_{p,z}$ and the isotropic gamma-ray luminosity of a burst at its peak flux, $L_{\gamma,p,iso}$ [204, 205].

The $E_{p,z}$-$E_{\gamma,iso}$ correlation is valid for Long GRBs, while the Short GRBs do not seem to follow the same trend [23]. Indeed, Short GRBs seem to follow a parallel track with respect to the Long ones, which means that, at the same value of $E_{p,z}$, the Short GRBs are systematically less energetic. This can be attributed to their shorter duration, which hints that luminosity may be more intrinsically related to $E_{p,z}$. Indeed, the $E_{p,z}$-$L_{\gamma,p,iso}$

does not separate Long and Short GRBs [206].

Another correlation has been proposed directly linked to the $E_{p,z}$-$E_{\gamma,iso}$ relation, in which the jet opening angle, θ_j, of the GRB emission is considered in the following way [207]: $E_\gamma = (1 - \cos(\theta_j))E_{\gamma,iso}$, so that a new relation $E_{p,z} - E_\gamma$ is defined. The jet opening angle is linked to the jet break detailed in the previous section and expresses how collimated the GRB is. This is a tighter correlation than the $E_{p,z}$-$E_{\gamma,iso}$ one, but, as we have already noted, the achromaticity requirement necessary for the geometrical nature of the jet break is not satisfied by every detected afterglow [23].

Three-parameter correlations have been discovered as well, like the $E_{p,z}$-$L_{\gamma,p,iso} - t_{b,z}$ [208], where $t_{b,z} = t_{obs,b}/(1+z)$ is the afterglow light curve break time in the rest frame of the burst measured in the optical band. Another three-dimensional correlation has been discovered between $E_{p,z}$, $L_{\gamma,p,iso}$, and $T_{0.45,z}$ [209], where $T_{0.45,z} = T_{0.45}/(1+z)$, and $T_{0.45}$ is the time spanned by the brightest 45% of the total counts above the background (Usually, the prompt emission duration is measured with the aforementioned $T_{0.90}$, which has a definition clearly linked to $T_{0.45}$).

Many other relations have been discovered as well between other observational features, for instance in [210, 211, 212]. For a more complete review see [23]. Finding correlations between GRB physical parameters is a fundamental step to shed light on their interior mechanism, discerning between different types of GRBs and, ultimately, using them as cosmological probes, by inferring their luminosities via these relations from features non-depending on their distance from us. Indeed, just these main objectives are enough to explain the interest surrounding GRBs correlations and their scientific applications, in particular in finding ways of making them tighter and tighter.

We now introduce the GRB correlation that has been used for our analysis. Historically, one of the possibilities introduced by the observations performed by Swift was the idea of using afterglow physical quantities to introduce new correlations [213, 214, 215]. The advantage of using afterglow features is the smaller variability characterizing them than the prompt physical quantities, which we recall may differ substantially between GRBs. One of these correlations is the so-called Dainotti relation [216], between the X-ray rest-frame end time of the plateau $T^*_{a,X}$ and its correspondent luminosity $L_{a,X}$. This particular correlation has been extensively studied and confirmed in [217, 215, 218]. This relation has been linked to the different theoretical models presented in the previous section, which could be able to physically explain it, such as the accretion onto the black hole [219], or the spin-down of a magnetar [220, 221, 195]. According to the latter model, we can link the physical parameters of the correlation to other quantities describing the magnetar itself, like the moment of inertia and the spin period, through the following equations

$$L_{0,49} \propto B_{p,15}^2 P_{0,3}^{-4} R_6^6, \tag{3.1}$$

$$T_{em,3} = 2.05 I_{45} B_{p,15}^2 P_{0,-3}^2 R_6^{-6}. \tag{3.2}$$

In these equations, $L_{0,49}$ is the plateau luminosity in $10^{49} ergs^{-1}$, I_{45} is the moment of inertia in units of 10^{45} g cm^2, $B_{p,15}$ is the magnetic field strength at the poles in units of 10^{15} G, R_6 is the radius of the NS in 10^6 cm and $P_{0,-3}$ is the spin period in milliseconds. From these equations, we can derive the following

$$\log L_0 \propto (\log(10^{52} I_{45}^{-1} P_{0,-3}^2) - \log(T_{em})), \tag{3.3}$$

where we note that the first term may be interpreted as a constant for a given fixed period of the magnetar and momentum of inertia, and the luminosity is inversely correlated with the rest frame time at the end of the plateau emission.

Another possibility concerns a modification of the microphysical parameters model [222] which considers jets viewed slightly off-axis [223].

Recently, this 2-D correlation has also been studied in the optical band, considering the same physical quantities in this new spectral region ($T^*_{a,OPT}$, $L_{a,OPT}$) [224]. Correlations in the optical band were already discussed in [225]. We will return to this point in the next chapter, in particular for the cosmological applications. Given that the slope of the optical relation is similar to the $X-$ray correlation, the physical interpretation of this relation can also be linked to the spin-down of a magnetar model.

This relation has also been extended by discovering a third parameter, linked to the relation itself in the X-ray wavelength, which is the peak prompt luminosity, $L_{peak,X}$, thus defining a new fundamental plane correlation for GRBs, involving both afterglow and prompt features. This fundamental plane presents an intrinsic scatter smaller than the one of the corresponding 2-D relation, and has been extensively studied in the following papers: [226, 25, 24, 227, 228, 229]. In particular, we shall see more in-depth the analysis performed in [24] in the next section, while in [25] we see the first use of this fundamental plane as a discriminator between GRB classes, in [229], instead, we see how this correlation has been used to discriminate among several scenarios of slow or fast cooling in a wind or a constant interstellar medium. Finally, in [227, 228] the closure relations and the correlation in the high-energy spectra using the Fermi-LAT observations have been analyzed. From a theoretical point of view, also the fundamental plane can be linked to the magnetar scenario [195], by the anti-correlation between L_{peak} and the spin period within the model of the pulsar spin-down found in [230].

3.4 GRB classes and the fundamental plane

We now go more in-depth into the analysis performed in [24], in which we have used the fundamental plane correlation for different GRB subclasses, to note if dissimilarities between the classes arise in the best-fit parameters of the correlation. We will show the sample selection as well as the most relevant results reached by the paper.

3.4.1 Sample selection and definition of subclasses

The classes considered are many of the ones mentioned in section 3.2, as well as other subclasses. A detailed description of the data set shall be given once the sample selection procedure will be shown, here we just say that, among the other categorizations, we have also divided the GRBs presenting an SNe association according to the classification shown in [231], which is as follows:

- (A) Clear spectroscopic evidence for a SN-GRB association.
- (B) A clear bump in the GRB light curve, suggesting an association with a SN.
- (C) The same bump described in the previous point, but without any spectroscopic evidence.
- (D) A significant bump on the light curve, but the properties of the SN are not completely consistent with other GRB-SNe associations, or the bump itself is not well sampled, or there is no GRB spectroscopic redshift.
- (E) A bump, with low significance or inconsistencies with other observed GRB-SNe identifications, but with the information of the spectroscopic redshift of the GRB.

In particular, we have gathered the categories (A), (B), and (C) in a separate subset. Also, we have introduced two novelties, the first related to a set of GRBs associated with KNe, and the second to a particularly strict defined subset of Long GRBs.

For the sample selection, we have analyzed all GRBs detected by Swift from 2005 January to 2019 August showing X-ray plateau afterglows and with known redshifts, spectroscopic or photometric, following for this last point [232]. The GRBs have been selected from the Greiner web page [1] and in the Gamma-ray Coordinates Network circulars and notices,[2] excluding redshifts for which there is only a lower or an upper limit.

[1] http://www.mpe.mpg.de/jcg/grbgen.html
[2] http://gcn.gsfc.nasa.gov/

We have downloaded the BAT + XRT light curves from the Swift web page repository. [3], and we have considered all the GRBs that can be fitted by the phenomenological W07 model [187]:

$$f(t) = \begin{cases} F_i \exp\left(\alpha_i \left(1 - \frac{t}{T_i}\right)\right) \exp\left(-\frac{t_i}{t}\right) & \text{for } t < T_i \\ F_i \left(\frac{t}{T_i}\right)^{-\alpha_i} \exp\left(-\frac{t_i}{t}\right) & \text{for } t \geq T_i, \end{cases} \tag{3.4}$$

where both the prompt (index 'i=*p*') γ-ray and the initial X-ray decay and the afterglow ('i=*a*') are modeled. The light curve $f_{tot}(t) = f_p(t) + f_a(t)$ contains two sets of four free parameters (T_i, F_i, α_i, and t_i), where t_i is the initial rise timescale, α_i is both the time constant of the exponential decay and the temporal power-law decay index of the plateau, and F_i is the measured γ-ray energy flux over a 1 s interval at the time T_i.

We have excluded the cases where the afterglow fitting procedure fails or where the determination of the 1 σ confidence intervals does not satisfy the criteria shown in [233] regarding the χ^2.

We have also discarded the GRBs whose light curves can be fitted by black body radiation instead of a PL or cutoff PL. We then followed the criteria shown in [234] to define equality in the light curve fitting of PLs and cutoff PLs. Where such equality is found, we choose the cutoff PL.

Under these criteria, the total sample reduces to 222 GRBs, which we divide into different subclasses. At this stage of the analysis, we define a subset that we call the "Platinum sample", which we are going to use also in the next chapter. This is a subset of the so-called Gold sample, defined in [226, 25]. Let us start from the Gold set: this is a subset composed of only Long GRBs with the following two morphological conditions: the beginning of the plateau should have at least five observed data points, and the plateau itself must not be too steep (the angle indicating the plateau's inclination must be less than $41°$). These criteria allow us to select 69 GRBs from our entire set.

From the Gold sample, we define a second, even more strict, subset, which is selected using both the criteria chosen to define the Gold set as well as the following:

- T_X is not inside a large gap in the data, which allows us to determine it with satisfactory accuracy.
- A long enough plateau duration (at least 500 s), without gaps after it.
- No flares and bumps at the start and during the plateau phase.

[3] http://www.swift.ac.uk/burst_analyser

All these criteria allow us to select 50 Platinum GRBs.

Regarding the Short GRBs, we have gathered in the same set all the proper Short GRBs, the SEE, and the intrinsically short (IS) GRB class, defined by having the rest frame $T^*_{90} = T_{90}/(1+z) < 2$ s [235].

Given these definitions, we now present the subsets used in our analysis. From the total sample of 222 GRBs, we find 138 Long GRBs, 20 XRFs, 22 GRBs with a SN association (SN-GRBs), 14 GRBs with a SN association of type A, B, or C (SN-GRBs-ABC) 43 Short GRBs, 11 ULGRBs, 8 GRBs associated with KNe (KN-GRBs), 69 Gold GRBs, and 50 Platinum GRBs. We have also divided our set following the [186] classification, finding 179 Type II GRBs and 43 Type I GRBs (all the Short GRBs in our case).

The ULGRBs of our set have been selected following [236]. We note again that some of these classes are not mutually exclusive, like for instance the Gold and Long sets. Lastly, we have further segregated the GRBs that may have an internal plateau, following the criteria of the very steep α_i shown in [188, 237]. 12 GRBs have been found following this feature, which we consider as a different class separated from all the rest. After this selection, the final sample is composed of a total number of 222 GRBs divided in the following way: 65 Gold GRBs, 47 Platinum GRBs, 129 Long GRBs, 43 Short GRBs, 22 SN-GRBs, 14 SN-GRB-ABC, 18 XRFs, 10 ULGRBs, 8 KN-GRBs, 167 Type II GRBs and 12 GRBs with internal plateaus. In Tables 3.1 and 3.2, lists regarding the SN-GRB and KN-GRBs and the related parameters used in the fundamental plane correlation are shown. As we will notice, these are one of the most interesting sets investigated in our analysis, because of the results we will achieve with them.

We now focus our attention on the KN-GRBs subset, stressing that the analysis concerning the association of KNe with correlations involving GRB features is a novelty for this kind of approach. As we have seen in section 3.2, one very important observation related to KN-GRBs association is related to the GW 170817 event, which is linked to the Short GRB 170817A, and the KN event AT 2017gfo [238].

Short GRBs are usually discovered through the detection of the γ-ray jet, which means that they are typically observed where the afterglow is the brightest. This implies that the KNe associated with them are more likely to be observed when the viewing opening angle is larger than the jet opening one [239].

We have based our selection of GRBs associated with KNe following the literature, with the idea to use the fundamental plane as a discriminant between classes even when the KN itself is not clearly detected. The 8 GRBs associated with KNe in our set are 060614A, 070714B, 130603B, 070809, 111117A, 140903A, 100625A, and 061201.

In [240, 241] four possible candidates (GRBs 080503, 050724, 070714B, and 061006) have been found for a KN-GRB association powered by a magnetar born after a merging

GRB	subclass	$L_{peak}\ (erg/s)$	$T_X^*\ (s)$	$L_X\ (erg/s)$	z
161219B	B	49.31 ± 0.03	3.95 ± 0.03	45.62 ± 0.03	0.147
060707	C	51.60 ± 0.15	2.94 ± 0.13	48.07 ± 0.10	3.08
081007	B	50.29 ± 0.05	3.40 ± 0.08	46.44 ± 0.06	0.529
090618	C	51.44 ± 0.01	3.485 ± 0.014	47.40 ± 0.02	0.54
091127	A	51.41 ± 0.02	3.81 ± 0.02	47.07 ± 0.02	0.49
060904B	C	50.47 ± 0.03	3.64 ± 0.08	46.36 ± 0.12	0.703
080319B	C	51.73 ± 0.03	5.08 ± 0.09	45.4 ± 0.1	0.937
101219B	B	50.09 ± 0.11	4.23 ± 0.17	45.1 ± 0.1	0.552
120422A	A	49.01 ± 0.08	5.13 ± 0.22	43.66 ± 0.12	0.28
130831A	B	50.862 ± 0.014	3.15 ± 0.09	47.05 ± 0.06	0.479
141004A	B	50.691 ± 0.014	3.11 ± 0.08	46.52 ± 0.09	0.57
171205A	A	47.26 ± 0.09	5.47 ± 0.11	42.06 ± 0.07	0.037
180728A	B	50.474 ± 0.004	3.821 ± 0.015	46.12 ± 0.01	0.117
060218	A	46.08 ± 0.09	5.06 ± 0.14	42.62 ± 0.16	0.033
090424	E	51.707 ± 0.025	2.81 ± 0.01	48.00 ± 0.01	0.544
100621A	E	50.961 ± 0.015	3.45 ± 0.06	47.1 ± 0.1	0.542
120729A	D	50.69 ± 0.04	3.27 ± 0.05	47.1 ± 0.1	0.8
050824	E	49.97 ± 0.14	4.82 ± 0.13	45.24 ± 0.07	0.83
051109B	E	47.76 ± 0.08	3.62 ± 0.13	43.6 ± 0.1	0.08
100418A	D	50.1 ± 0.1	5.33 ± 0.07	44.7 ± 0.1	0.08
150821A	E	53.15 ± 0.14	2.71 ± 0.02	48.53 ± 0.02	0.755
060729	E	49.91 ± 0.04	4.918 ± 0.013	45.97 ± 0.04	0.54

Table 3.1: Table with L_{peak}, T_X^*, L_X with their respective errors, z and the classification according to [231] of the 22 GRBs associated with SNe present in our sample. All the values presented here except the redshift are in logarithm.

GRB	$L_{peak}\ (ergs^{-1})$	$T_X^*\ (s)$	$L_X\ (ergs^{-1})$	z
060614A	49.51 ± 0.02	4.98 ± 0.03	43.81 ± 0.04	0.125
061201	49.00 ± 0.02	3.45 ± 0.09	45.04 ± 0.09	0.111
070809	49.06 ± 0.04	4.1 ± 0.2	44.1 ± 0.2	0.219
070714B	50.74 ± 0.02	2.95 ± 0.09	46.9 ± 0.1	0.92
100625A	50.09 ± 0.02	2.28 ± 0.24	46.0 ± 0.4	0.452
111117A	51.0 ± 0.2	2.5 ± 0.1	46.9 ± 0.2	2.21
130603B	50.28 ± 0.05	3.40 ± 0.05	46.1 ± 0.2	0.356
140903A	49.80 ± 0.03	4.16 ± 0.07	45.25 ± 0.06	0.351

Table 3.2: Table with L_{peak}, T_X^*, L_X with their respective errors, and z of the 8 GRBs associated with KNe present in our sample. All values presented here except the redshift are in logarithm.

event between two compact objects. These candidates have been noticed among 96 Short GRBs observed by Swift. Out of these GRBs, the SEE GRB 070714B belongs to our sample as well.

In [242], seven GRBs have been found among a set of 28 Short GRBs which are either associated with claimed KNe or present a shallow decay of the afterglow, which could be a signature of the KN, all of them with known redshift. Out of these seven GRBs, three are also present in our sample: GRBs 060614A, 070714B, and 130603B. GRB 070809 is associated with a KN, but with a less secure redshift according to [242]. GRBs 111117A and 100625A have a probability $> 1\%$ to be associated with KNe. However, given the lack of any other possible galaxy with a similarly low chance association, this connection is more probable than what was previously mentioned. GRB 061201 has a luminosity smaller than 0.35 of the luminosity of the GRB associated with AT2017gfo, which could be a possible reason explaining why the KN has not been clearly detected. Indeed, if a KN were to be present, it should be at least 5 times fainter than AT2017gfo in the blue component [242]. Finally, GRB 140903A is 15 times brighter than the GRB associated with AT2017gfo, meaning that this burst could have masked the KN [243].

3.4.2 Best-fit fundamental planes

We now present the methodology behind the best-fit analysis that we performed for the different subclasses, as well as the results. The fundamental plane is defined as follows:

$$\log L_X = C_o + a \times \log T_X^* + b \times \log L_{peak}, \tag{3.5}$$

where C_o, a, and b are the best-fit parameters that we intend to compute for each subclass. L_X and L_{peak} are defined as

$$L_X = 4\pi d_L^2(z)\, F_X(E_{min}, E_{max}, T_X^*) \cdot \boldsymbol{K}, \quad L_{peak} = 4\pi d_L^2(z)\, F_{peak}(E_{min}, E_{max}, T_X^*) \cdot \boldsymbol{K}, \tag{3.6}$$

where $d_L(z)$ is the luminosity distance, already defined in Eq. (2.17), computed assuming a flat ΛCDM model with $\Omega_M = 0.3$ and $H_0 = 70$ km s^{-1} Mpc^{-1}, $\boldsymbol{K}$ is the K-correction for cosmic expansion [244], and $(E_{min}, E_{max}) = (0.3, 10)$ and $(E_{min}, E_{max}) = (15, 150)$ keV are the limits of the Swift-XRT and BAT band-pass, respectively.

The best-fit has been computed using a Bayesian approach [27], naturally able to derive also the intrinsic scatter, σ_{int}, of the correlation. As for many derivations regarding best-fit analysis performed in this chapter as well as in chapters 4 and 5, the computations rely on *Cobaya* [245], a code for Bayesian analysis in python, that adopts a Markow-

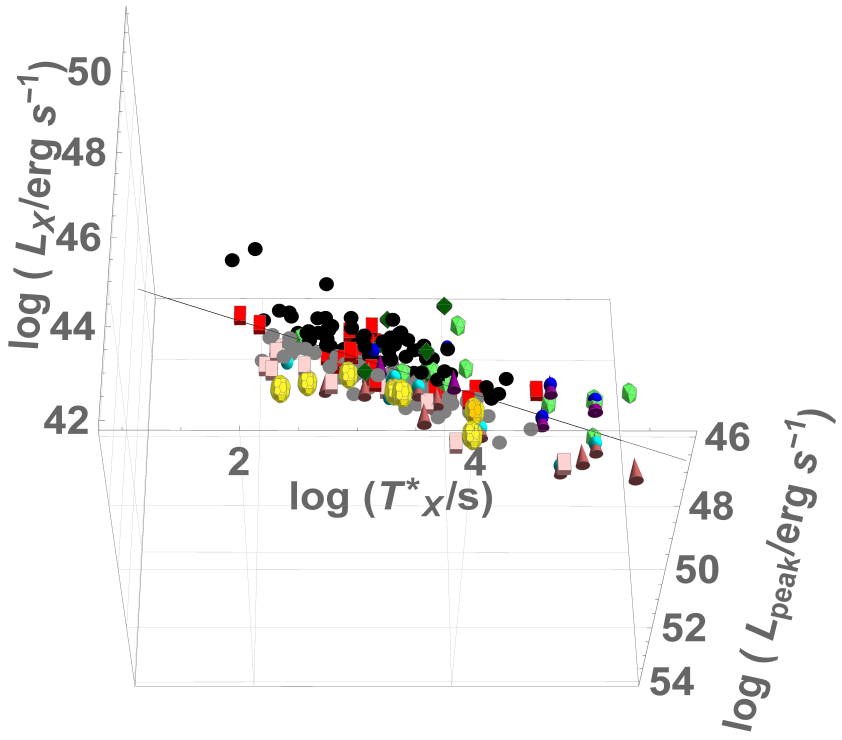

Figure 3.1: The best-fit fundamental plane for the 222 GRBs in the $L_X - T_X^* - L_{peak}$ parameter space, including SN-GRBs (purple cones), XRFs (blue spheres), Short GRBs (red cubes), Long GRBs (black circles), ULGRBs (green dodecahedrons), KN-GRBs (yellow truncated icosahedrons), and GRBs with internal plateau (dark green diamonds). Darker colors indicate GRBs above the plane, while lighter colors show GRBs below the plane. This figure shows the edge-on projection.

Chain Monte-Carlo (MCMC) method. The best-fit procedure has been performed for the total sample of 222 GRBs as well as for each of the subsets. The resulting fundamental plane (seen edge-on) for the entire sample is shown in Figure 3.1, while, some other best-fits, yielding the most interesting results and regarding the Platinum, KN-GRBs, and SN-GRBs-ABC sets, are shown in Figure 3.2. Finally, the other fits are gathered in Figure 3.3. We would like to note how, in Figure 3.1, the KN-GRBs all fall below the best-fit fundamental plane, thus already suggesting from this plot that they may obey a statistically different fundamental plane relation on their own.

The full results for all our computations are shown in Table 3.3. In particular, for the simple best-fit of the fundamental plane correlation, we refer to the first half of this table. Let us now discuss these results, taking the Gold fundamental plane as a reference point: we note that the intrinsic scatter for the Platinum sample is $\sigma_{int} = 0.34 \pm 0.04$, which is 12.8% smaller than the same quantity computed from the Gold sample. Also, we note that the smallest intrinsic scatter has been computed for the KN-GRB sample ($\sigma_{int} = 0.21 \pm 0.16$), with a reduction of σ_{int} of 46.1% compared to the Gold sample,

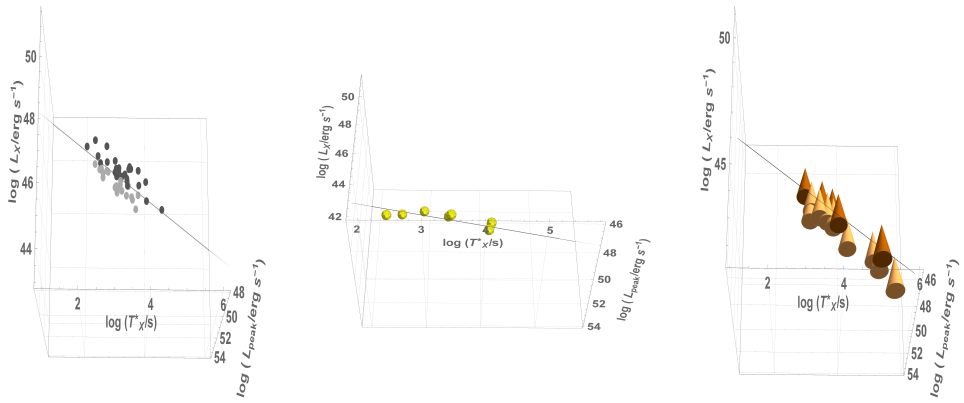

Figure 3.2: The best-fit fundamental plane for the Platinum sample (left panel), for the KN-GRBs sample (central panel), and for the SN-GRBs-ABC sample (right panel).

followed by the SN-GRB-ABC set ($\sigma_{int} = 0.29 \pm 0.10$).

Let us now do a first check on the compatibility of the different fundamental plane parameters with the results obtained for the Gold sample. The Platinum, Long, SN-GRB, ULGRB, KN-GRB, XRF, and internal plateau parameters are all compatible within 1 σ with respect to the Gold parameters. Regarding the sample for which no internal plateau is included, instead, a is compatible in 1 σ, b, and C_0 in 2 σ. For SN-GRB-ABC, a is compatible in 2 σ, b and C_0 in 1 σ. For the Short GRB sample, there is compatibility in 2 σ for a, in 3 σ for b and in 3.1 σ for C_0. For the Type II GRBs, there is a 2 σ compatibility for a, b, and C_0. We note that, for the KN-GRB plane, the a and b parameters are compatible within 1 σ with respect to the Short GRB ones, while the C_0 parameter is compatible within 2 σ. The difference in the best-fit parameters may suggest a different physical mechanism behind each subclass, as is the case for the Gold and Short GRBs.

We have further progressed in our analysis of the compatibility of the fundamental planes of the different subsets by computing the so-called z-score, defined as:

$$z = \frac{< x_1 > - < x_2 >}{\sqrt{\frac{\sigma_1^2}{N_1} - \frac{\sigma_2^2}{N_2}}}, \tag{3.7}$$

where $< x_i >$ and N_i are the mean and the size of the samples, respectively. We compute the z-score for all classes with respect to the Gold sample, which then is used to derive the probability P, for a sample to be compatible with the Gold set. The results are gathered in the first half of Table 3.4. We note that The KN-GRB plane has the highest z-score$= 10.18$, corresponding to a probability $P < 10^{-4}$ that the two samples are drawn from the same population, thus showing that this class is a clear outlier together with the SN-GRB, SN-GRB-ABC, and Short GRB classes. This result could be considered a hint that these categories can be produced by a distinct physical mechanism, like the fact that

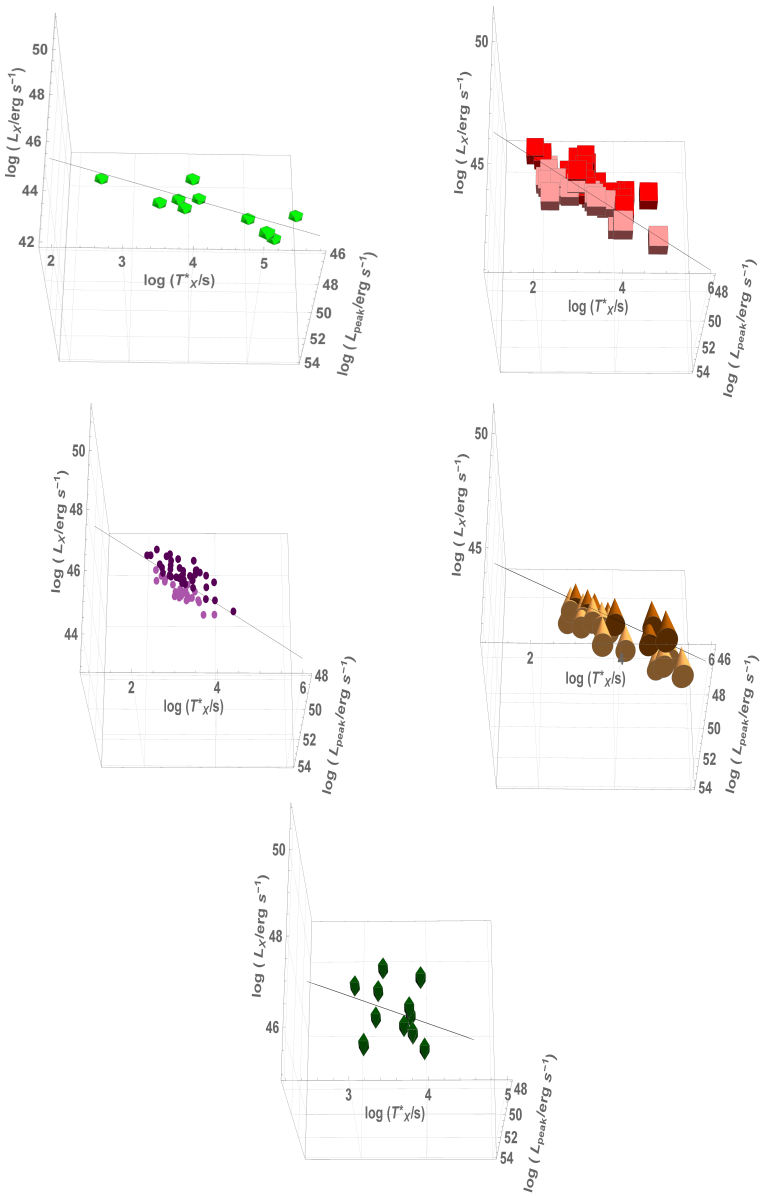

Figure 3.3: The best-fit fundamental plane for the ULGRBs (top left panel), for the Short sample (top right panel), for the Gold set (middle left panel), for all the GRBs associated with SNe (middle right panel), and lastly for the GRBs with internal plateau (bottom panel).

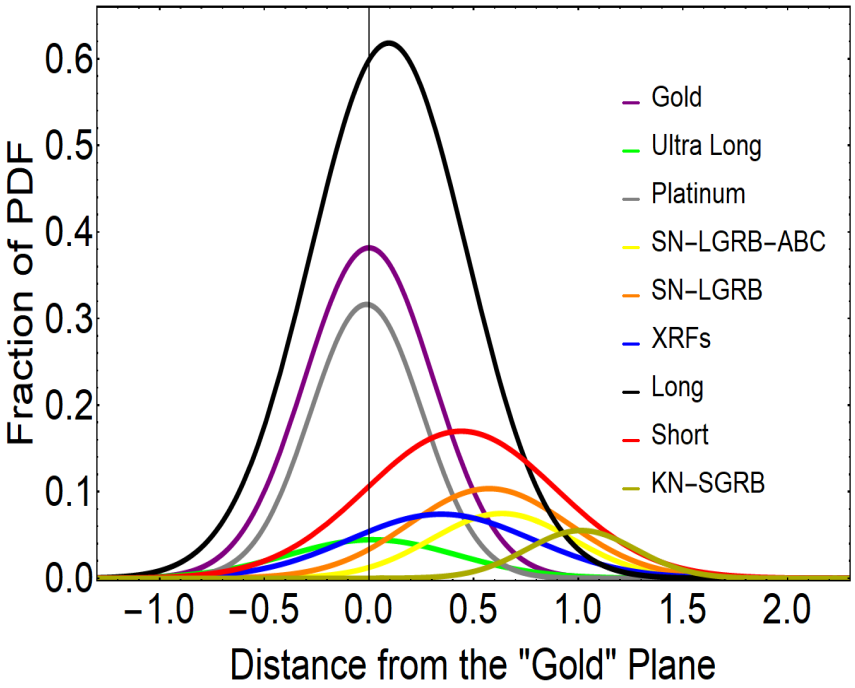

Figure 3.4: Gaussian fit of the histogram of the distance distribution from the gold fundamental plane for all classes. A line perpendicular to $x = 0$ is shown as the reference of the gold sample.

the KNe are linked to the Short GRBs, while the Gold is a subset composed of only Long GRBs, thus confirming the previous discussion regarding the central engines and progenitors.

The difference between these subclasses from the Gold fundamental plane can be clearly noted in Figure 3.4, where the Gaussian distributions of the geometric distance from the Gold fundamental plane are shown for each category. This fit shows the fractional probability distribution functions (PDFs) obtained so that the size of each class compared to the whole sample is taken into account. We note how the centers of the probability distributions for the KN-GRBs, Short GRB, and SN-GRBs are the furthest from the Gold fundamental plane. Other than in this work, the peculiar difference between the Gold sample and the SN-GRBs which we may note from this plot has already been noted in [25]. The z-score for the observed ULGRBs is very low (z-score=0.12), confirming that ULGRBs and Long GRBs may belong to the same physical population [246].

3.4.3 Correction for selection biases and evolutionary effects

The role of possible selection biases and evolutionary effects for the 2-dimensional Dainotti relation has already been studied in [215]. Studies on the L_{peak}-L_X relation have then

been performed in [218, 26]. Indeed, each physical quantity related to the fundamental plane correlation is affected by selection biases due to the instrumentation used to detect them as well as evolutionary effects depending on the redshift. To address this problem we have used the so-called Efron & Petrosian (EP) method [28], which employs a modification of the Kendall τ test to compute the statistical dependence among variables. τ is defined as

$$\tau = \frac{\sum_i (\mathcal{R}_i - \mathcal{E}_i)}{\sqrt{\sum_i \mathcal{V}_i}} \tag{3.8}$$

where R_i is the rank, $\mathcal{E}_i = (1/2)(i+1)$ is the expectation value, and $\mathcal{V}_i = (1/12)(i^2+1)$ is the variance. The rank R_i for each data point is determined from its position in the "associated sets", which include all objects that could have been detected given the observational limits.

In our case, the limits are given by the luminosities and the times, which means that we have to determine the evolution with the redshift for L_X, T_X^*, and L_{peak}. To compute the evolution of L_X and L_{peak}, we first find the flux limit, f_{lim}, at the end of the plateau. From this, we derive the minimum detectable luminosity at a given redshift: $L_{min}(z_i) = 4\pi D_L(z_i)^2 f_{lim} K$. Similarly, $T^*_{X,lim} = T_{X,lim}/(1+z)$ where $T_{X,lim}$ is the minimum end time of the plateau for a given observed sample and energy band.

The associated set for a GRB at a given z_i contains all objects that have luminosity $L_j \geq L_{min}$ and redshift $z_j \leq z_i$. The objects in the sample and the associated sets are indicated with *i* and *j*, respectively. The EP procedure requires conservative choices for the limiting values so that at least 90% of the original set is taken into account. Therefore, this method enables us to remove biases without substantially reducing the samples, and its reliability has been already verified with Monte Carlo simulations [215].

The fundamental plane correlation, once the selection effects are considered, becomes:

$$\log L_X - k_{L_a}\log(z+1) = a_{cor}\cdot(\log T_X^* - k_{T_X}\log(z+1)) + b_{cor}\cdot(\log L_{peak} - k_{L_{peak}}\log(z+1)) + c_{cor}, \tag{3.9}$$

The evolutionary functions of the redshift used in this work are the ones defined in [26], with the same coefficients. The results are presented in the second half of Table 3.3.

All the coefficients computed with this correction for all the samples involved in our analysis present a 1 σ compatibility with respect to the results derived without considering the evolution (the only exceptions are the b and C_0 parameters for the Short GRB sample, which are compatible within 2 σ).

Class	a	b	C_o	σ_{int}	N	a_{cor}	b_{cor}	C_{ocor}	σ_{intcor}
Gold	-0.82±0.13	0.55±0.11	22.2±5.6	0.39±0.04	65	-0.79±0.15	0.47±0.14	27.1±7.2	0.32±0.07
Platinum	-0.86±0.13	0.56±0.12	21.8±6.3	0.34±0.04	47	-0.90±0.16	0.50±0.16	25.6±8.2	0.22±0.10
Long	-0.98±0.07	0.62±0.06	19.1±3.1	0.43±0.03	129	-1.05±0.09	0.65±0.09	18.7±4.8	0.40±0.05
Short	-0.58±0.10	1.15±0.10	-9.7±5.0	0.38±0.05	43	-0.74±0.17	1.54±0.23	-27.8±12.0	0.55±0.11
SN-GRB	-0.81±0.14	0.72±0.07	13.2±3.9	0.42±0.08	22	-0.77±0.18	0.82±0.10	8.2±5.7	0.43±0.09
SN-GRB-ABC	-1.16±0.16	0.59±0.07	20.6±4.1	0.29±0.10	14	-1.18±0.18	0.65±0.09	18.3±5.2	0.22±0.10
XRFs	-0.81±0.19	0.69±0.13	14.6±6.7	0.54±0.10	18	-0.92±0.25	0.66±0.17	16.9±8.9	0.50±0.19
UL	-0.62±0.20	0.74±0.12	11.6±6.2	0.43±0.15	10	-0.72±0.27	0.94±0.19	2.9±9.8	0.51±0.23
KN-GRB	-0.83±0.22	0.80±0.25	8.5±12.9	0.21±0.16	8	-1.09±0.20	1.03±0.27	-1.5±13.3	0.24 ±0.12
Type II	-1.15±0.08	0.28±0.05	37.2± 2.6	0.66±0.05	167	-1.14±0.09	0.28±0.06	37.3±3.0	0.66 ± 0.05
Int. plateau	-0.4±0.4	0.36±0.24	30.9± 12.4	0.59±0.12	12	-0.28±0.88	0.64±0.58	14.8±30.3	0.55 ± 0.29
No int.plateau	-0.78±0.05	0.82±0.04	8.1± 2.2	0.50±0.03	210	-0.93±0.08	0.88±0.08	6.2±4.0	0.61 ± 0.04
Whole sample	-0.77±0.06	0.81±0.05	8.6± 2.5	0.52±0.03	222	-0.91±0.08	0.87±0.08	6.9±4.1	0.64 ± 0.04

Table 3.3: The best-fits for both the observed plane parameters (first half of the table), and the ones accounting for the evolution, indicated with the subscript “cor" (the second half of the table), σ_{int}, and number of GRBs for each category.

Considering these corrections, we note that the Platinum and SN-GRB-ABC samples have the smallest intrinsic scatter $\sigma_{Platinum,cor} = \sigma_{SN-GRB-ABC,cor} = 0.22 \pm 0.10$, followed by the KN-GRB ($\sigma_{KN-GRB,cor} = 0.24 \pm 0.12$). We then perform the same compatibility test previously mentioned between the different plane coefficients to the gold best-fit results. These tests show the following: the Platinum, XRF, and internal plateau parameters are all compatible in 1 σ. For the Long GRB, SN-GRB-ABC, and Type II samples, a is compatible in 2 σ, and b and C_0 are compatible in 1 σ. For the SN-GRB, ULGRB, and KN-GRB samples, a is compatible in 1 σ, and b and C_0 are compatible in 2 σ. For the sample without internal plateaus and the whole sample, a is compatible in 1 σ, and b and C_0 are compatible in 2 σ. Lastly, for the Short GRB sample there is compatibility in 3 σ for b and C_0, and in 1 σ for a.

We also compute the z-scores of the corrected set, alongside the probability, as previously done for the non-corrected results. The results are shown in the last two columns of Table 3.4. We note how, even if the values of the z-scores change with respect to the first case, the general conclusion does not: the KN-GRB distribution is still the furthest, with z-score=10.39, followed by the SN-GRBs and Short GRBs.

In conclusion, the major results reached in [24] show that it is indeed possible to discern the nature of particular GRBs following the fundamental plane correlation, at least for some subclasses for which a significant difference between the planes has been found, like for instance for the Long GRBs and the GRBs associated with the KNe. Regarding the former sample, it is interesting to show Figure 3.4.3, in which we focus our attention only on the Short GRBs and the GRBs associated with KNe. We note that, even if the KN-GRBs are all short in our sample, all of them fall below the Short GRBs' best-fit fundamental plane. This observational fact may hint at physical mechanisms which could bring differences between the Short GRBs depending on their possible association with a KN.

Class	z-score	N	Probability	z-score cor	Probability cor
Gold	0.00	65	1.00	0.00	1.00
Platinum	-0.22	47	0.83	-0.51	0.61
Long	1.89	129	0.06	1.54	0.12
SN-GRB	6.39	22	$\leq 10^{-4}$	8.07	$\leq 10^{-4}$
SN-GRB-ABC	6.51	14	$\leq 10^{-4}$	7.55	$\leq 10^{-4}$
XRF	3.15	18	0.002	3.80	0.0001
Short	5.57	43	$\leq 10^{-4}$	4.60	$\leq 10^{-4}$
Ultra Long	0.12	10	0.90	0.73	0.47
KN-GRB	10.18	8	$\leq 10^{-4}$	10.39	$\leq 10^{-4}$

Table 3.4: Table of z-scores for all classes, with the number of GRBs in each sample and the probability that the Gold fundamental plane and the other planes are drawn by the same distribution. On the right side of the table, we show z-scores without evolution, while on the left side those with evolution (cor).

We have also obtained particular low values for the intrinsic scatter for different fundamental planes, like for the newly defined Platinum sample, as well as for the KN-GRBs and the SNe-GRBs-ABC. This conclusion is of interest because a sample showing a tight relation with a small intrinsic scatter is the most suitable for cosmological applications. Indeed, in the following chapter, we will use the Platinum sample, together with other cosmological probes, to derive the values of some cosmological parameters. These results are also confirmed after the application of the EP method for the correction of selection biases and redshift evolution.

The difference between the subsets has been further confirmed using the z-score as well as by the visualization via the PDFs, through the Gaussian fits of every set around their respective planes. Regarding the KN-GRBs sample, a possible outcome, once the set becomes numerous enough with future observations, would be the possibility to use the fundamental plane also to discern between the progenitor mechanisms; indeed, a NS-BH merger can produce as much as 10 times more dynamical ejecta than a binary NS can [247].

3.4.4 A new study of the fundamental plane correlation

In [33] a further study of the fundamental plane correlation for the Platinum sample is present. We have first updated the evolutionary coefficients related to the EP method considering the entire sample of 222 GRBs, following the same procedure found in [26] for the coefficient used in [24], which was presented in the previous subsections. In doing so, the new coefficients to use in Eq. (3.9) are $k_{L_{peak}} = 2.24^{+0.30}_{-0.30}$, $k_{T_X} = -1.25^{+0.28}_{-0.27}$, $k_{L_X} = 2.42^{+0.41}_{-0.74}$. The plots from which these coefficients have been derived are visual-

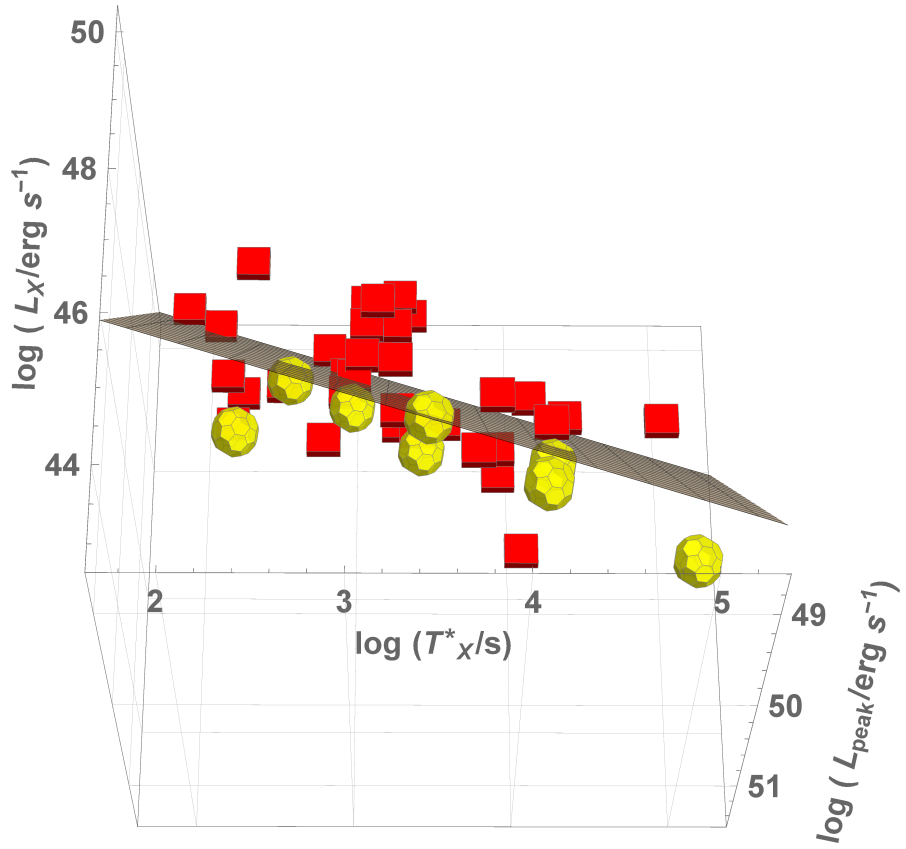

Figure 3.5: The $L_X - T^*_X - L_{peak}$ relation for the GRB sample with separated KN-GRB cases. We note here that all the KN-GRBs fall below the best-fitting plane.

ized in Figure 3.6. More specifically, the limiting values of these quantities, as previously described for L_{peak}, L_X, and T_X^*, are shown in the left panels of this figure, while the evolutionary coefficients themselves are shown in the right panels.

Using these new coefficients we can thus compute new best-fit parameters for the fundamental plane correlation regarding the Platinum sample once we include the correction for selection biases, finding $a_{\rm ev} = -0.85 \pm 0.12$, $b_{\rm ev} = 0.49 \pm 0.13$, $c_{\rm ev} = 25.4 \pm 6.9$, and $\sigma_{int} = 0.18 \pm 0.09$. We note how the new central value for intrinsic scatter is smaller than what has been found in [24], see Table 3.3.

We thus start our statistical reliability check with this new fundamental plane. In figure 3.7 we show the 2D projections of the fundamental planes for the Platinum sample, both with and without considering the evolutionary effects, as well as the errors on the data points, represented by the ellipses. We notice that when the correction for evolution is applied, the data points are closer to the plane (including the error bars), and fewer outliers are present compared to the computations in which the evolution is not taken into account. We confirm the stronger correlation when the evolutionary effects are considered via the Akaike information criterion (AIC) and the model weight: $B_i = e^{\frac{AIC_{min} - AIC_i}{2}}$ for each relation, where $AIC_{min} = MIN(AIC_{evolution}, AIC_{noev})$, and AIC_i is the AIC value corresponding to the relation for which the B parameter is computed. For each model we computed the "relative likelihood": $P_i = \dfrac{B_i}{\sum\limits_j B_j}$, obtaining $P_{evolution} = 0.99$ and $P_{noev} = 0.01$. Thus, the model with evolution is favored compared to the one without evolution.

In this analysis we have also used alternative methods to confirm the reliability of our results, focusing on other best-fit approaches. For instance, we considered the [212] Bayesian method, which takes into account a likelihood function slightly different from the D'Agostini fit. In doing so, results consistent within 1 σ with the derivations obtained previously have been found. We also used an online fitting procedure called "HyperFit" (https://hyperfit.icrar.org/, [248]), built to obtain the best-fit of linear models that consider heteroscedastic errors for multidimensional data using Bayesian inference. This tool offers the possibility to employ different algorithms and methods, which we used to compare with our results regarding the D'Agostini fitting, that we found consistent with these computations, as we may note for the smoothed histograms shown in figure 3.8, representing all our derivations obtained with the HyperFit routine both with and without the correction for evolutionary effects. Indeed, computing mean and standard deviation for both cases, we find $\sigma = 0.374 \pm 0.024$ for the non-evolution case and $\sigma = 0.237 \pm 0.043$ for the evolution, noting that they are both compatible within 1 σ with respect to the D'Agostini computations.

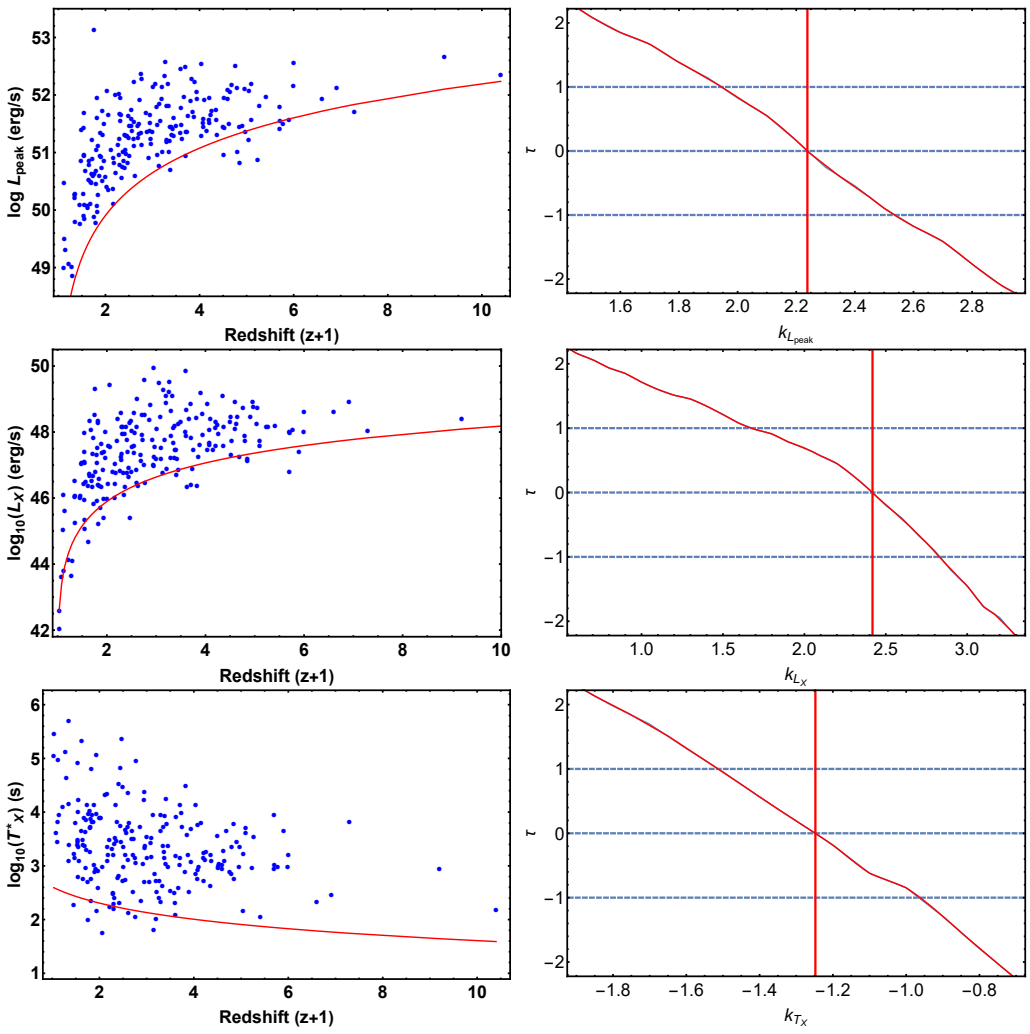

Figure 3.6: The application of the EP method to our entire sample for the parameters involved in the fundamental plane correlation. The limiting lines chosen for the EP method are visible in red. The left panels show the distribution of studied parameters versus $z+1$, while the right panels show the relation between τ and the evolutionary coefficients in red. The vertical red solid lines indicate the value for which $\tau = 0$ and thus the evolution is removed. The dashed blue lines represents the 1 σ for the evolution, which is determined for $\tau \leq 1$.

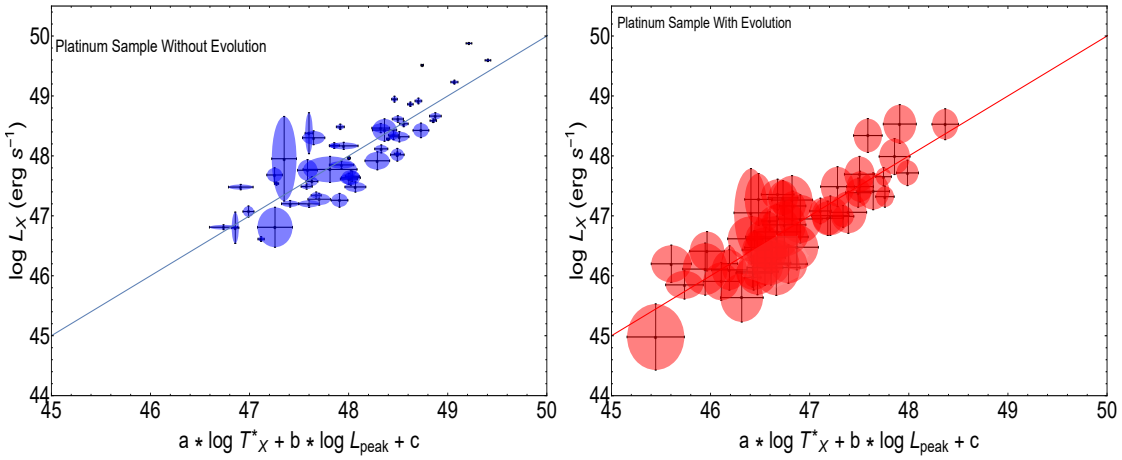

Figure 3.7: The 2D projections of the fundamental plane related to the Platinum sample without correcting for redshift evolution (left panel), and with the corrections for selection and evolutionary effects (right panel).

Figure 3.8: Paired smoothed histograms of the σ_{int} obtained for cases with and without evolution with different methods using the HyperFit online routine.

We also applied other best-fit algorithms: the Principal Component Analysis, the PCA, the PC Regression (PCR), and the Partial Least Squares (PLS) regression, where the latter two are regression methods based on PCA. Using the PCA we found: $a = -1.19$, $b = 0.44$, $c = 28.87$ and $a_{\rm cor} = -1.17$, $b_{\rm cor} = 0.49$, $c_{\rm cor} = 26.75$ for the no evolution and the evolution cases, respectively. When comparing the PCA results with the D'Agostini ones for the non-evolution case, the parameters a, b, and c are within 2.5, 1, and 1.1 σ, respectively; for the evolution case b_{cor} and c_{cor} are consistent in 1 σ, while a_{cor} is consistent in 2.7 σ. We also have to stress that the PCA fitting does not take into account the error bars, and thus does not consider the intrinsic scatter, which instead is computed by the aforementioned Bayesian approaches. This could be the main reason for the different results.

For PCR and PLS, we have used bootstrapping techniques to infer the errors on the best-fit parameters. The results provided by these methods are consistent within 1 σ with respect to the D'Agostini computations, thus giving more reliability to our conclusions.

3.5 BAO

As previously mentioned, BAO are fluctuations in the density of the visible baryonic matter of the Universe, caused by acoustic density waves in the primordial plasma of the early Universe. For their nature, they are physical processes that depend on the early stages of the Universe, which in turn are reflected in observations of the late type (i. e. cluster formations, galaxy distributions). They are linked to the acoustic peaks measured from the CMB [21]. These peaks occur because the cosmological perturbations excite sound waves in the relativistic plasma of the early Universe [249]. Then, the recombination process to a neutral gas happening at very high redshift values ($z \sim 1100$, [21]) strongly decreases the sound speed of the medium, thus effectively ending the wave propagation. In the time between the formation of the perturbations and the recombination, modes of different wavelengths can complete different numbers of oscillation periods. This translates the characteristic time into a characteristic length scale and produces a harmonic series of maxima and minima in the anisotropy power spectrum [21].

This also translates into the aforementioned relation between these early time processes and the perturbations in the power-matter spectrum of late times observations [250]. Indeed, considering a perturbation both for the baryonic and dark matter, the former will expand as a spherical wave, while the latter will grow in place [251]. At recombination, the expanding shell will have a radius roughly equal to 150 Mpc [21]. After this event, both dark matter and baryon perturbation start the formation of large-scale structures. Because the central perturbation in the dark matter is dominant compared to

the baryonic shell, the acoustic feature is manifested as a single spike in the correlation function at around 150 Mpc between pairs of galaxies. This scale is usually close to the sound horizon [252]. The early Universe presented many spherical perturbations, so the final density distribution is a linear superposition of the small-amplitude sound waves.

From its geometrical nature, we can see how the acoustic peaks allow measuring quantities linked to the angular diameter distance (Eq. 2.21), offering an alternative to the usual cosmological ladder related to the luminosity distance, considering also that the length scale of measurements related to this quantity allows us to reach observations at a wide range of redshifts. The BAO-related measurements have seen an impressive improvement in their precision during the past decade [76], which has proven to be mandatory for cosmological application, given that the acoustic features in the matter correlations are weak and on large scales [21]. The largest spectroscopic survey to date is the Baryon Oscillation Spectroscopic Survey (BOSS [253]) which was one of the main objectives of the Sloan Digital Sky Survey (SDSS)-III Collaboration [254]. Indeed, this collaboration completed spectroscopy on more than 1.5 million galaxies to produce BAO-related data points. This compilation has then been complemented with the extended Baryon Oscillation Spectroscopic Survey (eBOSS [255]), which was the cosmological survey within the SDSS-IV [256]. Other BAO-related surveys are the 6dF Galaxy Survey (6dFGS, [257]), and the WiggleZ Dark Energy Survey [258]. The correlation measurements have been performed using luminous red galaxies (LRGs), emission line galaxies (ELGs), quasars, and Lyman-α (Lyα) forests.

For the remainder of the analysis in this thesis, we consider two samples of BAO data: one taken from [259, 260], which consists of a total of 26 BAO-related data, while the other has been built gathering the observations of [257, 258, 261, 262, 76], which are a total of 16 BAO-related measurements, whose specific nature shall be detailed in the next chapter. All these BAO-related measurements have been built specifically for cosmological applications, measuring particular cosmological quantities at specific values of redshifts, which are all linked one to the other and to the angular diameter distance, as we shall see in the next chapter.

Chapter 4

Cosmological applications of GRBs, SNe Ia, and BAO

In this chapter, we shall see how the astrophysical objects presented in the previous one can be used for cosmological purposes, focusing our attention on the GRBs, for which an analysis based on simulations has been performed, together with applications considering real GRB data, which have been studied considering also BAO and SNe Ia measurements.

4.1 SNe Ia and BAO as cosmological probes

Let us start with the more conventional cosmological probes, SNe Ia and BAO, which shall be used both in the computations shown in this chapter as well as in the next.

As discussed in Chapter 3, SNe Ia, due to their intrinsic nature and physical mechanisms, can be used as standard candles after the standardization process that accounts for their different luminosities and light curve lengths. Many observational campaigns have focused their attention on SNe Ia and their use as the "third step" of the cosmological distance ladder. Given their link to the luminosity distance, the use of SNe Ia as cosmological probes is based upon the following equation, in which the distance modulus is defined starting from the luminosity distance d_L

$$\mu_{th,SNeIa} = m - M = 5\log(d_L) + 25, \tag{4.1}$$

where m is the apparent magnitude of the astrophysical object, M is its absolute magnitude, and the distance is expressed in Mpc. This quantity is confronted with the detected distance modulus μ_{obs} of the SNe Ia, from which a best-fit of the desired cosmological parameter (as well as of the absolute magnitude M) can be performed. As previously stated, for our analysis in this chapter we consider the Pantheon catalog [20], thus, we

also base ourselves on their analysis of the SNe Ia light curves. The detected distance modulus is defined as [263]

$$\mu_{obs,SNeIa} = m_B - M + \alpha x_1 - \beta c + \Delta M + \Delta B, \tag{4.2}$$

where x_1 is the stretch parameter for the light curve standardization, c is the color, m_B is the apparent magnitude detected in the B-band of a reference SN Ia with $c = 0$ and $x_1 = 0$, ΔM is a distance correction based on the galaxy mass in which the SN Ia has been detected, and finally, ΔB is a bias correction factor [20].

For the color and stretch parameters, the approach used in [20] is based on two different models, the first shown in [264] while the second presented in [265]. In their analysis, they consider the average of these two models, which represents the systematic part of the covariance error matrix of the distance modulus measurements, which shall be introduced shortly.

The Pantheon sample provides the quantities mentioned above as well as directly the apparent magnitudes m for each SN Ia, from which, once M is fixed, we obtain the detected distance modulus, that can be used to derive best-fit values of different cosmological parameters.

For the luminosity distance related to the SNe Ia, Eq. (2.17), the factor $(1+z)$ before the integral refers to the heliocentric redshift, that is the apparent redshift affected by the relative motion of the Sun, and not to the redshift observed in a cosmological rest frame [266], which instead has been used inside the integral of the same equation.

As we shall see, the reduced chi-squared used for our cosmological computations related to SNe Ia is defined as follows

$$\chi^2_{SNEIa} = (\mu_{th} - \mu_{obs})^T \times \mathcal{C}^{-1}_{SNEIa} \times (\mu_{th} - \mu_{obs}) \,, \tag{4.3}$$

where $\mathcal{C}^{-1}_{SNEIa}$ is the inverse of the covariance matrix of the Pantheon sample, that in turn is defined as [263]

$$\mathcal{C}_{SNEIa} = C_{sys} + D_{stat}, \tag{4.4}$$

where C_{sys} is the systematic part, which is linked to the aforementioned stretch and color models, while D_{stat} is a diagonal matrix associated with the statistical errors characterizing the distance measurements of every SN Ia. For a more complete discussion on the photometric treatment of the SNe Ia light curves as well as on the error estimates and the general analysis behind the Pantheon sample see [20]. Here we use their end-product for our analysis.

We now focus on how the BAO-related measurements have been used in our cosmo-

logical computations. The main, more practical, difference between BAO and SNe Ia as cosmological probes, apart from the fundamental physical differences that exist between the two objects, stays in the fact that while all the SNe Ia data are linked directly to the luminosity distance and thus to the distance modulus, BAO-related data give estimates of different quantities which are linked one to the other and the angular diameter distance, but they are not the same for every BAO data point, as instead happens to the SNe Ia.

Indeed, as we shall see, the BAO-related measurements involved in the first set of 16 BAO data points offer information about the following quantity

$$d_V(z) = \left[{d_M}^2(z) \frac{cz}{H(z)} \right]^{\frac{1}{3}}, \tag{4.5}$$

where d_M is the transverse comoving distance defined in Eqs. (2.18,2.19,2.20) and $H(z)$ is defined in Eq. (2.15). Also, other cosmological parameters derived by these BAO are the following

$$A(z) = \frac{100 d_V(z) \sqrt{\Omega_M h^2}}{cz}, \tag{4.6}$$

where $h = H_0/(100km\ s^{-1}Mpc^{-1})$; the so-called Hubble distance

$$d_H(z) = \frac{c}{H(z)}, \tag{4.7}$$

and the comoving distance itself. We note again that all these definitions are linked one to the other, but they are not the same. This is a relevant point when the covariance matrix has to be built using these heterogeneous measurements. It is also important to stress again that, behind each of these data points, there are usually thousands of observations regarding astrophysical objects, like galaxies, clusters of galaxies, quasars, and Lyman α forests [76].

It is also important to note that the majority of the BAO-related data are given considering a rescaling factor, r_d, which is the distance between the end of inflation and the decoupling of baryons from photons after the recombination epoch. It is roughly equal to $150Mpc$ and it is defined as [76]

$$r_d = \int_{z_d}^{\infty} \frac{c_s(z)}{H(z)} dz, \tag{4.8}$$

where $c_s(z)$ is the sound speed, while z_d is the redshift of the drag epoch, which in turn corresponds to the time when the baryons decouple from the photons, around a redshift $z = 1020$. It is possible to provide an approximation of r_d depending on the cosmological parameters. Indeed, the formula used in our analysis is as follows [267]

$$r_d = \frac{55.154 \cdot e^{[-72.3(\Omega_\nu h^2+0.0006)^2]}}{(\Omega_M h^2)^{0.25351}(\Omega_b h^2)^{0.12807}} Mpc, \tag{4.9}$$

where Ω_b is the baryonic density in the Universe, and Ω_ν is the neutrino density, which, for our computations, have been fixed according to the ΛCDM values ($\Omega_b \cdot h^2 = 0.02237$, $\Omega_\nu \cdot h^2 = 0.00064$, [2]).

In general, the chi-squared for the BAO can be written in the same form as the one related to the SNe Ia

$$\chi^2_{BAO} = (d_{B,th} - d_{B,obs})^T \times \mathcal{C}^{-1}_{BAO} \times (d_{B,th} - d_{B,obs}) \,, \tag{4.10}$$

where $d_{B,th}$ and $d_{B,obs}$ may correspond to the different physical quantities presented previously, and $\mathcal{C}_{BAO}$ is the corresponding covariance matrix.

In the analysis presented in this chapter, we have considered also a second set of 26 BAO-related measurements, gathered from [260]. In this case, all the data refer to the following quantity

$$d_s(z) = \frac{r_d}{d_V(z)}, \tag{4.11}$$

where r_d and $d_V(z)$ have been defined in Eqs. (4.9) and (4.5), respectively. The corresponding likelihood function remains of the same form presented in Eq. (4.10).

4.2 GRBs as cosmological tools

In this section, we will discuss how GRBs can be used as cosmological tools alongside the other probes, and which would be the expected advantage of these computations. This analysis is the main focus of [29, 32, 33].

4.2.1 Historical Introduction

Considering their incredible luminosity, GRBs may be detected by our instrument even in deep regions of the Universe, where not many other astrophysical objects can be observed. Indeed, we recall that the furthest GRB ever studied has been found at $z = 9.4$ [22]. This fact alone would make them ideal cosmological probes, able to extend the cosmological ladder up to regions way beyond the possibilities of SNe Ia, creating a bridge between the early and late-type observations, being ideally also model-independent, differently from CMB estimates.

Unfortunately, as shown in the previous chapter, the physics behind GRBs is not as well-understood as for more conventional standard candles, and huge variability exists

between the physical features of different GRBs, especially regarding their luminosity, whose observations show may spam between different orders of magnitude. Of course, the same has not been noted for other cosmological probes like SNe Ia. This fact alone makes their cosmological application difficult. Nevertheless, in the past two decades, efforts in using them as cosmological probes have been performed by the scientific community, considering the observed correlations introduced in the previous chapter. In this sense, the main difficulty is in finding a tight enough relation [23]: indeed, each correlation is characterized by an intrinsic dispersion, which has to be quantified and deeply studied, as shown in the previous chapter, in order to find, among the other scopes of such correlations, also possible cosmological applications. Another issue to be addressed is the so-called "circularity problem", which is the possibility to calibrate a given GRB correlation on a particular cosmological model, thus prohibiting us from using such relation for cosmological applications, in particular for the determination of parameters that influence the quantities involved in the relation itself.

Early computations related to this point were performed in [268, 269], where broad correlations were used in order to build Hubble diagrams with GRBs. Given the nature of these correlations, these data could not give any constraint on cosmological parameters [23]. In [270, 271, 272], the first cosmological constraints using GRBs were found, albeit with very large errors, which were consistent with the parameters of the ΛCDM model. These works used the $E_{p,z} - E_\gamma$ Amati correlation, introduced in the previous chapter. Another correlation used in the early days of GRB cosmology was the $E_{p,z}$-$L_{\gamma,p,iso} - t_{b,z}$ relation [208], with which similar results were obtained.

The $E_{p,z}$-$E_{\gamma,iso}$ correlation has been used widely in the literature also in more recent years (see, for instance, [273, 201], in which Hubble diagrams involving GRBs have been built and cosmological parameters were derived together with SNe Ia data). Even more recently, [274, 275] consider this relation for 6 different cosmological models, obtaining results comparable with other probes like BAO and SNe Ia.

In the following, we shall focus on the fundamental plane correlation, introduced and studied in the previous chapter. The 2-D Dainotti relation, from which the fundamental plane correlation has been derived, was one of the first correlations involving the afterglow which has been proposed as a cosmological tool [213, 214, 276, 277]. This correlation has also been employed as a cosmological tool recently in [278], where they obtained results consistent with the ΛCDM model by using a sample of Long GRBs. This result has been confirmed in [279], where they combined a set of Short GRBs with the previously cited sample of Long GRBs. This data set has been combined in [280, 281] with GRBs obeying the $E_{p,z}$-$E_{\gamma,iso}$ relation, obtaining again results consistent with the derivations obtained using other probes, like BAO.

As previously stated, this correlation has a solid theoretical grounding, being consistent with the magnetar model for GRBs [195], thus being a proper candidate for cosmological applications also from this point of view. The introduction of a third parameter in this correlation and, thus, the definition of the fundamental plane relation for GRBs, has allowed for a significant decrease of the intrinsic scatter [24], therefore addressing one of the major limitations of the general application of GRB correlations as cosmological tools. As previously stated, the fundamental plane, like the 2-D correlation, has a reliable physical explanation via the magnetar model [195], and it has been deeply studied in various aspects, as shown in the previous chapter.

The fundamental plane correlation and the 2-dimensional counterpart have also been studied in the optical bands: indeed, it has been found a similar relation among 102 GRBs between the optical rest-frame end time, $T_{\rm OPT}$, and the optical luminosity at the end of the plateau, $L_{\rm OPT}$ [224]. This optical relation has also been extended by adding the energy in the prompt emission, $E_{\rm iso}$ [282].

4.2.2 The fundamental plane relation as a cosmological tool: methodology

We now show how we have used the fundamental plane relation, described in equation 3.5, as a cosmological tool. For the sample selection, regarding the data set in the X-rays, we have chosen for our computations the Platinum sample described in the previous chapter (directly or as a baseline of simulations, as we will show). For the Optical data set, we have started from all GRBs included in [224, 283]. The optical data have been gathered from the observations performed by Swift Ultra-Violet/Optical Telescope (UVOT), as well as ground-based telescopes. For a more detailed description of the sample selection involving the optical data, see [224, 283]. In total, the Optical sample used in our analysis is composed of 45 GRBs. For the determination of the plateau, the best-fit for the [187] functional model has been used, as was the case for the X-Ray GRBs. Given the smaller sample size, defining an analogous of the Platinum sample for Optical GRBs is still not possible [29].

We now describe how we have used the fundamental plane correlation, Eq. (3.5) as a cosmological tool to infer different cosmological parameters. Our goal is to derive an expression of the distance modulus related to GRBs μ_{GRB} from the correlation. In order to do so, we recall that luminosities and fluxes are linked by Eqs. (3.6), where $d_L(z)$ is, again, the luminosity distance defined in Eq. (2.17). Using these relations, it is possible to derive the following equation, where we write $d_L(z)$ as a function of the other

parameters involved in the fundamental plane correlation

$$\log_{10}(D_{\rm L}) = \frac{a\log_{10}T_{\rm a}^{*}}{2(1-b)} + \frac{b\cdot(\log_{10}F_{\rm peak}+\log_{10}K_{\rm peak})}{2(1-b)} + \\ + \frac{(b-1)\log_{10}(4\pi)+c}{2(1-b)} - \frac{\log_{10}F_{\rm a}+\log_{10}K_{\rm a}}{2(1-b)}, \quad (4.12)$$

where we recall that $K_{\rm peak}$ and $K_{\rm a}$ are the K-corrections for cosmic expansion introduced in the previous chapter. If we now define the following new parameters: $a_1 = a/(2(1-b))$; $b_1 = b/(2(1-b))$; $c_1 = ((b-1)\log_{10}(4\pi)+C)/(2(1-b))$; $d_1 = -1/(2(1-b))$; $F_{\rm peak,\,cor} = F_{\rm peak}\cdot K_{\rm peak}$; and $F_{\rm a,\,cor} = F_{\rm a}\cdot K_{\rm a}$, and use the definition of the distance modulus, we finally obtain

$$\mu_{\rm obs,\,GRB} = 5\cdot(a_1\ \log_{10}(T_{\rm a}^{*}) + b_1\ \log_{10}(F_{\rm peak,cor}) + c_1 + d_1\ \log_{10}(F_{\rm a,cor})) + 25. \quad (4.13)$$

We have also computed the relative uncertainties on the GRB distance moduli, which are given by

$$\sigma_{\mu,i} = \sqrt{(5b_1\cdot\log F_{\rm p,err,cor})^2 + (5a_1\cdot\log F_{\rm X,err,cor})^2 + (5d_1\cdot\log T_{\rm X}^{*})^2}. \quad (4.14)$$

These equations allow us to define the cosmological likelihood for GRBs,

$$\mathcal{L}_{\rm GRB} = \sum_i \left(ln\left(\frac{1}{\sqrt{2\pi}\sigma_{\mu,i}}\right) - \frac{1}{2}\left(\frac{\mu_{\rm th,GRB},i - \mu_{\rm obs,GRB},i}{\sigma_{\mu,i}}\right)^2\right). \quad (4.15)$$

This likelihood can be used together with the ones linked to BAO and SNe Ia, introduced in the previous section, in order to have a complete likelihood, that can allow us to derive the cosmological parameters via a Bayesian approach, similar to what has been considered in the previous chapter [27], for all our cosmological probes. As we will see, we have used different combinations of our probes to infer different cosmological parameters like Ω_M and H_0. In order to avoid the previously mentioned circularity problem affecting GRBs, we note that we find the best-fit values of the fundamental plane correlation together with the cosmological parameters themselves, thus avoiding a direct dependence on the underlying cosmology.

4.3 GRB Cosmological Simulations

Before describing the results obtained with the real set of GRBs together with SNe Ia and BAO, in this section, we shall describe an analysis focused on the use of GRBs as

standalone cosmological probes, based on simulations employing the fundamental plane correlation of the real GRB data as a starting point, both for the X and Optical bands. These simulations have been performed in [29], by using python's MCMC sampler *emcee* [284], for the possibility of parallelizing the computations.

4.3.1 Number of GRBs to reach the studied limits

The idea behind this approach is to find how many GRBs lying precisely on a fundamental plane would be needed to obtain constraints on the cosmological parameters (in particular on Ω_M, for this analysis) with a comparable precision with respect to three results obtained for the SNe Ia found in the literature. More precisely, we investigate the threshold given by [30], where an error on Ω_M equal to 0.10 was found using 472 SNe Ia, by [31], where a $\sigma = 0.042$ on Ω_M has been computed using 740 SNe Ia, and finally by [20], where they found $\sigma = 0.022$ for the 1048 SNe Ia belonging to the Pantheon set. Thus, we wish to find how many GRBs lying exactly on the fundamental plane are needed in order to reach these limits, and estimate the number of years necessary to achieve these numbers. These GRBs have been simulated in order to satisfy exactly the fundamental plane correlation, with the physical quantities (and their errors) built using the distributions of the data points considered to build the Platinum (and Optical) data sets, using, as the baseline, the best-fits of fundamental planes provided by these two sets (and their subsets, as we will see).

We first consider different baselines for the fundamental plane correlation, starting from what we have obtained using the entire Platinum sample. As an example of our simulations, we show some results in Figure 4.1, in order to visualize the general trend we have found for our computations on the precision of $\Omega_{\rm M}$. We note the general improvement in it due to the addition of more simulated GRBs, but we also note how the required precision is not yet reached for any of the thresholds considered even with 200 simulated GRBs. We thus analyze results considering even more simulated GRBs. As a further computation, we also consider the case in which we take into account halved error for the starting distributions on the physical quantities used as starting points for our simulations, with the idea that future GRB observations with more updated instruments should also be able to decrease the observational error on the parameters involved in the fundamental plane correlation.

The first results are shown in Figure 4.2. We note how the mean value of $\Omega_{\rm M}$ stabilizes around 0.3 rather quickly for both tests (especially for the computation involving halved errors, right panel, in which we can see a faster decrease of the scatter on $\Omega_{\rm M}$ with the number of GRBs). We also note the general decrease in the error for the cosmological parameter. From this plot, we now wish to find the number of GRBs necessary to reach

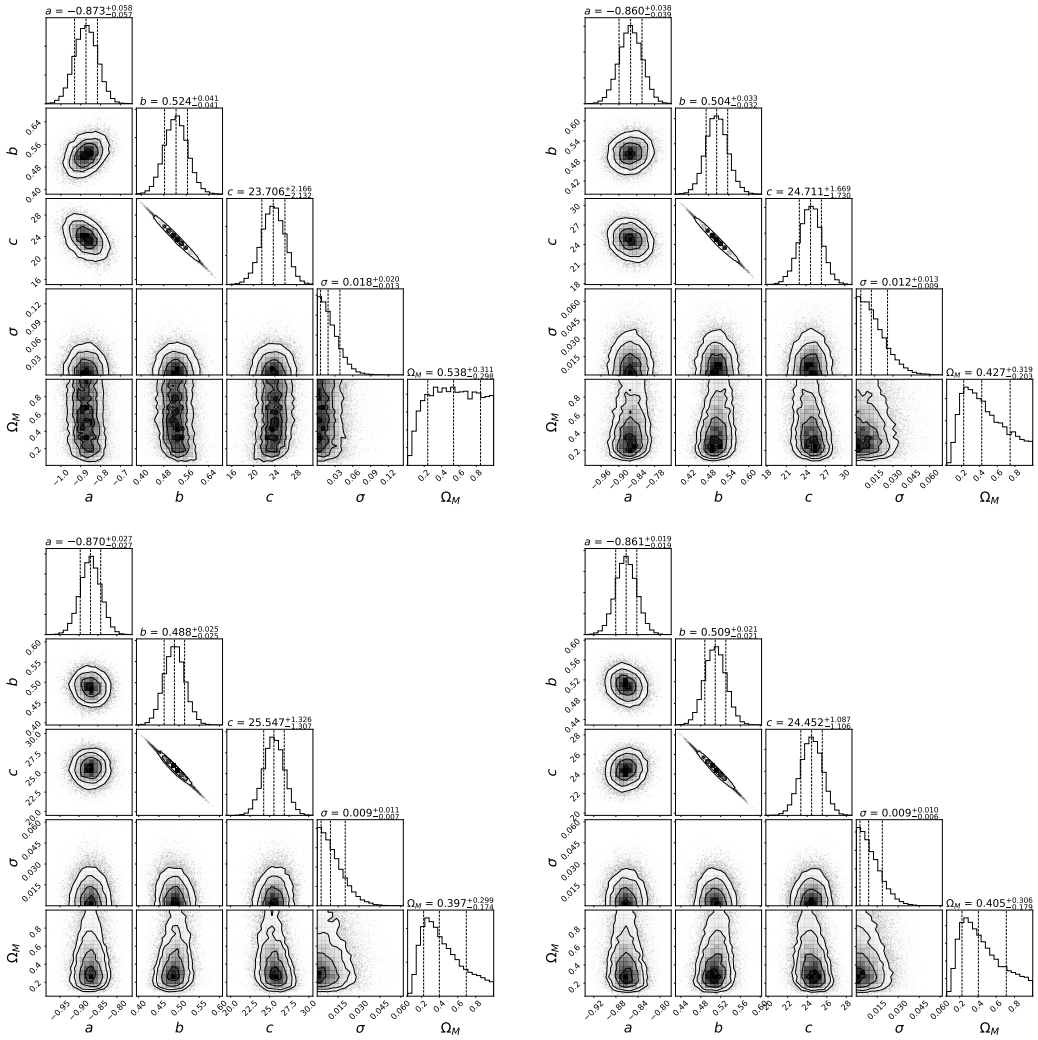

Figure 4.1: Results of the simulations for $\Omega_{\rm M}$ given 50 (top left), 100 (top right), 150 (bottom left), and 200 (bottom right) GRBs simulated off the Platinum fundamental plane. With the dotted lines, we indicate the mean percentile with its respective errors.

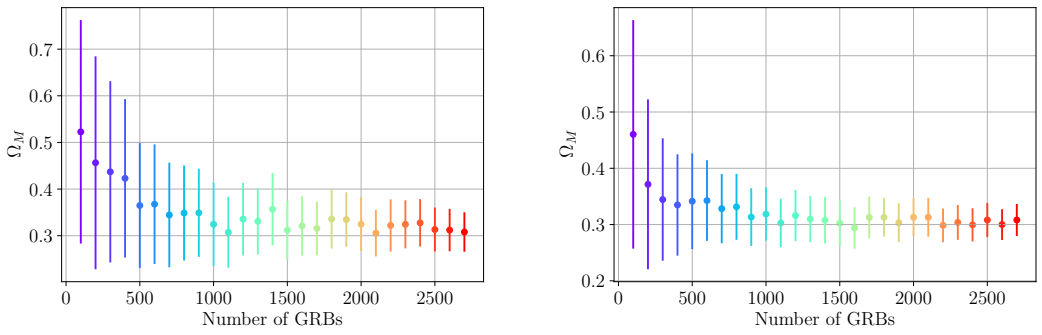

Figure 4.2: Left panel: the mean values of $\Omega_{\rm M}$ vs. the numbers of GRBs obeying the X-ray fundamental plane to converge upon a value of $\Omega_{\rm M}$ using GRBs as the standalone probe by considering the observed error bars. Right panel: the same as the left panel, but considering the halved error bars for the simulations.

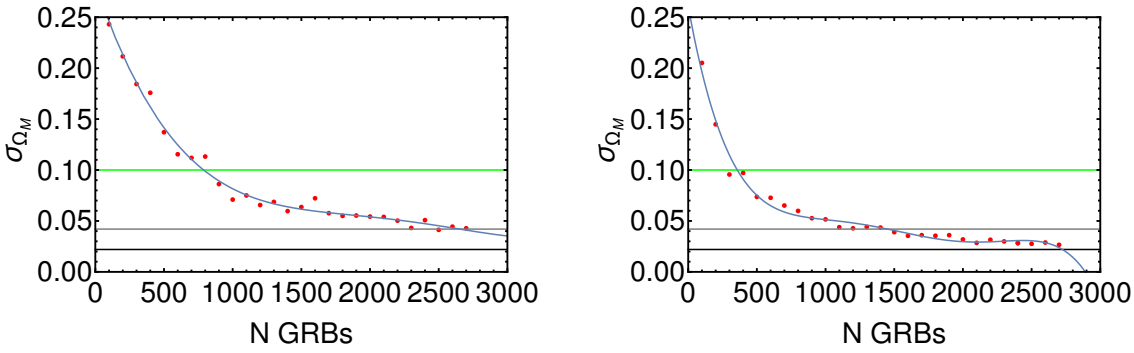

Figure 4.3: Left and right panels show the error plots for undivided and halved error bars, respectively, for the Platinum sample. The green, grey and black lines identify the [30, 31, 20] errors on $\Omega_{\rm M}$, respectively. The blue line, instead, denotes a polynomial fitting function used for the extrapolation of the exact GRB numbers for which we have achieved the SNe Ia thresholds.

the aforementioned thresholds obtained by the SNe Ia data, so that we focus on the error on $\Omega_{\rm M}$ rather than on the value of the parameter itself. In order to do so, we employ a polynomial best-fit function to our data (number of GRBs versus the error on $\Omega_{\rm M}$) and find the exact number from this function. The results are shown in Figure 4.3. From these figures, we can infer that, regarding the simulations with non-halved errors (left panel), 789 GRBs are needed to reach the same precision obtained in [30], 2653 GRBs are instead needed to reach the limit shown in [31], while we have not been able to achieve the [20] precision with this particular simulation.

We now focus on the right panel, where the simulations with the halved errors are shown. We note again how, in this instance, the decrease of the scatter with the number of simulated GRBs is faster than what we have obtained for the previous case, and this fact is reflected in the number of GRBs necessary to reach the three thresholds. Indeed, we find that only the first two simulations performed by us have uncertainties on $\Omega_{\rm M}$ higher than the [30] limit, which thus is reached with 357 GRBs according to our polynomial fit. For the [31] limit, we note that 1452 GRBs are needed. Finally, we expect to reach the [20] limit with 2724 GRBs from our simulations. We would like to stress again that the hypothesis of errors halved in future observations is, at least, realistic, given the technological improvements we are assisting in recent years. For instance, in [283] it has been tested that, with the current sample, a mean error reduction of 47.5% is viable with light curve reconstruction (LCR) methods [29] when we consider the error bars on the time at the end of the plateau, $T_{\rm a}$, and its corresponding flux.

We now move to the simulations based on the 45 GRBs belonging to the Optical sample. Following the same procedure as what we have explained regarding the Platinum

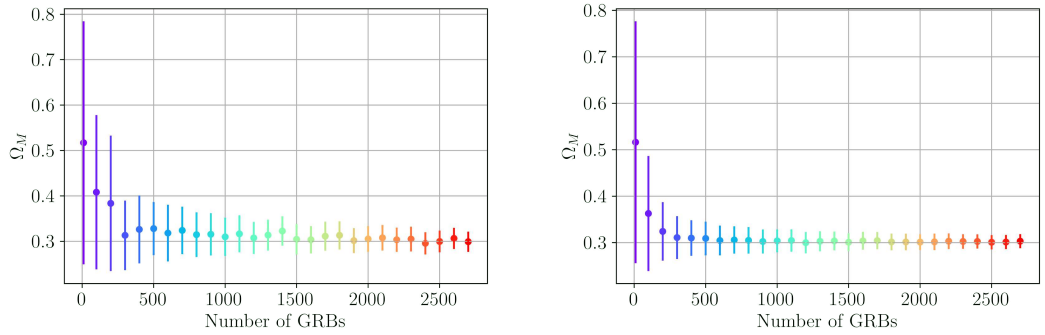

Figure 4.4: left panel: the mean values of Ω_M vs. the numbers of GRBs obeying the optical fundamental plane to converge upon a value of Ω_M using GRBs as the standalone probe by considering the observed error bars. Right panel: the same as the left panel, but considering the error bars divided by 2.

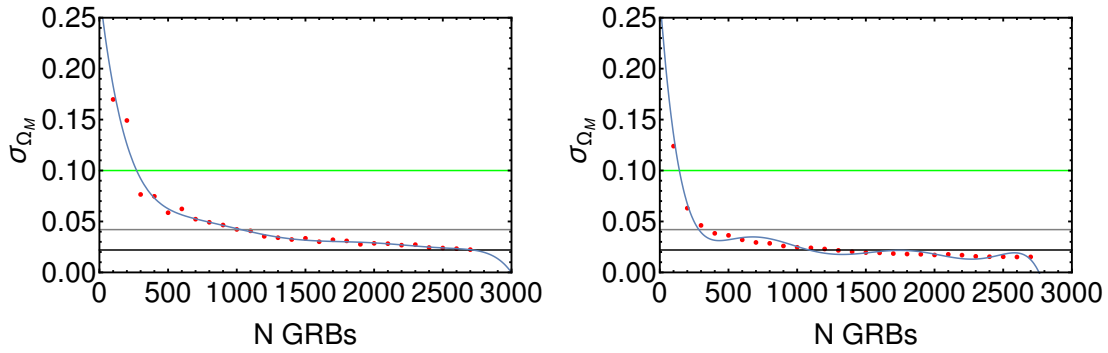

Figure 4.5: The plots show the number of simulated GRBs versus the error on Ω_M derived by the simulations starting from the full Optical sample. On the left panel, we have the undivided errors for the physical quantities related to the GRBs, while, on the right panel, we have divided these errors by 2. The green, grey, and black lines identify the [30, 31, 20] errors on Ω_M, respectively.

set, the results of our simulations are visualized in Figure 4.4, while the polynomial best-fits are shown in Figure 4.5. Interestingly, even if the baseline of the simulations is smaller, and fewer selection criteria have been applied to the optical GRBs, we note that in this case the simulations actually converge faster than those performed for the X-rays data, especially when the errors are halved. Even the Optical sample with undivided errors produces simulations that converge faster than those obtained with the X-ray set and halved errors.

This fact is confirmed by the polynomial best-fit. Indeed, we find that we need only 271 and 142 GRBs with undivided and halved errors, respectively, to reach the [30] limit, and 1031 and 489 GRBs, respectively, to reach the [31] one. Furthermore, with these simulations, we are finally able to reach the [20] limit with the non-halved errors: in order to do so, we need 2718 and 1086 GRBs, considering undivided and halved errors,

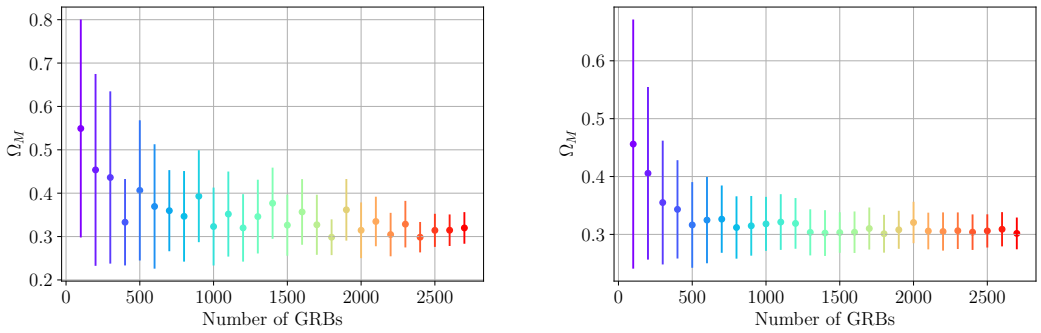

Figure 4.6: Left panel: the mean values of $\Omega_{\rm M}$ vs. the numbers of GRBs obeying the Platinum fundamental plane simulated with the 10 closest GRBs (undivided errors). Right panel: the same as the left panel, but considering the plane simulated with the 20 a posteriori GRBs instead of 10 with halved errors.

respectively.

We now continue our analysis by considering subsets of the Platinum and Optical samples as the baseline of our simulations. The first trimming of these samples has been decided "a priori", choosing the GRBs whose best-fitting fundamental plane shows a near 0 intrinsic scatter by taking the closest GRBs to the fundamental planes derived by the full sets. An alternative method has been followed as well, looking for the number of GRBs belonging to the Platinum sample that forms the set which, acting as a baseline, presents the faster convergence of the simulations. This method has also been applied to the Optical sample. These samples, chosen "a posteriori" are composed of 20 Platinum and 25 Optical GRBs, respectively. The general results regarding the trimmed analysis, in particular where the aforementioned thresholds have been reached, are reported in Table 4.1. We also show some of the plots representing the best-fit on Ω_M with the relative error versus the number of simulated GRBs, from which these results have been achieved via the aforementioned polynomial fit. For instance, the dependence of the derived $\Omega_{\rm M}$ with the number of simulated GRBs for the a priori trimming of the Platinum sample and considering halved errors is shown in the left panel of Figure 4.6, while, in the right panel, we find the same dependence but considering the a posteriori trimming as a baseline for the simulations. We note an improvement in the velocity of the convergence with respect to the full Platinum as a baseline case for the a posteriori computation, as expected given how it has been built.

Another example of our results is illustrated in Figure 4.7, where this time the a posteriori trimmed sample of optical GRBs is shown, both with undivided errors (left panel) as well as with halved errors (right panel). We may note the higher convergence speed even at low simulated numbers of GRBs, especially in comparison with the corresponding full data set simulations.

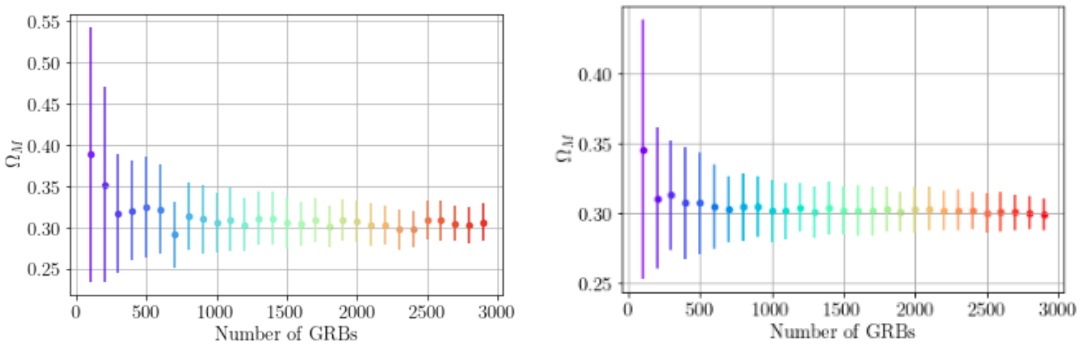

Figure 4.7: Left panel: the mean values of Ω_M vs. the numbers of GRBs obeying the optical fundamental plane simulated starting from the 25 a posteriori GRBs. Right panel: the same as the left panel, but considering the error bars divided by 2.

Number of GRBs with Plateaus Needed						
GRB Sample	Conley et al. (2011)		Betoule et al. (2014)		Scolnic et al. (2018)	
	n = 1	n = 2	n = 1	n = 2	n = 1	n = 2
PLAT	789	357	2653	1452	-	2724
OPT	271	142	1031	284	2718	1086
PLATtrim (a priori)	847	399	2705	1788	2839	2649
OPTtrim (a priori)	330	112	829	393	2870	1513
PLATtrim (a posteriori)	646	354	2699	1466	-	2719
OPTtrim (a posteriori)	244	36	685	350	2104	822

Table 4.1: The first column shows the sample, while the successive ones the numbers of GRBs needed for the limits set by [30, 31, 20], for both the full and halved error bars. We put a hyphen when the limit is not reached.

We note from this table that, while the a priori trimming, in general, does not reduce the number of GRBs necessary to reach the SNe Ia limits, the a posteriori simulations actually achieve higher precision with a smaller number of simulated GRBs in many cases, especially for the [30] limit.

4.3.2 GRBs cosmology timetable

We now shall derive in how many years these limits could be realistically achieved by the real future GRB data. For these computations, we also consider the possibility to use machine learning (ML) techniques in order to infer the redshift of GRBs otherwise unidentified [285], hypothesizing the doubling of the sample size at a given time due to these techniques, as well as light curves reconstruction methods [283], that, as previously discussed, should allow for a mean error reduction of 47.5%.

For the considered observational missions, we have taken into account the still operating Swift observatory, as well as future missions that should be launched in the next years. In particular, we considered the future contribution of the Space Variable Objects Monitor (SVOM, [286]), and the Transient High Energy Sources and Early Universe Surveyor (Theseus, [287]). SVOM should be launched in June 2023 and should act as a pathfinder for Theseus. It is expected to observe 80 GRBs per year for a mission planned to last 3 years, thus it should collect ~ 240 GRBs throughout the course of its lifetime, with $\sim 1-2$ triggers per week expected [288]. Theseus has, instead, a very tentative launch date in 2037. It is expected to observe 300-700 GRBs per year, and it has an expected lifetime of 3.45 years.

For our computations, we hypothesize that the effective lifetimes of these two future missions will be actually prolonged, as has already happened to other astrophysical missions. In particular, we guess that Theseus's lifetime will be at least as long as Konus-Wind's (27 years). We also assume that the SVOM mission will be prolonged to at least 15 years. For our deductions, we also take into account that our Platinum sample of 50 GRBs has been selected out of 1064 GRBs presenting X-rays observed by Swift-XRT up until August 2019, and that our 45 Optical GRBs set has been selected from 761 GRBs with optical observations from January 1997 up to December 2018, including those without redshift measurements and detected plateaus. We project the proportionalities to future data both in X-ray and optical bands in order to obtain our estimates.

To summarize, our hypotheses have brought us to the following prerequisites and considerations:

- Lifetime of Theseus = 27 years, with an estimated launch date in 2037.
- Lifetime of SVOM = 15 years, with an estimated launch date in 2023.

- Total number of GRBs observed throughout the lifetime of Theseus = 18900.
- Total GRBs observed throughout the lifetime of SVOM = 1350.
- Current rates of detection of Swift = 89.45 yr^{-1}.
- For X-ray wavelengths, we assume that the ratio (0.82) of the total number of GRBs observed by Swift-XRT (1064) from 2005 January until 2019 August compared to the total number of GRBs observed by Swift (1305) will be the same ratio of GRBs observed by the ECLAIRs (4-120 keV) on board of SVOM and the X-Gamma rays Imaging Spectrometer (XGIS, 2-20 MeV) and Soft X-ray Imager (SXI, 0.3-5 keV) on board of Theseus.
- For optical wavelengths, we assume that the ratio (0.39) of the total number of optical afterglows (761) observed from 1997 up to December 2018, compared to the total number of GRBs by all missions (1942), is again the same as the one observed by the Infrared Telescope (IRT, 0.7-1.8 μm) on Theseus, and as the Visible Telescope (VT, 540-600 nm) on board of SVOM.

Lastly, for optical wavelengths, we also consider ground-based telescopes, expecting a detection rate that shall remain the same as what we observe nowadays also in the future years, assuming that, even if some ground-based telescopes will stop their operations, new missions will take their places keeping the same detection rate (realistically, the rate should increase, given that new technological advances will be performed, but we prefer a conservative assumption on this particular point). Keeping in mind all these hypotheses, we finally obtain the results visualized in Tables 4.2 and 4.3.

We have divided these results into two tables because the [20] threshold has been reached predominantly by the Optical simulations. We note how dividing the errors in two has always a beneficial effect even for the year to achieve these limits, as expected given that it decreases the number of GRBs necessary to reach such thresholds. We also note that, for the [30] limit, in an ideal situation with all halved errors, and ML and LCR approaches already applied, for the Optical sample we should already be able to reach these limits, while, without all these hypotheses and looking only at the raw, real data, we reach these thresholds in 2055 for the Platinum sample and 2045 for the Optical set, once the a posteriori baselines are considered.

Regarding the [31] limit, instead, the earliest year in which we fall below the threshold is in 2038 with the full Optical sample and 2056 for the full Platinum sample, if we consider halved errors and LCR methods. These are the time periods we infer from our simulations in which GRBs should be able to constraint alone cosmological parameters with a precision similar to what is currently achieved by SNe Ia. Adding also the ML

GRB Sample		Conley et al. (2011)				Betoule et al. (2014)			
		n = 1	n = 2	n = 1 (47.5% LCR)	n = 2 (47.5% LCR)	n = 1	n = 2	n = 1 (47.5% LCR)	n = 2 (47.5% LCR)
PLAT	# GRBs (Plateau)	789	357	374	169	2653	1452	1260	689
	# GRBs (Total)	16789	7596	7975	3608	56455	30898	26816	14676
	Year Achieved	2060	2044	2045	2037	2129	2085	2078	2056
PLAT + ML	# GRBs (Total)	8394	3798	3987	1804	28227	15449	13408	7338
	Year Achieved	2045	2037	2038	2026	2080	2058	2054	2043
OPT	# GRBs (Plateau)	271	142	128	67	1031	284	489	134
	# GRBs (Total)	4582	2401	2176	1140	17435	4802	8281	2281
	Year Achieved	2046	2038	2038	2026	2093	2047	2060	2038
OPT + ML	# GRBs (Total)	2291	1200	1088	570	8717	2401	4140	1140
	Year Achieved	2038	2027	2025	Now	2061	2038	2045	2026
PLATtrim (10)	# GRBs (Plateau)	847	399	402	189	2705	1788	1284	849
	# GRBs (Total)	18024	8490	8561	4033	57562	38048	27342	18073
	Year Achieved	2062	2045	2046	2038	2131	2097	2078	2062
PLATtrim (10) + ML	# GRBs (Total)	9012	4245	4280	2016	28781	19024	13671	9036
	Year Achieved	2046	2038	2038	2027	2081	2064	2054	2046
OPTtrim (10)	# GRBs (Plateau)	330	112	156	53	829	393	393	186
	# GRBs (Total)	5580	1894	2650	899	14019	6646	6659	3156
	Year Achieved	2050	2037	2039	2022	2081	2054	2054	2041
OPTtrim (10) + ML	# GRBs (Total)	2790	947	1325	449	7009	3323	3329	1578
	Year Achieved	2040	2023	2029	Now	2055	2042	2042	2032
PLATtrim (20)	# GRBs (Plateau)	646	354	306	168	2699	1466	1282	696
	# GRBs (Total)	13746	7533	6529	3578	57434	31196	27281	14818
	Year Achieved	2055	2044	2045	2037	2131	2085	2078	2057
PLATtrim (20) + ML	# GRBs (Total)	6873	3766	3264	1789	28717	15598	13640	7409
	Year Achieved	2043	2037	2036	2025	2081	2058	2054	2044
OPTtrim (25)	# GRBs (Plateau)	244	36	115	25	685	350	325	166
	# GRBs (Total)	4126	608	1959	289	11584	5918	5502	2811
	Year Achieved	2045	now	2037	Now	2072	2051	2050	2040
OPTtrim (25) + ML	# GRBs (Total)	2063	304	979	144	5792	2959	2751	1405
	Year Achieved	2037	Now	2024	Now	2051	2040	2040	2030

Table 4.2: In the first column, we show all the samples considered in our analysis. In the three rows associated with each sample definition, we find the number of GRBs necessary to reach the specified limit with detected plateau phases belonging to the future Platinum and Optical sets under the same criteria considered by us, the total number of GRBs needed, and the expected year in which this number is achieved with observed data. For each row, we show results related to samples with the errors undivided, the errors halved, the errors undivided considering LCR, and finally, the errors halved including LCR. The overarching columns three and four give these estimates considering the precision reached by [30] and [31], respectively. A sample "+ ML" implies that machine learning techniques are employed to double the initial sample size by redshift inference.

GRB Sample		Scolnic et al. (2018)			
		n = 1	n = 2	n = 1 (47.5% LCR)	n = 2 (47.5% LCR)
OPT	# GRBs (Plateau)	2718	1086	1291	515
	# GRBs (Total)	45964	18365	21833	8723
	Year Achieved	2197	2097	2140	2061
OPT + ML	# GRBs (Total)	22982	9182	10916	4361
	Year Achieved	2113	2063	2069	2046
OPTtrim (10)	# GRBs (Plateau)	2870	1513	1363	718
	# GRBs (Total)	48534	23054	12153	19840
	Year Achieved	2207	2123	2114	2074
OPTtrim (10) + ML	# GRBs (Total)	24267	12793	11527	6076
	Year Achieved	2118	2076	2072	2052
OPTtrim (25)	# GRBs (Plateau)	2104	822	999	390
	# GRBs (Total)	35580	13900	16900	6602
	Year Achieved	2159	2080	2091	2054
OPTtrim (25) + ML	# GRBs (Total)	17790	6950	8450	3301
	Year Achieved	2094	2055	2060	2042

Table 4.3: In the first column we show all the combinations of Optical GRBs used. The three rows associated with each sample show 1) the needed number of GRBs having observed plateau phases, 2) the total number of GRBs needed, and 3) the year in which that number of GRBs is achieved with observed data. These rows are repeated for samples with the errors undivided, the errors halved, the errors undivided considering LCR, and finally, the errors halved including LCR. These estimates are given considering the precision reached by [20]. Again, with ML we take into account possible machine-learning techniques.

approaches, we ideally reach this limit in 2026 (4 years from now) for the Optical sample and in 2043 for the Platinum sample considering halved errors.

In Table 4.3 we see the years in which the optical simulations reach the [20] limit. We see that, for the most ideal case, this limit should be reached in 2042. This baseline does not take into account the idea that, with more optical GRBs, in the future we should be able to define an analogous of the Platinum sample also for the optical band, thus improving, even more, their constraint capabilities. Furthermore, as we keep investigating the physics of GRB progenitors and central engines, we will be able to better define GRB classes and samples, thus continuing to improve the precision of our results, as well as shed more and more light on the mechanisms behind these objects. Nevertheless, even with some drawbacks and the ideal nature of some of the hypotheses used in our investigation, we still expect the time periods deduced by us to be indicative of the future of GRBs' standalone cosmology.

4.4 GRBs, SNe Ia, and BAO

In this section, we will show the results related to the derivation of cosmological parameters that we obtained using the real data of GRBs together with the other probes, more specifically SNe Ia and BAO. In this section, a good part of the analysis performed in [29, 32, 33] will be shown.

4.4.1 Using the full samples

As previously introduced, the data sets used are the following: the Pantheon sample of SNe Ia [20], 16 BAO-related measurements, [76, 257, 258, 261, 262], and the Platinum and Optical samples of GRBs previously discussed. The idea is to combine the different likelihoods to infer the values and, more importantly, the precision of these values, of cosmological parameters like Ω_M and H_0. For the GRB samples, we also employ the EP method to correct for evolutionary effects and selection biases, as we did in the previous chapter, in order to find if this correction has also an influence on cosmological results.

The first results are gathered in Table 4.4.1, where the inferred cosmological parameters for the following combinations of sets are collected: SNe Ia, BAO, SNe Ia+ BAO, BAO+GRBs without evolution corrections, BAO+GRBs with evolution corrections, SNe Ia+BAO+GRBs without evolution corrections, SNe Ia+BAO+GRBs with evolution corrections. In this case, the GRBs are those belonging to the X-rays Platinum sample. When we compute only Ω_M, we fix $H_0 = 70\ km\ s^{-1}Mpc^{-1}$, while, when we derive only H_0, we fix $\Omega_M = 0.3$. This will also be true for all the computations we are going

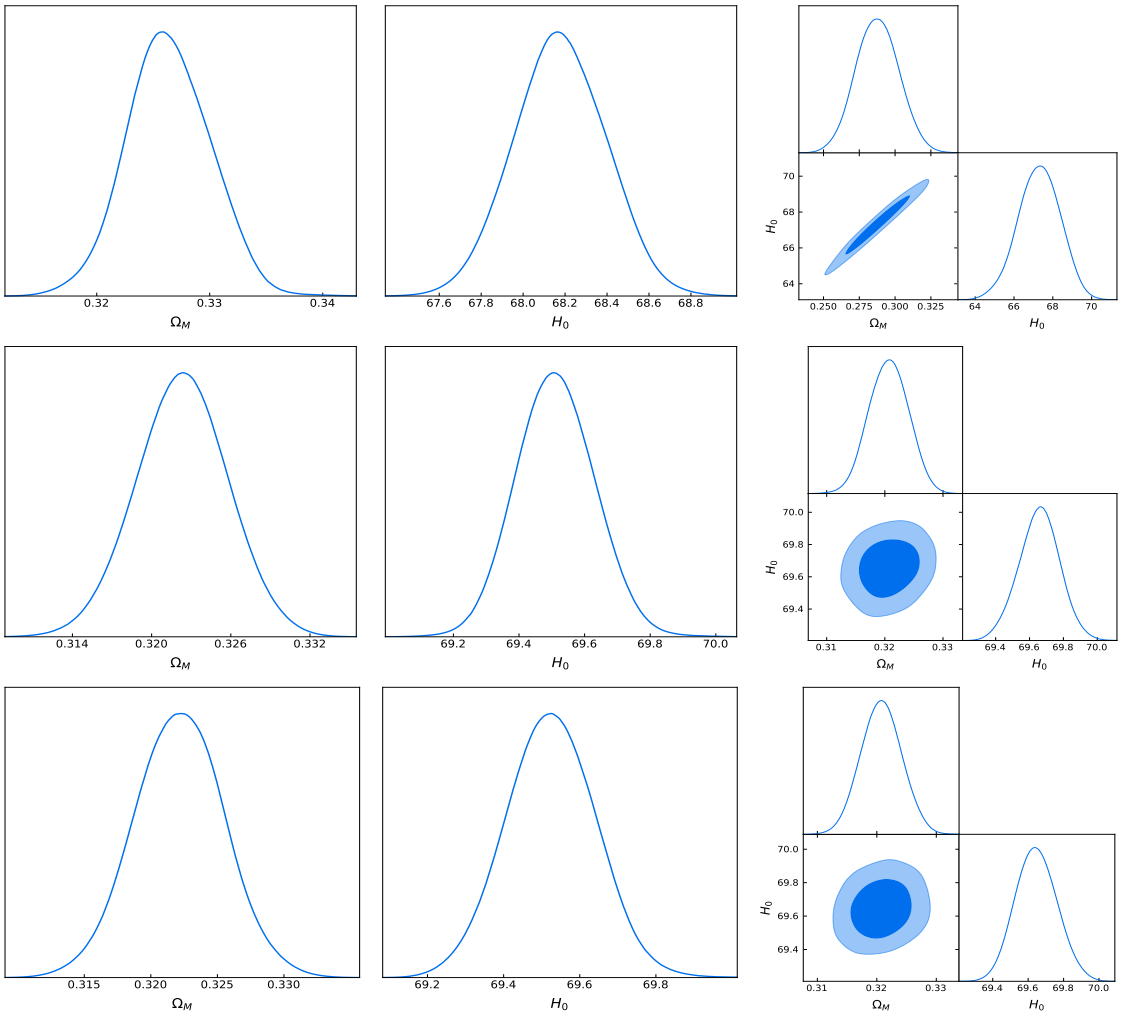

Figure 4.8: Posterior contours computed for the full samples of SNe Ia, BAO, and GRBs. On the upper panels, the results for BAO+GRBs without evolution are shown varying Ω_M alone (upper left), H_0 alone (upper center), and Ω_M and H_0 together (upper right). On the central panels, instead, the results for SNe Ia+BAO+GRBs without evolution are shown, in the same order as before. The same is visualized in the bottom panels, where the evolutionary effects regarding GRBs are taken into account.

Sample	Ω_M	H_0 $km\ s^{-1}Mpc^{-1}$	Ω_M and H_0 $km\ s^{-1}Mpc^{-1}$
SNe Ia	0.299 ± 0.009	69.98 ± 0.14	0.298 ± 0.020 70.014 ± 0.313
BAO	0.326 ± 0.004	68.17 ± 0.23	0.286 ± 0.015 67.19 ± 1.09
SNe Ia+BAO	$\$0.322 \pm 0.003$	69.53 ± 0.12	0.321 ± 0.003 69.64 ± 0.12
BAO+GRBs NO EV	0.326 ± 0.004	68.17 ± 0.22	0.289 ± 0.015 67.41 ± 1.08
BAO+GRBs EV	0.326 ± 0.004	68.17 ± 0.22	0.286 ± 0.015 67.22 ± 1.05
BAO+SNe Ia+GRBs NO EV	0.322 ± 0.003	69.53 ± 0.12	0.321 ± 0.003 69.64 ± 0.12
BAO+SNe Ia+GRBs EV	0.322 ± 0.003	69.53 ± 0.11	0.321 ± 0.003 69.64 ± 0.12

Table 4.4: The table shows the results of our cosmological computations for the full SN Ia, BAO, and GRB Platinum samples. With "EV" we indicate the correction for redshift evolution and selection biases regarding the GRB sample.

to show in this section. Lastly, we study the case in which we vary both these values contemporaneously. We also note that in these derivations we are keeping ourselves inside the ΛCDM paradigm and that these parameters have been derived while also computing the best-fit coefficients of the fundamental plane correlation, thus avoiding the aforementioned circularity problem.

We may note the beneficial effect of adding more cosmological probes with respect to using SNe Ia as standalone candles: for instance, we notice that the smallest scatter on H_0 has been reached by the SNe Ia+BAO+GRBs set with evolution corrections. This beneficial effect is predominantly due to the addition of BAO to the Pantheon SNe Ia sample (that we keep as a reference point), but we note that also GRBs bring a positive contribution, because the SNe Ia+BAO+GRBs sets provide a precision that is slightly better or comparable to the SNe Ia+BAO one. Even in the cases in which they do not improve the overall precision on the cosmological parameters, their contribution remains important because they are able to extend, by their nature, the cosmological ladder up to $z = 5$ (for the Platinum sample), keeping in mind that GRBs can be detected at even higher redshifts.

In Figure 4.8 we visualize the contour plots of some of the results presented in the table, more specifically the BAO+GRBs without evolution, SNe Ia+BAO+GRBs without evolution, and SNe Ia+BAO+GRBs with evolution sets. We note the higher precision reached by the latter two computations than the former for every cosmological parameter

Sample	$\Omega_{\rm M}$	Sample	$\Omega_{\rm M}$
SNe Ia	0.299 ± 0.009		
PLAT+SNe Ia	0.299 ± 0.009	PLAT+SNe Ia (EV)	0.299 ± 0.009
PLATtrim+SNe Ia	0.299 ± 0.009	PLATtrim+SNe Ia (EV)	0.299 ± 0.008
OPT+SNe Ia	0.299 ± 0.009	OPT+SNe Ia (EV)	0.299 ± 0.008
OPTtrim+SNe Ia	0.299 ± 0.009	OPTtrim+SNe Ia (EV)	0.299 ± 0.009

Table 4.5: Results for Ω_M taking into account the Platinum and Optical GRB samples together with SNe Ia. In the second column, we do not consider the evolutionary corrections, while in the fourth we do.

studied in our analysis.

Next, we shall compare the Optical and Platinum samples as direct cosmological tools, using them together with the SNe Ia set. We will also consider the possibility of using the a priori trimmed samples introduced in the previous section [29]. The results are shown in Table 4.5 for Ω_M.

We note how, in general, the precision of the results remains unvaried, with a reduction, albeit not decisive, of the scatter on Ω_M for the trimmed Platinum sample and the Optical set once the evolutionary effects are taken into account.

These cosmological computations allow us to draw a Hubble diagram related to the GRBs. This is shown, for the Platinum sample, in figure 4.9. We note how the majority of the data points are consistent with the best-fit cosmological line. We also note that a few data points are not consistent with the best-fit curve within 1 σ. This could be due to large dispersion effects that may be related to the errors on the measured quantities in our fit, but still, given the majority of the data points are well-fitted by our derived cosmological model, this shows a good hint for the reliability of GRBs as cosmological tools.

To confirm the reliability of our analysis, we have also considered a different sample for BAO measurements regarding our cosmological computations. Indeed, taking into account the values found in [260] instead of those used up to now, we have performed the same computations concerning the aforementioned cosmological parameters. The related results are shown in Table 4.4.1. Comparing these with the ones obtained with the previous BAO set, we note that the latter achieves a higher precision for every computation, especially regarding Ω_M. We also note the difference in the computed central values, again predominantly on when we derive Ω_M fixing H_0.

With the new BAO sample, we have also investigated parameters going beyond the classical ΛCDM model. Indeed, we have computed the dark energy parameter w for a wCDM model (for which we recover the ΛCDM model if we fix $w = -1$), and the curvature density Ω_K, thus not imposing the universe to be flat. The results for these

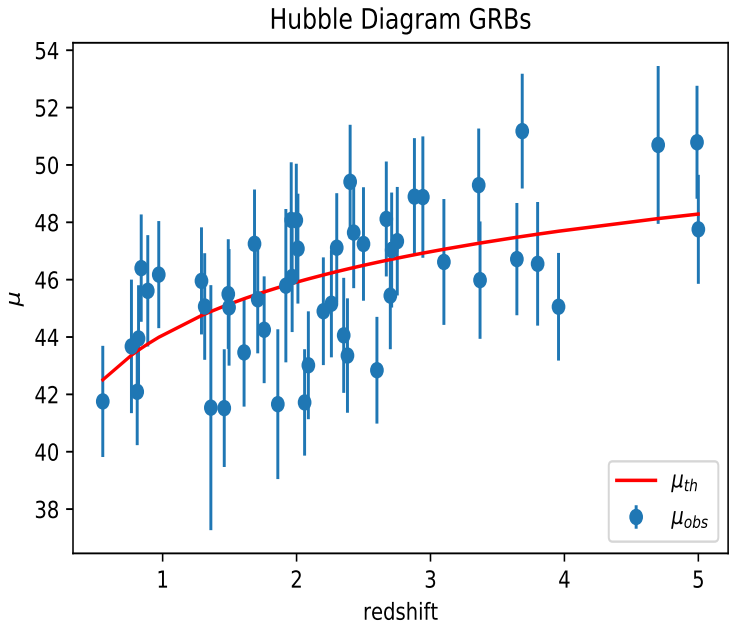

Figure 4.9: The Hubble diagram computed considering only the Platinum GRBs used in our computations.

Sample	Ω_M	H_0 $km\ s^{-1}Mpc^{-1}$	Ω_M and H_0 $km\ s^{-1}Mpc^{-1}$
SNe Ia+BAO	0.304 ± 0.006	69.69 ± 0.13	0.311 ± 0.007 69.82 ± 0.13
BAO+SNe Ia+GRBs NO EV	0.306 ± 0.006	69.94 ± 0.13	0.310 ± 0.007 69.84 ± 0.15
BAO+SNe Ia+GRBs EV	0.306 ± 0.006	69.94 ± 0.14	0.310 ± 0.007 69.83 ± 0.16

Table 4.6: The table shows the results of our cosmological computations for the full SN Ia, the 26 BAO measurements of [260], and GRB Platinum samples. With "EV" we indicate the correction for redshift evolution and selection biases regarding the GRB sample.

Sample	Ω_k	w
SNe Ia	-0.003 $\pm$ 0.018	-1.000 ± 0.018
SNe Ia+BAO	-0.016 $\pm$ 0.012	-1.017 ± 0.014
BAO+SNe Ia+GRBs NO EV	-0.017 $\pm$ 0.012	-1.017 ± 0.014
BAO+SNe Ia+GRBs EV	-0.013 $\pm$ 0.011	-1.017 ± 0.015

Table 4.7: The table shows the results of our cosmological computations for the full SN Ia, the 26 BAO measurements of [260], and GRB Platinum samples, for two new cosmological parameters going beyond the ΛCDM model.

Bin	Mean z	z range	SNe	BAO	GRBs
1	0.038	$0.010 \leq z \leq 0.094$	209	0	0
2	0.156	$0.096 \leq z \leq 0.203$	209	2	0
3	0.248	$0.203 \leq z \leq 0.298$	209	0	0
4	0.375	$0.299 \leq z \leq 0.503$	209	3	0
5	1.071	$0.503 \leq z \leq 5$	212	11	50

Table 4.8: The table shows the number of bins, the average redshift of each bin, and the number of SNe Ia, BAO, and GRBs in every bin considering the division in the redshift ranges displayed in the second column.

further computations are visualized in Table 4.4.1. Here, we may note that our results are consistent (or close to being consistent) with the ΛCDM model within 1-σ. We have to also note that these values have been computed by keeping fixed all the aforementioned cosmological parameters.

4.4.2 The Binned analysis

To further investigate the weight of GRBs in our cosmological computations, taking into account the Platinum sample, in [32] we have decided to divide our data sets into 5 different bins, in order of increasing redshift, in such a way that all GRBs belong to the last bin. Each bin division has been performed so that every one of those contains the same number of SNe Ia (with the exception of the last bin, which has 3 more SNe Ia with respect to the others). This bin division has brought us to the subsets detailed in Table 4.8, in which we can also see the redshift intervals for each bin. For this analysis, we go back to the 16 BAO data-set used previously [76].

As we can see, the BAO data points are gathered inside bins 2, 4, and 5. We now move to the computations themselves. As done in the previous section, we compute Ω_M keeping H_0 fixed, H_0 keeping Ω_M fixed, and Ω_M and H_0 contemporaneously, recalling that the fixed values are those previously mentioned. For each of these cases, we consider the GRBs both with and without the corrections for evolutionary effects and selection biases.

Ω_M (SNe Ia)	Ω_M (SNe Ia+BAO)	Ω_M (SNe Ia+BAO+GRBs) No EV	Ω_M (SNe Ia+BAO+GRBs) EV
0.387 ± 0.143	-	-	-
0.259 ± 0.038	0.298 ± 0.031	-	-
0.334 ± 0.025	-	-	-
0.272 ± 0.016	0.314 ± 0.006	-	-
0.295 ± 0.013	0.326 ± 0.005	0.326 ± 0.005	0.326 ± 0.005

Table 4.9: The table shows in the first column the results for Ω_M for the bins of SNe Ia alone, in the second column the results for Ω_M with SNe Ia+BAO, in the third column the same results for SNe Ia+BAO+GRBs without accounting for the evolutionary effects for GRBs, and in the last column the same combination considering the evolutionary effects.

The first results, related to Ω_M, are shown in Table 4.9. For each bin, all the possible sub-sets have been considered, taking into account which particular data point belongs to each bin. Commenting on the results, we see that, as for the full sets, also in this case a beneficial effect due to adding more probes to the SNe Ia, whose standalone results are taken as reference points, as usual, has been noted. This trend will be verified also for the computations regarding H_0, and Ω_M, H_0 together. Indeed, we note that the highest precision has been reached from the results given by bin 5 when at least SNe Ia and BAO are considered: $\Omega_M = 0.326 \pm 0.005$, which is also the same result obtained once GRBs are taken into account, both accounting or not for evolutionary effects. Adding more probes to the SNe Ia does indeed increase the precision of the cosmological calculations because bin 5 presents more BAO and GRBs. This is true even if the GRB and BAO sets are considerably smaller than the SNe Ia sample, even after the bin division (albeit we have to recall that behind the BAO-related data there are hundreds of thousands of observations regarding galaxies and clusters of galaxies [76]).

Regarding the central values obtained for each bin, we note that all the results for Ω_M are consistent within 1 σ once we take into account the BAO data. We also note that BAO measurements have the most relevant impact concerning the decrease of the cosmological uncertainties with respect to the SNe Ia alone computations. The decrease on the scatter (σ) of Ω_M for bin 5 compared to the SNe Ia alone is 62% for GRBs+BAO+SNe Ia both for the case of evolution and the one of no evolution, as well as for the SNe Ia+BAO set. We also note that the most significant decrease comes for bins 4 and 5, where the most non-SNe Ia probes are found.

In Figure 4.10, some salient contour plots are shown, related in particular to bin 5. We note how similar they are when we compare the SNe Ia+BAO and GRBs+SNe Ia+BAO results, and their improved precision with respect to the SNe Ia computations.

We now comment on the results obtained for H_0, shown in Table 4.10. We again note the increase in the precision of our results obtained by adding GRBs and BAO to SNe Ia. Indeed, We note that, in this case, the best precision is reached again by bin 5 when we

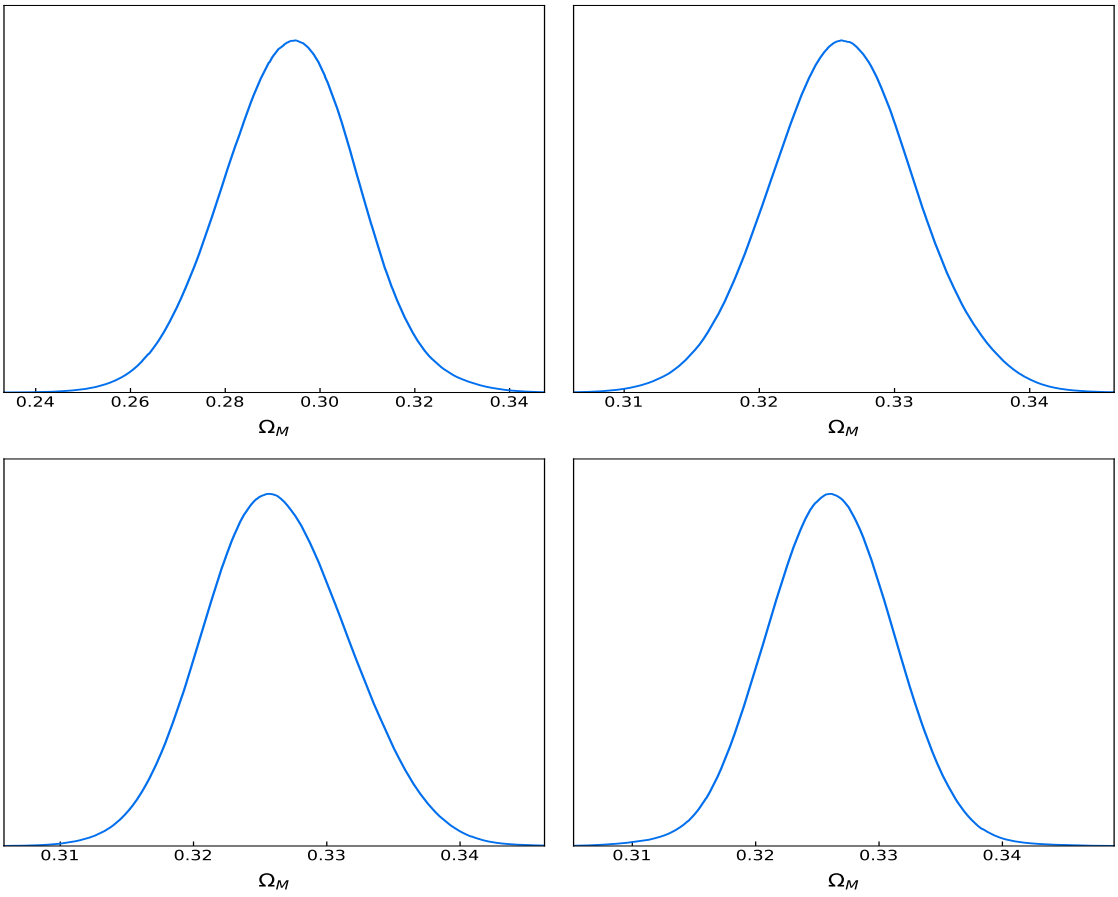

Figure 4.10: Results of the cosmological computations of bin 5, varying only Ω_M, for SNe Ia (top left panel) SNe Ia+BAO (top right panel), and GRBs+SNe Ia+BAO, both without (bottom left panel) and with (bottom right panel) considering the evolutionary effects.

H_0 (SNe Ia) $km\ s^{-1}Mpc^{-1}$	H_0 (SNe Ia+BAO) $km\ s^{-1}Mpc^{-1}$	H_0 (SNe Ia+BAO+GRBs) No Ev $km\ s^{-1}Mpc^{-1}$	H_0 (SNe Ia+BAO+GRBs) Ev $km\ s^{-1}Mpc^{-1}$
70.50 ± 0.40	-	-	-
69.55 ± 0.29	69.52 ± 0.32	-	-
70.37 ± 0.35	-	-	-
69.46 ± 0.33	69.16 ± 0.27	-	-
69.80 ± 0.45	68.61 ± 0.26	68.61 ± 0.26	68.61 ± 0.26

Table 4.10: Similarly to Table 4.9, this table shows the results obtained for H_0 for the same bins used in the previous table, this time fixing the values of Ω_M.

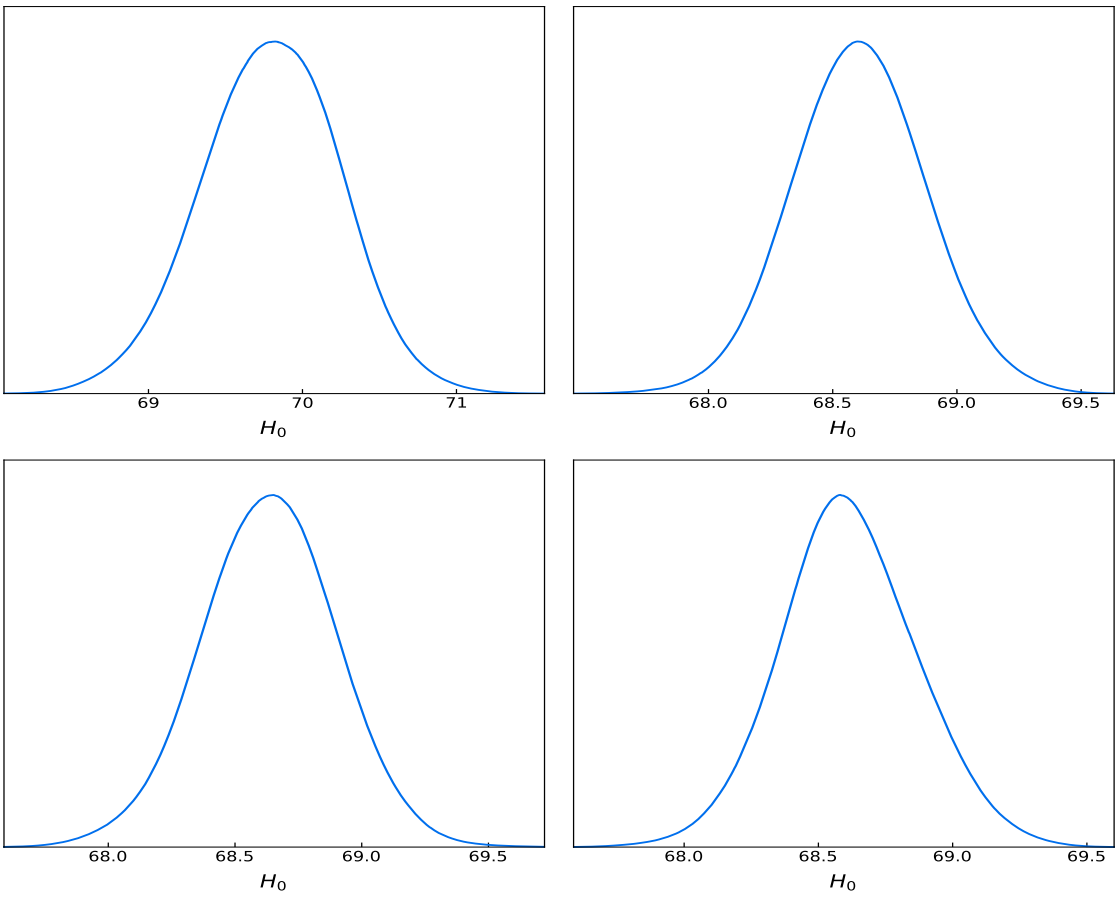

Figure 4.11: Results of the cosmological computations of bin 5, varying only H_0, for SNe Ia (top left panel) SNe Ia+BAO (top right panel), and GRBs+SNe Ia+BAO, both without (bottom left panel) and with (bottom right panel) considering the evolutionary effects.

consider BAO+SNe Ia and BAO+SNe Ia+GRBs both with and without evolution. Again, the most relevant contribution comes from the BAO measurements, while the highest contribution of GRBs is allowing, due to their nature, to extend the cosmological ladder. The clearest improvement in the precision comes, again, from bin 5, where we note that the scatter on H_0 goes from $0.45\ km\ s^{-1}Mpc^{-1}$ for the SNe Ia only sub-set to $0.26\ km\ s^{-1}Mpc^{-1}$ for all the other subsets belonging to bin 5, thus bringing us to a 42.2% decrease on the scatter. In Figure 4.11, again, some contour plots are shown, related in particular to bin 5, this time for H_0. We note again the similarities between the SNe Ia+BAO and GRBs+SNe Ia+BAO results, and the improved precision of both of them with respect to the SNe Ia computations.

Finally, we address the case in which we vary Ω_M and H_0 contemporaneously, whose results are presented in Table 4.11. We note that for bins 1 and 3 the computations do not converge for the particular prior interval chosen for our Bayesian analysis ($0 < \Omega_M < 1$) when we consider only the SNe Ia: these cases are indicated with NA inside the table. Like for the other computations, the scatter is reduced by adding other probes to the SNe Ia, especially due to BAO. In particular, for bin 4, when we consider SNe Ia+BAO, we reach a precision for Ω_M and H_0 similar to what has been obtained when we vary these two parameters alone: $H_0 = 69.27 \pm 0.28$ when we vary them contemporaneously vs. $H_0 = 69.16 \pm 0.27$ when we keep Ω_M fixed, and $\Omega_M = 0.311 \pm 0.006$ when we vary both of them vs. $\Omega_M = 0.314 \pm 0.006$ when we keep H_0 fixed. When we consider bin 5 the same precision is reached for Ω_M for SNe Ia+BAO and GRBs+SNe Ia+BAO both with and without considering evolutionary effects. For H_0, instead, the most precise value is reached when only BAO+SNe Ia are considered, followed by the case of GRBs with evolution. The least precise measurement (excluding the SNe Ia case) belongs to the case of GRBs with no evolution. Regarding the percentage decrease on the scatter for bin 5, for Ω_M we obtain a 90.8% decrease for all the cases in which we add probes to the SNe Ia, while for H_0 we obtain an 85.2% decrease when we compare SNe Ia to SNe Ia+BAO, an 84.2% decrease when we compare SNe Ia to SNe Ia+BAO+GRBs without evolution, and an 84.7% decrease when we compare SNe Ia to SNe Ia+BAO+GRBs with evolution.

Lastly, in Figure 4.12, the results for H_0 and Ω_M are shown for the same cases. The same conclusions related to the other contour plots apply also here.

The general trend shown in the previous three tables allows us to deduce that GRBs bring a marginal contribution to the increase in the precision of the cosmological parameters, overshadowed by the other two types of cosmological probes. We still think that this is an interesting result, given that they are still able to extend the cosmological ladder with no harm to the precision itself. Nevertheless, we further investigate their contribution by adding a new subset, which we call bin 6, composed of all the astrophysical objects that

Ω_M (SNe Ia) H_0 (SNe Ia)	Ω_M (SNe Ia+BAO) H_0 (SNe Ia+BAO)	Ω_M (SNe Ia+BAO+GRBs) No Ev H_0 (SNe Ia+BAO+GRBs) No Ev	Ω_M (SNe Ia+BAO+GRBs) Ev H_0 (SNe Ia+BAO+GRBs) Ev
NA 71.20 ± 0.88	- -	- -	- -
0.60 ± 0.20 67.4 ± 1.4	0.429 ± 0.072 68.679 ± 0.605	- -	- -
NA 64.8 ± 2.2	- -	- -	- -
0.339 ± 0.140 68.88 ± 2.38	0.311 ± 0.006 69.27 ± 0.28	- -	- -
0.314 ± 0.065 69.37 ± 2.03	0.317 ± 0.006 69.11 ± 0.30	0.317 ± 0.006 69.11 ± 0.32	0.317 ± 0.006 69.11 ± 0.31

Table 4.11: Similarly to the two previous tables, this table shows the same analysis, but for the case where Ω_M and H_0 are computed contemporaneously. We indicate with "NA" (not available) the runs for Ω_M that do not converge in the allocated intervals.

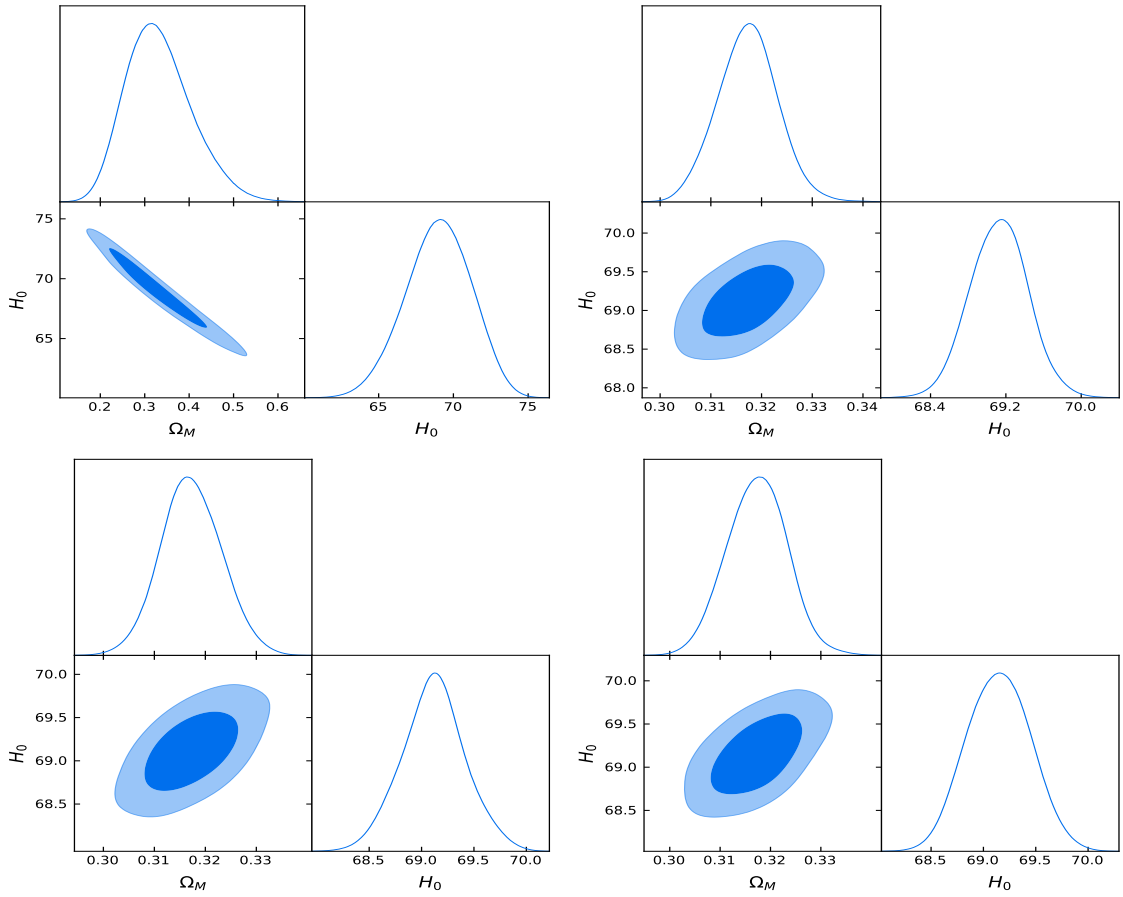

Figure 4.12: Results of the cosmological computations of bin 5, varying both Ω_M and H_0, for SNe Ia (top left panel) SNe Ia+BAO (top right panel), and GRBs+SNe IA+BAO, both without (bottom left panel) and with (bottom right panel) considering the evolutionary effects.

Ω_M (GRBs+BAO) No Ev	H_0 (GRBs+BAO) No Ev	Ω_M (GRBs+BAO) Ev	H_0 (GRBs+BAO) Ev
0.272 ± 0.038	67.83 ± 3.50	0.271 ± 0.037	68.45 ± 3.60

Table 4.12: Results obtained considering the BAO and GRBs belonging to bin 6 varying: 1) Ω_M alone without evolution; 2) H_0 alone without evolution; 3) Ω_M alone with evolution, and 4) H_0 alone with evolution.

present a redshift beyond the one of the furthest SN Ia belonging to the Pantheon sample ($z = 2.26$). The probes that satisfy this requirement are 2 BAO-related measurements and 23 GRBs. The results for this new bin are shown in Table 4.12.

In this table, we note how, albeit the precision of the results is worse than what has been obtained in the previous computations, as expected given the limited number of data points, we still manage to obtain close contours for the cosmological parameters even with a relatively small sample size of cosmological probes. The results have been derived both with and without considering the corrections due to the evolutionary effects related to GRBs.

4.4.3 Calibrating GRBs on SNe Ia

We now present some further cosmological computations regarding GRBs performed in [33]. In particular, we have already mentioned that, for the cosmological ladder approach, one could set up a standard candle by calibrating it with other cosmological probes. For the case of GRBs, we refer, again, to the SNe Ia, considering the following methodology:

1. we first fit the GRB fundamental plane correlation (as usual, considering also the intrinsic scatter) for the part of our GRBs sample whose redshift overlaps with the redshift range of SNe Ia, which corresponds to 25 GRBs. For this computation, we fix the values for the H_0 and Ω_M parameters considering the results obtained by SNe Ia alone (using $H_0 = 70\ km\ s^{-1}Mpc^{-1}$ and $\Omega_M = 0.3$ as we did in the previous computations, being values close to those obtained from SNe Ia).

2. We have then performed our cosmological computations as previously shown for GRBs, but this time fixing the fundamental plane correlation parameters to what we have found in the previous step, thus varying only the cosmological ones. This time, for the priors, we have considered Gaussian priors with 3 σ based on the values of [20]. We have again performed our computations both with and without considering the evolutionary effects for GRBs. The Gaussian priors are justified by the fact that the underlying physics behind the fundamental plane is not expected to vary within any cosmological model, given that the magnetar framework does not depend on cosmology, but rather on the fundamental physics of compact objects.

Considering evolution	parameters varied	Ω_M	H_0	w
without evolution	Ω_M	0.292 ± 0.068	**70**	**-1**
without evolution	H_0	**0.30**	73.286 ± 3.007	**-1**
without evolution	Ω_M and H_0	0.295 ± 0.064	73.358 ± 3.006	**-1**
without evolution	w	**0.30**	**70**	-1.094 ± 0.673
with evolution	Ω_M	0.316 ± 0.068	**70**	**-1**
with evolution	H_0	**0.30**	72.762 ± 3.227	**-1**
with evolution	Ω_M and H_0	0.306 ± 0.060	73.264 ± 3.082	**-1**
with evolution	w	**0.30**	**70**	-0.743 ± 0.694

Table 4.13: Cosmological parameters obtained using GRB alone calibrated on SNe Ia using Gaussian priors. In the first column, we show if evolution has been considered or not. In the second column, we define which cosmological parameters are left free to vary. In the next three columns, we present the values of parameters with error bars obtained in our computation for each given case, showing in bold the fixed values of the other cosmological quantities.

Considering evolution	parameters varied	$<\Omega_M>$	$<H_0>$	$<w>$
without evolution	Ω_M	0.50 ± 0.28	**70**	**-1**
without evolution	H_0	**0.30**	74.11 ± 14.48	**-1**
without evolution	w	**0.30**	**70**	-1.01 ± 0.56
with evolution	Ω_M	0.59 ± 0.27	**70**	**-1**
with evolution	H_0	**0.30**	79.04 ± 13.12	**-1**
with evolution	w	**0.30**	**70**	-0.88 ± 0.58

Table 4.14: Averaged cosmological parameters obtained using GRB alone calibrated on SNe Ia using flat priors, running 100 times the best-fit computations. In the first column, we show if evolution has been considered or not. In the second column, we define which cosmological parameters are left free to vary. In the next three columns, we present the values of parameters with error bars obtained in computation for each given case, showing in bold the fixed values of the other cosmological quantities.

3. Finally, we have performed the same computations, but considering flat priors for the cosmological parameters. For this case, 100 best-fit runs have been performed for each derivation, and the average cosmological results of these runs are shown.

The results for these two procedures are gathered in Tables 4.13 and 4.14. For the Gaussian prior results, we note that they are all consistent with those found for the ΛCDM model, with H_0 consistent with the values achieved by the late-type measurements. This was to be expected given the methodology followed for this particular section, which cannot allow us to explore parameter spaces that may lead to exotic scenarios, but rather to test the reliability of GRBs as cosmological probes. It is also noticeable that, according to our computations, the current data for GRBs analyzed by us are not competitive with more popular cosmological probes, especially for the precision achieved on the parameters, but still, as previously mentioned, a beneficial effect is at hand because of the possibility of exploring high redshift regions.

This is more evident from the results obtained considering flat priors, from which we may note higher uncertainties on the best-fit values than those obtained by using the Gaussian prior, even after the averaging procedure. Indeed, we may note scatters that are more than three times bigger for all the cosmological parameters if we compare flat priors with the Gaussian ones, with one, remarkable, exception. Indeed, the w results are more precise for the flat priors than the Gaussian ones. It is not clear why this result has been obtained only for this particular parameter. We also note the high central value for Ω_M, which could be investigated once more GRB data are at our disposal. This effect could not have been analyzed in the simulations shown previously for how they have been built (we recall that the focus was the study of the achieved uncertainties rather than the cosmological parameters themselves.)

Chapter 5

Extended Electromagnetism and its cosmological and astrophysical applications

In this chapter, we are going to show a novel framework, which changes drastically the point of view usually adopted for the cosmological observations, that we have followed in the previous discussions. In fact, we will focus here on the messengers of the astrophysical objects rather than the objects themselves. Indeed, we are going to introduce the so-called extended theories of electromagnetism (ETE), and see how they can change the nature of cosmological observations.

5.1 Extended Electromagnetism: Introduction

The Maxwellian theory provides a complete and precise description of the majority of electromagnetic phenomena, being also covariant in its formulation and thus "surviving" the revolution in fundamental physics that happened in the last century, which has brought the advent of Quantum Mechanics and GR. Nevertheless, we wonder if this theory is an approximation of a broader one, as Newtonian theory is for GR (and GR itself could be for an ETG or a complete Quantum Gravity paradigm). The reasons that have brought us to do so are the following [35]: i) the Maxwellian formulation of electrodynamics leads to severe issues in the self-force problem (radiation reaction) of charged point particles, as non-physical pre-acceleration and run-away solutions [289]; ii) any modification of the phenomena of electrodynamics will also be related to a modified space-time geometry; iii) if we were to assume the incompatibility between GR and Quantum Mechanics, a new paradigm combining the geometric and quantum aspects of our world has to be different from at least one of these theories which, in turn, would also change the Maxwell

equations.

From a more fundamental point of view, also the Standard Model (SM) has been showing limitations that may ask for an extension of it, like the aforementioned nature of dark matter and dark energy, the imbalance between matter and anti-matter [290], and the evidence of massive neutrinos [291, 292], which leaves, according to the SM, the photon to be the only free confirmed massless particle. An extension of this theory could open a new world which would affect also electromagnetism as we know it.

Leaving aside the SM for a moment, the first idea of a massive photon was proposed by de Broglie in 1922 [37], who also managed to estimate an upper limit of its mass (around 10^{-53} kg) through dispersion analysis [293, 294]. Then, the first modified Maxwell equations were written in a non-covariant form [295]. His student Proca wrote a Lagrangian for electrons, positrons, neutrinos, and photons [38, 296] laying down the first massive electromagnetic theory, which was consistent with the Lorentz(-Poincaré) Symmetry (LoSy), but was not gauge invariant [34].

The de Broglie-Proca (dBP) electromagnetic equations read as [297]

$$\nabla \cdot \mathbf{E} = \frac{\rho}{\epsilon_0} - \mathcal{M}^2 V, \tag{5.1}$$

$$\nabla \times \mathbf{B} = \mu_0 \mathbf{J} + \mu_0 \epsilon_0 \frac{\partial E}{\partial t} - \mathcal{M}^2 A, \tag{5.2}$$

$$\nabla \cdot \mathbf{B} = 0, \tag{5.3}$$

$$\nabla \times \mathbf{E} = -\frac{\partial B}{\partial t}, \tag{5.4}$$

where $\mathcal{M}$ is the photon rest mass, which is also the inverse of its Compton length

$$\mathcal{M} = \frac{1}{\lambda_C} = \frac{m_\gamma c}{\hbar}, \tag{5.5}$$

where m_γ is the mass of the photon. We note that the differences between these equations and the Maxwellian ones are in the massive terms in Eqs. (5.1, 5.2), which involve also the scalar potential V and vector potential A, thus giving them the property of not being gauge invariant, because of the direct involvement of these potentials in the equations, which we do not find in the standard electromagnetic theory.

Later developments of extended electromagnetism were based on physics that was beyond the classical SM, which was explored with the so-called Standard Model Extension (SME) [298, 299], where the photons acquire an effective mass, causing a dispersion relation which is in general of the fourth order with respect to the four-momentum, pro-

portional to the Lorentz-Poincaré Symmetry Violation (LSV) factors, as studies on light propagation in SME show [300, 301].

The SME-LSV factors linked to a possible effective mass of the photon are a vector k_α^{AF} when the handedness of the Charge conjugation-Parity-Time reversal (CPT) symmetry is odd, and a tensor $k_A^{\alpha\nu\rho\sigma}$, when the CPT symmetry is even [34]. In particular, k_α^{AF} always induces an effective mass, while $k_A^{\alpha\nu\rho\sigma}$ only in a particular context. Indeed, for the SME considering k_α^{AF}, Eq. (5.2) becomes

$$\nabla \times \mathbf{B} = \mu_0 \mathbf{j} + \mu_0 \epsilon_0 \frac{\partial \mathbf{E}}{\partial t} + k_0^{\mathrm{AF}} \mathbf{B} - \mathbf{k}^{\mathrm{AF}} \times \frac{\mathbf{E}}{c} \,, \tag{5.6}$$

where k_0^{AF} and $\mathbf{k}^{\mathrm{AF}}$ are the time and space components of the LSV vector. If $k_0^{\mathrm{AF}} = 0$, we obtain

$$m_\gamma = \frac{\hbar |\mathbf{k}^{\mathrm{AF}}|}{c} x \,, \tag{5.7}$$

where x is an angular factor depending on the difference between the preferred frame and observer directions, which is equal to one in the photon rest frame [300].

Another possible extension of electromagnetism is the so-called non-linear electromagnetism. One of the first examples of such a theory is detailed in the Born-Infeld papers [40, 302]. It was introduced to solve the infinite self-force of punctiform charges, and it has been shown that it can be treated as an approximation, in some versions, of string theory [303]. Another renowned non-linear electromagnetic theory has been proposed in [41] which was derived as an effective classical field theory for Quantum Electro-Dynamics. Both these theories are LoSy invariant, which is a relevant difference with respect to the SME approach.

Many peculiar features arise in the extended theories of electromagnetism, not observed in the Maxwellian theory: for instance, in the de Broglie-Proca theory, we observe that the energy-momentum density tensor θ_α^τ of the photon is not conservative also for constant background electromagnetic fields[39, 34]. This is because we find, for this tensor, that the novel mass term couples with the background potential time-derivative. Non-conservation in a vacuum is also found in the SME theories, for which three different massive contributions have been derived [34]. This non-conservation has important consequences on astrophysical and cosmological observations [35]. Indeed, we can translate the variation of the energy-momentum density tensor into a photon energy variation, and thus to a frequency shift, which is not found in the Maxwellian theory, as we shall see in more detail in the next sections.

Let us now confront the different terms of $\partial_\alpha \theta_\tau^\alpha$ both in the Maxwellian theory as well as in the ETE. For Maxwell, we find

$$\partial_\alpha \theta^\alpha_\tau = j^\alpha f_{\alpha\tau} - \frac{1}{\mu_0}(\partial_\alpha F^{\alpha\beta}) f_{\beta\tau} \,, \tag{5.8}$$

where j^α is an external current, $f_{\beta\tau}$ is the electromagnetic field tensor of the photon, and $F_{\beta\tau}$ the same tensor for the background.

For the de Broglie-Proca electromagnetism, instead, we have already noted that the photons interact directly with the potentials because of the massive terms, this translates into a variation of the energy-momentum density tensor in the following way

$$\partial_\alpha \theta^\alpha_\tau = j^\alpha f_{\alpha\tau} - \frac{1}{\mu_0}(\partial_\alpha F^{\alpha\beta}) f_{\beta\tau} + \frac{1}{\mu_0}\mathcal{M}^2(\partial_\tau A^\beta) a_\beta \,. \tag{5.9}$$

We note a new term in Eq. (5.9), which does not appear in Eq. (5.8), depending on the mass of the photon itself as well as the background potential. This allows us to conclude that the photon energy is not conserved even if the background field is constant, thus giving us a new contribution to the frequency shift not appearing in the standard electromagnetism framework. We also note that, in the absence of a background field, the energy-momentum tensor does conserve itself even in this non-standard electromagnetic scenario.

Let us now consider the same equation for the SME-LSV. As previously mentioned, we can have two non-standard different contributions, represented by the vector k^{AF}_α or by the tensor $k^{\alpha\nu\rho\sigma}_A$. We focus our attention on the terms directly involved with an effective photon mass, recalling that k^{AF}_α always induces an effective mass term. Differently from the LSV tensor, the LSV vector violates the CPT theorem. The frequency shift is thereby an observable of CPT violation since it also depends on the LSV vector [35]. The frequency shift, in this case, can be written as [34]

$$\begin{aligned}\partial_\alpha \theta^\alpha_\tau = j^\nu f_{\nu\tau} - \frac{1}{\mu_0}(\partial_\alpha F^{\alpha\nu}) f_{\nu\tau} - \frac{1}{\mu_0}\Bigg[\frac{1}{2}(\partial_\alpha k^{\mathrm{AF}}_\tau) g^{\alpha\nu} a_\nu - \frac{1}{4}(\partial_\tau k^{\alpha\nu\kappa\lambda}_{\mathrm{F}}) f_{\alpha\nu} f_{\kappa\lambda} + \\ \partial_\alpha (k^{\alpha\nu\kappa\lambda}_{\mathrm{F}} F_{\kappa\lambda}) f_{\nu\tau} + k^{\mathrm{AF}}_\alpha G^{\alpha\nu} f_{\nu\tau}\Bigg] \,,\end{aligned} \tag{5.10}$$

where $G^{\alpha\nu}$ and $g^{\alpha\nu}$ are the dual electromagnetic fields for the background and the photon, respectively. We note that in this equation, apart from the first two Maxwellian terms, there are other non-standard contributions, whose nature is explained in the following [34]:

- The first two terms are background independent, thus implying that the energy-momentum tensor does not conserve itself, even in the absence of a background field, if the LSV fields are space-time dependent. This is a peculiar feature of SME, because, as we have already seen, the de Broglie-Proca energy tensor does

conserve itself in the same situation.

- A non-constant space-time-depending term in which we find derivatives of the LSV tensor coupled with the background field.
- A constant term depending on the background, coming from the Carroll-Field-Jackiw (CFJ) electrodynamics [304].

Let us now try to give an estimate of the frequency shift due to the LSV terms following a heuristic methodology, considering an actual astrophysical observation, following the computations performed in [39]. Starting from Eq. (5.10), under certain assumptions (in particular, considering a low-frequency regime and a constant k_0^{AF}), we obtain:

$$\partial_\alpha \theta_0^\alpha = j^i f_{i0} - \frac{1}{\mu_0}[(\partial_\alpha F^{\alpha i}) f_{i0} + k_\alpha^{AF} G^{\alpha i} f_{i0}]. \tag{5.11}$$

Because we are interested in finding, from this equation, the frequency shift of the photon along its path x, we consider the absence of an external current, and rewrite this equation in the following way, explicating the electric and magnetic fields of the photon ($\mathbf{e}$ and $\mathbf{b}$), as well as its vector potential $\mathbf{a}$:

$$\begin{aligned} \frac{1}{2}\frac{\partial}{\partial t}\left(\epsilon_0 \mathbf{e}^2 - \frac{k_0^{AF}}{\mu_0 c}\mathbf{e}\cdot\mathbf{a} + \frac{\mathbf{b}^2}{\mu_0}\right) + \frac{1}{\mu_0}\frac{\partial}{\partial x}(\mathbf{e}\times\mathbf{b})_x = \\ -\frac{c}{\mu_0}\left(\partial_x F^{xi} + k_0^{AF} G^{0i}\right) f_{i0}. \end{aligned} \tag{5.12}$$

The first term on the right-hand side of this equation is estimated to be negligible and thus dropped for the next computations. Also, we assume the absence of inter-galactic medium magnetic field fluctuations over long time scales, which means that we consider only the time fluctuations in the emitting galaxy and in the Milky Way. Taking into account the detection of an object at $z = 0.5$, the correspondent look-back time[1] is $t_{LB} = 1.57 \times 10^{17}$ s. Considering a fixed cosmological ΛCDM model with $H_0 = 70$ km/s per Mpc, $\Omega_M = 0.3$ and $\Omega_\Lambda = 0.7$, we take into account a parameter, which we define as ρ, that considers the different possible orientations of the magnetic fields encountered by the photon in its path to us. The magnetic fields are themselves estimated to be around $10^{-10}/10^{-9}$ T as an order of magnitude.

Thus, the energy density change of the wave due to the second term is

$$\Delta E = \frac{c}{\mu_0} k_0^{AF} |B f_{i0}| \rho t_{LB} \approx 1.02 \times 10^{23} k_0^{AF} \rho |f_{i0}|, \tag{5.13}$$

[1] the look-back time is the time in which a photon reaches us from a particular source. It is directly linked to the previously introduced light-travel distance (Eq. 2.22)

which brings to a frequency shift $\Delta\nu$ equal to

$$\Delta\nu \approx \frac{1.02 \times 10^{23}}{h} k_0^{AF} \rho |f_{i0}| = 1.55 \times 10^{56} k_0^{AF} \rho |f_{i0}|. \tag{5.14}$$

It is now necessary to compute $|f_{i0}| = |\mathbf{e}|/c$. In a first, Maxwellian, approximation, we may write the classic intensity I as $I = \epsilon_0 c e^2 = \epsilon_0 c^3 f_{i0}^2$.

We consider a typical frequency linked to a SN Ia observation, which corresponds to the silicon absorption line: $\nu = 4.86 \times 10^{14} Hz$. The monochromatic AB magnitude is based on flux measurements that are calibrated in the absolute unit [305] as the logarithm of the spectral density SFD as, in the appropriate scales of measurement [39]

$$m_{AB} = -2.5 \log_{10} SFD - 48.6. \tag{5.15}$$

For $m_{AB} = -19$ we obtain $SFD = 1.44 \times 10^{-15}$ Js^{-1} Hz^{-1} m^{-2}. Integrating over the frequency width of a bin of $2.37 THz$, we compute $I = 3.4 \times 10^{-3}$ Js^{-1} Hz^{-1} m^{-2}, from which we finally have

$$\Delta\nu \approx 5.87 \times 10^{47} k_0^{AF} \rho. \tag{5.16}$$

The range of the measurements obtained for k_0^{AF} is very wide, as is the parameter ρ, which, when it assumes very low values ($\rho \approx 10^{-23}$ [39]), indicates an extreme misalignment of the magnetic field. The important point is that this shift can have a relevant influence on the frequency measurement of a particular source, and thus on its inferred redshift. As we shall see in the following.

5.2 Dark Energy and Electromagnetic frequency shift

In this section we will present the work performed in [35], in which we have followed a drastic change in the framework of the ΛCDM model to derive a new, further component of the total redshift measured for an astrophysical source and used it to find the same effects normally attributed to the dark energy, studying cosmological models where the latter is not considered. This analysis has then been complemented by considering the most updated SNe Ia set, as we will see.

5.2.1 A new redshift contribution for Cosmology

The frequency shift due to the non-standard electromagnetic phenomena can bring, among other possible effects, also to a shift in the measured redshift of the astrophysical sources. This idea can change drastically the cosmological conclusions due to such observations.

This novel contribution to the total redshift, which we call z_S, does not depend only on the distance between the source and us itself, but also on the electromagnetic fields encountered by the photon during its journey to us. Thus, two astrophysical sources at the same distance could have different z_S, and a different total redshift z. Not only that, but z_S, differently from the cosmological redshift z_C, can either be blue or red. Indeed, in the former case, this would imply that the photon actually gains energy during its journey to us, while in the latter it loses energy via non-standard interactions with the background electromagnetic fields.

It is important to note that this discussion applies to every non-standard electromagnetic effect, from the massive photon of the de Broglie-Proca theory to the non-linear electromagnetism to the SME, because the optical frequency shift can be linked to any non-standard electromagnetic effect.

We recall the definition of $z = \Delta\nu/\nu_o$, where $\Delta\nu = \nu_{\rm e} - \nu_o$ is the difference between the observed ν_o and emitted $\nu_{\rm e}$ frequencies, or else $z = \Delta\lambda/\lambda_{\rm e}$ for the wavelengths. Then, for the cosmological expansion $\lambda_{\rm e}$ stretches to $\lambda_{\rm C}$; that is, $\lambda_{\rm C} = (1 + z_{\rm C})\lambda_{\rm e}$. We recall that the quantity $z_{\rm C}$ refers only to expansion.

The wavelength $\lambda_{\rm C}$ could be further stretched or, conversely, shrunk for the non-standard electromagnetic shift $z_{\rm S}$ to $\lambda_{\rm o} = (1 + z_{\rm S})\lambda_{\rm C} = (1 + z_{\rm S})(1 + z_{\rm C})\lambda_{\rm e}$. But since $\lambda_{\rm o} = (1 + z)\lambda_{\rm e}$, we have $1 + z = (1 + z_{\rm C})(1 + z_{\rm S})$; thus

$$z = z_{\rm C} + z_{\rm S} + z_{\rm C}z_{\rm S} := z_{\rm o} \, , \tag{5.17}$$

where $z_{\rm o}$ is the spectroscopically or photometrically observed z. We note that the second order is non-negligible.

As we shall see, we are going to derive $z_{\rm S}$ both for mock data as well as for real cosmological observations. The procedure for computing $z_{\rm S}$ considers that the expansion of the Universe is solely represented by $z_{\rm C}$, for which we derive the cosmological distances (and not for the observed redshift z). From Eq. (5.17), $z_{\rm C}$ is given by

$$z_{\rm C} = \frac{z - z_{\rm S}}{1 + z_{\rm S}} \, . \tag{5.18}$$

We note again that if $z_{\rm S}$ is blue (negative), the photon gains energy in the path to us due to one of the non-standard electromagnetic processes. This in turn means that the expansion redshift $z_{\rm C}$ is bigger than the observed z, which implies that the astrophysical object is further than what we could have detected in the ΛCDM model. If instead $z_{\rm S}$ is red (positive), the photon loses energy in its path, implying that $z_{\rm C}$ is smaller than z, meaning that the astrophysical object is closer to us than what it would have been dictated by the ΛCDM model.

We now link the $z_{\rm S}$ with other astrophysical parameters: in particular, we hypothesize

Type	1	2	3	4
$d\nu$	$k_1\nu dr$	$k_2\nu_e dr$	$k_3 dr$	$k_4\nu_o dr$
ν_o	$\nu_e e^{k_1 r}$	$\nu_e(1+k_2 r)$	$\nu_e + k_3 r$	$\frac{\nu_e}{1-k_4 r}$
$z_{\rm S}$	$e^{-k_1 r} - 1$	$-\frac{k_2 r}{1+k_2 r}$	$-\frac{k_3 r}{\nu_e + k_3 r}$	$-k_4 r$
k_i	$-\frac{\ln(1+z_{\rm S})}{r}$	$-\frac{z_{\rm S}}{r(1+z_{\rm S})}$	$-\frac{\nu_e z_{\rm S}}{r(1+z_{\rm S})}$	$-\frac{z_{\rm S}}{r}$
r	$-\frac{\ln(1+z_{\rm S})}{k_1}$	$-\frac{z_{\rm S}}{k_2(1+z_{\rm S})}$	$-\frac{\nu_e z_{\rm S}}{k_3(1+z_{\rm S})}$	$-\frac{z_{\rm S}}{k_4}$

Table 5.1: The different variations of the frequency ν can be summarised by four different cases of proportionality: 1) to the instantaneous frequency and the distance; 2) to the emitted frequency and the distance; 3) to the distance only; 4) to the observed frequency and the distance. These variations determine the frequency observed ν_o, the shift $z_{\rm S}$, the parameters k_i, and the distance r.

four different behaviors for this quantity, which has been considered proportional to:

- the instantaneous frequency and the distance;
- the emitted frequency and the distance;
- only the distance;
- the observed frequency and the distance (although it is not clear why the shift should be dependent on the observed frequency rather than on the emitted one, we have still analyzed this case together with the others).

The relations between $z_{\rm S}$, the distance r, and the frequency ν that are shown in Table 5.1. We note that, in this table, the aforementioned proportionality has been schematized by the k_i parameters.

Regarding the distance r, we have chosen to use in the following computations the light-travel distance defined in Eq. (2.22), which is the actual length traveled by the photon in an expanding universe. Also, as we shall see in the next sections, the k_i parameters may be considered individually for each source, as well as in common for every source. In the first case we can infer effects that can be dependent not only on the distance itself but also on other possible factors, while, for the second computation, the k_i parameter can be treated as a new, proper, cosmological parameter. Both instances have advantages and disadvantages, and both have been studied.

As previously mentioned, the main goal of this analysis is to compute which values of $z_{\rm S}$ are necessary to reproduce the effects normally attributed to the dark energy, thus fundamentally changing the perspective, focusing on the photon themselves rather than

on the astrophysical objects observed. In order to do so, we consider three different cosmological models, for all of which we have set $\Omega_\Lambda = 0$:

- Cosmological model A: we set $\Omega_M = 0.3$ and consider $\Omega_K = 0$, implying a flat universe where the "cosmic triangle" relation $\Omega_M + \Omega_K + \Omega_\Lambda = 1$, is not satisfied a priori. Nevertheless, we still consider this case with the idea that the contribution normally attributed to the dark energy could be completely replaced by the effect of $z_{\rm S}$ a posteriori. This approach supposes that $z_{\rm S}$ is a manifestation of the LSV vacuum energy in string models, in the case of SME [306].

- Cosmological model B: we take into account an open universe model, where $\Omega_M = 0.3$ and $\Omega_K = 0.7$, so that $\Omega_K + \Omega_M = 1$.

- Cosmological model C: we return to the Einstein-de Sitter cosmological model [307], which is a flat, matter-dominated universe with $\Omega_M = 1$. This was one of the most popular cosmological models before the advent of the dark energy hypothesis [308].

5.2.2 Methodology and mock redshift results

We now start describing the methodology followed in [35] as well as the first results reached using mock redshifts. As previously stated, our main goal is to find the values of the parameters provided by the ETE framework to match the effects usually attributed to dark energy according to the ΛCDM model. From the data points in our cosmological computations, we first consider a set of mock redshifts at regular intervals that do not correspond to any observation. The interval chosen starts at $z = 0$ and stops at $z = 11$, which is of the order of magnitude of the furthest detected galaxy [309]. For these, we compare the luminosity distance of a hypothetical astrophysical object at that specific redshift given by the ΛCDM model with the same distance computed in one of the aforementioned cosmological models, considering only the contribution of the cosmological redshift $z_{\rm C}$ as defined in Eq. (5.18), then, a best-fit has been performed, matching the values of z_S with these mock redshifts.

For the real data, we use first the Pantheon sample, to which we will add later the BAO-related measurements, considering the 16 BAO data points used in the previous chapter. For the SNe Ia data, as mentioned above, we have chosen to compute the best-fit values of the k_i parameters and $z_{\rm S}$ both considering each SN Ia individually as well as finding a general value valid for all SNe Ia, through a general best-fit that accounts for the covariance matrix of the systematic and statistical errors (as done for the cosmological

computations shown in the previous chapter). For both cases, we have used the distance-modulus like we previously did, which we recall is defined as (length units in Mpc)

$$\mu = m - M = 5 \log_{10} [d_{\rm L}(z_{\rm C})] + 25 \, . \tag{5.19}$$

We have fixed the value for the absolute magnitude M for the SNe Ia belonging to the Pantheon sample to -19.35 [263], to avoid the degeneracy with H_0.

When we evaluate the effect for each SN Ia individually, we minimize the following quantity for each SN Ia

$$\chi^2_1 = \frac{(\mu_{obs} - \mu_{th})^2}{(\mu_{obs,err})^2} \, , \tag{5.20}$$

where μ_{obs} is the distance-modulus given by the Pantheon sample with the corresponding error $\mu_{obs,err}$, while μ_{th} is the theoretical distance-modulus computed according to our cosmological models including $z_{\rm S}$. We emphasize that this is not the χ^2 of the entire Pantheon sample: the values derived by these computations individually belong to each SN Ia. The advantage of this approach is the possibility to find singular values of $z_{\rm S}$ linked to only one SN Ia each, thus allowing us to find for SNe Ia at the same distance different values of $z_{\rm S}$, that could depend not only on the distances but also on the environments in which the SNe Ia reside, as well as on the proper path of the photons to us and the electromagnetic fields they encounter.

For the second approach, instead, we consider the entirety of the SNe Ia set and find a best-fit value for the k_i parameters, which is valid for the entire sample. To do this, we employ Eq. (4.3), shown in the previous chapter, for the minimization process. For this approach, $z_{\rm S}$ depends only on the light-travel distance between a specific SN Ia and us. The advantages of this analysis are the characterization of the three cosmological models through single k_i values, and even the possibility of treating the k_i values as cosmological parameters like H_0 or Ω_M, allowing us to draw new Hubble diagrams taking into account these processes.

Related to the BAO data, as previously mentioned, we are going to use the same set of 16 BAO introduced in section 4.1, thus following the same equations for the best-fit analysis.

As in the previous cosmological computations, we use a Bayesian approach, assigning flat priors (specified in the next section) for the variables under consideration, employing Cobaya.

Lastly, for our analysis, we have fixed H_0 to three different values: $H_0 = 67, 70, 74$ km s^{-1} per Mpc, to understand how this value affects the results on $z_{\rm S}$.

We now present the results related to the mock redshifts for the three cosmological models and the three different values of H_0 considered by us. The results are shown in

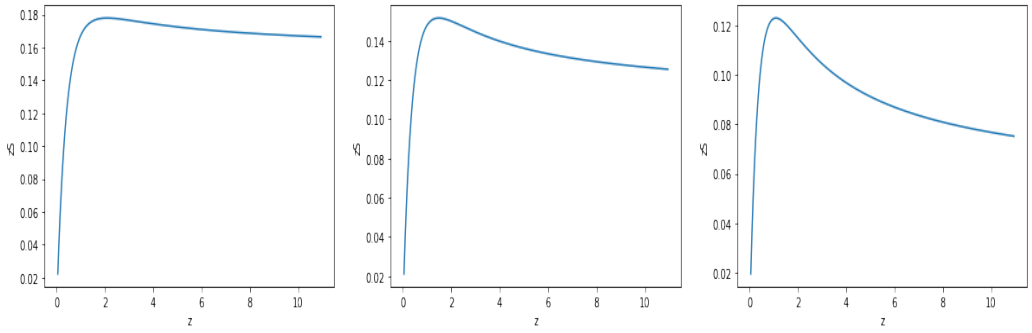

Figure 5.1: Plots of $z_{\rm S}$ versus the mock z for the Cosmological model A, where $\Omega_M = 0.3$, $\Omega_k = \Omega_\Lambda = 0$. We have considered $H_0 = 67, 70, 74$ km s^{-1} per Mpc for the left, central and right panels, respectively. The peaks for the absolute values of $z_{\rm S}$ have been reached for $z = 2.1$ (left panel), $z = 1.5$ (central panel), and $z = 1.1$ (right panel). We note that, in all cases, the shifts are towards the red, and thus dissipative.

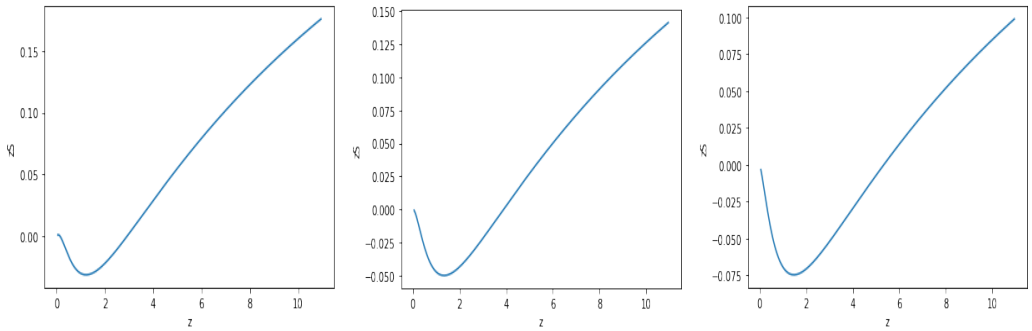

Figure 5.2: Plots of $z_{\rm S}$ versus the mock z for the Cosmological model B, where $\Omega_M = 0.3$, $\Omega_k = 0.7$, and $\Omega_\Lambda = 0$. We have considered $H_0 = 67, 70, 74$ km s^{-1} per Mpc for the left, central and right panels, respectively. The minima for the values of $z_{\rm S}$ correspond to $z = 1.2$ (left panel), $z = 1.35$ (central panel), and $z = 1.45$ (right panel). The shifts are towards the red or the blue, depending on the value of z.

Figures 5.1, 5.2, and 5.3.

Let us now comment on these results, starting from Figure 5.1, in which we show the relation between $z_{\rm S}$ and the mock redshift z for the Cosmological model A. We note that, in this case, $z_{\rm S}$ is always positive, thus red, which means that in this model the non-standard effects are dissipative for the photons. This occurs for all three values of H_0 considered. We also note a peak for $z_{\rm S}$ for the values z considered in Figure 5.1, after which we see a decrease in the value of $z_{\rm S}$, with a variable steepness depending on the fixed value of H_0. Indeed, we observe that the steepness of the curve after the peak increases when we decrease the value of H_0.

In Figure 5.2, instead, we show the results for the Cosmological model B. We note a very different behavior than the previous results: $z_{\rm S}$ has a negative peak for z in the region around 1.3 (the precise values are stated in the caption of Figure 5.2) then increases

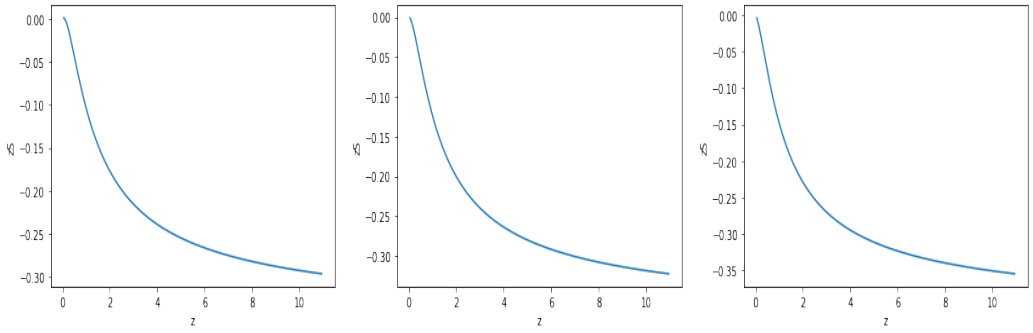

Figure 5.3: Plots of $z_{\rm S}$ versus the mock z for the Cosmological model C, where $\Omega_M = 1$, $\Omega_k = \Omega_\Lambda = 0$. We have considered $H_0 = 67, 70, 74$ km s^{-1} per Mpc for the left, central and right panels, respectively. We note that for the left panel, the shifts are toward the red and the blue; while only toward the blue for the central and right panels.

monotonically, becoming positive. The value of H_0 affects the size of the negative peak as well as the steepness during the subsequent increase, but it does not affect the overall behavior. We recall that a negative $z_{\rm S}$ indicates an increase in the energy of the photons due to the non-standard electromagnetic effects.

The third set of three plots, Figure 5.3, shows the behavior of $z_{\rm S}$ versus the mock redshift z for the Cosmological model C. We observe, again, different results with respect to the previous two cosmological models. Indeed, we note that $z_{\rm S}$ is always negative, and decreases with z. Once more increasing H_0 shifts the curve downward without changing the overall behavior.

In summary, our tests with mock redshifts have shown us that, for the relation between $z_{\rm S}$ and z, the cosmological model considered is way more impactful than the fixed value of H_0, yielding completely different results between one to the other. We anticipate that this conclusion applies also to the computations regarding the real data. We also note that our results for the Cosmological model B are in agreement with those found in [34] with a similar procedure.

5.2.3 SNe Ia individual results

We now show the results obtained using the Pantheon sample, both considering each SN Ia on its own as well as in doing a general fit. Let us start with the individual results, which are shown in Figures 5.4, 5.5, and 5.6. In each of these figures, we show the histograms of $z_{\rm S}$ for the three cosmological models (the first row of each figure) and the plots of $z_{\rm S}$ versus z (second row).

Let us now comment on these plots. In Figure 5.4, we are considering the Cosmological model A. In the histograms shown in the first row, we see that the peak value of

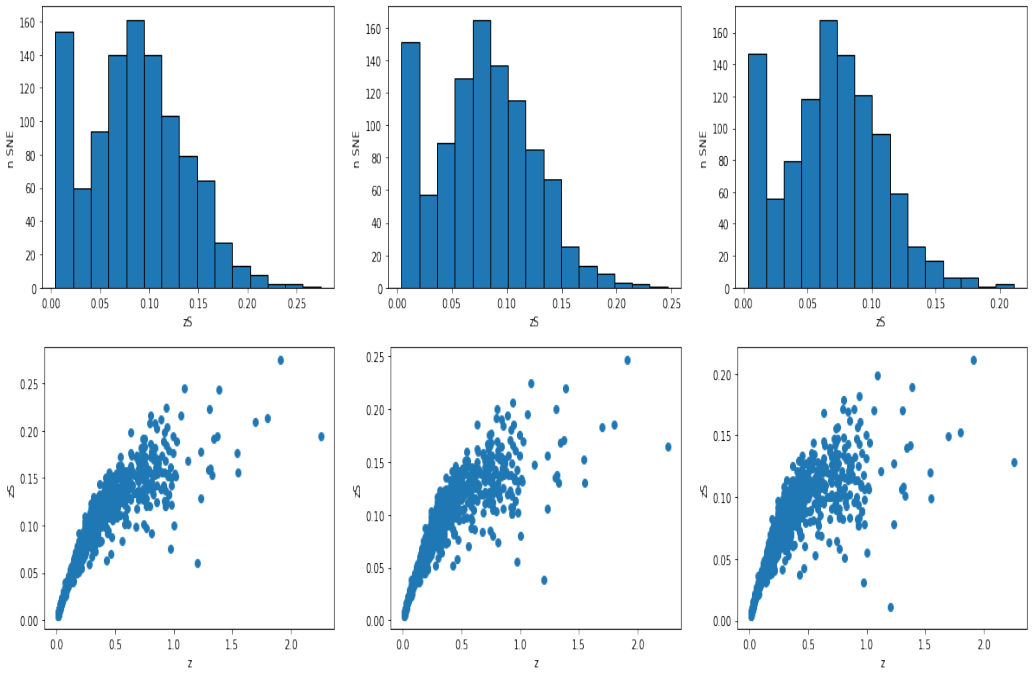

Figure 5.4: The first row shows the histograms of $z_{\rm S}$ for the Cosmological model A, where $\Omega_M = 0.3$, $\Omega_k = \Omega_\Lambda = 0$, related to the Pantheon sample. The second row shows the scatter plot $z_{\rm S}$ versus z. H_0 assumes the values 67 (first and fourth panels), 70 (second and fifth panels), 74 (third and sixth panels), km s^{-1} per Mpc.

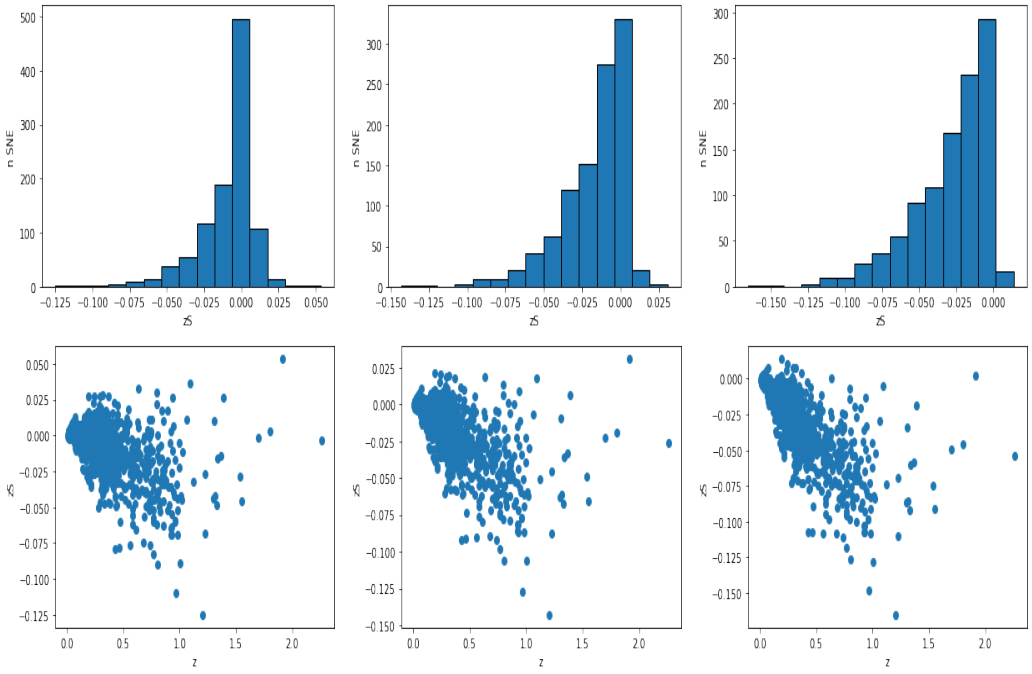

Figure 5.5: The first row shows the histograms of $z_{\rm S}$ for the Cosmological model B, where $\Omega_M = 0.3$, $\Omega_k = 0.7$, and $\Omega_\Lambda = 0$, related to the Pantheon sample. The second row shows the scatter plot $z_{\rm S}$ versus z. H_0 assumes the values 67 (first and fourth panels), 70 (second and fifth panels), 74 (third and sixth panels), km s^{-1} per Mpc.

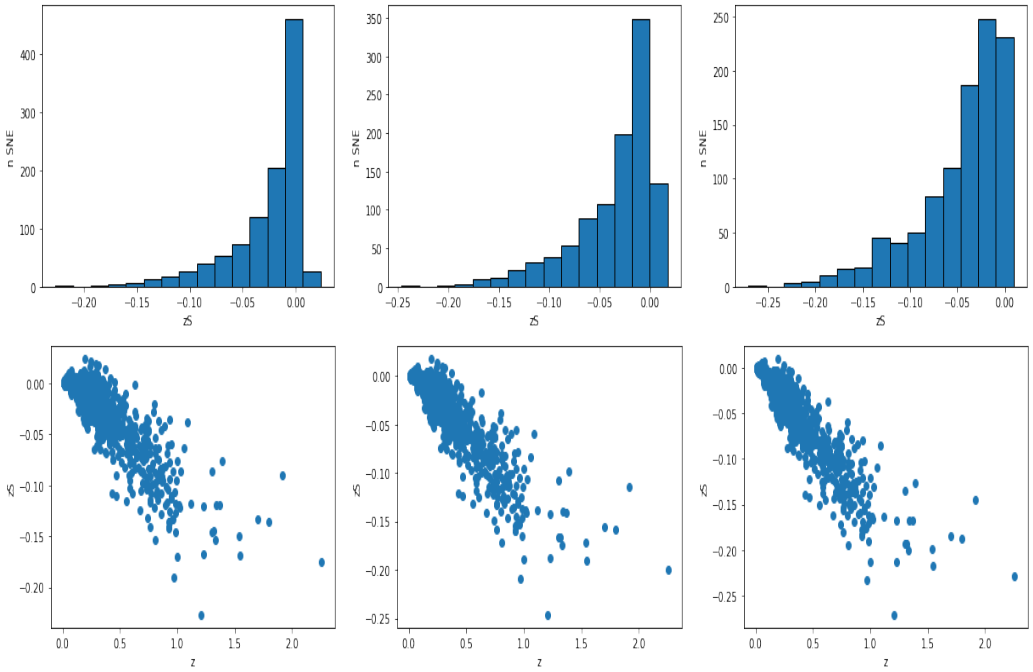

Figure 5.6: The first row shows the histograms of $z_{\rm S}$ for the Cosmological model C, where $\Omega_M = 1$, $\Omega_k = \Omega_\Lambda = 0$, related to the Pantheon sample. The second row shows the scatter plot $z_{\rm S}$vs$z$. H_0 assumes the values 67 (first and fourth panels), 70 (second and fifth panels), 74 (third and sixth panels), km s^{-1} per Mpc.

$z_{\rm S}$ is below 0.1, and decreases when we increase the value of H_0. Also, we note that $z_{\rm S}$ is always positive, confirming the mock redshift trends, for which the non-standard electromagnetic effects are dissipative. In the second row, we visualize the behavior of $z_{\rm S}$ with respect to the detected z, as in the mock redshift case. This time, we see a clear dispersion of the points obtained by our computations, probably due to the uncertainties in the real measurements, especially on the distance modulus.

Comparing these results with those obtained in the corresponding case for the mock redshifts (Figure 5.1), we find that, where the studied z overlap, there is a similar trend in the values of $z_{\rm S}$ between the two cases. Also, we note the same decrease in the peak value of $z_{\rm S}$ both in the real data computations and in the mock z test. We also notice that higher values of $z_{\rm S}$ are reached from the real data than the test with mock redshift. This could be an effect due to the already mentioned dispersion. Finally, the $z_{\rm S}$ values get lower by increasing H_0 as in the mock redshift test.

We now consider Figure 5.2, where the same plots described previously are shown for the Cosmological model B. From the histograms in the first row, we note that the peak of $z_{\rm S}$ is close to 0. We also see that the majority of the $z_{\rm S}$ inferred values are negative. Increasing H_0 shifts the majority of SNe Ia to more negative values of $z_{\rm S}$. Looking at the second row, we see the general trend of $z_{\rm S}$, which we compare with the results obtained

with the mock redshift displayed in Figure 5.2, we see that the negative peak predicted with the mock redshifts is more visible with the real data. We also note that raising the value of H_0 increases the absolute value of the negative peak reached by $z_{\rm S}$, as expected from the mock redshift plots. We then notice that the positive values of $z_{\rm S}$ can be found at both low and high z. This could be due to data dispersion or to the changing sign of the non-standard electromagnetic contribution, at low and high values of z, respectively. The former was not observed for the mock redshifts, conversely from the latter. We also note that the scattering seems to decrease in the third plot, for the highest value for H_0.

In Figure 5.6, we consider the Cosmological model C. Looking at the first row, we see in the histograms that the great majority of $z_{\rm S}$ is negative, especially for larger H_0. This trend can be noted also in the second row, where we notice that the positive values of $z_{\rm S}$ are found at low z, from which a monotonic decrease is observed. This behavior confirms the mock redshifts test, Figure 5.3, with the positive values probably linked to data dispersion.

Generally, the behavior observed for the mock redshifts is confirmed by real data in the common z range for all the Cosmological models. Thereby, we are induced to assume that the predicted behavior of $z_{\rm S}$ for large redshifts, beyond the Pantheon catalog range, can be coincident with those computed by the mock redshifts test. The discrepancies, namely the dispersion and the values of $z_{\rm S}$ themselves, can be ascribed to the natural observational uncertainties on the provided quantities.

We now use the relationships shown in Table 5.1 to compute the k_i parameters for each SN Ia studied as well as for each cosmological model and value of H_0. The results are visualized in Table 5.2, where we present the mean and standard deviation of the distributions obtained for the k_i parameters. We note that a negative value of k_i for $i = 1, 4$ means a positive value for $z_{\rm S}$ and vice versa, while for $i = 2, 3$ the sign depends also on the denominator. For our computations, we have chosen for the emitted frequency k_3, $\nu_e = 6.74 \times 10^{14} s^{-1}$, which is an optical frequency in the B-Band.

The absolute values of the k_i parameters are in the range $4 \times 10^{-6} - 8.5 \times 10^{-5}$ per Mpc for $i = 1, 2, 4$, and of 10^{10} per Mpc s^{-1} for $i = 3$. This difference in the order of magnitude for $i = 3$ is due to the frequency implicitly incorporated in k_3. We thus conclude that we obtain results for the k_i with a similar order of magnitude, with the exception of k_3. We note a relatively high standard deviation in comparison with the mean, due to the dispersion in the data that was already visualized in the previous plots. We recall that these results do not assume the meaning of a best-fit of k_i for all the SNe Ia, which will be presented later, but allow us to predict the expected order of magnitude of the general computations.

Cosmology	k_1	k_2	k_3	k_4
A, $H_0 = 67$	$(-8.18 \pm 2.15) \times 10^{-5}$	$(-7.89 \pm 2.20) \times 10^{-5}$	$(-5.28 \pm 1.47) \times 10^{10}$	$(-8.49 \pm 2.10) \times 10^{-5}$
A, $H_0 = 70$	$(-7.69 \pm 2.13) \times 10^{-5}$	$(-7.44 \pm 2.16) \times 10^{-5}$	$(-4.98 \pm 1.45) \times 10^{10}$	$(-7.96 \pm 2.10) \times 10^{-5}$
A, $H_0 = 74$	$(-7.03 \pm 2.11) \times 10^{-5}$	$(-6.82 \pm 2.13) \times 10^{-5}$	$(-4.57 \pm 1.42) \times 10^{10}$	$(-7.24 \pm 2.10) \times 10^{-5}$
B, $H_0 = 67$	$(0.39 \pm 1.53) \times 10^{-5}$	$(0.40 \pm .54) \times 10^{-5}$	$(0.27 \pm 1.07) \times 10^{10}$	$(0.42 \pm 1.67) \times 10^{-5}$
B, $H_0 = 70$	$(1.34 \pm 1.57) \times 10^{-5}$	$(1.37 \pm 1.61) \times 10^{-5}$	$(0.92 \pm 1.08) \times 10^{10}$	$(1.32 \pm 1.54) \times 10^{-5}$
B, $H_0 = 74$	$(2.72 \pm 1.63) \times 10^{-5}$	$(2.77 \pm 1.69) \times 10^{-5}$	$(1.79 \pm 1.10) \times 10^{10}$	$(2.66 \pm 1.57) \times 10^{-5}$
C, $H_0 = 67$	$(1.66 \pm 2.31) \times 10^{-5}$	$(1.73 \pm 2.41) \times 10^{-5}$	$(1.16 \pm 1.62) \times 10^{10}$	$(1.61 \pm 2.23) \times 10^{-5}$
C, $H_0 = 70$	$(2.73 \pm 2.38) \times 10^{-5}$	$(2.83 \pm 2.53) \times 10^{-5}$	$(1.89 \pm 1.69) \times 10^{10}$	$(2.63 \pm 2.25) \times 10^{-5}$
C, $H_0 = 74$	$(4.17 \pm 2.49) \times 10^{-5}$	$(4.33 \pm 2.71) \times 10^{-5}$	$(2.90 \pm 1.81) \times 10^{10}$	$(4.01 \pm 2.30) \times 10^{-5}$

Table 5.2: Mean and standard deviation values of the k_i parameters issued from the individual computations of $z_{\rm S}$, for the three cosmological models. The computations have been performed considering the distances in Mpc, which means that the k_i parameters are in Mpc^{-1} for $i = 1, 2, 4$ and Mpc^{-1} s^{-1} for $k = 3$, while the values for H_0 are in km s^{-1} per Mpc.

5.2.4 Best-fit for k_i and inclusion of BAO data

We now search the k_i parameters valid for every SN Ia. We will first analyze the results considering uniquely the Pantheon sample, and later we will add the BAO data.

An iterative procedure has been performed using Eqs. (5.18, 2.22, 2.17), and Table 5.1 in the following way

$$z \to r(z) \to k_i(z) \to z_{\rm S}(z) \to z_{\rm C}(z) \to r(z_{\rm C}) \to k_i(z_{\rm C}) \to \text{and back again.}$$

Starting from the observed redshift z of the Pantheon sample, we compute the light-travel distance and, by our Bayesian procedure, we derive the best-fit values for the k_i parameters via Eq. (4.3). These parameters have been used to derive $z_{\rm S}$ and $z_{\rm C}$. Once we know $z_{\rm C}$, we go back to the best-fit derivation of the k_i parameters using this new value for the expansion redshift instead of z, to compute a new light-travel distance and repeat the procedure. We stop the iteration once the difference between the light-travel distances computed in two subsequent steps falls below a certain threshold (in particular, a mean difference between these two values of $\sim$ 1 Mpc considering all SNe Ia). The same approach has been used for the BAO, considering the appropriate likelihood equations for each data point, as explained in the previous chapter.

Considering the three cosmological models and fixing the values of H_0, as it was done for the individual SNe Ia computations, we again gather 9 different cases. For the Bayesian computations, we have chosen flat priors for each parameter, whose intervals have been identified case by case, keeping in mind the values obtained in the previous computation for individual SNe Ia. The results obtained for the k_i parameters are shown in Table 5.3.

As previously mentioned, considering the k_i parameters as general, cosmological,

Cosmology	k_1	k_2	k_3	k_4
A, $H_0 = 67$	$(-8.19 \pm 0.02) \times 10^{-5}$	$(-7.74 \pm 0.02) \times 10^{-5}$	$(-5.17 \pm 0.01) \times 10^{10}$	$(-8.53 \pm 0.03) \times 10^{-5}$
A, $H_0 = 70$	$(-7.66 \pm 0.03) \times 10^{-5}$	$(-7.30 \pm 0.02) \times 10^{-5}$	$(-4.89 \pm 0.02) \times 10^{10}$	$(-8.00 \pm 0.03) \times 10^{-5}$
A, $H_0 = 74$	$(-7.01 \pm 0.03) \times 10^{-5}$	$(-6.72 \pm 0.02) \times 10^{-5}$	$(-4.51 \pm 0.01) \times 10^{10}$	$(-7.29 \pm 0.02) \times 10^{-5}$
B, $H_0 = 67$	$(0.39 \pm 0.04) \times 10^{-5}$	$(0.39 \pm 0.04) \times 10^{-5}$	$(0.26 \pm 0.03) \times 10^{10}$	$(0.39 \pm 0.04) \times 10^{-5}$
B, $H_0 = 70$	$(1.34 \pm 0.04) \times 10^{-5}$	$(1.34 \pm 0.05) \times 10^{-5}$	$(0.90 \pm 0.03) \times 10^{10}$	$(1.32 \pm 0.04) \times 10^{-5}$
B, $H_0 = 74$	$(2.60 \pm 0.04) \times 10^{-5}$	$(2.63 \pm 0.04) \times 10^{-5}$	$(1.76 \pm 0.03) \times 10^{10}$	$(2.58 \pm 0.04) \times 10^{-5}$
C, $H_0 = 67$	$(1.52 \pm 0.04) \times 10^{-5}$	$(1.54 \pm 0.04) \times 10^{-5}$	$(1.02 \pm 0.03) \times 10^{10}$	$(1.51 \pm 0.04) \times 10^{-5}$
C, $H_0 = 70$	$(2.56 \pm 0.04) \times 10^{-5}$	$(2.58 \pm 0.04) \times 10^{-5}$	$(1.73 \pm 0.03) \times 10^{10}$	$(2.54 \pm 0.04) \times 10^{-5}$
C, $H_0 = 74$	$(3.96 \pm 0.04) \times 10^{-5}$	$(4.02 \pm 0.05) \times 10^{-5}$	$(2.69 \pm 0.04) \times 10^{10}$	$(3.91 \pm 0.05) \times 10^{-5}$

Table 5.3: The best-fit values with the relative errors for the k_i parameters, considering the general best-fit for all the SNe Ia belonging to the Pantheon sample, for the three cosmological models. The computations have been performed considering the distances in Mpc, which means that the k_i parameters are in Mpc^{-1} for $i = 1, 2, 4$ and Mpc^{-1} s^{-1} for $k = 3$, while the values for H_0 are in km s^{-1} per Mpc. The numbers in the first column indicate the cosmological model considered, in the same order as the one illustrated in the main text.

ones implies that the non-standard electromagnetic effects represented by those depend only on the distance between the astrophysical objects and us. Nevertheless, we note how the results in Tables 5.2 and 5.3 are very similar. Indeed, they are consistent within 1 σ level (even if this is not very informative given the high standard deviations found in Tab. 5.2), and in some cases, they present identical mean values, at the level of the chosen precision. Conversely, the computed uncertainties of the general parameters are two orders of magnitude smaller than those obtained in the previous computations, even if we have to remind the two distinct meanings of these quantities: the first is the standard deviation of a distribution formed by the k_i computed from each SN Ia data point, while the latter is the computed uncertainty of a single, best-fit value valid for every data point for the k_i parameters.

Once we have computed the best-fit values of k_i we used those to derive the $z_{\rm S}$ for every SNe Ia using the relations in Table 5.1. The histograms summarizing these results for k_1 (the other k_i bring to very similar conclusions) are shown in Figures 5.7, 5.8, and 5.9.

In Figure 5.7, the results concerning the Cosmological model A are shown. The positive values for $z_{\rm S}$ reflect the negative sign for k_1. It is worth noticing that the magnitudes reached by $z_{\rm S}$ are similar to those computed in the individual cases. Again, these values decrease with the increase of H_0, without changing the overall distribution, as we have seen in the corresponding previous cases.

In Figure 5.8, the results concerning the Cosmological model B are shown. Once more, the negative values for $z_{\rm S}$ are due to the positive sign of k_1. The main difference with the individual SNe Ia computation lies in the magnitude of $z_{\rm S}$, with its maximum absolute value being smaller; further, we do not obtain positive $z_{\rm S}$ values, found in the

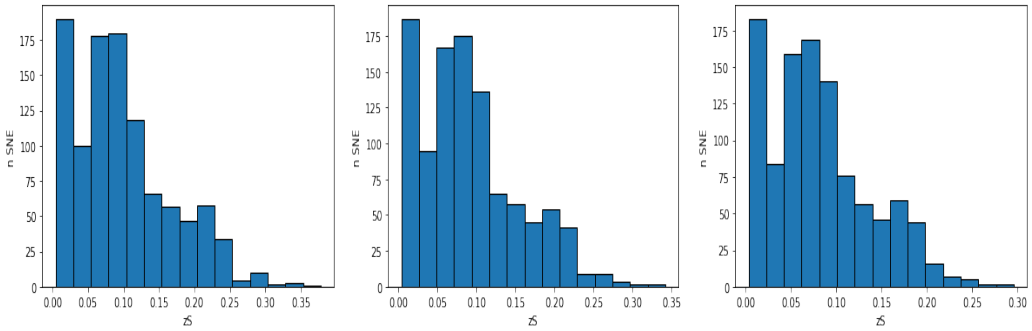

Figure 5.7: Histograms of the computed $z_{\rm S}$ from the k_1 parameter considering the Cosmology model A, where $\Omega_M = 0.3$, $\Omega_k = \Omega_\Lambda = 0$ ($H_0 = 67, 70, 74$ for the left, central and right panels. The values for H_0 are in km s^{-1} per Mpc).

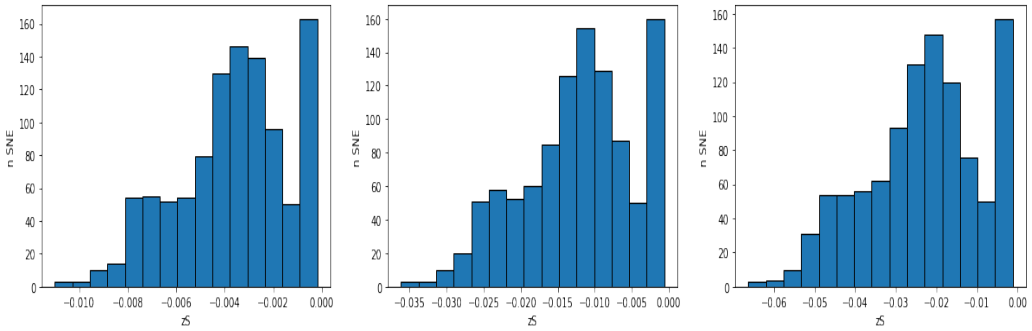

Figure 5.8: Histograms of the computed $z_{\rm S}$ from the k_1 parameter considering the Cosmology model B, where $\Omega_M = 0.3$, $\Omega_k = 0.7$, $\Omega_\Lambda = 0$ ($H_0 = 67, 70, 74$ for the left, central and right panels. The values for H_0 are in km s^{-1} per Mpc).

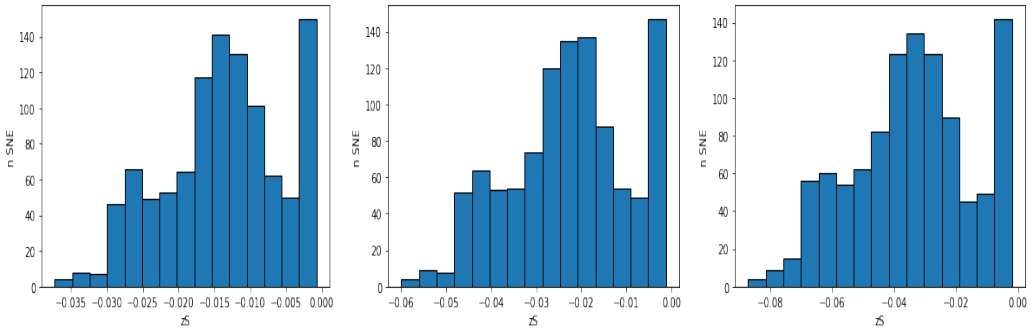

Figure 5.9: Histograms of the computed $z_{\rm S}$ from the k_1 parameter considering the Cosmology model C, where $\Omega_M = 1$, $\Omega_k = \Omega_\Lambda = 0$ ($H_0 = 67, 70, 74$ for the left, central and right panels. The values for H_0 are in km s^{-1} per Mpc).

corresponding individual cases beforehand, as expected given that the sign of all the $z_{\rm S}$ depends on the one of the best-fit value of k_1. This method does not lead to the same variability on $z_{\rm S}$, which is due to the higher precision of k_1 in the general computation, that accompanies a smaller spread on the results for $z_{\rm S}$. Finally, increasing H_0 determines a larger absolute mean value of $z_{\rm S}$.

In Figure 5.9, the results for the Cosmological model C are shown. We obtain only negative $z_{\rm S}$, with a larger mean absolute value than what has been obtained in Figure 5.8, but smaller than those computed for the individual cases, in Figure 5.6. Again, increasing H_0 increases the mean absolute value for $z_{\rm S}$.

As previously mentioned, the idea to treat the k_i parameters as general ones allows us to use them as proper cosmological parameters, so that we can build the Hubble diagrams of the Pantheon sample or the three cosmological models. These diagrams are shown in Figure 5.10.

In these diagrams, the theoretical curve represented by the black line is consistent with the majority of the data points, especially for the Cosmology model B. Instead, in the other models, the theoretical curve falls below the data points for high redshifts, for the three values of H_0. We quantify the goodness of the fits using the computations shown in Table 5.4, where we note the reduced χ^2, corresponding to the k_1 best-fit value, the root mean squared deviation (RMSD), and the normalized root mean squared deviation (NRMSD) for k_1. We observe that the results indicate that the lowest values are associated with Cosmological model B, which we recall is a non-flat cosmological model. Thus, these statistical indicators confirm our previous comments concerning Figure 5.10. The other cosmological models show acceptable fits too, although worse than the fit obtained using the Cosmological model B.

We now add the BAO data to our set, to see what kind of differences their addition would bring to the overall results. Due to their nature (we recall that they are not luminosity distance-based) we show the results for the k_i parameters without the Hubble diagrams. The results are gathered in Table 5.5, which we compare with those in Table 5.3. For all k_i, considering the Cosmological model A, the BAO data contribute with a negative value, and thus they bring a positive contribution to $z_{\rm S}$, strengthening previous findings. Instead, for the Cosmological models B and C, the impact of considering BAO may strengthen or weaken previous findings, even changing the sign of the shift. For the Cosmological model C, it is very interesting that for $H_0 = 70$ km s^{-1} per Mpc, we find the values of k_i consistent with zero, despite the large errors. This derivation may be relevant because it corresponds to $z_{\rm S} = 0$ in a universe assumed without dark energy. Recalling that the Cosmological model C considers $\Omega_M = 1$, this implies that this particular combination of SNe Ia+BAO leads to the same results regarding the redshifts of

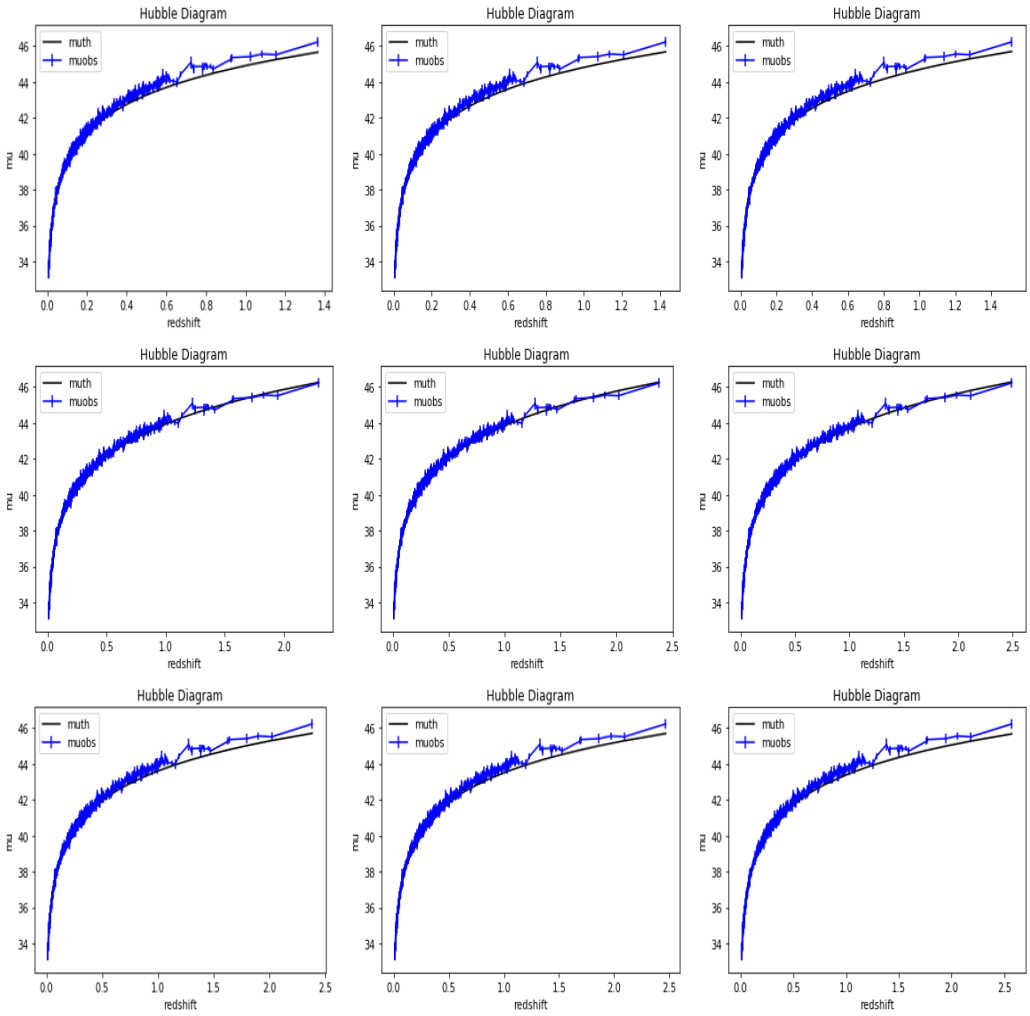

Figure 5.10: The Hubble diagrams for the three cosmological models, one for each row, based upon the best-fit values of k_1 with data from the Pantheon sample, with the three values of H_0 (67, 70, 74 km s^{-1} per Mpc, one for each column. The black lines represent the models, while the blue marks trace the SNe Ia data with their errors. We underline that the redshift on the x-axis is the computed expansion redshift $z_{\rm C}$. This explains why the interval on the x-axis changes between different cosmological models.

Cosmology	Reduced χ^2	RMSD	NRMSD
A, $H_0 = 67$	1.58	0.244	0.154
A, $H_0 = 70$	1.62	0.247	0.155
A, $H_0 = 74$	1.59	0.244	0.155
B, $H_0 = 67$	1.08	0.165	0.150
B, $H_0 = 70$	1.07	0.164	0.150
B, $H_0 = 74$	1.06	0.162	0.150
C, $H_0 = 67$	1.46	0.228	0.151
C, $H_0 = 70$	1.47	0.230	0.151
C, $H_0 = 74$	1.47	0.230	0.151

Table 5.4: Best-fit statistics for the k_1 parameter in all the cases considered in our work. The NRMSD has been derived from the RMSD divided by the difference between the maximum and minimum values of the difference between the theoretical and observed distance modulus. The mean value of the uncertainty on the observed data is $\Delta_{\mu obs} = 0.142$. The values for H_0 are in km s^{-1} per Mpc. The numbers in the first column indicate the cosmological model considered, in the same order as what is illustrated in the main text.

Cosmology	k_1	k_2	k_3	k_4
A, $H_0 = 67$	$(-8.72 \pm 0.02) \times 10^{-5}$	$(-8.22 \pm 0.02) \times 10^{-5}$	$(-5.49 \pm 0.01) \times 10^{10}$	$(-9.19 \pm 0.02) \times 10^{-5}$
A, $H_0 = 70$	$(-8.37 \pm 0.02) \times 10^{-5}$	$(-7.92 \pm 0.02) \times 10^{-5}$	$(-5.30 \pm 0.01) \times 10^{10}$	$(-8.85 \pm 0.02) \times 10^{-5}$
A, $H_0 = 74$	$(-7.88 \pm 0.02) \times 10^{-5}$	$(-7.49 \pm 0.02) \times 10^{-5}$	$(-5.02 \pm 0.01) \times 10^{10}$	$(-8.28 \pm 0.02) \times 10^{-5}$
B, $H_0 = 67$	$(1.23 \pm 0.03) \times 10^{-5}$	$(1.23 \pm 0.03) \times 10^{-5}$	$(0.82 \pm 0.02) \times 10^{10}$	$(1.21 \pm 0.03) \times 10^{-5}$
B, $H_0 = 70$	$(1.23 \pm 0.04) \times 10^{-5}$	$(1.24 \pm 0.04) \times 10^{-5}$	$(1.40 \pm 0.02) \times 10^{10}$	$(2.07 \pm 0.03) \times 10^{-5}$
B, $H_0 = 74$	$(3.24 \pm 0.03) \times 10^{-5}$	$(3.30 \pm 0.03) \times 10^{-5}$	$(2.21 \pm 0.02) \times 10^{10}$	$(3.20 \pm 0.03) \times 10^{-5}$
C, $H_0 = 67$	$(-0.91 \pm 0.03) \times 10^{-5}$	$(-0.91 \pm 0.03) \times 10^{-5}$	$(-0.61 \pm 0.02) \times 10^{10}$	$(-0.91 \pm 0.04) \times 10^{-5}$
C, $H_0 = 70$	$(0.31 \pm 3.43) \times 10^{-7}$	$(-0.77 \pm 3.77) \times 10^{-7}$	$(-0.81 \pm 2.31) \times 10^{8}$	$(-0.29 \pm 3.81) \times 10^{-7}$
C, $H_0 = 74$	$(1.23 \pm 0.03) \times 10^{-5}$	$(1.24 \pm 0.04) \times 10^{-5}$	$(0.84 \pm 0.03) \times 10^{10}$	$(1.22 \pm 0.04) \times 10^{-5}$

Table 5.5: Results for the k_i parameter considering the general best-fit for SNe Ia belonging to the Pantheon sample together with the BAO constraints, for the three cosmological models. The values for H_0 are in km s^{-1} per Mpc. The numbers in the first column indicate the cosmological model considered, in the same order as what is illustrated in the main text.

the ΛCDM model, at least concerning this specific computation, without introducing the dark energy.

In conclusion, the analysis performed in [34] presented in this section has the objective to find, under the fundamental hypothesis of the absence of dark energy and the presence of ETE effects, what would be the contributions necessary for such effects to match the observations. Of course, such an alternative theory has to have a strong conceptual basis to actually be accounted as a possible contender for the ΛCDM model from a theoretical point of view. Furthermore, it has to coherently account for all possible astrophysical and cosmological observations. In [34], a brief discussion regarding other probes usually used in cosmology, such as the CMB and the weak lensing, is presented as well.

For instance, the concept of time dilation has been taken into account, whose observations [310, 311] have ruled out the tired light hypothesis [312], according to which the redshift of the astrophysical sources is entirely due to the photon losing energy in a static universe. This theory suffers from different shortcomings [313]. Our approach differs in the sense that we do not halt completely the expansion of the universe, but, in some sense, we complement it with a new mechanism. Furthermore, while the tired light process is always dissipative, the non-standard electromagnetic effects could actually allow the photons to gain energy in their path to us.

Regarding the CMB, instead, referring to the discussion in [34], the data, being model-dependent, can be interpreted to fit different cosmological models [314]. Furthermore, the CMB on its own is limited in constraining the dark energy hypothesis, since it is not one of the six free parameters, but it is derived using subsequent assumptions [315]. Indeed, information related to the dark energy content in our Universe depends also on the distance between the CMB and us, given that in the early times for the ΛCDM model the effects of dark energy were negligible, which would mean that a reinterpretation of the redshift does not change the intrinsic physics of the CMB [35].

Another probe that has been used to derive information related to the dark energy is the weak lensing, more specifically the deformation linked to the shear [77, 78]. This quantity also depends on the value of the redshift at which the weak lensing has been detected. Thus, we expect that the recasting of the redshift would affect these measurements roughly in the same way as the probes used in our analysis, namely, with a further contribution to the total redshift being able to reproduce the effects of the dark energy.

5.2.5 The Pantheon+ Analysis

We now complete our previous findings by considering the very novel Pantheon+ set of 1701 light curves taken from 1550 SNe Ia [36], which is the successor of the Pantheon sample used and discussed in the previous sections and chapters. This is the main focus of [53]. Considering the same methodology regarding the best-fit analysis expressed above, we compute new results regarding the non-standard frequency shifts for this new set, comparing these with the results obtained for the Pantheon sample and highlighting the differences. We first note that the Pantheon+ sample has the same redshift range as the Pantheon set, having more low-redshift SNe Ia. Also, we note that, while for the Pantheon sample uncertainties regarding the redshift measurements were absent, they have been introduced for the Pantheon+ set, allowing a direct comparison of them with the non-standard frequency shifts computed by us, in order to understand if these possible effects are of the same order of magnitude than the uncertainties themselves. Furthermore, the Pantheon+ sample data also include directly the distance modulus, differently from the

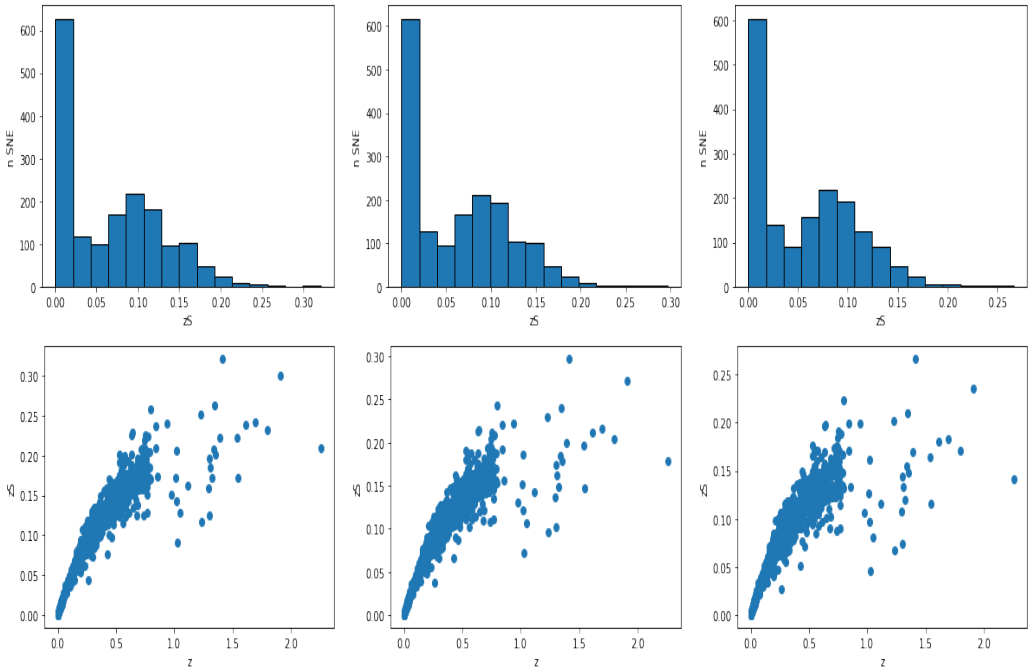

Figure 5.11: The first row shows the histograms of z_S for the Cosmological model A, where $\Omega_M = 0.3$, $\Omega_k = \Omega_\Lambda = 0$, related to the Pantheon+ sample. The second row shows instead the scatter plot z_S versus z. We fixed the values for H_0 to 67 (first and fourth panels), 70 (second and fifth panels), 74 (third and sixth panels), km s^{-1} per Mpc.

Pantheon set, obtained by using a fiducial absolute magnitude for SNe Ia derived by the SH0ES 2021 Cepheid host distances [36, 12].

In showing these new results, we follow the same order presented for the Pantheon sample computations. Given that the mock redshifts are not affected by the new set, let us start with the individual computations. The results are visualized in Figures 5.11, 5.12, and 5.13.

Regarding Figure 5.11, where we consider the Cosmological model A, in the histograms visualized in the first row, we note a peak for z_S consistent with zero, followed by a distribution presenting a secondary peak, which is consistent or slightly below $z_S = 0.1$, depending on the value for H_0. The maximum value reached for z_S depends on H_0 as well. We note that in these computations z_S is always positive for every value of H_0.

Comparing these histograms with the corresponding ones obtained for the Pantheon sample, Figure 5.4, we note the following points:

- In both cases, z_S is always positive, confirming also the results obtained with the mock redshift for the same cosmological model, Figure 5.1.

- In 5.4, the peak of z_S consistent with zero is also present, but is not as predominant as in the new results, being of the same magnitude as the secondary peak.

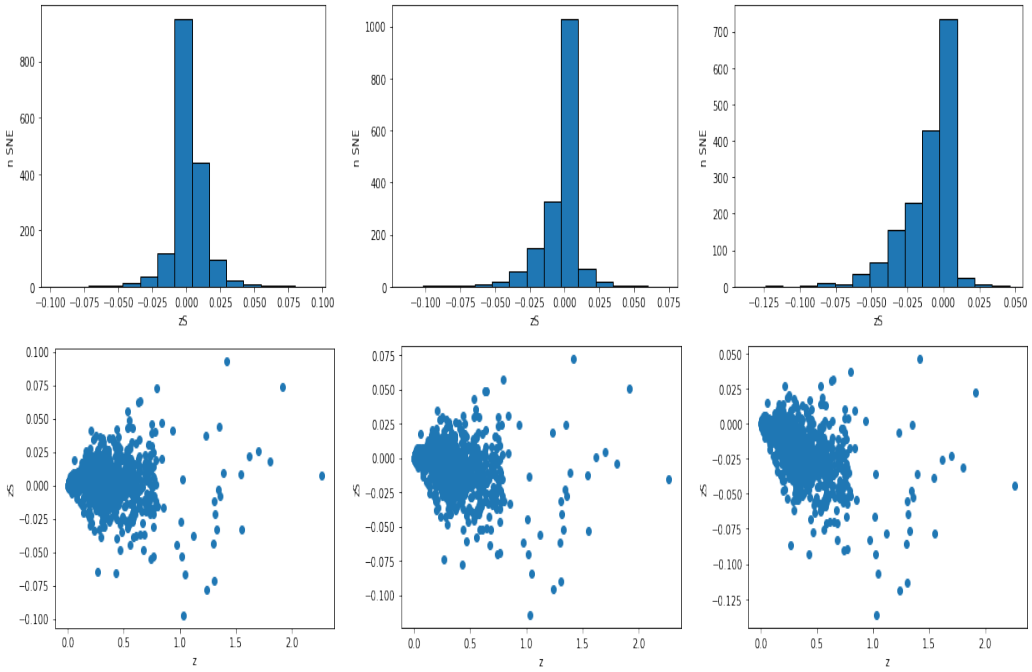

Figure 5.12: The first row shows the histograms of $z_{\rm S}$ for the Cosmological model B, where $\Omega_M = 0.3$, $\Omega_k = 0.7$, and $\Omega_\Lambda = 0$, related to the Pantheon+ sample. The second row shows the scatter plot $z_{\rm S}$ versus z. We fixed the values for H_0 to 67 (first and fourth panels), 70 (second and fifth panels), 74 (third and sixth panels), km s^{-1} per Mpc.

- The new distribution is wider: both the secondary peak as well as the maximum value of $z_{\rm S}$ are bigger than those obtained with the new result, and this is true for all the values of H_0.

- the dependency on the value of H_0 is very similar between the two results: increasing H_0 decreases both the value of the secondary peak as well as of the maximum.

In the second row of Figure 5.11, we show the scatter plots visualizing the behavior of $z_{\rm S}$ versus the detected z. As for Figure 5.4, we note a dispersion probably due to the uncertainties on the distance modulus. In general, the scatter plots obtained with the two SNe Ia sets are similar. The main difference between the results achieved by the SNe Ia sets is the peak at low redshifts noted in the histograms, which is due to the increased number of low redshift SNe Ia in the Pantheon+ sample.

We now comment on the findings shown in Figure 5.12, in which we take into account the Cosmological model B. The main feature of the histograms shown in the first row is the predominant peak for $z_{\rm S}$ around 0. We also note a very interesting behavior depending on the fixed value of H_0: for $H_0 = 67$ km s^{-1} per Mpc, the distribution is fairly symmetric around 0, while increasing the value of H_0 breaks this symmetry, having a bigger tail for negative values for $z_{\rm S}$ than the positive end of the distribution. The result for $H_0 = 67$

km s^{-1} per Mpc is particularly interesting: indeed, a z_S consistent with zero would imply that the open cosmological model without dark energy is able to reproduce the results of the ΛCDM model without invoking the z_S contribution, even if we see also a large dispersion of the computed values, from which we deduce that the overall effect due to z_S is not negligible.

Comparing these results with those obtained for the corresponding case in Figure 5.5, we note that we did not find the same symmetric behavior with the Pantheon sample: indeed, the majority of the z_S was negative even for $H_0 = 67$ km s^{-1} per Mpc. We also note that the intervals of the z_S obtained in the two computations have comparable widths, with the Pantheon+ results being more shifted to positive values than what we have obtained for the corresponding Pantheon cases. We also note the peak near $z_S = 0$, to which we give the same explanation concerning the findings observed in Figure 5.11.

On the second row, we see the scatter plots, similar to what we have shown in Figure 5.11. It is clear, from this plot, the symmetric behavior for $H_0 = 67$ km s^{-1} per Mpc, which is broken by increasing the value of H_0. We also note that the negative values of z_S seem to increase with the redshift, especially for $H_0 = 70$ and $H_0 = 74$ km s^{-1} per Mpc. Finally, we also note that the scattering characterizing these plots seems to decrease with H_0. Interestingly, these plots are different from the results achieved with the mock redshift in the corresponding case, especially for $H_0 = 67, 70$ km s^{-1} per Mpc. This could be because of the variability shown for the low redshift SNe Ia.

Let us now discuss the results shown in Figure 5.13 for the Cosmological model C. Looking at the first row, where the histograms of z_S are shown, we note that the majority of the z_S seems to be negative, as was the case for the same computations for the Pantheon sample, Figure 5.6. Instead, this is not the case, as we shall note when we will compute the k_i parameters, because the number of negative and positive z_S is closer than what we would expect from these plots, especially for $H_0 = 67$ km s^{-1} per Mpc. The number of negative z_S increases with the value of H_0, as again was the case for the previous computations. In general, we can see that this is the case where the results obtained for the Pantheon+ and Pantheon sets are more alike. The main difference is in the peak near $z_S = 0$, as in the other computations, to which we give the same reasoning as in the previous two cases. In the second row, we note from the scatter plots that z_S becomes more negative at high redshifts, as was the case for the results in Figure 5.6. Indeed, even from this plot, we can appreciate the similarity between the two results (and also with the mock redshift for the same cosmological model). Regarding the maximum (in absolute value) reached by z_S, we note that it increases with the value of H_0, and also that it is bigger for the Pantheon sample than for the Pantheon+ set.

Given that the new Pantheon+ sample provides also an estimate of the errors on the

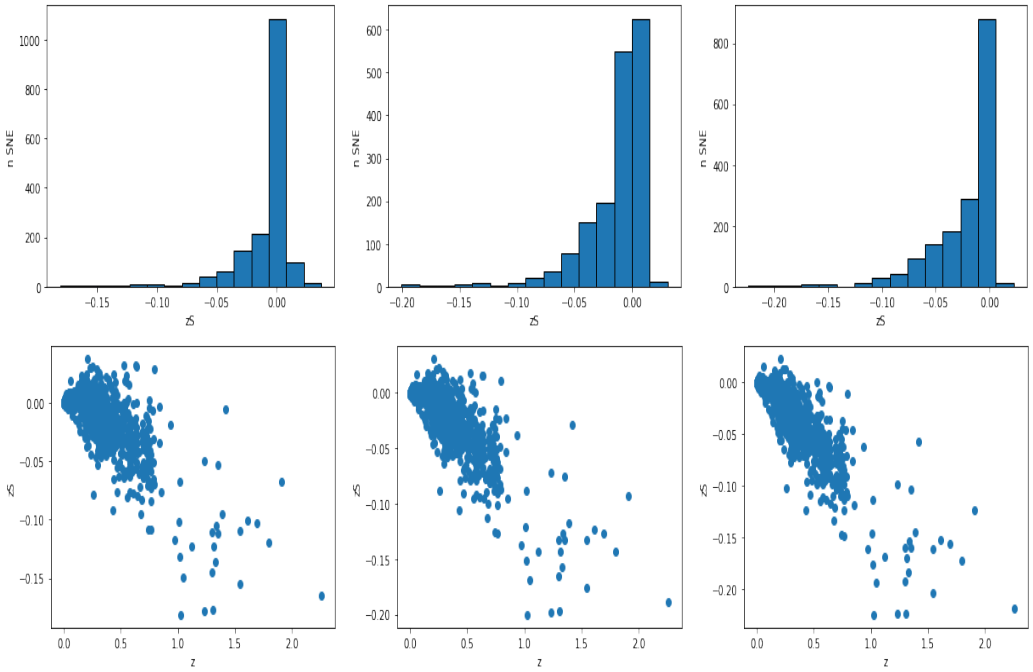

Figure 5.13: The first row shows the histograms of $z_{\rm S}$ for the Cosmological model C, where $\Omega_M = 1$, $\Omega_k = \Omega_\Lambda = 0$, related to the Pantheon+ sample. The second row shows the scatter plot $z_{\rm S}$vs$z$. We fixed the values for H_0 to 67 (first and fourth panels), 70 (second and fifth panels), 74 (third and sixth panels), km s^{-1} per Mpc.

Cosmology	$H_0 = 67$	$H_0 = 70$	$H_0 = 74$
Cosmology A	32.1	30.14	27.8
Cosmology B	3.06	2.51	3.39
Cosmology C,	3.25	3.38	5.37

Table 5.6: The median of the distributions of the ratios between the computed $z_{\rm S}$ and the uncertainties provided by the Pantheon+ sample. The values for H_0 are in km s^{-1} per Mpc.

observed redshifts, we can compare the magnitude of our results regarding $z_{\rm S}$ to them, in order to understand if, by considering the uncertainties on the measurements, a similar effect to what we deduced for the non-standard shift can be achieved by the observational errors themselves. We thus compute the ratio between $z_{\rm S}$ and the errors, from which we derive the median of the related distributions. The results are gathered in Table 5.6, in which we note that the $z_{\rm S}$ are consistently predominant over the uncertainties provided by the Pantheon+ sample, which implies that their contributions cannot be accounted for by errors in the measurements.

As we did with the Pantheon set, from these computations and using the relations in Table 5.1, we can now compute the k_i parameters for each SN Ia belonging to the Pantheon+ sample. This has been done for every cosmological model and value for H_0

Cosmology	k_1	k_2	k_3	k_4
A, $H_0 = 67$	$(-9.94 \pm 2.46) \times 10^{-5}$	$(-9.67 \pm 2.56) \times 10^{-5}$	$(-6.48 \pm 1.71) \times 10^{10}$	$(-1.02 \pm 0.24) \times 10^{-4}$
A, $H_0 = 70$	$(-9.45 \pm 2.44) \times 10^{-5}$	$(-9.20 \pm 2.52) \times 10^{-5}$	$(-6.16 \pm 1.69) \times 10^{10}$	$(-9.71 \pm 2.36) \times 10^{-5}$
A, $H_0 = 74$	$(-8.77 \pm 2.41) \times 10^{-5}$	$(-8.57 \pm 2.47) \times 10^{-5}$	$(-5.74 \pm 1.66) \times 10^{10}$	$(-9.00 \pm 2.35) \times 10^{-5}$
B, $H_0 = 67$	$(-1.01 \pm 1.95) \times 10^{-5}$	$(-1.00 \pm 1.95) \times 10^{-5}$	$(-0.67 \pm 1.31) \times 10^{10}$	$(-1.02 \pm 1.95) \times 10^{-5}$
B, $H_0 = 70$	$(-0.06 \pm 1.95) \times 10^{-5}$	$(-0.05 \pm 1.95) \times 10^{-5}$	$(-0.03 \pm 1.31) \times 10^{10}$	$(-0.06 \pm 1.94) \times 10^{-5}$
B, $H_0 = 74$	$(1.22 \pm 1.94) \times 10^{-5}$	$(1.24 \pm 1.96) \times 10^{-5}$	$(0.83 \pm 1.31) \times 10^{10}$	$(1.21 \pm 1.93) \times 10^{-5}$
C, $H_0 = 67$	$(-0.19 \pm 2.43) \times 10^{-5}$	$(-0.17 \pm 2.46) \times 10^{-5}$	$(-0.12 \pm 1.65) \times 10^{10}$	$(0.20 \pm 2.40) \times 10^{-5}$
C, $H_0 = 70$	$(0.84 \pm 2.46) \times 10^{-5}$	$(0.87 \pm 2.52) \times 10^{-5}$	$(0.59 \pm 1.69) \times 10^{10}$	$(0.81 \pm 2.42) \times 10^{-5}$
C, $H_0 = 74$	$(2.23 \pm 2.52) \times 10^{-5}$	$(2.29 \pm 2.62) \times 10^{-5}$	$(1.53 \pm 1.75) \times 10^{10}$	$(2.17 \pm 2.44) \times 10^{-5}$

Table 5.7: Mean and standard deviation values of the k_i parameters derived from the individual computations of $z_{\rm S}$, for the three cosmological models. The computations have been performed considering the distances in Mpc, which means that the k_i parameters are in Mpc^{-1} for $i = 1, 2, 4$ and Mpc^{-1} s^{-1} for $k = 3$, while the values for H_0 are in km s^{-1} per Mpc, as usual.

previously considered. The results are illustrated in Table 5.7, where we show the mean and the standard deviation of the k_i distributions. For our computations, as we did for the Pantheon set, we choose for the emitted frequency k_3, $\nu_e = 6.74 \times 10^{14} s^{-1}$, which is an optical frequency in the B-Band.

The derived values for the k_i parameters present the same order of magnitude as those found in the Pantheon sample, shown in Figure 5.2: indeed, we note that all the new results are consistent with the old findings within 1 σ. As in the Pantheon results, the computed standard deviation is of the same order of magnitude (or even higher) that the mean values, and we obtain results consistent with 0 for the Cosmological models B and C. This was expected from the plots shown beforehand, because of the presence of both positive and negative $z_{\rm S}$, and because of the general dispersion observed for the real data.

We now describe the results obtained for the general best-fit computations, again considering the now usual 9 cases (3 cosmological models, 3 fixed values for H_0), from which we derive our estimations for the k_i best-fits. The results obtained for the k_i parameters are shown in Table 5.8.

We first note how the results, albeit having different meanings, shown in Tables 5.7 and 5.8 are consistent within 1 σ, as was the case for the Pantheon computations, Tables 5.2 and 5.3. We also note how the uncertainties for the general case are, for the majority of the computations, significantly smaller than the scatters derived for the singular computations, still reminding the conceptual difference between the two values.

Comparing Tables 5.8 and 5.3, we instead note how, contrary to what we obtained for the Table 5.2, not all the new k_i parameters derived in this work are consistent with those derived for the Pantheon set: indeed, a direct comparison expressing in how many σ the values are (identified by the sum of the errors on the two results) is shown in Table 5.9. We note that the highest discrepancies have been found for the Cosmological model

Cosmology	k_1	k_2	k_3	k_4
Cosmology A, $H_0 = 67$	$(-9.84 \pm 0.69) \times 10^{-5}$	$(-8.85 \pm 0.69) \times 10^{-5}$	$(-5.88 \pm 0.41) \times 10^{10}$	$(-1.05 \pm 0.08) \times 10^{-4}$
Cosmology A, $H_0 = 70$	$(-9.38 \pm 0.73) \times 10^{-5}$	$(-8.47 \pm 0.63) \times 10^{-5}$	$(-5.66 \pm 0.45) \times 10^{10}$	$(-1.01 \pm 0.09) \times 10^{-4}$
Cosmology A, $H_0 = 74$	$(-8.70 \pm 0.73) \times 10^{-5}$	$(-7.93 \pm 0.74) \times 10^{-5}$	$(-5.27 \pm 0.46) \times 10^{10}$	$(-9.17 \pm 0.86) \times 10^{-5}$
Cosmology B, $H_0 = 67$	$(-0.68 \pm 1.21) \times 10^{-5}$	$(-0.67 \pm 0.97) \times 10^{-5}$	$(-3.63 \pm 7.46) \times 10^{9}$	$(-0.70 \pm 1.22) \times 10^{-5}$
Cosmology B, $H_0 = 70$	$(0.26 \pm 1.22) \times 10^{-5}$	$(0.26 \pm 1.21) \times 10^{-5}$	$(2.20 \pm 8.69) \times 10^{9}$	$(0.27 \pm 1.33) \times 10^{-5}$
Cosmology B, $H_0 = 74$	$(1.54 \pm 1.27) \times 10^{-5}$	$(1.53 \pm 1.35) \times 10^{-5}$	$(1.06 \pm 0.87) \times 10^{10}$	$(1.55 \pm 1.24) \times 10^{-5}$
Cosmology C, $H_0 = 67$	$(-0.24 \pm 1.13) \times 10^{-5}$	$(-0.23 \pm 1.31) \times 10^{-5}$	$(0.07 \pm 7.64) \times 10^{9}$	$(0.56 \pm 1.22) \times 10^{-5}$
Cosmology C, $H_0 = 70$	$(0.77 \pm 1.43) \times 10^{-5}$	$(0.74 \pm 1.20) \times 10^{-5}$	$(5.57 \pm 7.91) \times 10^{9}$	$(0.80 \pm 1.29) \times 10^{-5}$
Cosmology C, $H_0 = 74$	$(2.12 \pm 1.59) \times 10^{-5}$	$(2.05 \pm 1.69) \times 10^{-5}$	$(1.37 \pm 1.02) \times 10^{10}$	$(2.19 \pm 1.61) \times 10^{-5}$

Table 5.8: The best-fit values with the relative errors for the k_i parameters, considering the general best-fit for all the SNe Ia belonging to the Pantheon+ sample, for the three cosmological models. The computations have been performed considering the distances in Mpc, which means that the k_i parameters are in Mpc^{-1} for $i = 1, 2, 4$ and Mpc^{-1} s^{-1} for $k = 3$, while the values for H_0 are in km s^{-1} per Mpc.

Cosmology	k_1	k_2	k_3	k_4
Cosmology A, $H_0 = 67$	2.32	1.56	1.69	2.37
Cosmology A, $H_0 = 70$	2.26	1.8	1.64	2.26
Cosmology A, $H_0 = 74$	2.22	1.59	1.62	2.14
Cosmology B, $H_0 = 67$	Below 1	1.05	Below 1	Below 1
Cosmology B, $H_0 = 70$	Below 1	Below 1	Below 1	Below 1
Cosmology B, $H_0 = 74$	Below 1	Below 1	Below 1	Below 1
Cosmology C,$H_0 = 67$	1.50	1.31	1.29	Below 1
Cosmology C, $H_0 = 70$	1.22	1.48	1.43	1.31
Cosmology C, $H_0 = 74$	1.13	1.13	1.25	1.03

Table 5.9: Table of the comparisons between the results shown in Table 5.8 and the corresponding findings in 5.3. The numbers shown are the ratios between the difference between the two mean values and the sum of the corresponding errors. If this number is below 1 (i. e., the two results are consistent) we just show "Below 1" in the table.

A, while for the Cosmological model B the results are almost always consistent within 1 σ. One interesting difference regards the results with $H0 = 67$ km s^{-1} per Mpc for the Cosmological models B and C: indeed, we note how the old results presented a positive mean value, while the new findings show a negative mean. This would imply a change of the sign for the related $z_{\rm S}$, as we will see. This difference could be because, as previously shown, there are more data points that would be more consistent with a negative value for $z_{\rm S}$ in the Pantheon+ sample, as well as because the new results are consistent with zero.

Indeed, another key difference between the old and new derivations is in the magnitude of the related uncertainty: for the new results, this is significantly higher than what we obtained in Table 5.3. One possible reason for this conclusion is the higher number of probes in the new set, which would bring to a higher possible variability for the $z_{\rm S}$, even if this uncertainty is still smaller than that derived for the individual SN Ia case (keeping in mind the different meanings between the two quantities).

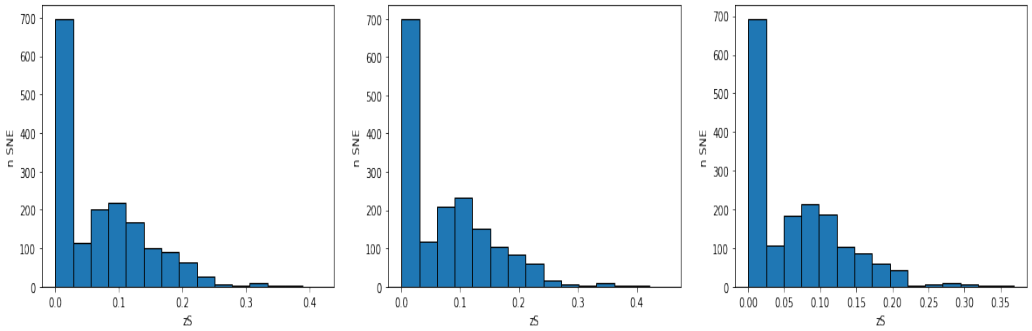

Figure 5.14: Histograms of the computed $z_{\rm S}$ from the k_1 parameter considering the Cosmological model A, where $\Omega_M = 0.3$, $\Omega_k = \Omega_\Lambda = 0$ ($H_0 = 67, 70, 74$ for the left, central and right panels. The values for H_0 are in km s^{-1} per Mpc).

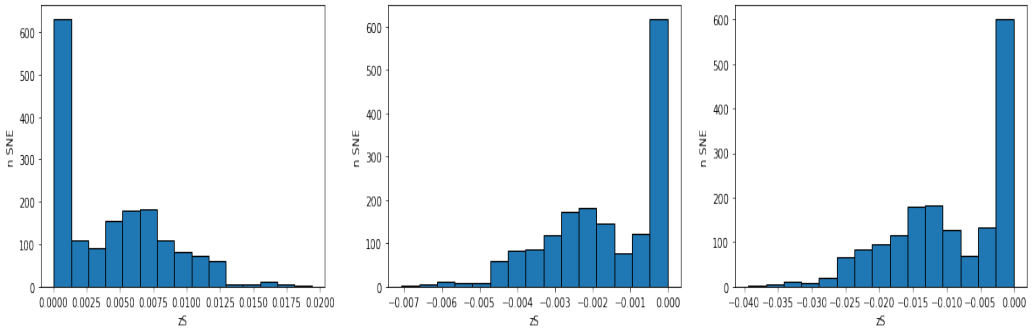

Figure 5.15: Histograms of the computed $z_{\rm S}$ from the k_1 parameter considering the Cosmological model B, where $\Omega_M = 0.3$, $\Omega_k = 0.7$, $\Omega_\Lambda = 0$ ($H_0 = 67, 70, 74$ for the left, central and right panels. The values for H_0 are in km s^{-1} per Mpc).

As we did previously for the Pantheon sample, we derive from the best-fit of the k_i parameters the $z_{\rm S}$ for the entire data set. The results are shown in Figures 5.14, 5.15, and 5.16, where we show the histograms of the computed $z_{\rm S}$. We visualize the results related to k_1 because no significant difference has been observed for the k_i parameters even with the new set.

We now comment on the results shown in these histograms starting from Figure 5.14, where the findings related to the Cosmological model A are visualized. As we expected from the formula inside Table 5.1, the $z_{\rm S}$ values derived from this model are always positive for every H_0. We again note the peak for $z_{\rm S} \sim 0$, which is due to the additional low redshift SNe Ia present in the Pantheon+ sample. We also note that increasing H_0 decreases the maximum value obtained for $z_{\rm S}$, as was the case for the individual computations, of which they keep the same general order of magnitude. This feature was present also in the results obtained for the Pantheon sample, Figure 5.7.

We now move to the histograms visualized in Figure 5.15, which are the results related to the Cosmological model B. We note that the $z_{\rm S}$ are rather small and that for

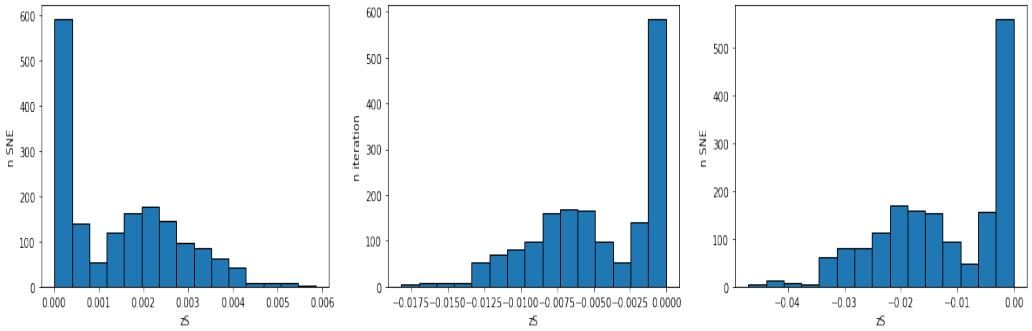

Figure 5.16: Histograms of the computed $z_{\rm S}$ from the k_1 parameter considering the Cosmological model C, where $\Omega_M = 1$, $\Omega_k = \Omega_\Lambda = 0$ ($H_0 = 67, 70, 74$ for the left, central and right panels. The values for H_0 are in km s^{-1} per Mpc).

$H_0 = 67$ km s^{-1} per Mpc they are positive, while, for the other two values, they are negative. This depends on the mean value of the general parameter k_1, which was negative for $H_0 = 67$ and positive for $H_0 = 70, 74$ km s^{-1} per Mpc. This effect has been hinted at by the corresponding individual results, for which a rather symmetric distribution around $z_{\rm S} = 0$ has been found for $H_0 = 67$ km s^{-1} per Mpc, which has then moved to more negative values for $H_0 = 70, 74$ km s^{-1} per Mpc. As for the Pantheon computations, given how the $z_{\rm S}$ are computed in this second approach, we can only have either an entirely positive or negative set of results for $z_{\rm S}$ for a singular histogram. The changing sign in the results was not observed for the results derived from the Pantheon sample, Figure 5.8, for which negative values for $z_{\rm S}$ were observed also for $H_0 = 67$ km s^{-1} per Mpc. We also note that the $z_{\rm S}$ for the new computations are, in general, smaller than those obtained by the old derivations. Regarding the changing sign, this could be because of the symmetric behavior observed in the new results (which is shown also from the general low values for $z_{\rm S}$), which was not observed with the Pantheon sample, in concordance with the shift due to the increasing value of H_0. We also note the usual peak at $z_{\rm S} = 0$ due to the new low redshift SNe Ia.

We now comment on the results shown in Figure 5.16, where we find the Cosmological model C. We may note some similarities with respect to the Cosmological model B results, albeit here we also notice how the $z_{\rm S}$ are usually larger. Indeed, we see that for $H_0 = 67$ km s^{-1} per Mpc we obtain positive values for $z_{\rm S}$, while we find negative ones for $H_0 = 70, 74$ km s^{-1} per Mpc. Again, this difference has not been noted, neither for the individual SNe Ia results nor for the derivations for the Pantheon results, Figure 5.9. The reasons behind this difference are the same as those illustrated for the Cosmological model B. In general, we note that the relation between the computed $z_{\rm S}$ and the fixed value of H_0 is the same as what we observed in the old Pantheon sample for all the cosmological models considered.

Cosmology	$H_0 = 67$	$H_0 = 70$	$H_0 = 74$
Cosmology A	33.6	31.32	28.71
Cosmology B	2.06	0.77	4.46
Cosmology C,	0.69	2.21	5.92

Table 5.10: The median of the distributions of the ratios between the computed $z_{\rm S}$ and the uncertainties provided by the Pantheon+ sample. The values for H_0 are in km s^{-1} per Mpc.

As we did for the individual computations, we can now compare our $z_{\rm S}$ with the correspondent uncertainties provided by the Pantheon+ sample. The ratios for the k_1 parameter are shown in Table 5.10. We observe again that, in general, the $z_{\rm S}$ are higher than the observational errors, with the only exceptions for Cosmological model B, $H_0 =$ 70 km s^{-1} per Mpc, and Cosmological model C, $H_0 = 67$ km s^{-1} per Mpc, where the median displays that the two quantities are of the same order of magnitude. This is linked to the small values for the k_1 parameters found in those specific cases.

One effect that we find for both Pantheon and Pantheon+ results is the contribution of H_0. Indeed, we note that increasing the value of H_0 shifts the derived $z_{\rm S}$ in the same way for all the cases considered, namely making them more negative. This is because, as we can note from Eq. (2.18), H_0 is inversely proportional to the distance, thus, the effect of decreasing the distance is opposed by the more negative values of $z_{\rm S}$ in our comparison with the real data, which we recall increases the distance of the astrophysical probes from us.

We now draw the Hubble diagrams for the Pantheon+ sample, as done for the Pantheon set, considering the $z_{\rm S}$ effects for all the cosmological models and values of H_0 considered. Again, we focus on the k_1 parameters. The diagrams are shown in Figure 5.17. We may note that, even if we are considering a new sample, the behavior of these diagrams is similar to that obtained with the Pantheon sample: the best-fit has been visually reached by the Cosmological model B for all the values for H_0. For the other two cosmological models, we see the theoretical black line fall below the data points at high redshifts, as was the case for the Pantheon sample. Still, for all our computations, the theoretical curve is consistent with the majority of the data points belonging to the Pantheon+ sample. We note again that the redshift on the x-axis in these plots is the cosmological redshift $z_{\rm C}$, which we note is very similar to the one obtained for the Pantheon sample.

As we did for the Pantheon sample, to verify the goodness of our fits we have computed some statistical indicators, namely the reduced χ^2, corresponding to the k_1 best-fit value, the RMSD, and the NRMSD, which have been derived for all the k_i parameters. The results are visualized in Table 5.11. Comparing these results with those obtained

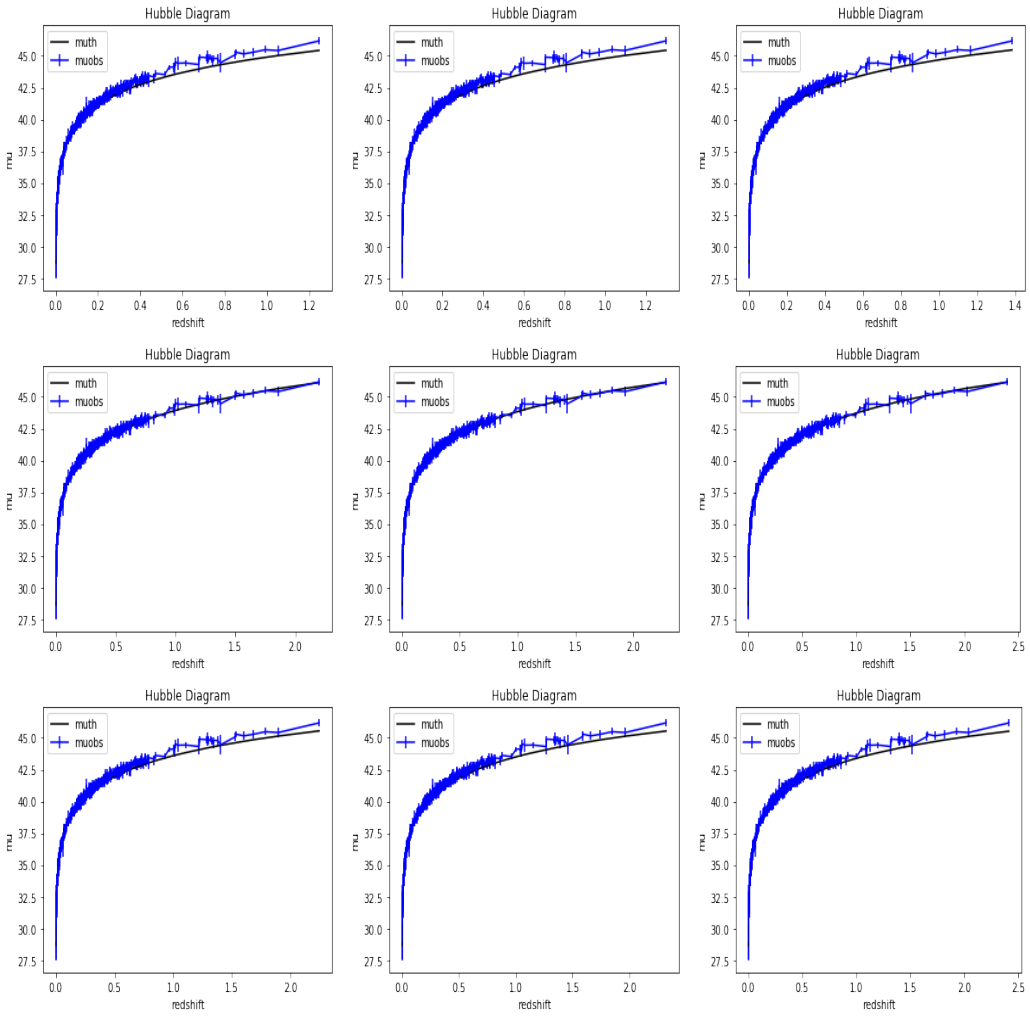

Figure 5.17: Best-fit for the Hubble diagrams computed for our cosmological models (one for each row), using k_1 with data from the Pantheon+ sample, with the usual three values of H_0 (67, 70, 74 km s^{-1} per Mpc, one for each column. The black lines represent the models, while the blue curve the SNe Ia data with their respective errors. We underline that the red shift on the x-axis is the computed expansion redshift z_{C}, which is why it changes between cosmological models.

Cosmology	Reduced χ^2	RMSD	NRMSD
Cosmology A, $H_0 = 67$	0.007	0.240	0.106
Cosmology A, $H_0 = 70$	0.009	0.259	0.111
Cosmology A, $H_0 = 74$	0.009	0.257	0.111
Cosmology B, $H_0 = 67$	0.003	0.186	0.087
Cosmology B, $H_0 = 70$	0.003	0.183	0.086
Cosmology B, $H_0 = 74$	0.003	0.183	0.086
Cosmology C, $H_0 = 67$	0.006	0.225	0.104
Cosmology C, $H_0 = 70$	0.006	0.226	0.104
Cosmology C, $H_0 = 74$	0.006	0.228	0.104

Table 5.11: Best-fit statistics for the k_1 parameter in all the cases considered in our work. As for the previous computation, the NRMSD has been computed by dividing the RMSD by the difference between the maximum and minimum values of the difference between the theoretical and observed distance modulus. The mean value of the uncertainty on the observed data is $\Delta_{\mu obs} = 0.243$, which is higher than the correspondent value for the Pantheon set, $\Delta_{\mu obs} = 0.142$. The values for H_0 are in km s^{-1} per Mpc.

from the Pantheon computations, Table 5.4, we note that we infer, in general, better fits: indeed, while the RMSD remains of the same order of magnitude, we note a significant decrease for the NRMSD and especially for the reduced χ^2. We also note that, as in the Pantheon computations, the Cosmological model B achieves the most consistent best-fit results with the real data, confirming our comments in regards to Figure 5.17. The other cosmological models show also acceptable fits, better than their Pantheon counterparts, although worse than the results obtained by the Cosmological model B.

We now add the BAO set also to the Pantheon+ sample. The results related to the k_i parameters are gathered in Table 5.12. Comparing the results shown here with Table 5.8, we note a general significant decrease in the uncertainties regarding our results, for all the considered cases, arriving at the order of magnitude of the precision reached by the Pantheon set. We also note that the mean values of the Cosmological model A are very similar between the two cases, while we see a significant shift to positive values for the k_i parameters for the Cosmological model B, and negative ones for the Cosmological model C. We also note that we do not obtain results consistent with zero anymore for any of the considered cases. Regarding the comparison with the corresponding table for the Pantheon set, Table 5.5, we notice a negative shift of the results for the Cosmological models A and C, while the opposite has been found in the Cosmological model B. Previously, with the combination of SNe Ia and BAO considering the Pantheon sample, we obtained for some particular cases results consistent with zero, which we do not find here. This is because of the differences between the Pantheon and Pantheon+ results.

Cosmology	k_1	k_2	k_3	k_4
Cosmology A, $H_0 = 67$	$(-9.53 \pm 0.03) \times 10^{-5}$	$(-8.84 \pm 0.03) \times 10^{-5}$	$(-5.91 \pm 0.02) \times 10^{10}$	$(-10.03 \pm 0.04) \times 10^{-5}$
Cosmology A, $H_0 = 70$	$(-9.37 \pm 0.03) \times 10^{-5}$	$(-8.71 \pm 0.03) \times 10^{-5}$	$(-5.84 \pm 0.02) \times 10^{10}$	$(-10.09 \pm 0.03) \times 10^{-5}$
Cosmology A, $H_0 = 74$	$(-9.13 \pm 0.03) \times 10^{-5}$	$(-8.53 \pm 0.03) \times 10^{-5}$	$(-5.71 \pm 0.02) \times 10^{10}$	$(-9.78 \pm 0.04) \times 10^{-5}$
Cosmology B, $H_0 = 67$	$(2.59 \pm 0.05) \times 10^{-5}$	$(2.63 \pm 0.05) \times 10^{-5}$	$(1.76 \pm 0.04) \times 10^{10}$	$(2.54 \pm 0.04) \times 10^{-5}$
Cosmology B, $H_0 = 70$	$(5.94 \pm 0.09) \times 10^{-5}$	$(5.39 \pm 0.10) \times 10^{-5}$	$(2.28 \pm 0.04) \times 10^{10}$	$(3.25 \pm 0.04) \times 10^{-5}$
Cosmology B, $H_0 = 74$	$(4.34 \pm 0.06) \times 10^{-5}$	$(4.49 \pm 0.06) \times 10^{-5}$	$(3.00 \pm 0.04) \times 10^{10}$	$(4.22 \pm 0.06) \times 10^{-5}$
Cosmology C, $H_0 = 67$	$(-4.80 \pm 0.05) \times 10^{-5}$	$(-4.65 \pm 0.06) \times 10^{-5}$	$(-3.12 \pm 0.04) \times 10^{10}$	$(-4.91 \pm 0.06) \times 10^{-5}$
Cosmology C, $H_0 = 70$	$(-4.17 \pm 0.07) \times 10^{-5}$	$(-4.08 \pm 0.05) \times 10^{-5}$	$(-2.73 \pm 0.03) \times 10^{10}$	$(-4.28 \pm 0.06) \times 10^{-5}$
Cosmology C, $H_0 = 74$	$(-3.30 \pm 0.06) \times 10^{-5}$	$(-3.25 \pm 0.06) \times 10^{-5}$	$(-2.16 \pm 0.04) \times 10^{10}$	$(-3.36 \pm 0.07) \times 10^{-5}$

Table 5.12: Results for the k_i parameter considering the general best-fit for SNe Ia of the Pantheon sample together with the BAO constraints, for the three cosmological models. The values for H_0 are in km s^{-1} per Mpc.

5.3 Finding the mass of the photons

Up to now, we have worked on possible consequences of a new shift contribution without worrying about the particular non-standard electromagnetic phenomenon which may cause it. We now move to a more fundamental level by showing a series of experiments and analyses whose aim has been to find a possible mass of the photon, or at least an upper limit for it. It is important to note that a definitive test of a zero-particle mass cannot be performed, considering that, for the Heisenberg principle in the energy-time form applied to our universe, the minimum possible detectable mass is of the order of 10^{-69} kg [316, 317], thus the upper limits estimations will inevitably end at that point if it will be ever reached experimentally. The first estimation was due to de Broglie himself, who used dispersion analysis to give an estimate of the upper limit equal to 10^{-53} kg. For a general critique of the results achieved before 2008, see [297]. In laboratory tests, one of the most stringent upper limits has been reached by testing Coulomb's law [318], finding an experimental upper limit equal to 2×10^{-50} kg. For a more complete review of tests performed on the Earth, more specifically which physical fundamental law they are testing and what are the experimental apparatuses, see [319].

Moving to the astrophysical observations, studies regarding the mass of the photon have been performed using Fast Radio Bursts (FRBs), which are transient radio pulses whose length goes from a fraction of a millisecond to a few milliseconds, caused by some high-energy astrophysical process not yet completely understood, using dispersion analysis [320, 321]. Indeed, if the photon actually has a mass, its velocity will depend on it, so we would notice, from an astrophysical signal of this kind, a temporal lag between the different frequencies of that signal itself. In particular, this time lag between two photons with energies E_1, E_2 has the form (using the natural units):

$$\Delta t_{m_\gamma} = \frac{m_\gamma^2}{2H_0}\left(\frac{1}{E_1^2} - \frac{1}{E_2^2}\right) H_\gamma(z), \tag{5.21}$$

where $H_\gamma(z)$ is defined as

$$H_\gamma(z) = \int_0^z \frac{dz'}{(1+z')^2\sqrt{\Omega_\Lambda + (1+z')^3\Omega_m}}. \tag{5.22}$$

Noticing that this time lag could also be due to the interactions with the intergalactic medium [321], it is also important that these two lags have different dependencies on the redshift of the astrophysical source. From these observations, one of the best results achieved is an upper limit equal to 3.9×10^{-51} kg at a 95% confidence level [322]. These limits may suffer a certain degree of ambiguity since the plasma and photon time delays are indistinguishable in the measurements [323], if gamma-ray frequencies are not considered [324]. A space project has also been proposed in order to further improve the limits given by the dispersion analysis [323].

Currently, the most strict upper limits found for the photon mass have been derived using magnetohydrodynamics arguments considering the de Broglie-Proca equations based on the Parker Model for the solar wind [55], near the Earth and Pluto magnetospheres, respectively [325, 326]. In particular, the orders of magnitude found in these works are 10^{-52} kg and 10^{-54} kg, respectively. The latter limit has been denominated to be the actual upper limit of the photon mass by the latest release of the Particle Data Group [5]. However, in [327] a critique of this result can be found, according to which this conclusion has been reached via a particular model with its associated assumptions, and only marginally by data points collected from the missions Pioneer and Voyager. In particular, the test used a set of three data: magnetic field, ion density, and particle velocity. Also, there is no analysis regarding the errors related to these quantities, so a change to these data points could alter significantly the computed upper limit.

In [327] other three possible upper limits for the photon mass have been found by looking for deviations from Ampere's law in the solar wind, using the Cluster constellation data, a mission composed of four identical spacecraft. The method will be explained in more detail in the next section, given that it is similar to the analysis that will be shown in that section, here we say that it is based on the comparison between the particle current densities measured by the instruments on board of each spacecraft with a mean rotational current density derived with the curlmeter method, which shall be detailed in the next pages. Considering three different assumptions regarding the vector potential of the magnetic field, they found the following three upper limits: 1.4×10^{-49} kg, 1.6×10^{-50} kg, and 3.4×10^{-51} kg.

Other upper limits for the photon mass have been found in the past decades in a plethora of different environments and experiments, also using different physical approaches, even in the astrophysical field. For a more complete list see [4, 5]. The im-

Smallest (Heisenberg) measurable mass for any particle is 1.3×10^{-69} kg for Δt = age of the Universe			
Reference	Value (kg)	Method	Comment
[328, 329, 330]	3×10^{-63} 3×10^{-58}	Modelling the galactic potential	Defined as speculative in [297]. Absence of data and error analysis. The final estimate is based on a space-time constant galactic magnetic field and on the applicability of the virial theorem and of the equilibrium of the interstellar gas. Difference of 5 orders of magnitude between estimates.
[331]	3×10^{-56}	Modelling Crab Nebula magnetohydrodynamic waves via polarisation plates	The authors state in the abstract that their arguments are "not rigorous". Absence of data and error analysis.
[332, 333, 334]	2.4×10^{-55} 1.8×10^{-53}	Torsion pendulum	Defined as speculative in [297]. The final estimate of the torque is based on assumed exceptional values of galactic magnetic fields and potential.
[335]	10^{-52}	Low frequency resonance circuits	Method defined of "dubious validity" by [5].
[336]	3.6×10^{-52}	Speed of 5-50 Hz lightning discharges in the troposphere	Assumption that the frequency shift due to photon mass would be linear rather than quadratic.
[337]	8×10^{-52}	Jupiter magnetic field	The authors are concerned by the neglected systematic effects.
[338, 339]	10^{-51} 4×10^{-51}	Satellite data of Earth's magnetic field	Reliable estimate depending upon precise magnetic field mapping current and systematic errors.
[340]	1.3×10^{-51}	Alfvén waves in the interplanetary medium	Another upper limit of 1.1×10^{-52} is also proposed, but indicated as less reliable.

Table 5.13: Summary of some photon mass upper limits below 10^{-50} kg not cited in the main text.

portant point is that a very large room for improvement exists, given the many orders of magnitude between these estimations and the theoretical limit for the smallest possible mass. Also, it seems that even if the accepted limit is 10^{-54} kg, every limit which is around 10^{-51} kg deserves a worthy analysis given the discrepancies between the different results. Nevertheless, many more estimates on the upper limit of the photon mass exist, some defined as "speculative" in [297, 5]. Other limits, not cited previously, as well as some comments about them, are shown in Table 5.13.

For the LSV parameters, which we recall may be linked to an effective photon mass, a great disparity of results exists between upper limit estimates, as high as from 18 to 24 orders of magnitude: $|\vec{k}^{\rm AF}| < 4 \times 10^{-7}$ m^{-1} or 5×10^{-4} m^{-1}, and $k_0^{\rm AF} < 5 \times 10^{-10}$ m^{-1} for laboratory tests [341]; $|\vec{k}^{\rm AF}| \simeq k_0^{\rm AF} < 5 \times 10^{-28}$ m^{-1} for astrophysical estimates [342]. The latter are close to the Heisenberg limit.

5.4 Testing the Ampère-Maxwell law using MMS data

5.4.1 Data selection and methodology

We are now going to describe the analysis performed in [54] performed in order to derive an eventual new upper limit (or a possible estimation of a photon mass under certain hypotheses), by testing the Ampère-Maxwell using the Magnetospheric Multiscale (MMS) Mission data [42], which is a constellation of four satellites flying in a tetrahedral formation exploring regions near the Earth. The mission was launched in 2015, with the main goal of studying the magnetic reconnection processes occurring in highly conducting plasma, for which the magnetic topology is rearranged and magnetic energy is converted to kinetic energy, thermal energy, and particle acceleration, happening on the frontier between Earth's Magnetosphere and the solar wind region. With time, MMS has also been used for other studies and applications, thus exploring other regions of the Magnetosphere and the solar wind surrounding it. Different detectors have been mounted on each satellite composing the MMS constellation, like The Fast Plasma Investigation (FPI, [343]) which was developed to measure the differential directional flux of magnetospheric electrons and ions and, thus, the particle currents for both electron and ions, and the Fluxgate Magnetometer (FGM, [344]), being able to measure the magnetic fields inside the plasma.

The idea of our work is to study the Ampère-Maxwell law, comparing (from now on we shall refer to the current densities as just current) the particle current appearing on the right-hand side of the equation with the $\nabla \times B$ operator on the left-hand side. If the two values are discordant and the current associated with the electric field is negligible, then we could assume that such discrepancies are actually due to non-standard electromagnetic effects, thus validating Eq. (5.2) or Eq. (5.6). Under this hypothesis, we write down these equations as

$$\vec{j}_B = \vec{j}_P + \vec{j}_E + \vec{j}_{nM} \ , \tag{5.23}$$

where $\vec{j}_B = \nabla \times \vec{B}/\mu_0$, $\vec{j}_P = \vec{j}$, $\vec{j}_E = \epsilon_0(\partial \vec{E}/\partial t)$, and $\vec{j}_{nM}$ indicates the non-Maxwellian terms.

For the data set, we have used the Automated Multi-Dataset Analysis AMDA website [345], where the data of many campaigns and instruments regarding plasma physics, including MMS[2,3], are gathered.

Let us now go into more detail regarding the methodology followed in this analysis. The particle current is defined as

[2]https://mms.gsfc.nasa.gov/index.html
[3]https://lasp.colorado.edu/mms/sdc/public

$$\vec{j}_P = q(n_i\vec{v}_i - n_e\vec{v}_e) \,, \tag{5.24}$$

where n_i (n_e) are the ion (electron) particle densities in the plasma, while $\vec{v}_i$ ($\vec{v}_e$) are the ion (electron) velocities in the medium. We note that in this instance we did not use the quasi-neutrality assumption, according to which we should have $n_i \sim n_e$, even if later in the analysis we have confirmed its validity. Both the densities and velocities, as well as their errors, are measured by the FPI instruments on board of MMS and thus provided by AMDA. Of course, if we write the current for each Cartesian component (x, y, z) we have $j_P^x = q(n_i v_i^x - n_e v_e^x)$ and similarly for y, z; the modulus is $j_P = \sqrt{(j_P^x)^2 + (j_P^y)^2 + (j_P^z)^2}$.

The error on j_P has been computed through error propagation processes starting from the errors on the densities and the velocities provided by AMDA [346, 347]. For instance, regarding the x component we find $\Delta j_P^x = q\left(v_i^x \Delta n_i + n_i \Delta v_i^x + v_e^x \Delta n_e + n_e \Delta v_e^x\right)$ and similarly for y, z, so that the total error is

$$\Delta j_P = \frac{1}{j_P}\left(|j_P^x|\Delta j_P^x + |j_P^y|\Delta j_P^y + j_P^z|\Delta j_P^z\right) \,. \tag{5.25}$$

These computations refer to the particle current measured by each of the four satellites. For our comparisons, we take the average of these currents and their respective errors.

Regarding j_B, AMDA provides an estimate of this quantity, but not a direct experimental error. In order to find the associated uncertainties, we have built an algorithm able to compute both j_B and its error using the curlmeter technique [43, 348]. This technique allows us to find an estimate of j_B (which we call rotational current), inside the tetrahedron formed by the four spacecraft, considering the magnetic field measurements of each spacecraft as well as the displacement of the spacecraft themselves. This technique is based on a linear approximation for the variation of the gradients of the magnetic field inside the region. Given its nature, this is why we have decided to compare it to the average of the particle currents measured by each satellite. For this method, $\vec{j}_B$ is defined as ($\ell = 1, 2, 3, 4$, [349])

$$\vec{j}_B = \frac{1}{\mu_0}\sum_{\ell=1}^{4} \vec{k}_\ell \times \vec{B}_\ell \,, \tag{5.26}$$

where $\vec{k}_l$ are the reciprocal vectors of the tetrahedron, defined by ($\vec{r}_{ij} = \vec{r}_j - \vec{r}_i$, where i and j refer to the spacecraft positions)

$$\begin{aligned}\vec{k}_1 =& \frac{\vec{r}_{23}\times\vec{r}_{24}}{\vec{r}_{21}\cdot(\vec{r}_{23}\times\vec{r}_{24})}, \quad \vec{k}_2 = \frac{\vec{r}_{31}\times\vec{r}_{34}}{\vec{r}_{32}\cdot(\vec{r}_{31}\times\vec{r}_{34})},\\ \vec{k}_3 =& \frac{\vec{r}_{24}\times\vec{r}_{21}}{\vec{r}_{23}\cdot(\vec{r}_{24}\times\vec{r}_{21})}, \quad \vec{k}_4 = \frac{\vec{r}_{32}\times\vec{r}_{31}}{\vec{r}_{34}\cdot(\vec{r}_{32}\times\vec{r}_{31})}\ .\end{aligned} \tag{5.27}$$

We have verified that the value of j_B derived by us using this method compares satisfactorily with the one provided by AMDA. As expected, the errors on $\vec{j}_B$ depend on the uncertainties of the magnetic field and the separations between the spacecraft. For the former, we consider a constant value $\Delta B = 0.1 \times 10^{-9}$ T for each component of the magnetic field [350], while for the latter we consider a relative error equal to 1% of the separation distance [351]. After a lengthy error propagation computation, we arrive at writing the error on the q component for a single spacecraft (thus for a single ℓ in the previously shown sum)

$$\Delta j^q_{\ell\ B} = (|k^r_\ell| + |k^s_\ell|)\Delta B + |B^r_\ell|\Delta k^s_\ell + |B^s_\ell|\Delta k^r_\ell\ , \tag{5.28}$$

r, s being the other components. The final error on the q^{th} component of $\vec{j}^q_B$ is

$$\Delta j^q_B = \sum_{\ell=1}^{4} \Delta j^q_{\ell\ B}\ , \tag{5.29}$$

which is then used, together with the other components, to find the error on the value of j_B. We stress that these are results of instrumental error propagation.

We now start describing the data selection. We have considered almost six years of measurements, from November 2015 to September 2021, especially from the FPI and FGM instruments on every spacecraft. We picked only "burst mode" data [42], which are the ones providing the highest time resolution collected by MMS. For the first results, we have selected the data for which 1) Both the rotational and particle currents are available and 2) The particle current measured from each spacecraft are all consistent, within their errors, with one to the other. The last point has been considered to give more reliability to the hypothesis behind the curlmeter technique so that both methods are measuring the same effective current under this assumption.

We have chosen to download the data using a sampling of 1 s, to have a significant number of data points for our analysis. The various instruments actually provide the majority of the data of interest in the order of magnitude of ten milliseconds, thus, we have, first of all, verified that the sampling chosen by us actually gives a mean on the specifically chosen interval of 1 s. This is relevant because, for its nature, the curlmeter technique is not able to identify high-frequency components for the currents, which we

have naturally deleted in our mean process and, thus, erased a possible systematic effect that could jeopardize our conclusions.

Taking into account the previous caveats, in total, we have considered in our computations approximately 3.8×10^6 data points in time, for each of which we have downloaded and 82 physical quantities: the ion and electron component velocities for four spacecraft (24), distances in components between spacecraft and the coordinates of the barycenter (18), the electric field at the first spacecraft (3), the electron and ion densities (8), the parallel and perpendicular electron and ion temperatures (16), the magnetic field (12), and the detection time (1), both for the comparisons themselves as well as for further reliability checks of our results.

As a first check, we have verified, given our sampling time, that $\vec{j}_E$ is effectively several orders of magnitude smaller than both the rotational and particle currents, as well as their eventual differences. $\vec{j}_E$ has been computed from the ratio of the electric field variation over the sample interval of 1 s. More quantitatively, we have found an average of $\vec{j}_E = 1.4 \times 10^{-14}$ Am^{-2}, which is at least six orders of magnitude smaller than the averages of the curl and particle currents. We have thus confirmed the possibility of directly comparing $\vec{j}_B$ with $\vec{j}_P$ to find an eventual value for $\vec{j}_{nM}$ as shown in Eq. (5.23), thus assuming that every possible inconsistency between the two currents is due to non-standard electromagnetic effects (i. e. a photon mass, either real for the dBP theory or effective for SME), as previously stated. Indeed, we compare the two currents considering their respective errors, and label "inconsistencies" the data points where the two corresponding currents do not overlap considering their error bands. Instead, a "consistency" occurs when the two current bands overlap. For the consistencies, we provide a definition for a possible upper limit for $\vec{j}_{nM}$, as the smallest amount to add (subtract) to (from) one of the two currents to get an inconsistency case. These two situations are illustrated in Figure 5.18.

Summarizing this procedure, we can write

$$|\vec{j}_\rho| - \Delta|\vec{j}_\rho| - \left(|\vec{j}_\epsilon| + \Delta|\vec{j}_\epsilon|\right) = \underset{overlap}{\overset{gap}{\gtrless}} 0 \,, \tag{5.30}$$

where $\rho, \epsilon = B, P$ depending on whether $|\vec{j}_P| - \Delta|\vec{j}_P|$ is larger or smaller than $|\vec{j}_B| - \Delta|\vec{j}_B|$. This analysis has been carried out for the modulus and for the Cartesian components. In the latter case, we define an inconsistency if a gap emerges from at least one of the three axes.

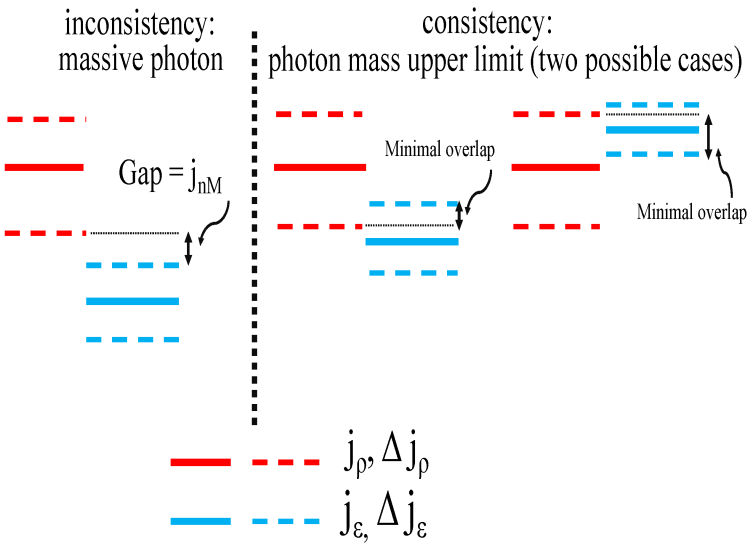

Figure 5.18: The red and blue lines represent the currents, and, if dotted, the error bounds. In the left panel, we show the case of inconsistency, where the gap implies $\vec{j}_{nM} \neq 0$. Instead, in the right panel, the case of consistency, for which, moving upward or downward one of the two bands, we would fall in the inconsistency case, thus defining an upper limit for $\vec{j}_{nM}$. This computation has been carried out for the modulus and each component.

5.4.2 Results

We now show the results obtained for our comparisons using the aforementioned data set and methodology. First, considering the entire data at our disposal, we find 2% of inconsistencies for the modulus and 5.2% in Cartesian components. As expected, the inconsistencies in the latter case are more numerous than those found in the former one, because of the more relaxed criteria for the inconsistency definition. Interestingly, albeit for a small percentage, inconsistencies have actually been found. This can be noted in Figure 5.19, in which the computations for Eq. (5.30) are illustrated. The inconsistencies are represented by the positive values in this plot. Considering the scheme explained in Figure 5.18, we can now draw our distributions for the consistencies and inconsistencies derived by our comparisons for the entire set of data studied in our analysis. These are shown in Figure 5.20.

We now further investigate our results. For the application of the curlmeter technique the displacement of the spacecraft, and thus the specific form of the tetrahedron, is important because this technique is sensible also to the singular separations of the four spacecraft locations [352]. This is why we have further refined our analysis by considering the so-called geometrical quality factor [42], which has already been introduced for the Cluster constellation. In particular, we employ the form related only to the volume

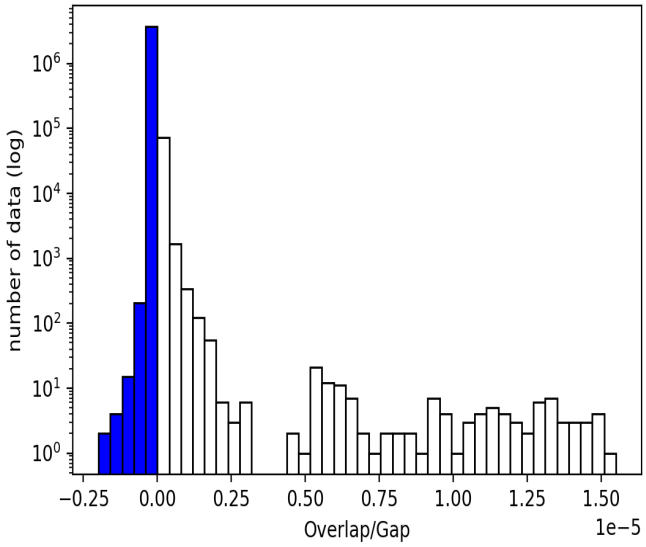

Figure 5.19: Histogram of Eq. (5.30) for all the burst data studied in our analysis. Most values are negative, indicated with blue bars, on the left of and close to zero. The positive values, white bars, on the right of zero, corresponding to the inconsistencies, range from 1.1×10^{-12} Am^{-2} to 1.5×10^{-5} Am^{-2}.

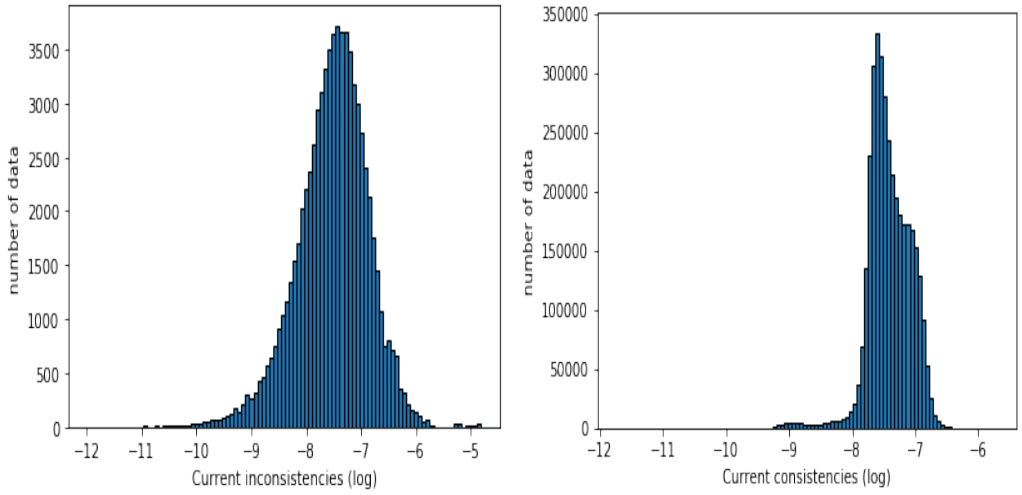

Figure 5.20: Histograms of the inconsistencies (left panel) and consistencies (right panel) found for the entire set of data, according to our comparisons. The values for the currents are presented in Am^{-2}.

	j_B	Δj_B	j_P	Δj_P
Mean (Inconsistencies)	4.9×10^{-8}	6.9×10^{-8}	2.0×10^{-7}	5.3×10^{-8}
Mean (Consistencies)	2.0×10^{-8}	1.8×10^{-7}	3.9×10^{-8}	2.4×10^{-8}

Table 5.14: The average values for the currents and their errors, considering the data with $Q > 0.7$, [Am^{-2}].

of the tetrahedron: $Q = V_a/V_r$, where V_a is the actual volume of the tetrahedron in a given moment, while V_r is the volume of the regular tetrahedron having as side the average of the separations between the spacecraft. We have computed this factor for all the data points, selecting for this second run only those that present $Q > 0.7$, and then make our comparisons taking into account only these data points. By doing so, the percentages of inconsistencies slightly increase to 2.2% for the modulus and slightly decrease to 4.8% for the components. Thus, we conclude that this quality check does not influence our conclusions regarding the discrepancies in a significant manner, concluding that the reliability and the results of our comparisons are not dependent upon the shape of the tetrahedron itself. In Table 5.14 we report the averages of the particle and rotational currents for the high-quality factor data points, noting the orders of magnitude of difference with the previously presented displacement current.

As a further step, we have investigated the physical zones in which MMS flies, to see if there is a dependence between the number of inconsistencies found and the conditions of the plasma itself. In order to do so, we have studied the pressures, in particular, the ram p_R, magnetic p_M, and thermal p_T pressures, at each data point, defining the following scheme: if $p_R > 10\ max(p_M, p_T)$, we identify the region as the solar wind; if $0.3\ min(p_M, p_T) < p_R < 4\ max(p_M, p_T)$, as the magnetosheath; if $10\ p_R < p_M$, as the magnetosphere. The region of undetermined data points between the solar wind and the magnetosheath is named zone I, whereas all the rest of the undetermined data have been gathered inside zone II.

The results, both for the effective number of data points as well as in percentages, considering also the aforementioned quality check, are detailed in Table 5.4.2.

We note how, even if the data points in the solar wind are a minority (4.5% of the total data set) a considerable amount of inconsistencies (gaps) has been found in this particular region. Indeed, summing the inconsistencies in the solar wind and in the undetermined zone I, we find that 76% $(42473/55916)$ in modulus and 65% $(77847/119850)$ for the components of the total inconsistencies are found in 14% of the total data set. This derivation is interesting, because it links the inconsistencies to a particular physical zone, thus underlying possible physical phenomena which would favorite this discrepancy in the solar wind, where indeed we also find the highest percentages of inconsistencies with

Results	Solar Wind	Zone I	Magnetosheath	Zone II	Magnetosphere
Gaps (M)	24376	18097	10669	2203	571
Overlaps (M)	92190	261103	1033981	356592	707595
Gaps (C)	34813	43034	35422	5421	1160
Overlaps (C)	81753	236166	1009228	353374	707006
Data by region/total data	4.5%	9.5%	42.9%	14.1%	29%
Gaps by region/total gaps (M)	39%	31.1%	24%	4.5%	1.4%
Gaps/total data by region (M)	21%	6.4%	1.0%	0.6%	0.1%
Gaps/total data by region (C)	29.9%	15.3%	3.3%	1.5%	0.2%

Table 5.15: Results in modulus (M) and components (C) on gaps (inconsistencies) and overlaps (consistencies) for burst data and $Q > 0.7$, analyzed by region, in number and percentages.

respect to the total solar wind data points analyzed (21% for the modulus and 29.9% for the components), forming a remarkable minority of the data analyzed in that particular region.

Even if we may work under the assumption that all the possible inconsistencies are due to non-standard electromagnetic effects, we are aware that this might not be the case, and that other, possibly systematic effects could be at hand, even if calibrations on the instruments and studies on systematic uncertainties have been performed [42, 343, 344, 346, 347], for instance, on the intrinsic charge created by the instrumentation itself [353]. Indeed, reducing errors and possible systematic effects has been one of the main objectives of the MMS mission: the instrumentation enables regular cross-calibration and validation of the FPI measurements, thus reducing systematic errors to within a few percent, and providing suitable accuracy to calculate current density directly from particle observations [347]. Similarly, calibrations have been performed on the FGM instruments as well [344].

Even considering the above caveats, we have still performed further analysis to confirm the reliability of our results. Indeed, one possible source of systematic errors could be found in an environment with low ion and electron densities, given the possibility that the instruments could not detect densities below a certain threshold. Regarding this point, we have investigated the possible correlation between densities and inconsistencies, not finding any. This comforts us because if discrepancies were due to this systematic effect, a clear correlation should have been seen. We have also studied the density in the solar wind+zone I data, where the majority of the inconsistencies lie. We have found that the electron density has an average of 22.96 cm^{-3} and a median of 11.88 cm^{-3}, while the ion density has an average of 22.85 cm^{-3} and a median of 12.1 cm^{-3}. Considering as low densities the one below a certain threshold (5 cm^{-3}), we have found that only in 13.6% and 8.6% of cases the electron and ion densities, respectively, are smaller than this limit.

5.4.3 Estimating the ETE parameters

In this section we shall derive, from the previous computations, our estimates on the mass of the photons (and its effective counterpart in the LSV theory) from the inconsistencies found, keeping in mind the assumption according to which they would entirely be due to non-standard electromagnetic effects, and the corresponding upper limit from the consistencies. In order to do so, we first have to find the modulus of the vector potential, that we need to use in Eqs. (5.2, 5.6). Thus, we focus on the solar wind+zone I region, where the majority of the inconsistencies lie, and we apply the [55] model for the solar wind to derive the potential. Indeed, it is possible to show that for this model, in spherical coordinates, defined by taking as center the Sun and considering the Coulomb gauge, the vector potential becomes [354]

$$A_r = \frac{2b}{3}\left[1 - \frac{3}{2}x - x\ln\left(1+x\right)\right], \tag{5.31}$$

$$A_\theta = \frac{2b}{3}\sin\theta\left[\frac{x}{1+x} + \ln(1+x)\right]\left(\frac{\cos\theta}{x}\right), \tag{5.32}$$

$$A_\phi = \frac{a}{r\sin\theta}(1+x), \tag{5.33}$$

where $x = |\cos\theta|$ and, at 1 AU and for magnetic fields equal to 5 nT, $a = 3.54 \times 10^{-9}$ T AU^2 and $b = 3.54 \times 10^{-9}$ T AU for a diagonal direction. Given that we are interested only in the modulus of the vector potential and at a fixed distance (1 AU) because we aim to study the solar wind around the Earth, after some computations we find a direct proportionality between the modules A and B for this particular region: $A = \sqrt{11/6}BR$, where R is 1 AU. Knowing this, we are able to compute the modulus of the vector potential for each data point inside the solar wind and zone I regions.

Once we do so, we are finally able to compute our mass estimate (or the upper limits) using the following formula

$$m_\gamma = \frac{\hbar\sqrt{\mu_0}}{c}\sqrt{\frac{|\vec{j}_{nM}|}{|\vec{A}|}}\ \text{kg}\,. \tag{5.34}$$

from which we also derive the LSV parameter using Eq. (5.7). The results, both for the mass estimations as well as for the upper limits for all the data analyzed in our work, are shown in Figure 5.21.

From this figure, we may note that the minimum, average, and median values of the upper limit distribution are very similar to the corresponding values of the photon mass distribution. This is due to our definition of the upper limit, which involves the

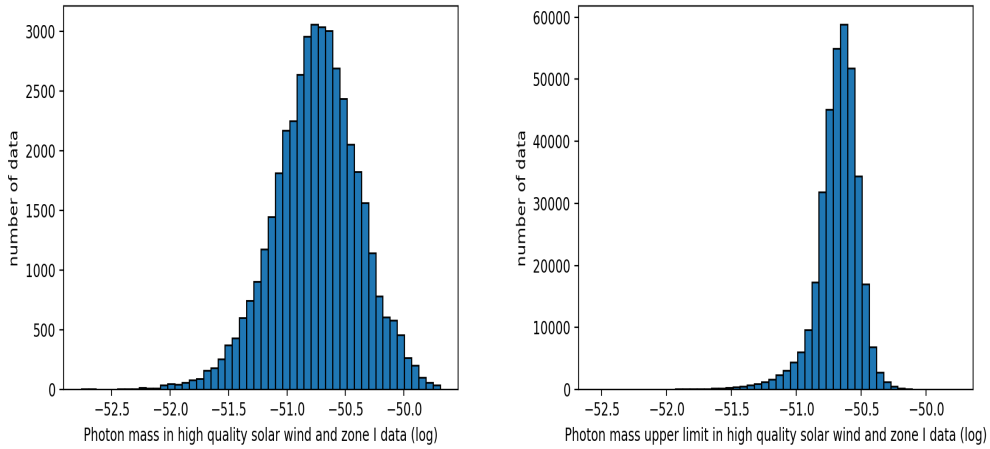

Figure 5.21: Left panel: for the solar wind and zone I regions burst data and $Q > 0.7$, we show the histogram of the photon mass derived from the inconsistencies. The minimum value is 1.7×10^{-53} kg, while the average is 2.5×10^{-51} kg. Right panel: the upper limits for the same region and quality factor. Here, the minimum is 1.8×10^{-53} kg, the average 2.2×10^{-51} kg, and the median 2.2×10^{-51} kg. In both figures, the x-axis is in logarithmic scale.

minimal displacement, upward or downward, of the currents considering their errors. Regarding the values themselves, we note that they are in the same order of magnitude intervals as the values obtained in the literature presented previously. Incidentally, we also note again that we find discrepancies between the currents, which according to our assumptions would imply a value for the photon mass, in a minority of the cases. We choose to consider the minimum value, 1.7×10^{-53} kg, of the distribution as our estimate, because that would be viable for all the cases in which discrepancies have been found. We have to stress again the previously mentioned caveats, that do not allow us to state that we have formally found a mass of the photon, we just state that, if the discrepancies between the instrumental detection are due to non-standard electromagnetic effects, then they would be explained by these estimates for the massive terms. Nevertheless, the significant amount of inconsistencies found in the solar wind is worthy of scrupulous scrutiny. Instead, for the upper limit estimate, we consider the average of our distribution, 2.2×10^{-51} kg, as the reference value, being more representative of all the values found for each data point, thus being consistent with the order of magnitude of the results found in the literature.

Incidentally, from these results we can also derive the values of the LSV parameters: indeed, we find, for the inconsistencies, a minimum equal to $|\vec{k}^{\mathrm{AF}}| = 4.9 \times 10^{-11}$ m^{-1}, an average of 7.1×10^{-9} m^{-1}, and a median equal to 5.18×10^{-9} m^{-1}. For the upper limits, instead, we find as the minimum 5.2×10^{-11} m^{-1}, the average 6.3×10^{-9} m^{-1},

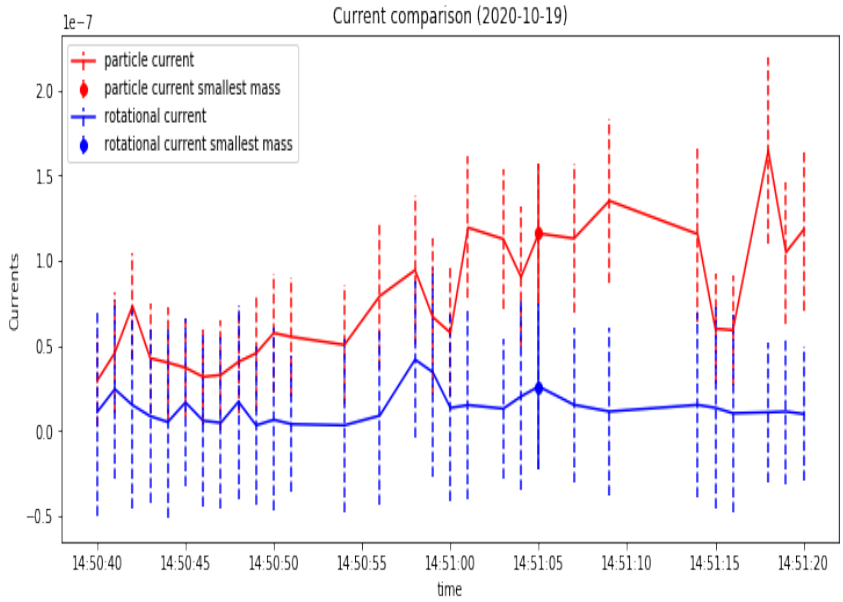

Figure 5.22: The smallest presumed photon mass, see the spots, has been derived from the comparison that occurred on 19 October 2020, at 14h 51m 05s, in the zone I burst data and $Q = 0.82$. The particle current $j_P = (1.2 \pm 0.4) \times 10^{-7}$ Am^{-2}, and the rotational current $j_B = (2.6 \pm 4.9) \times 10^{-8}$ Am^{-2} produced a difference of 7.4×10^{-12} Am^{-2}. This difference is not visible on the vertical axis carrying units which are five orders of magnitude larger. The vertical dotted lines are the errors. The potential of 3.8×10^3 Tm^{-1} leads to a mass of 1.7×10^{-53} kg, and thereby $|\vec{k}^{\mathrm{AF}}| = 4.9 \times 10^{-11}$ m^{-1}.

and, finally, the median 6.2×10^{-9} m^{-1}. We have also isolated the data point in which the smallest mass has been found, and we show it in Figure 5.22, where we also note four inconsistency points around the one related to the smallest presumed mass (the latter highlighted with the dots).

Chapter 6

Extended Gravity and oscillating stars

In this chapter, we shall introduce in more detail a particular ETG, known as $f(R)$-Gravity, and its application to the stellar structure of non-compact objects. For the entire chapter, we are going to use the signature (+,-,-,-). This analysis is the main goal of [Sarracino et al. 2023, in preparation].

6.1 Field Equations for $f(R)$-Gravity

Let us derive the field equations for $f(R)$-Gravity starting from a variational principle. Neglecting the material component of the Lagrangian, the variation of the action reads as [46]

$$\delta \int \sqrt{-g} f(R) d^4x = 0, \tag{6.1}$$

where f can be any analytical function of the Ricci scalar R. We note that the main difference between this equation and the Einstein-Hilbert action is precisely in the presence of this function (we recall that, for GR, $f(R) = R$).

In a local reference frame, we find

$$\delta \int \sqrt{-g} f(R) d^4x = \int [\delta\sqrt{-g} f(R) + \sqrt{-g}\delta(f(R))] d^4x. \tag{6.2}$$

The right-hand side of this equation, using properties of the metric, can be rewritten as

$$\int \sqrt{-g}\left[f'(R)R_{\mu\nu} - \frac{1}{2}g_{\mu\nu}f(R)\right]\delta g^{\mu\nu} d^4x + \int \sqrt{-g} f'(R) g^{\mu\nu}\delta R_{\mu\nu} d^4x, \tag{6.3}$$

where the prime symbolizes a derivative with respect to R. Considering that we are working in an inertial reference frame, and the relation between the Ricci tensor and

Christoffel symbols $\Gamma^{\sigma}_{\alpha,\beta}$, we find

$$g^{\mu\nu}\delta R_{\mu\nu} = g^{\mu\nu}\partial_{\alpha}(\delta\Gamma^{\sigma}_{\mu\nu}) - g^{\mu\sigma}\partial_{\sigma}(\delta\Gamma^{\nu}_{\mu\nu}) = \partial_{\sigma}W^{\sigma}, \tag{6.4}$$

where we have defined

$$W^{\sigma} = g^{\mu\nu}\Gamma^{\sigma}_{\mu\nu} - g^{\mu\sigma}\Gamma^{\nu}_{\mu\nu}. \tag{6.5}$$

Using this definition in the second integral of Eq. (6.3), we find

$$\int \sqrt{-g}f'(R)g^{\mu\nu}\delta R_{\mu\nu}d^4x = \int \sqrt{-g}f'(R)\partial_{\sigma}W^{\sigma}d^4x. \tag{6.6}$$

Solving by parts and using the divergence theorem, we arrive at the following equation

$$\int \sqrt{-g}f'(R)g^{\mu\nu}\delta R_{\mu\nu}d^4x = -\int \partial_{\sigma}[\sqrt{-g}f'(R)]W^{\sigma}d^4x. \tag{6.7}$$

It is now necessary to explicate the factor W^{σ} in terms of the metric, which can be done using the properties of the Christoffel symbol. In doing so, we obtain [46]

$$W^{\sigma} = \partial^{\sigma}(g_{\mu\nu}\delta g^{\nu\mu}) - \partial^{\mu}(g_{\mu\nu}\delta g^{\sigma\nu}), \tag{6.8}$$

that we can insert in Eq. (6.7) to derive

$$\int \sqrt{-g}f'(R)g^{\mu\nu}\delta R_{\mu\nu}d^4x = \int \partial_{\sigma}[\sqrt{-g}f'(R)][\partial^{\mu}(g_{\mu\nu}\delta g^{\sigma\nu}) - \partial^{\sigma}(g_{\mu\nu}\delta g^{\nu\mu})]d^4x. \tag{6.9}$$

Integrating the previous equation by parts, and deleting null terms due to the divergence theorem, we find

$$\int \sqrt{-g}f'(R)g^{\mu\nu}\delta R_{\mu\nu}d^4x = \int g_{\mu\nu}\partial^{\sigma}\partial_{\sigma}[\sqrt{-g}f'(R)]\delta g^{\mu\nu}d^4x - \int g_{\mu\nu}\partial^{\mu}\partial_{\sigma}[\sqrt{-g}f'(R)]\delta g^{\sigma\nu}d^4x, \tag{6.10}$$

that we can finally substitute in Eq. (6.3) to obtain the expression for the variation of the action in $f(R)$-Gravity

$$\delta\int \sqrt{-g}f(R)d^4x = \int \sqrt{-g}\left[f'(R)R_{\mu\nu} - \frac{1}{2}g_{\mu\nu}f(R)\right]\delta g^{\mu\nu}d^4x + \int g_{\mu\nu}\partial^{\sigma}\partial_{\sigma}[\sqrt{-g}f'(R)]\delta g^{\mu\nu}d^4x - \int g_{\alpha\nu}\partial^{\mu}\partial_{\sigma}[\sqrt{-g}f'(R)]\delta g^{\mu\nu}d^4x. \tag{6.11}$$

For this variation to be 0, the integrand has to be null, so we must have

$$f'(R)R_{\mu\nu} - \frac{1}{2}f(R)g_{\mu\nu} = \nabla_\mu\nabla_\nu f'(R) - g_{\mu\nu}\Box f'(R), \tag{6.12}$$

where $\Box = g^{\mu\nu}\nabla_\mu\nabla_\nu$ is the d'Alembertian operator. These equations are the field equations for a general $f(R)$-Gravity theory without matter; as we can see, differently for the field equations of GR, which were of the second order, these are of the fourth order with respect to the metric. We also note that the field equations of GR are recovered in the particular case $f(R) = R$ [91]. The most straightforward class of these ETGs, which considers $f(R) = R + \alpha R^2$, has been applied for the inflationary paradigm, as already mentioned in Chapter 2 [45]. This equation can be rewritten as

$$G_{\mu\nu} = \frac{1}{f'(R)}\left[\frac{1}{2}(f(R) - f'(R) + f'(R)_{;\mu;\nu} - g_{\mu\nu}\Box f'(R)\right], \tag{6.13}$$

where $G_{\mu\nu}$ is the usual Einstein tensor and ";" is the covariant derivative. The last equation shows us how we can find a "geometrical" contribution to the impulse-energy tensor due to the further components found in Eq. (6.12) with respect to the GR ones.

Let us now consider the matter part of the Lagrangian, that we have not taken into account in the previous derivation. This is necessary because we wish to apply the $f(R)$-Gravity formalism to the stellar structure of non-compact objects, thus in situations in which the material term clearly cannot be neglected. In this case, the action becomes

$$\mathcal{A} = \int \sqrt{-g}[f(R) + \chi\mathcal{L}]d^4x = 0. \tag{6.14}$$

Deriving the field equations following the same procedure expressed before, we find

$$f'(R)R_{\mu\nu} - \frac{1}{2}f(R)g_{\mu\nu} - \nabla_\mu\nabla_\nu f'(R) + g_{\mu\nu}\Box f'(R) = \chi T_{\mu\nu}, \tag{6.15}$$

where we recall that $T_{\mu\nu}$ is the energy-momentum tensor, as defined in Eq. (2.9). Finally, we show the trace of Eq. (6.15), which shall be used in the computations that we are going to show in the next section

$$3\Box f'(R) + f'(R)R - 2f = \chi T. \tag{6.16}$$

6.2 The $f(R)$-Gravity stellar structure equations

We are interested in applying these equations to the structure of non-compact stars, thus in the Newtonian limit. In order to do so, we note that, because the function $f(R)$ is

analytical, we can expand it to the second order of the Taylor series. For this expansion, the Ricci scalar becomes [355, 356]

$$R \sim R^{(2)}(t, \bar{x}) + \mathcal{O}(4), \tag{6.17}$$

where $R^{(n)}$ denotes a quantity of order n; so the $n - th$ derivative of Ricci function can be developed as:

$$f^n(R) \sim f^n(R^{(2)}(t, \bar{x}) + \mathcal{O}(4)) \sim f^n(0) + f^{n+1}(0)R^{(2)} + \mathcal{O}(4). \tag{6.18}$$

Using this expansion and stopping at the lowest order of the fields in the trace equation (6.16), we note that we find $f(0) = 0$. This means that space-time is asymptotically Minkowskian and that we are discarding a cosmological constant term in this analysis, whose contribution is irrelevant at the stellar levels we wish to study. At these limits, the field equations become (taking $f'(0) = 1$ for simplicity):

$$\Delta\Phi + \frac{R^{(2)}}{2} + f''(0)\Delta R^{(2)} = -\chi\rho, \tag{6.19}$$

and

$$3f''(0)\Delta R^{(2)} + R^{(2)} = -\chi\rho, \tag{6.20}$$

where ρ is the energy density, Δ is the Laplacian in the flat space-time, and Φ is the gravitational potential. Eqs. (6.19) and (6.20) can be considered the modified Poisson equations for $f(R)$-Gravity. Indeed, for $f''(0) = 0$, we recover the Newtonian formulation, which we recall is

$$\Delta\Phi = 4\pi G\rho. \tag{6.21}$$

It is possible to show that at $\mathcal{O}(2)$ order [52]

$$R^{(2)} \simeq \frac{1}{2}\Delta g_{00}^{(2)} - \frac{1}{2}\Delta g_{ii}^{(2)}, \tag{6.22}$$

where $g_{00}^{(2)}$ and $g_{ii}^{(2)}$ are components of $g_{\alpha\beta}$ at the Newtonian order. This last equation can be rewritten as

$$R^{(2)} \simeq \Delta(\Phi - \Psi), \tag{6.23}$$

where Ψ is a second gravitational potential related to the components $g_{ii}^{(2)}$ [52]. Using this new potential, the modified Poisson equations become

$$\Delta\Phi + \Delta\Psi - 2f''(0)\Delta^2\Phi + 2f''(0)\Psi^2 = 2\chi\rho, \tag{6.24}$$

and

$$\Delta\Phi - \Delta\Psi + 3f''(0)\Delta^2\Phi - 3f''(0)\Psi^2 = -\chi\rho. \tag{6.25}$$

As previously stated, This system is equivalent to the mass conservation equation for $f(R)$-Gravity. The modified gravitational potential Φ can be computed in this limit, for which we have [357]

$$\Phi = -\frac{GM}{r} + \delta(t)\lambda^2\frac{e^{-r/\lambda}}{r}, \tag{6.26}$$

where $\lambda^2 = 6f''(0)$ and $\delta(t)$ is an arbitrary function of time. We here note that we find a Yukawa-like correction to the usual gravitational potential of the Newtonian theory, as we were mentioning in Chapter 2. This is relevant for different reasons: for instance, this property implies that in the Newtonian limit for $f(R)$-Gravity the Gauss theorem does not hold, because the force is not proportional to $|x|^{-2}$, which in turn means that the equivalence between a spherically symmetric distribution and point-like distribution having the same mass, typical of Newtonian dynamics, is not valid anymore [49].

As previously stated, we wish to apply this formalism to the stellar structure of non-compact objects. In turn, this implies that we have to find the stellar structure equations for $f(R)$-Gravity. We here recall these equations in the Newtonian formalism for static spherical stars [358]:

$$\frac{dP}{dr} = -\frac{GM}{r^2}\rho, \tag{6.27}$$

$$\frac{dM}{dr} = 4\pi r^2\rho, \tag{6.28}$$

$$\frac{dL}{dr} = 4\pi r^2\rho\epsilon, \tag{6.29}$$

$$\frac{dT}{dr} = -\frac{3}{4ac}\frac{K\rho}{T^3}\frac{L}{4\pi r^2} \tag{6.30}$$

$$= -\left(1 - \frac{1}{\gamma}\right)\frac{\mu m_H}{k}\frac{GM}{r^2}. \tag{6.31}$$

Eq. (6.27) expresses the hydrostatic equilibrium and shows that, in order to have a static star, a pressure gradient must exist to counteract the gravitational force. Eq. (6.28) is the mass conservation equation, that describes how the internal mass of the star must vary with the distance from the center. We have already found the analogous of this equation in $f(R)$-Gravity in Eqs. (6.24) and (6.25). Eq, (6.29) is the energy conservation equation, which links the luminosity of the star with its density via the ϵ parameter. Eqs. (6.30) and (6.31) are the energy transport equations, where Eq. (6.30) holds if the radiative transport dominates while Eq. (6.31) is valid if convention prevails. The form

presented here for Eq. (6.31) is true only in the adiabatic hypothesis [358].

In Eq. (6.29), ϵ is the energy generated per unit mass per second, and has different physical contributions: $\epsilon = \epsilon_g + \epsilon_n + \epsilon_\nu$, where ϵ_g is the gravitational energy contribution (which does not appear in the static configuration), ϵ_n is the energy produced by nuclear reactions and ϵ_ν is the energy transported by neutrinos. In Eq. (6.30) k is the Rosseland mean opacity [358] that accounts for all the possible physical absorption processes inside the star. Once we insert the physical inputs (which are the equation of state that links the pressure and the density, and the functional forms of the energy density and the opacity) and we define the appropriate boundary conditions, it is possible to solve this system to compute all the physical parameters of the star.

We also recall that in Newtonian theory, the gravitational potential is

$$\Phi = -\frac{GM}{r}, \tag{6.32}$$

from which we can see that Eq. (6.27) can be also written as:

$$\frac{dP}{dr} = \frac{d\Phi}{dr}\rho. \tag{6.33}$$

It is possible to show that the mass conservation equation (6.28) is equivalent to the Poisson Equation in spherical symmetry:

$$\frac{1}{r^2}\frac{d}{dr}\left(r^2\frac{d\Phi}{dr}\right) = 4\pi G\rho, \tag{6.34}$$

thus confirming the association between this particular equation and the modified Poisson equations previously introduced.

We will now find the hydrostatic equilibrium equation for GR which, as we shall see, is also viable in $f(R)$-Gravity if the Ricci scalar is constant, or depends only on the radial coordinate (i.e. time-independent, spherical symmetry and static configuration, which is the one studied in our analysis [91]). We start with the metric

$$ds^2 = e^{\nu(r)}c^2dt^2 - e^{\lambda(r)}dr^2 - r^2d\Omega^2, \tag{6.35}$$

where ν and λ are functions depending only on the radial coordinate. We note that, if we do not explicate these functions, the metric has the same form as what is employed for GR computations. We obtain [46]

$$\sqrt{-g} = e^{\frac{\nu+\mu}{2}}r^2 sin\theta. \tag{6.36}$$

Considering a perfect fluid in the rest frame we have

$$g_{\alpha\beta}u^{\alpha}u^{\beta} = 1, \tag{6.37}$$

and

$$u^{k} = 0. \tag{6.38}$$

Eq. (6.37) implies that

$$g_{00}(u^{0})^{2} = 1, \tag{6.39}$$

from which

$$u^{0} = \frac{1}{\sqrt{g_{00}}} = e^{-\frac{\nu}{2}}, \tag{6.40}$$

which means that the quadrivelocity vector is equal to [46]

$$u^{\alpha} = \left(e^{-\frac{\nu}{2}}, 0, 0, 0\right). \tag{6.41}$$

The energy-impulse tensor for a perfect fluid is equal to

$$T^{\alpha\beta} = (\epsilon + P)u^{\alpha}u^{\beta} - Pg^{\alpha\beta}. \tag{6.42}$$

Using the equations reported above, we can derive its expression for this particular case:

$$T^{\alpha\beta} = diag\left(\epsilon e^{-\nu}, Pe^{-\lambda}, \frac{P}{r^{2}}, \frac{P}{r^{2}sin\theta}\right), \tag{6.43}$$

and

$$T^{\alpha}_{\beta} = diag\big(\epsilon, -P, -P, -P\big). \tag{6.44}$$

Now we can write the energy conservation equation

$$T^{\beta}_{\alpha;\beta} = 0, \tag{6.45}$$

by considering the following relation valid for any symmetric tensor

$$T^{\beta}_{\alpha;\beta} = \frac{1}{\sqrt{-g}}\frac{\partial}{\partial x^{\beta}}\left(\sqrt{-g}T^{\beta}_{\alpha}\right) - \frac{1}{2}g_{\mu\nu,\alpha}T^{\mu\nu}. \tag{6.46}$$

Using all the previous equations for the energy-impulse tensor and the metric, it is possible to show that, from Eq. (6.46), in the case $\alpha = 1$, we can derive the following equation [46]

$$\frac{dP}{dr} = -\frac{1}{2}(\epsilon + P)\frac{d\nu}{dr}. \tag{6.47}$$

We would like to stress again how this derivation is valid both for GR and $f(R)$-Gravity, as long as we do not explicitly define the $\nu(r)$ and $\lambda(r)$ functions in the metric. This is relevant also for the discussion regarding the Jordan and Einstein frames applied to ETGs [11]. Indeed, we note how in the Jordan Frame, where we modify the geometrical part of the Einstein equations (in this case by considering a function of the Ricci scalar) while keeping the material one unvaried, the hydrostatic equation is not modified by the effects of extended gravity, while this is not true in the Einstein frame, where, conversely, we modify only the material part, keeping the geometrical portion unvaried by transforming the action in such a way that we eliminate the explicit dependence on new fields, and so we add more terms to the energy-impulse tensor giving the hydrostatic equilibrium equation, in general, a different form.

In the Newtonian limit, $\epsilon \simeq \rho c^2 >> P$ and $\nu \simeq \frac{2\Phi}{c^2}$ [46], where in this case Φ is the modified gravitational potential for $f(R)$-Gravity previously introduced. This implies that, as long as we do not explicitly write down the gravitational potential, the form of the hydrostatic equilibrium equation is the same for GR and $f(R)$-Gravity also in the weak field limit.

We now analyze the last three equations of the stellar structure system. Because we are modifying only the gravitational part of the physics inside the star, while the nuclear, optical, and thermodynamical phenomena are unaffected by this modification (at least at the first level), we do not expect these equations to change their form, if we express them in term of the modified gravitational potential given by $f(R)$-Gravity.

Using the definition of ϵ ($\epsilon = dL/dm$, where dm is the infinitesimal mass) [358], we can see that the luminosity equation remains unvaried in $f(R)$-Gravity

$$\frac{dL}{dr} = 4\pi r^2 \rho \epsilon. \tag{6.48}$$

The first energy transport equation does not change because only the luminosity appears as a quantity depending on the rest of the system, while we can manipulate the second equation concerning convection using Eq. (6.32) to obtain

$$\frac{dT}{dr} = -\left(1 - \frac{1}{\gamma}\right)\frac{\mu m_H}{k}\frac{d\Phi}{dr}, \tag{6.49}$$

that is valid for $f(R)$-Gravity because of the hydrostatic equilibrium equation.

In conclusion, the stellar structure system for a static, spherical symmetric non-compact star in $f(R)$-Gravity is

$$\frac{dP}{dr} = -\frac{d\Phi}{dr}\rho, \tag{6.50}$$

$$\Delta\Phi + \Delta\Psi - 2f''(0)\Delta^2\Phi + 2f''(0)\Delta^2\Psi = 2\chi\rho, \tag{6.51}$$

$$\Delta\Phi - \Delta\Psi + 3f''(0)\Delta^2\Phi - 3f''(0)\Delta^2\Psi = -\chi\rho, \tag{6.52}$$

$$\frac{dL}{dr} = 4\pi r^2 \rho\epsilon, \tag{6.53}$$

$$\frac{dT}{dr} = -\frac{3}{4ac}\frac{K\rho}{T^3}\frac{L}{4\pi r^2} \tag{6.54}$$

$$= -\left(1 - \frac{1}{\gamma}\right)\frac{\mu m_H}{k}\frac{d\Phi}{dr}. \tag{6.55}$$

We can see that we have one more equation with respect to the GR system, which is linked to the modified Poisson Equation, and the correction brought by the gravitational potential. In general, both the GR and $f(R)$-Gravity systems have to be solved numerically by introducing further physical information, like the opacity and the energy generation form inside the stellar structure, but, if we assume that the pressure depends only on the density, we can divide this system into two different sub-systems: the first, composed of Eqs. (6.19, 6.20, 6.33), represents the mechanical part of the physics inside the star; while the second, formed by the remaining equations, gives the thermodynamical and optical parts [47]. This assumption is used in what follows in this chapter.

6.3 The Lane-Emden equations for GR and $f(R)$-Gravity

We now introduce the Lane-Emden equations for GR and the derivation for the equivalent equations in $f(R)$-Gravity. We start from the polytropic assumption, according to which the pressure and the density of the stellar object are related by the following formula

$$P = K\rho^{\gamma} = K\rho^{1+\frac{1}{n}}, \tag{6.56}$$

where K is the polytropic constant, and γ the polytropic exponent. Instead of γ, it is conventionally used the polytropic index n in the literature, defined as

$$n = \frac{1}{\gamma - 1}. \tag{6.57}$$

For GR, introducing this relation in the hydrostatic equilibrium equation (6.27) allows us to obtain [47]

$$\frac{d\Phi}{dr} = -\gamma K\rho^{\gamma-2}\frac{d\rho}{dr}. \tag{6.58}$$

If $\gamma \neq 1$ (that is the case of isothermal spheres of an ideal gas) this equation can be integrated

$$\rho = \left(\frac{-\Phi}{(n+1)K}\right)^n. \tag{6.59}$$

If we now introduce the previous equation in the right-hand side of the Poisson Equation (6.21) we find an ordinary differential equation for Φ

$$\frac{d^2\Phi}{dr^2} + \frac{2}{r}\frac{d\Phi}{dr} = 4\pi G\left(\frac{-\Phi}{(n+1)K}\right)^n. \tag{6.60}$$

We now define two dimensionless variables, z and w, as:

$$z = Ar, \tag{6.61}$$

$$A^2 = \frac{4\pi G}{(n+1)^n K^2}(-\Phi_c)^{n-1} = \frac{4\pi G}{(n+1)K}\rho_c^{\frac{n-1}{n}}, \tag{6.62}$$

$$w = \frac{\Phi}{\Phi_c} = \left(\frac{\rho}{\rho_c}\right)^{1/n}, \tag{6.63}$$

where Φ_c and ρ_c are the gravitational potential and the density at the center of the star, respectively. Thus, z and w are two dimensionless quantities, the former representing the radius of the star, while the latter the gravitational potential. At the center of the star, we have $z = 0$ and $w = 1$. Using these new variables we obtain

$$\frac{1}{z^2}\frac{d}{dz}\left(z^2\frac{dw}{dz}\right) + w^n = 0. \tag{6.64}$$

The previous equation is the so-called Lane-Emden for GR, which allows us to describe the stellar structure of the stars under the polytropic assumption. Indeed, once solved, it is possible to reintroduce the dimensional quantities to derive parameters like for instance the central density and the radius of the star. This equation presents analytical solutions for three values of the polytropic index:

$$n = 0 : w(z) = 1 - \frac{1}{6}z^2 \tag{6.65}$$

$$n = 1 : w(z) = \frac{sin(z)}{z} \tag{6.66}$$

$$n = 5 : w(z) = \frac{1}{(1 + z^2/3)^{1/2}}. \tag{6.67}$$

while, for the other values, a numerical approach is required [47], we also note that $n = 5$ is the upper limit of the polytropic index for which we may find a physical solution, given that it represents the limit between finite and infinite solutions.

We now aim to find the corresponding equations for $f(R)-$Gravity, starting from the same polytropic assumption [49, 48]. We recall that this time we need to use the modified Poisson equations (6.19, 6.20), while the form for the hydrostatic equation remains the same as that regarding GR, as previously demonstrated. In doing so, we obtain, defining

$m^2 = -1/3f''(0)$:

$$(\Delta - m^2)R^{(2)} = \chi m^2 \rho. \tag{6.68}$$

This equation can be solved by using the Green function method [356], from which we find

$$R^{(2)} = A_n \chi m^2 \int d^3x' G(\bar{x}, \bar{x}') \Phi^n(x'). \tag{6.69}$$

It is possible to show that there are two choices of Green functions for spherically symmetric systems [359], which are

$$G(\bar{x}, \bar{x}') = -\frac{1}{4\pi} \frac{e^{-m|x-x'|}}{|x-x'|}, \tag{6.70}$$

for $m^2 > 0$ and

$$G(\bar{x}, \bar{x}') = C_1 \frac{e^{-im|x-x'|}}{|x-x'|} + C_2 \frac{e^{im|x-x'|}}{|x-x'|}, \tag{6.71}$$

for $m^2 < 0$, where $C_1 + C_2 = -\frac{1}{4\pi}$. Considering Eq. (6.70) we obtain the first Modified Lane-Emden (MLE) Equation:

$$\frac{d^2w}{dz^2} + \frac{2}{z}\frac{dw}{dz} + w^n = \frac{m\xi_0}{8}\frac{1}{z}\int_0^{\xi/\xi_0} dz' z' \left[e^{-m\xi_0|z-z'|} - e^{-m\xi_0|z+z'|}\right] w(z')^n, \tag{6.72}$$

where

$$z = \frac{|x|}{\xi_0}; \quad w(z) = \frac{\Phi}{\Phi_c}; \quad \xi_0 = \sqrt{\frac{3}{2\chi A \Phi_c^{n-1}}}; \quad A^2 = \frac{4\pi G \rho_c}{K}. \tag{6.73}$$

Φ_c and ρ_c are the gravitational potential and the density in the center of the star, respectively, while n is the polytropic index.

Instead, using Eq. (6.71) we obtain

$$\frac{d^2w}{dz^2} + \frac{2}{z}\frac{dw}{dz} + w^n = \frac{m\xi_0}{8}\frac{1}{z}\int_0^{\xi/\xi_0} dz' z' \left[e^{-im\xi_0|z-z'|} - e^{-im\xi_0|z+z'|}\right] w(z')^n. \tag{6.74}$$

The boundary conditions of Eqs. (6.72) and (6.74) are $w(0) = 1$ and $w'(0) = 1$.

The difference between Eqs. (6.74) and (6.72) is the presence of the imaginary unit in the exponential functions, which can be used to represent oscillating behaviors. The correction brought by $f(R)$-Gravity with respect to GR is regulated by the $m\xi_0$ value, while the difference between these two equations and the corresponding ones for GR is in the fact that these have an integro-differential form, with the integral part regulated by the scale factor $m\xi_0$, which depends both on the physical features of the studied object as well as on the particular weak field limit of the studied $f(R)$-Gravity theory.

These equations can be solved analytically only for $n = 0$ and $n = 1$ [49], and only following particular assumptions for the latter index. For all the other values of the polytropic index, they have to be solved numerically.

6.4 Numerical solutions of the MLE Equations

A numerical solution has been computed for the Lane-Emden Equations for both GR and $f(R)-$Gravity. In order to do so, we follow the procedure shown in [48]. This is based on an iterative algorithm, which can be written as

$$\frac{d^2w_i}{dz^2} + \frac{2}{z}\frac{dw_i}{dz} + w_i^n = \frac{m\xi_0}{8z}\mathcal{N}[w_{i-1}], \tag{6.75}$$

where in the right hand of the equation we are using the function w_{i-1} computed at the $(i-1)^{th}$ iteration. For this algorithm, this term can be considered as a source term of a nonlinear second-order differential equation. We can now rewrite the equation as a system of two first-order differential equations:

$$\begin{aligned} \frac{dw_i}{dz} &= k_i, \\ \frac{dk_i}{dz} &= -\frac{2}{z}k_i - w_i^n + \frac{m\xi_0}{8z}\mathcal{N}[w_{i-1}], \end{aligned} \tag{6.76}$$

with boundary conditions $w_i(0) = 1$ and $k_i(0) = 1$. For the first step, we set $w_0 = 1$ as a starting point. This system has to be solved until convergence is reached, which in our case happened after 5 iterations.

The solution of Eqs. (6.75) and (6.76) at the i^{th} iteration can be obtained via a coupled 4th order Runge-Kutta integration method, up to the value $z_{max} = \xi/\xi_0$, with the aforementioned initial conditions. This is a numerical procedure generalizing the Euler Method. The integral represented by $\mathcal{N}[w(z')]$ can be solved using the Gauss-Legendre quadrature, because of the smooth and regular behavior of the function $w(z)$, according to the definition

$$\int_0^{\xi/\xi_0} f(z)dz \sim \frac{\xi}{2\xi_0}\sum_{j=1}^{n} q(z_j) f\left(\frac{\xi}{2\xi_0}z_j + \frac{\xi}{2\xi_0}\right), \tag{6.77}$$

where

$$q(z_j) = \frac{2}{(1-z_j^2)[P_n(z_j]^2}, \tag{6.78}$$

are the weights, z_j are the j^{th} roots of the Legendre polynomial $P_n(z_j)$, and n is the total number of the nodes. As it is built, such a quadrature rule provides an exact result

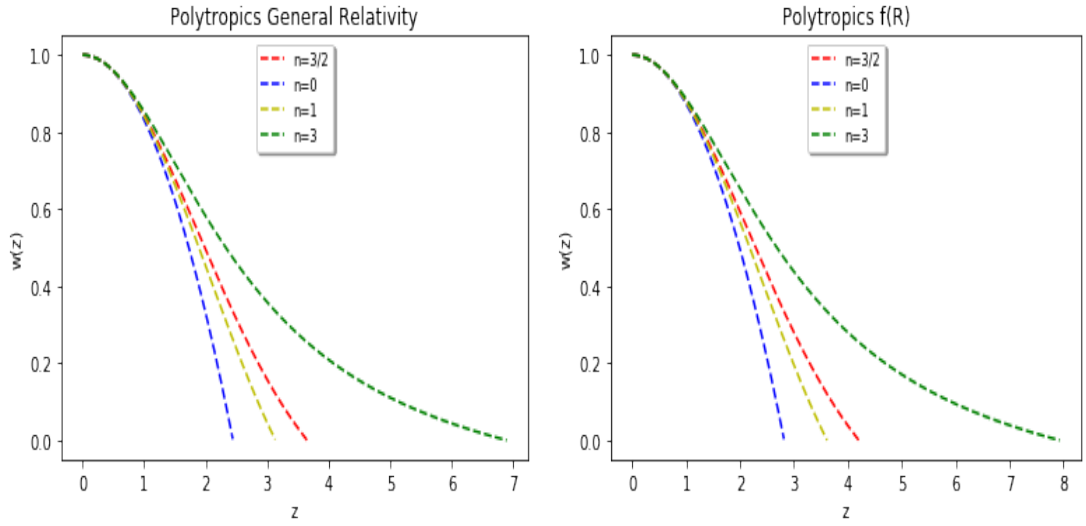

Figure 6.1: Left panel: solutions of the Lane-Emden equation in GR for the values of the polytropic index considered. Here $m\xi_0 = 0$. Right panel: the same for $f(R)$-Gravity. Here $m\xi_0 = 1$.

for polynomials of degree $2n - 1$ or less, and it is the more precise the more $f(z)$ is well-approximated by these polynomials.

The two input parameters are the polytropic index n and the product $m\xi_0$; the latter is linked to the correction brought by $f(R)$-Gravity, (in fact, as previously stated, $1/m\xi_0$ defines the characteristic scale of the correction to the Newtonian potential, which has a Yukawa-like form for Eq. (6.72) and an oscillating behavior for Eq. (6.74)). The dimensionless radius of the star $z_{max} = \xi/\xi_0$ is not a free parameter given by hand but is derived from the solution considering the point where the function $w(z)$ reaches 0.

Using this algorithm, we have solved the MLE equations taking into account $m\xi_0 = 1$. We have computed the solutions for GR as well, which we recall is recovered by taking $m\xi_0 = 0$. We have chosen to solve these equations for $n = 0; 1; 3/2;$ and 3. This is because the most interesting cases from a physical point of view are $n = 3/2$ and $n = 3$, which are the indexes able to schematize the degenerate electron structure in white dwarfs in non-relativistic and relativistic environments [47] and have been also used for the stellar structure of main sequence stars like the Sun [358]. A first comparison is shown in Figure (6.1), where we see the polytropic functions found for GR in the left panel, and those derived for $f(R)$-Gravity, for Eq. (6.72), in the right panel.

Let us now discuss these first results. We recall that z is the dimensionless radius while $w(z)$ is the dimensionless gravitational potential inside the star. A direct comparison with the GR case displays that, in $f(R)$-Gravity, the polytropic functions are wider. In particular, in such theories, the maximum dimensionless radius of the star, represented by the point where $w(z_{max}) = 0$, is bigger than the corresponding radius in GR, derived

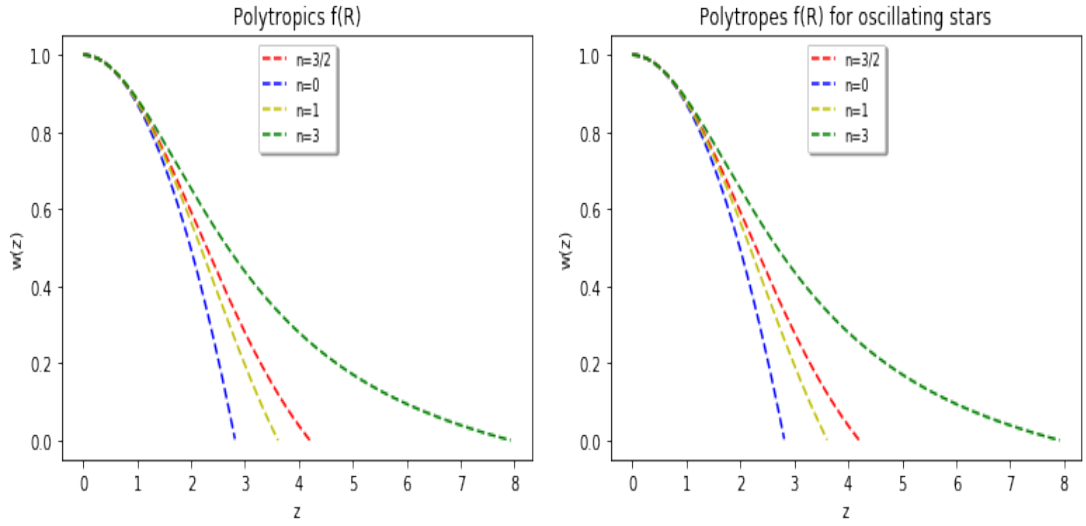

Figure 6.2: Left panel: Solutions of the MLE equation in $f(R)$-Gravity for the values of the polytropic index considered. Here $m\xi_0 = 1$ (the same plot presented in the right panel of Figure 6.1). Right panel: the same solutions for the Second MLE with oscillating behavior.

from the same initial conditions. We also note that the difference between these two theories grows with the value of the polytropic index n. The direct conclusion that we can infer from these plots is that, given the same initial conditions, $f(R)$-Gravity allows for wider stars than those represented by GR. We also note that, as we shall see, this difference depends on the scale factor $m\xi_0$.

We now present a second comparison, between the numerical solutions of the two possible MLE equations, which are shown in Figure 6.2, wherein the left panel we show the solutions for Eq. (6.72) (the ones already shown in Figure (6.1)), while on the right we see the solutions for Eq. (6.74). Comparing the results obtained from these two equations, we can see that they coincide for $m\xi_0 = 1$ (apart from some very slight differences for $n = 3$ and $n = 3/2$). This means that we can include stellar structures having an oscillating behavior (schematized by the oscillating potential shown in Eq. (6.74)) in the solutions obtained by our theoretical scheme.

The differences between the results given by GR and $f(R)$-Gravity depend on the value chosen for $m\xi_0$. A substantial variation appears if we choose $10^{-4} \leq L_y/\xi_0 \leq 1$, with $L_y = 1/m$ [48], where the radius computed by the $f(R)$-Gravity model is consistently bigger than the value provided by GR, as shown in Figure 6.1. We can consider L_y/ξ_0 as a new length scale that quantifies the correction brought by $f(R)$-Gravity to the results derived by GR, that we recover outside this interval.

6.5 Physical results

Having found the polytropic functions for both GR and $f(R)-$Gravity, our goal now is to use these functions to find physical parameters defining the stars, looking for differences characterizing these two theories. The first two parameters are the mass and the gravitational energy of the stellar object, which in general are defined as

$$M = \int_0^R \rho(\bar{x}) d\bar{x}, \tag{6.79}$$

and

$$E_g = \int_0^R \Phi(\bar{x})\rho(\bar{x}) d\bar{x}. \tag{6.80}$$

Recalling that we have $\Phi = w\Phi_c$, $\Phi_c = \rho_c^{1/n}(n+1)K$ and $\rho = \rho_c w^n$, these two equations can be rewritten as

$$M = 4\pi\xi_0^3\rho_c \int_0^{z_{max}} w^n z^2 dz, \tag{6.81}$$

and

$$E_g = -4\pi\xi_0^3(n+1)K\rho_c^{1/n+1} \int_0^{z_{max}} w^{n+1} z^2 dz. \tag{6.82}$$

For GR, it is possible to prove that these two equations can be solved analytically to obtain

$$M = 4\pi\rho_c R^3 \left(-\frac{1}{z}\frac{dw}{dz}\right)_{z=z_{max}}, \tag{6.83}$$

and

$$E_g = -\frac{3}{5-n}\frac{GM^2}{R}. \tag{6.84}$$

While for $f(R)-$Gravity they need to be solved numerically [48]. A direct comparison between these quantities in GR and $f(R)-$Gravity may be performed by deriving the ratios, defined as

$$\frac{M_{f(R)}}{M_{GR}} = \frac{\int_0^{z_{max}} w_{f(R)}^n z^2 dz}{\int_0^{z_{max}} w_{GR}^n z^2 dz}, \tag{6.85}$$

and

$$\frac{E_{f(R)}^g}{E_{GR}^g} = \frac{\int_0^{z_{max}} w_{f(R)}^{n+1} z^2 dz}{\int_0^{z_{max}} w_{GR}^{n+1} z^2 dz}. \tag{6.86}$$

This computation, performed in [48], shows that for the $m\xi_0$ values for which the radius computed by the two theories differ substantially, the mass and the gravitational binding energy provided by $f(R)$-Gravity can be up 50% bigger than the corresponding GR case [48], while outside this interval there is not a difference between these two theories. This conclusion is valid both in the oscillating and non-oscillating cases, given

their similarities. These results tell us that it is possible to include very massive structures in the theoretical scheme given by $f(R)$-Gravity, which cannot be considered by the corresponding GR case, as it has already been noted by the wider dimensionless radii found in the previous section. We also stress that we can recover the GR results for the opportune values of $m\xi_0$.

The free parameters that act as the starting points of our derivations of the other observed quantities of the stars are the central density, ρ_c, the polytropic index, n, and the polytropic constant, K. We note that, inside the ratios given in Eqs. (6.85) and (6.86) these parameters do not appear, making these ratios independent from them.

Another quantity that can be derived from Eqs. (6.72) and (6.74) is the radius of the star, defined as $R = \xi_0 z_{max}$. Using a luminosity-mass relation (we here refer to the formula shown in [360]), it is possible to estimate from our model the stellar luminosity. Furthermore, we can also be able to compute the period of an oscillating star, starting from a period-mass-luminosity relation of the following form [361]

$$P \approx \left(\frac{R}{R_\odot}\right)^{3/2}\left(\frac{M}{M_\odot}\right)^{-1/2}. \tag{6.87}$$

The last equation can be derived from the virial theorem starting from the Newtonian gravitational potential, thus we can apply similar reasoning to $f(R)-$Gravity starting from Eq. (6.26) and deriving the corresponding period-luminosity relation. For the modified potential, we consider $m^2 = 2/\lambda^2$, $m = L/\xi_0$ and choose the arbitrary function of time δ to be

$$\delta(t) = -\frac{qGM}{\xi_0^2}, \tag{6.88}$$

for dimensional reasons, where q is an arbitrary dimensionless constant. The presence of this parameter allows us to recover the results given by GR as well as modify them. Choosing $q = 30$, we find that the modified gravitational potential becomes

$$\Phi = -\frac{GM}{r}\left(1 + \frac{10e^{-\frac{rL}{\sqrt{2}\xi_0}}}{L^2}\right). \tag{6.89}$$

Plugging this equation into the virial theorem and deriving from that the period-mass-radius relation, we get a correction to the computed period equal to

$$P_1 = P_0\left(1 + \frac{10e^{-\frac{rL}{\sqrt{2}\xi_0}}}{L^2}\right)^{-1/2}, \tag{6.90}$$

where P_0 is the period computed from the Newtonian potential in GR. We found that the magnitude of this correction does not depend on the free values of ρ_c and K, but only on

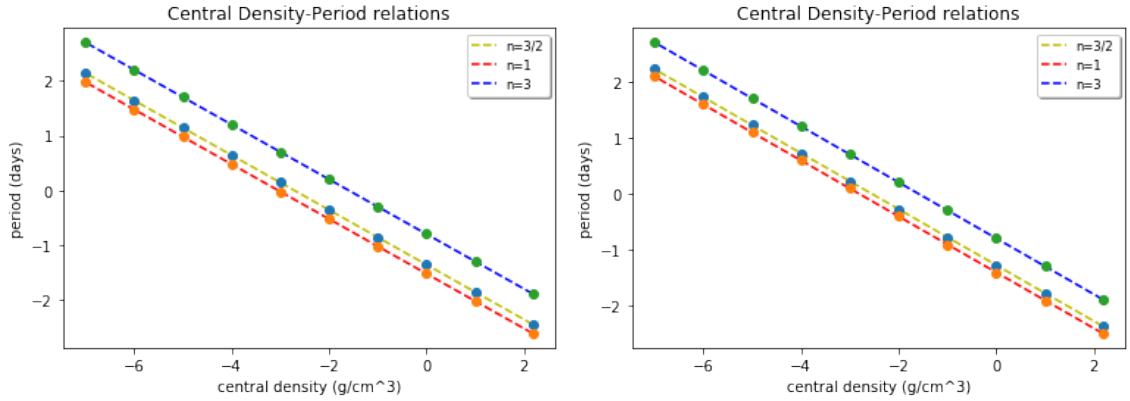

Figure 6.3: Left panel: central density-period relation for $f(R)$-Gravity for different values of the polytropic index. Right panel: the same for GR. Both plots are on a logarithmic scale.

the polytropic index: in particular, the total period becomes smaller, decreasing of 18.6% for $n = 3/2$, of 24.9% for $n = 1$ and of 1.79% for $n = 3$. Of course, these results depend on the form of δ chosen as well as on the value of q.

Varying the initial values of ρ_c, K, and n, we have used the model explained above to compute mass, luminosity, radius, and period for both GR and $f(R)$-Gravity, by fixing $m\xi_0 = 1$ as in the previous section for the polytropic computations, and both for the results of Eqs. (6.72) and (6.74). The main conclusions achieved in our analysis are the following:

- The period does not depend on K, but only on ρ_c and n.
- For $n = 1$, the radius does not vary with ρ_c, but it depends only on K.
- For $n = 3$, the mass and the luminosity do not change with ρ_c, but only with K.
- For $n = 3/2$, decreasing ρ_c by a factor of 10^3 has the same effect as increasing K by a factor of 10.

These conclusions can be applied both for GR and $f(R)$-Gravity. Regarding the differences between the oscillating and non-oscillating solutions for the $f(R)$-Gravity model, we note that very slight variations (the biggest discrepancy is of the order of 10^{-2}) arise between the physical parameters computed in these two situations. This is consistent with the results reached in the previous section, shown in Figure 6.2, according to which the solutions of the two MLE equations are very similar.

In Figure 6.3 the central density-period relation computed by our model is shown both for $f(R)$-Gravity (left panel) and GR (right panel) for different values of n. We note the linear behavior (in log scale). We also note how, given the same value of the central

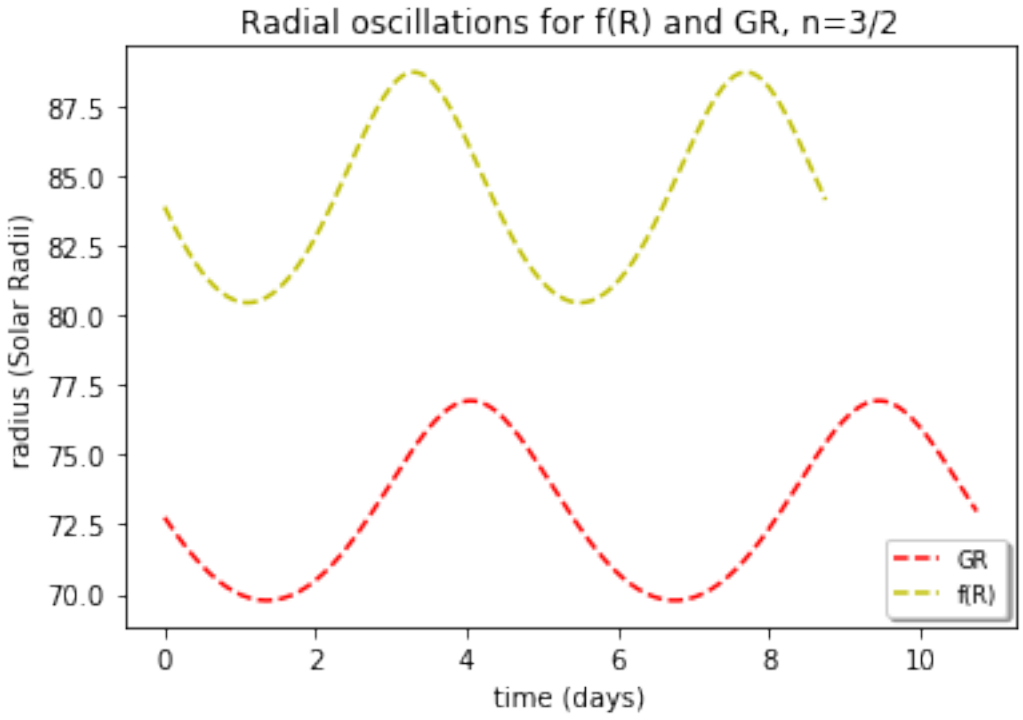

Figure 6.4: The oscillations of the radius computed by our model during two periods. This plot shows both GR and $f(R)$-Gravity results.

density, the computed periods for $f(R)-$Gravity are slightly smaller than the respective ones for GR. The differences in the periods computed by these models shown in Figure 6.3 exist because of both the correction on the period itself given by Eq. (6.90) as well as on the different physical parameters derived by the solutions shown in Figure 6.1.

We next introduce a periodic variable behavior in our initial coefficients, to compute how much our physical parameters, in particular the radius, change during a period for a variable star. Starting from a particular initial condition for our parameters (ρ_c, K) and computing from that the radius and the period, we simulate a sinusoidal behavior for the central density and determine how much the radius of the stellar object changes with ρ_c. To obtain a radial variability of around 10% (which is what is typically observed for Cepheid variables, see [362]) we have to start from a 57% variability on the central density. For $n = 3/2$, the results are shown in Figure 6.4 both for GR and $f(R)$-Gravity. The main conclusions that we derive from this figure are the following:

- The period for the result given by $f(R)$-Gravity is smaller than what has been derived by GR. This is because of the correction on the period shown in Eq. (6.90).
- The starting values of the radii for $f(R)$-Gravity and GR are different, even if the same initial conditions are used. This is because of the different solutions given by the Lane-Emden and MLE equations, respectively.

- The curves are not symmetrical around the starting values, but the maxima are further from them than the minima. This behavior is consistent with the real light curves of Cepheids [363].
- The amplitudes of the curves are different, being the ones related to the $f(R)$-Gravity bigger than the same variations computed for GR.

The results of our $f(R)$-Gravity model are able to reproduce real data related to observed oscillating stars: for instance, the values obtained for our variability example: ($R = 83.9\,R_{\odot}$, $M = 6.95\,M_{\odot}$, $L = 2169\,L_{\odot}$, $P = 4.39\,d$) are comparable with those observed for the Classical Cepheid Eta Aquilae A ($R = 66 \pm 22\,R_{\odot}$, $M = 5.7\,M_{\odot}$, $L = 2630\,L_{\odot}$, $P = 7.18\,d$ [364, 365]). This is not a coincidence because of our freedom in choosing the initial parameters, for which we could also recover the GR results.

Even if the results achieved have been considering a rather simple model for oscillating stars, we can note how interesting differences arise in the computed physical parameters of the stellar structures. As possible future investigations, it would be interesting quantifying these differences using more realistic models for the structure and general behavior of variable stars, like Classical Cepheids and RR Lyrae [366, 367, 368].

Chapter 7

Discussion and conclusions

In this thesis, we have studied different frontiers of astrophysics and cosmology, both observational and theoretical. Indeed, from the observational point of view, we have studied a novel cosmological tool, the GRBs, that would allow us to explore deep zones of the Universe, unreachable by more standard cosmological probes like SNe Ia. We have first studied a particular correlation, the so-called fundamental plane relation for GRBs, between three physical features of these astrophysical objects, namely between the X-ray rest-frame end time of the plateau T_a^*, its correspondent luminosity L_a, and the peak prompt luminosity, L_{peak}, considering, for the X-rays, a set of 222 GRBs chosen between those observed by the Swift satellite. As a starting point, we have divided these GRBs into different classes according to their features, highlighting the new definition of the Platinum sample, which is a set of Long GRBs with very strictly defined qualities, as well as the results obtained using the sets of GRBs associated with KNe and SNe. We have computed the best-fit parameters of the fundamental plane correlation for each subclass. We found that the smallest intrinsic scatter related to the best-fit correlations, one for every subset, has been achieved for the three sets previously mentioned in this paragraph.

This result has been confirmed also after we considered corrections due to selection biases and redshift evolution via the so-called EP statistical method. Thus, this result allowed us to conclude that, between the different subclasses studied, the Platinum, the GRB-KNe, and GRB-SNe a/b/c sets are the most suitable ones to be used for cosmological applications, at least for the criteria related to the tightness of the best-fit plane. We also note that accounting for the selection biases and redshift evolutionary effects reduces the intrinsic scatter for these sets, especially for the Platinum sample.

We have also studied the differences between the best-fit fundamental plane parameters for the subclasses considered by computing the z-scores of each of them with respect to the Gold sample, a set of Long GRBs from which the Platinum has been derived. We

note how some statistically significant differences have been found between some sets, as we may note from the Gold sample vs. the GRB-KNe comparison, from which we can conclude that the fundamental plane correlation can be used also as a tool to discern between different subclasses, thus linking observational features and correlations involving GRB observed quantities to their intrinsic physics, like the central engine or the nature of their progenitors.

This study has then been refined from a statistical point of view, focusing on the Platinum sample itself, by computing new evolutionary coefficients using the EP method for the entire set of 222 GRBs, and by using alternative best-fit methods as a reliability check for our results regarding the fundamental plane and its intrinsic scatter. The new correction has allowed us to reach effectively one of the smallest intrinsic scatter in the literature regarding GRBs correlations up to date, especially for relations involving afterglow features, while further statistical studies, based on other Bayesian approaches as well as on PCA analysis, show a comfortable concordance with the results obtained using the D'Agostini method.

All the aforementioned analysis allowed us to conclude that, regarding the X-ray observations, the Platinum sample is the most appropriate to be used as a baseline for our cosmological application of GRBs. The fundamental plane correlation has also been studied in the optical wavelengths, allowing us to study possible cosmological methodologies also in this new light window. Indeed, cosmological computations have been carried out both via simulations and with real GRBs data, used as standalone probes for the former and together with SNe Ia and BAO data for the latter.

Regarding the simulations, our goal was to find how many GRBs would be needed lying exactly on the best-fit fundamental plane of real GRB data, in order to find a precision on Ω_M comparable with what has been computed using SNe Ia by different works in the literature, and thus finding an approximate timetable for the future concerning the standalone GRB cosmology based on the fundamental plane correlation. We have done so with both the Platinum X-ray sample and the Optical set, and both considering the full errors on the parameters used as the baseline for our simulated distributions and halving them, supposing that an increasing precision shall be reached in the future.

We found out that, in general, decreasing the errors used as a baseline for our simulations does indeed help the convergence of the simulation themselves, requiring a smaller number of simulated GRBs to reach the prefixed thresholds on the precision regarding Ω_M. We have also noted that, surprisingly, the simulations performed starting from the Optical sample as the baseline converge faster than those which have been computed considering the X-ray set, even if all the selection criteria used for the latter could not be considered for the former given the paucity of data points. This interesting result could

hint at the possibility that optical GRBs are indeed the future preferred path for their general application as cosmological tools. As a baseline of our simulations, we have also used trimmed sub-sets of the Platinum and Optical samples. In particular, we have selected the 10 closest X-rays and optical GRBs, so that the best-fit fundamental plane presents an intrinsic scatter close to 0 (the "a priori" trimming), as well as an alternative, "a posteriori" trimming, based on further simulations, whose aim was to find out how many real GRBs, used as a baseline, would yield the highest precision on Ω_M given the same number of simulated GRBs, without halving the errors. For the latter computations, we have found two sets of 20 X-rays and 25 optical GRBs, respectively. In doing so, we concluded that, in general, the a priori trimmed sample gives comparable prediction with respect to the derivations obtained by using the entire sets as a baseline, while the a posteriori derivations generally improve such predictions, giving a higher precision for the same number of simulated GRBs in all cases where we do not halve the errors and, thus, reaching the desired precision faster.

Using these simulations, we have derived, via a polynomial fit, exactly how many GRBs would be needed to match the imposed thresholds, from which we derive the expected number of years in which these limits would be reached. In order to do so, we have considered the number of detected GRBs per year from the Swift missions, as well as from future telescopes, such as SVOM and Theseus. We have also taken into account the possibility of using machine learning techniques to halve the required number of GRB detected with an observable redshift, as well as statistical LC reconstruction methods to decrease the error bars on the physical quantities used in our correlations. The results show that in general, the next decades will be very fruitful for the use of GRBs as standalone cosmological probes, which should be able to match the same precision achieved by the SNe Ia without depending on the previous steps of the cosmological ladder, and without being dependent of the so-called circularity problem.

We now move to the cosmological computations related to the real GRBs data, used together with other probes, more specifically SNe Ia and BAO. We first compute Ω_M using the entire sets, as well as the a priori trimmed sub-samples, of Optical and Platinum GRBs, with SNe Ia, finding values for the errors which are the same (or slightly smaller) than the results derived considering SNe Ia alone.

Next, we focus on the Platinum sample, which represents the currently most studied wavelength concerning GRBs afterglows. We use the entire set and add also BAO data to derive Ω_M, H_0, and both these quantities contemporaneously. The first results, in which we use the entire BAO and SNe IA sets, show that considering the SNe Ia alone achieved precision as a reference point, the highest beneficial effect related to the precision of the cosmological derivations is achieved by adding the BAO to the SNe Ia. We also note

that adding GRBs allows us to obtain comparable, or even slightly smaller, uncertainties. Keeping in mind that the GRBs belonging to the Platinum sample explore regions going up to $z = 5$, this result shows the beneficial effect of adding GRBs to the other cosmological probes, offering the possibility of exploring deeper parts of the Universe without sacrificing the precision on the results. This is true both with and without considering the corrections due to selection biases and evolutionary effects. We have also employed two different BAO sets, to fortify even more the reliability of our analysis and compare the precision achieved by the two samples.

We further studied the contribution of the GRBs to our results by dividing our samples into 5 bins, in order of increasing redshift, so that each of the bins presents the same number of SNe Ia belonging to the Pantheon sample (with the only exception of Bin 5, which presents 3 more SNe Ia with respect to the others). Incidentally, all the GRBs belong to the last bin, together with 11 out of the 16 BAO-related measurements. Thus, this binning division allows us to further appreciate the contribution of the other probes to the SNe Ia results, even if the SNe Ia themselves are still the majority of the data points in each of the bins (more than 200 in each of them).

The computations performed using the binned analysis confirm the conclusions reached using the entire sets, namely that the most relevant contribution to the precision of the results (taking again the results attained by the SNe Ia as a reference point) has been achieved by adding the BAO measurements to the SNe Ia data, with the addition of GRBs marginally influencing the precision already obtained by the SNe Ia+ BAO sets, both with and without considering the correction for evolutionary effects. More in detail, the biggest improvements have been reached when we consider bins 4 and 5, where we find more BAO and GRBs. This conclusion has been reached for all the computations performed and for all the cosmological parameters. Thus, the findings obtained for the full samples still stand, keeping in mind that future GRB missions and observational campaigns will decrease the uncertainties of the observed quantities, as well as increase the number of detected GRBs, as we have seen from the discussion related to the simulations. We have also studied possible calibration results of GRBs, fixing the parameters of the correlation using GRBs in the same redshift range of SNe Ia and deriving from those cosmological results, finding, in general, encouraging results for the future of GRB cosmology.

We now move from an observational frontier of cosmology to a more theoretical one (albeit still using SNe Ia and BAO data sets). One reason why the scientific community is interested in finding more cosmological probes is to fix the tensions brought by the ΛCDM standard cosmological model (or at least find the underlying physics behind such tensions). We now go beyond this model and start questioning some of the fundamental

assumptions on which is based. One possible game-changing idea would be to start investigating not the astrophysical objects, but the messengers themselves. Indeed, we have studied what a new, optical contribution to the measured cosmological redshift of astrophysical sources would bring. This new shift has an optical origin, due to non-standard electromagnetic effects, and thus does not depend on the expansion of the Universe itself. Working under this hypothesis, we have studied three cosmological models without dark energy, to compute how relevant the further shift due to non-standard electromagnetism should be in order to match the observations. We also recall that, differently from the cosmological shift, the non-standard electromagnetic one could also be blue, depending on the environment of the source as well as on the path of the photon itself, and also that, for this framework, two sources observed at the same distance could, in principle, present different total redshifts.

We have first studied a sample of mock redshifts not corresponding to any observation spanning up to $z = 11$, a redshift similar to those of the most distant objects observed up to now, and confront the hypothetical luminosity distance of the observations found at such redshift in our cosmology model without dark energy with the ΛCDM model. We have found that the physical interpretation of such comparisons is strictly linked to the cosmological model studied: indeed, for the first cosmological model, in which we recall we have fixed $\Omega_M = 0.3$, $\Omega_k = \Omega_\Lambda = 0$, we have found that all the non-standard redshift contributions must be red, thus positive. Instead, completely different behaviors have been found for the second cosmological model, in which we have fixed $\Omega_M = 0.3$, $\Omega_k = 0.7$, and $\Omega_\Lambda = 0$, where we have derived z_S being both positive and negative, following a first decreasing, then increasing trend. Finally, different results have been found also for the last cosmological model, in which we have fixed $\Omega_M = 1$, $\Omega_k = \Omega_\Lambda = 0$, where we have computed all negative z_S and an overall decreasing trend with the redshift. We have also changed the fixed values of H_0, considering three different values of it, for every cosmological model considered. We have noted slight differences due to this change when we compared the results achieved by the same cosmological model, which shifts the obtained results to smaller values of z_S without changing the overall behavior. We recall that a negative z_S implies that the photons gain energy while crossing (inter-)galactic fields and, thus, that the astrophysical objects are actually farther than what we deduce from the observed z. Of course, the opposite is true for a positive value of z_S.

We next started our analysis regarding real data. We first considered the SNe Ia Pantheon sample, for which we derived the z_S both using an individualistic approach (i. e., we derived z_S for each SN without considering the general likelihood and the related covariance matrix) as well as general computations (in which we have derived the k_i

parameters, strictly linked to the z_S ones, as a general best-fit, thus using the SNe Ia likelihood and the related covariance matrix). Both approaches present advantages, in particular, the individual procedure allows us to appreciate effects in the derived values for z_S which could not be linked to only the distance itself, while the general computation allows us to treat the non-standard electromagnetic effects encapsulated in the k_i as a cosmological parameter like H_0 or Ω_M.

For the individual results, considering the three aforementioned cosmological models and the three fixed values for H_0, we obtain results that match, at least tentatively, with those obtained by the mock computations, where the two redshift intervals overlap. The main difference between the simulated and real results is in the dispersion found in the latter, which is expected due to the possible measurement errors and different environments of the SNe Ia. Thus, the conclusions achieved for the mock redshift results are also confirmed here.

Regarding the general results, we note how the central values obtained as best-fit for the k_i parameters are remarkably consistent with the mean of the individual computations, albeit a way smaller dispersion has been found in this case, as it may be expected given its general nature. These computations have also allowed us to infer Hubble diagrams from the SNe Ia data in our non-standard cosmological models, computing the best-fit curve and comparing it with the real data. We find that all our results provide an acceptable fit considering the real data, with the best-fit reached by the second cosmological model, in which an open universe is taken into account, being the most consistent with the real data.

We have added the BAO data to our computations, finding a shift in the results either positive or negative, depending on the cosmological model considered. An interesting result has been obtained for the third cosmological model, $H_0 = 70$ km s^{-1} per Mpc, where we find k_i consistent with 0, which would imply that, from a cosmological point of view, our model without dark energy provides the same results than the ΛCDM model for that particular fixed value of H_0.

We have then performed the same computations, but taking into account the novel Pantheon+ sample, which is an update of the Pantheon set used in all our previous computations regarding the SNe Ia. Given that the simulated redshifts do not depend on this particular point, we moved directly to the real data, considering both the individual as well as general estimates. We have performed the same computations previously presented, comparing them with the respective previous cases, and, as a novelty, also with the redshift errors, which are provided by the Pantheon+ catalog but not by the Pantheon one.

The comparisons regarding the individual cases show a predominance for low values

(in modulus) of the z_S distribution, which was less remarkable for the Pantheon results. This is probably because of the higher relative number of low redshift SNe Ia, on which the Pantheon+ update was predominantly focused. Nevertheless, the general behavior has not been modified by considering the new set, apart from the second cosmological model, in which a nearly symmetric distribution around $z_S = 0$ has been found for $H_0 = 67,70$ km s^{-1} per Mpc. We also note that the z_S are, in general, larger than the errors themselves (more than one order of magnitude for the first cosmological model). The averages of the related k_i distributions are consistent with those derived from the Pantheon set.

Regarding the general best-fit, instead, we have found more noticeable differences for the Pantheon+ sample computations with respect to the Pantheon findings, especially for the second and third cosmological models: indeed, while the first model presents results which are remarkably similar to the Pantheon computations, apart from the peak near $z_S = 0$ due to the low redshift SNe Ia, for the second and third cosmological models, instead, we note a shift in the sign for the k_i parameters when we fixed $H_0 = 67$ km s^{-1} per Mpc. This may be due to the general low values of the k_i parameters found for these particular cases. Indeed, we recall that, while the z_S may have different signs between one another for the individual computations, this cannot be achieved by the general fit, considering that they depend directly on the sign of the singular value for k_i, which means that they are either all positive or all negative. Also, we note that the best-fit values for the k_i parameters are consistent with 0 for the second and third cosmological models, when we fix $H_0 = 67,70$ km s^{-1} per Mpc, differently from the Pantheon computations. We also note that the derived uncertainty for these best-fit values is generally higher than the corresponding Pantheon case. Differences were to be expected between the general best-fit values, given the differences in the samples themselves. We also plotted Hubble diagrams, similarly to what we did for the Pantheon case, finding fits that are statistically better than their Pantheon counterparts. Once again, the most precise fit has been achieved by the open cosmological model. Lastly, we deduced that adding BAO data to the Pantheon+ set has the same effect derived for the Pantheon computations, as expected given that we did not change the BAO set.

We note that, for all the analysis regarding both the Pantheon and Pantheon+ sets, increasing the value of H_0 shifts the derived $z_{\rm S}$ in the same way, namely making them more negative. This is because H_0 is inversely proportional to the distance, and thus the effect of decreasing the distance is opposed by the more negative values of $z_{\rm S}$ in our comparison with the real data.

We also present a discussion regarding other probes and how we would expect the non-standard shift to influence them. It is important to stress that such an alternative approach has to be based on solid physical grounding to truly be competitive with the

widely accepted and successful ΛCDM model. Indeed, the computations regarding z_S previously discussed do not consider the particular, non-standard electromagnetic phenomenon at hand which may cause it. This makes finding and studying these effects a mandatory requirement for this kind of approach. As we have seen, one possible extension is the possibility to attribute a mass to photons, following the so-called dBP formalism. Different experiments and analyses in the literature have been performed in order to find an upper limit to the mass of the photons.

In our investigation, we aimed to achieve this goal using the MMS data, a constellation of four satellites studying the solar wind surrounding Earth's magnetosphere and the magnetosphere itself. More specifically, we have compared the particle current, that is the current measured by each satellite starting from the plasma velocities and densities, with the rotational one, which is given by the curl of the magnetic field computed by using the so-called curlmeter method, taking into account the hypothesis that every possible inconsistency between the two currents is due to a dBP contribution due an intrinsic mass of the photon, or an LSV parameter in the SME framework. In order to do so, we have computed the errors for both these quantities starting from the data downloaded from the AMDA website. We have considered for our analysis data gathered in almost 6 years of observations, in the burst region, which is the highest quality data collection in the MMS data set, especially regarding the time resolution, thus working with 3.8×10^6 data points, for each of which we have collected different physical quantities, that have been used either in the comparison itself or in reliability checks.

The results found by us tell us that, while in the majority of the cases the two currents, considering their errors, are indeed consistent, inconsistencies have been found in some cases (2.2% for the modulus, 4.8% for the vector components), which, under our assumptions, would presume a mass for the photon, at least according to this minority of data points. For the consistencies cases, an upper limit can still be computed, being represented by the smallest amount to add (or subtract) to (from) one of the two currents to get an inconsistency case. We have also added a quality factor keeping into account the geometry of the tetrahedron formed by the MMS satellites. In doing so, we do not observe a significant modification of the percentage representing the inconsistency cases.

Then, we divided our data set into different regions, finding, for each data point, to which physical area (solar wind, magnetosheath, magnetosphere) it may belong, following criteria based on the relations between the different pressures (ram p_R, magnetic p_M, and thermal p_T pressures) derived for that particular point. Indeed, if $p_R > 10\ max(p_M, p_T)$, we identify the region as solar wind; if $0.3\ min(p_M, p_T) < p_R < 4\ max(p_M, p_T)$, as magnetosheath; if $10\ p_R < p_M$, as magnetosphere. The region of undetermined data points between the solar wind and the magnetosheath is named zone I,

presenting features that are intermediate between the magnetosheath and the solar wind, while all the other undetermined data points are instead gathered in zone II.

In doing so, we have noted that the majority of the inconsistencies are found in the solar wind and zone I regions. Indeed, we note that 76% of the inconsistencies for the modulus, and 65% for the components, lie in these two regions, which represent only 14% of the total data. This conclusion is very interesting because it allows us to deduce that there are physical regions in which the inconsistencies between the two currents are way more frequent than in others.

Given that the majority of the inconsistencies are found in the solar wind+zone I regions, we can use the Parker model for the solar wind to infer the vector potential for each of these points, starting from the measured magnetic fields. In doing so, we can finally compute the presumed mass of the photons for the inconsistencies, and the upper limits for the consistencies, taking into account the aforementioned caveats. In particular, we have found that the minimum of the photon mass distribution is 1.74×10^{-53} kg, the average is 2.48×10^{-51} kg, and the median is 1.82×10^{-51} kg. These results are in the same order of magnitude as the majority of experiments and deductions related to this subject, even if in those only an upper limit is considered.

From these estimates we can also derive the values for parameters linked to another non-standard electromagnetic quantity: the LSV parameter, $|\vec{k}^{\mathrm{AF}}|$, which we recall represents an effective mass of the photon in the SME formalism and that can be linked to an effective mass, and so to the previous findings regarding the dBP mass.

Different reliability checks have been performed by us to confirm the findings of our analysis:

- we have confirmed that the current due to the time derivative of the electric fields is negligible given the time sampling chosen by us.
- We have confirmed that the time sampling chosen by us is derived by a mean process, thus all the high-frequency components, which cannot be accounted for by the curlmeter techniques, have been naturally discarded by our analysis.
- We have not noted any correlation between the densities related to particular data points and the inconsistencies, thus the latter cannot be due to a systematic issue linked to the failing of the instruments in detecting some electrons (or ions) due to the low density.
- We have considered only data points in which the particle currents measured by each MMS satellite are consistent with one another.

Nevertheless, we cannot conclude that we have actually found the mass of the photon: albeit the collaboration working on MMS has addressed many systematic effects related to the instruments used in our analysis as well as calibration processes, still possible errors could be at hand, that could have influenced our results. Furthermore, the inconsistencies represent only a minority of cases in the studied six years of data and measurements, thus cannot allow us to conclude that a definitive mass exists given the majority of consistencies, and would instead allow only for an estimate of the upper limit. Nevertheless, we are able to state that, if the inconsistencies we have found are actually due to non-standard electromagnetic effects, the related dBP mass (or LSV parameter) are those previously shown, of course, if that is the case, a dedicated analysis would be in order to understand why these effects arise only for this particular minority.

Considering the estimates on the upper limits on the photon mass given by the consistencies, instead, we have found a minimum equal to 1.84×10^{-53} kg, an average equal to 2.21×10^{-51} kg, and a median equal to 2.17×10^{-51} kg. These results are in the same order of magnitude regions of both the results achieved in the literature as well as of our estimates regarding the inconsistencies. Given that the majority of our comparisons show consistencies, the average of them is our estimate regarding the photon mass upper limit.

We now move from the electromagnetic extension to a gravitational one, and from cosmology to stellar astrophysics. Indeed, ETGs have been studied in the literature to all these scales, from the "small" neighborhood of compact objects to the entire Universe, to test if they are able to recover the results of GR where the latter is consistent with the observations, while also overcoming its limits. In this analysis, we have studied the stellar structure of non-compact objects (including variable starts), using a particular ETG: $f(R)-$Gravity. Indeed, we have derived the stellar structure system for $f(R)$-Gravity related to non-compact stars, finding an interesting result related to the hydrostatic equilibrium equation, which is the same as in GR for the Jordan frame, as long as the potential is not expressed explicitly. We have also noted that the main difference between this system and the one related to GR is in the Poisson Equation, that in $f(R)$-Gravity becomes a system of two fourth-order equations.

In general, in order to obtain the solution of the stellar structure starting from this system, assumptions related to the energy density and opacity are mandatory, but, working under the polytropic relation, thus linking the pressure to the density without involving the temperature, results can be achieved by using only the mechanical part of the aforementioned system. Indeed, we have analyzed polytropic models in $f(R)$-Gravity, and compared them to the classical GR case, finding for the former framework two different modified Lane-Emden equations, depending on the particular Green function chosen to derive these equations, which are integro-differential equations depending on the partic-

ular $f(R)$-model represented by the parameter m. These equations can be solved analytically with an exact solution only for $n = 0$, and for $n = 1$ considering particular caveats, differently from the GR case, for which an analytical solution can be found for $n = 0, 1$, and 5.

Thus, we have solved numerically these equations for different values of the polytropic index. From a physical point of view, the most interesting cases are the non-relativistic ($n = 3/2$) and the highly relativistic ($n = 3$) limits of completely degenerate gas that we can find in a white dwarf, neutron stars, and the core of less evolved stars, also, $n = 3$ has been used to fit successfully the values observed for the Sun [358]. Thus, solutions for both the modified Lane-Emden equations as well as for the Lane-Emden equation in GR have been found, yielding polytropic functions linking the dimensionless radius with the dimensionless potential. We have noted that, for the same polytropic index, in $f(R)$-Gravity, the radius is systematically bigger than in GR, and the difference increases with the polytropic index itself. We also note that the two modified Lane-Emden equations yield almost identical results. This is interesting because the oscillating behavior of one of them can be used in relation to variable stars, which thus can be encompassed in our formalism. It is interesting to note that the oscillating behavior of these stellar structures has not been given by hand, but it is a natural consequence of the system solution.

From these solutions, we can derive different physical quantities related to the stellar structure itself, like the radius, mass, and gravitational binding energy of stellar structures. It is also important to stress that we can recover the classical results from the $f(R)$-Gravity case by choosing appropriate values for the second derivative of the Taylor expansion of the function $f(R)$. This means that $f(R)$-Gravity can recover the cases already well described by GR.

We have then computed the period for oscillating stars using the modified potential for the weak limit in $f(R)$-Gravity, and compared it with the same quantity derived from GR, starting from the same initial conditions given by the central density and the polytropic parameter, stressing the differences between the results given by the two theories. Again, flexibility due to a particular assumption in this computation is achieved, because of the degree of freedom we have in choosing a particular parameter involved in the modified potential, and thus in the period for $f(R)$-Gravity. We have then simulated a sinusoidal behavior for one of the free parameters studied in our model, to show the behavior of the radius over two periods, again comparing the results achieved by $f(R)$-Gravity and GR.

Further analysis and new outlooks are possible for all the work presented in this thesis. For instance, future GRBs observations will improve our knowledge both on the physical mechanism behind these fascinating objects as well as on the correlations

between their physical parameters, with new GRBs belonging to the Platinum sample as well as the possibility to define even more refined subsets. These would be in turn used for cosmological applications, as our work regarding the GRB simulations shows.

Regarding the extension of electromagnetic theory, it is possible to further analyze this paradigm both from an observational and theoretical point of view. Observationally, we could improve and amply the analysis presented here for its cosmological contribution, trying to understand how the other cosmological parameters would behave in this new framework, and involving other cosmological probes. Also, it would be possible to look for other evidence for testing the possible mass of photons, or upper limits on this quantity, which, as we have seen, can be performed in different environments, as close as Earth's magnetosphere and as far as the observations related to FRB, speculated of being of extra-galactic origin, recalling that there also exist laboratory experiments which are not linked to astrophysical observations. Theoretically, a strong physical ground is mandatory for this theory to be actually competitive with the ΛCDM model. Indeed, it is necessary to understand what exactly is the physical mechanism behind the assumed non-standard shifts, alternatives being the dBP theory, the extension of the Standard Model, or non-linear electromagnetism.

Finally, for the ETGs, in particular for our application to the stellar structure of non-compact objects, some outlooks are the following: it would be interesting to apply $f(R)$-Gravity to models for the stellar structure which do not forecast a polytropic relation between the pressure and the density inside the star. In particular, this approach would be useful to compare our results with more realistic models for oscillating stars, like Classical Cepheids and RR Lyrae, that include the temperature and the metallicity, which play a fundamental role in the study of these stars. Also, it would be possible to apply this framework to different ETGs, in particular for their weak limits, to understand which one of those resembles better the real data (although, as we have seen in our work, different free parameters are present which allow tuning our conclusions to the real data).

The study of stellar structures can be a very important test-bed for $f(R)$-Gravity, which we recall is a theory widely used both in cosmological and strong gravitational field environments, where the shortcomings of GR are more evident; indeed, in order to have a valid gravitational theory, it has to be adequate at all scales, stellar ones included, which means that finding actual detected effects due to ETGs at these scales could confirm even more their reliability, with the caveat that they have to reproduce the results obtained by GR where it is most successful. Of course, this applies also to the cosmological scales.

It would also be possible to merge the different branches studied in this thesis, like studying both ETE and ETG at the cosmological scale using the observations concerning

cosmological probes, to understand which of the two frameworks influences more the results. Regarding this point, we may look at a recent result concerning a particular ETG model, known as the $f(T)$ teleparallel gravity model [44], in which the action is expressed by

$$\mathcal{A} = \frac{1}{16\pi G}\int d^4x e[T + f(T)] + \mathcal{A}_m, \tag{7.1}$$

where $f(T)$ is a generic function of the torsion scalar T, $\mathcal{A}_m$ is the action related to the matter terms, and $e = \sqrt{-g}$ is the metric determinant. Obtaining the Friedman equations for this theory considering a flat Friedman-Robertson-Walker metric we find [44]

$$E(z) = \sqrt{\Omega_r(1+z)^4 + \Omega_M(1+z)^3 + \frac{1}{T_0}[f - 2Tf']}, \tag{7.2}$$

where $T = 6H$ holds. We note that the main difference between this equation and Eq. (2.16) is in the last term, which substitutes the dark energy density. This framework has been used considering three specific forms of the $f(T)$ function, in concordance with real data (CMB, the Pantheon sample, BAO, DES) to derive the free parameters on which the ΛCDM model is based upon. Introducing our formalism for $z_{\rm S}$, i. e., including computations regarding the finding of the values of cosmological parameters in ETG theories, like this one, also the further redshift contribution that has been analyzed in chapter 5, it would be interesting to consider both modifications using real data as we previously did, to understand how the two extensions compare with each other when both are employed contemporaneously to infer cosmological parameters in models without a constant dark energy contribution.

Other examples in the literature exist where ETG models have been considered to constrain observational parameters using real data. For example, [369] used a particular $f(R)$-Gravity exponential model in conjunction with real data (SNe Ia, BAO, $H(z)$, CMB) to constrain four free parameters of his theory, finding a concordance with the observed data similar to the ΛCDM model. Comparisons with the observations considering this exponential model were found in [370, 371].

From a more theoretical point of view, many other possible cosmological models going beyond GR and considering ETG have been studied by the scientific community [372, 107]. Finding a comparison with one of these models with our approach linked to the frequency shifts, rather than on underlying gravitational and cosmological theory, would allow us to infer which of the two modifications would bring the greater impact on the cosmological results, and if or how an improvement with respect to the ΛCDM model is at hand. Adding GRBs to these tests in the future would also be possible, given their ability to explore high-redshift regions, especially after new data points shall be acquired by present and future missions.

In conclusion, all the computations performed in this thesis have the aim to explore the frontiers of standard cosmology and astrophysics, testing novel applications (both observational and cosmological) in the boundaries of these two theories, going beyond the standard framework by proposing changes to the general paradigm itself and comparing the achieved results with those commonly known. The promising results reached in this thesis pave the way to further future analysis, aiming at overcoming limits that are one of the main focus of discussions inside the astrophysical community, while keeping the successes of the standard theory (GR and ΛCDM model), which, we recall once again, are way more numerous of the current known shortcomings.

Bibliography

[1] A. Einstein. “Die Grundlage der allgemeinen Relativitätstheorie”. In: *Ann. Phys. (Leipzig)* 354 (1916), p. 769.

[2] N. Aghanim et al. “Planck 2018 results”. In: *Astronomy & Astrophysics* 641 (2020), A6. DOI: 10.1051/0004-6361/201833910. URL: http://dx.doi.org/10.1051/0004-6361/201833910.

[3] T. M. C. Abbott et al. “First Cosmology Results using Type Ia Supernovae from the Dark Energy Survey: Constraints on Cosmological Parameters”. In: *The Astrophysical Journal* 872.2 (2019), p. L30. DOI: 10.3847/2041-8213/ab04fa. URL: http://dx.doi.org/10.3847/2041-8213/ab04fa.

[4] P. A. Zyla and the Particle Data Group. “Review of particle physics”. In: *Progr. Theor. Exp. Phys.* (2020), p. 083C01.

[5] R. L. Workman and the Particle Data Group. “Review of particle physics”. In: *Progress of Theoretical and Experimental Physics* (2022), p. 083C01. DOI: 10.1093/ptep/ptac097.

[6] A. G. Riess et al. “Observational Evidence from Supernovae for an Accelerating Universe and a Cosmological Constant”. In: *The Astronomical Journal* 116.3 (1998), pp. 1009–1038. DOI: 10.1086/300499. URL: http://dx.doi.org/10.1086/300499.

[7] P. Salucci et al. “Einstein, Planck and Vera Rubin: Relevant Encounters Between the Cosmological and the Quantum Worlds”. In: *Frontiers in Physics* 8 (2021). DOI: 10.3389/fphy.2020.603190. URL: http://dx.doi.org/10.3389/fphy.2020.603190.

[8] R. W. Schnee. “Introduction to dark matter experiments”. In: *Physics of the Large and the Small* (2011). DOI: 10.1142/9789814327183_0014. URL: http://dx.doi.org/10.1142/9789814327183_0014.

[9] V. A. Mitsou. "Overview of searches for dark matter at the LHC". In: *Journal of Physics: Conference Series* 651 (2015), p. 012023. DOI: 10.1088/1742-6596/651/1/012023. URL: http://dx.doi.org/10.1088/1742-6596/651/1/012023.

[10] E. Aprile et al. "The XENON1T dark matter experiment". In: *The European Physical Journal C* 77.12 (2017). DOI: 10.1140/epjc/s10052-017-5326-3. URL: http://dx.doi.org/10.1140/epjc/s10052-017-5326-3.

[11] S. Capozziello and M. De Laurentis. "Extended Theories of Gravity". In: *Physics Reports* 509.4-5 (2011), pp. 167–321. DOI: 10.1016/j.physrep.2011.09.003. URL: https://doi.org/10.1016/j.physrep.2011.09.003.

[12] A. G. Riess et al. "A Comprehensive Measurement of the Local Value of the Hubble Constant with 1 km/s/Mpc Uncertainty from the Hubble Space Telescope and the SH0ES Team". In: *The Astrophysical Journal Letters* 934.1 (2022), p. L7. DOI: 10.3847/2041-8213/ac5c5b. URL: https://doi.org/10.3847/2041-8213/ac5c5b.

[13] E. Abdalla et al. "Cosmology Intertwined: A Review of the Particle Physics, Astrophysics, and Cosmology Associated with the Cosmological Tensions and Anomalies". In: *Journal of High Energy Astrophysics* 34 (2022), pp. 49–211. DOI: 10.1016/j.jheap.2022.04.002. URL: https://doi.org/10.1016/j.jheap.2022.04.002.

[14] S. Joudaki et al. "CFHTLenS revisited: assessing concordance with Planck including astrophysical systematics". In: *Monthly Notices of the Royal Astronomical Society* 465.2 (2016), pp. 2033–2052. DOI: 10.1093/mnras/stw2665. URL: https://doi.org/10.1093/mnras/stw2665.

[15] T. M. C. Abbott et al. "Dark Energy Survey Year 3 results: Cosmological constraints from galaxy clustering and weak lensing". In: *Physical Review D* 105.2 (2022), p. 023520. DOI: 10.1103/physrevd.105.023520. URL: https://doi.org/10.1103/physrevd.105.023520.

[16] S. Chandrasekhar. "The Maximum Mass of Ideal White Dwarfs." In: *Astrophysical Journal* 74 (1931), p. 81. DOI: 10.1086/143324.

[17] D. A. Howell et al. "The type Ia supernova SNLS-03D3bb from a super- Chandrasekhar-mass white dwarf star". In: *Nature* 443.7109 (2006).

, pp. 308–311. DOI: 10.1038/nature05103. URL: https://doi.org/10.1038/nature05103.

[18] L. Rezzolla, E. R. Most, and L. R. Weih. "Using Gravitational-wave Observations and Quasi-universal Relations to Constrain the Maximum Mass of Neutron Stars". In: *The Astrophysical Journal* 852.2 (2018), p. L25. DOI: 10.3847/2041-8213/aaa401. URL: https://iopscience.iop.org/article/10.3847/2041-8213/aaa401.

[19] P. Feola et al. "Mass-radius relation for neutron stars in $f(R) = R+\alpha R^2$ gravity: A comparison between purely metric and torsion formulations". In: *Physical Review D* 101.4 (2020), p. 044037. DOI: 10.1103/physrevd.101.044037. URL: https://journals.aps.org/prd/abstract/10.1103/PhysRevD.101.044037.

[20] D. M. Scolnic et al. "The complete light-curve sample of spectroscopically confirmed SNe Ia from Pan-STARRS1 and cosmological constraints from the combined Pantheon sample". In: *Astrophys. J.* 859 (2018), p. 101. DOI: 10.3847/1538-4357/aab9bb. URL: https://iopscience.iop.org/article/10.3847/1538-4357/aab9bb.

[21] D. J. Eisenstein et al. "Detection of the Baryon Acoustic Peak in the Large-Scale Correlation Function of SDSS Luminous Red Galaxies". In: *The Astrophysical Journal* 633.2 (2005), pp. 560–574. DOI: 10.1086/466512. URL: http://dx.doi.org/10.1086/466512.

[22] A. Cucchiara et al. "A photometric redshift of z $\sim$ 9.4 for GRB 090429B". In: *The Astrophysical Journal* 736.1 (2011), p. 7. DOI: 10.1088/0004-637x/736/1/7. URL: https://iopscience.iop.org/article/10.1088/0004-637X/736/1/7.

[23] P. Kumar and B. Zhang. "The physics of gamma-ray bursts and relativistic jets". In: *Physics Reports* 561 (2015), pp. 1–109. DOI: 10.1016/j.physrep.2014.09.008. URL: https://www.sciencedirect.com/science/article/abs/pii/S0370157314003846.

[24] M. G. Dainotti et al. "The X-Ray Fundamental Plane of the Platinum Sample, the Kilonovae, and the SNe Ib/c Associated with GRBs". In: *The Astrophysical Journal* 904.2 (2020), p. 97. DOI: 10.3847/1538-4357/abbe8a. URL: https://iopscience.iop.org/article/10.3847/1538-4357/abbe8a.

[25] M. G. Dainotti et al. “A Study of the Gamma-Ray Burst Fundamental Plane”. In: *The Astrophysical Journal* 848.2 (2017), p. 88. DOI: 10.3847/1538-4357/aa8a6b. URL: https://iopscience.iop.org/article/10.3847/1538-4357/aa8a6b.

[26] M. G. Dainotti et al. “A study of gamma ray bursts with afterglow plateau phases associated with supernovae”. In: *Astronomy & Astrophysics* 600 (2017), A98. DOI: 10.1051/0004-6361/201628384. URL: https://doi.org/10.1051/0004-6361/201628384.

[27] G. D’Agostini. “Fits, and especially linear fits, with errors on both axes, extra variance of the data points and other complications”. In: (2005). DOI: 10.48550/ARXIV.PHYSICS/0511182. URL: https://arxiv.org/abs/physics/0511182.

[28] B. Efron and V. Petrosian. “A Simple Test of Independence for Truncated Data with Applications to Redshift Surveys”. In: *The Astrophysical Journal* 399 (1992), p. 345. DOI: 10.1086/171931.

[29] M. G. Dainotti et al. “Optical and X-ray GRB Fundamental Planes as cosmological distance indicators”. In: *Monthly Notices of the Royal Astronomical Society* 514.2 (2022), pp. 1828–1856. DOI: 10.1093/mnras/stac1141. URL: https://doi.org/10.1093/mnras/stac1141.

[30] A. Conley et al. “Supernova Constraints and Systematic Uncertainties from the First Three Years of the Supernova Legacy Survey”. In: *The Astrophysical Journal Supplement Series* 192.1, 1 (2011), p. 1. DOI: 10.1088/0067-0049/192/1/1. URL: https://doi.org/10.1088/0067-0049/192/1/1.

[31] M. Betoule et al. “Improved cosmological constraints from a joint analysis of the SDSS-II and SNLS supernova samples”. In: *Astronomy & Astrophysics* 568, A22 (2014), A22. DOI: 10.1051/0004-6361/201423413. URL: https://doi.org/10.1051/0004-6361/201423413.

[32] M. G. Dainotti, G. Sarracino, and S. Capozziello. “Gamma-ray bursts, supernovae Ia, and baryon acoustic oscillations: A binned cosmological analysis”. In: *Publications of the Astronomical Society of Japan* 74.5 (2022), pp. 1095–1113. DOI: 10.1093/pasj/psac057. URL: https://doi.org/10.1093/pasj/psac057.

[33] M. G. Dainotti et al. “The gamma-ray bursts fundamental plane correlation as a cosmological tool”. In: *Monthly Notices of the Royal Astronomical Society* 518.2

(2022), pp. 2201–2240. DOI: 10.1093/mnras/stac2752. URL: https://doi.org/10.1093/mnras/stac2752.

[34] A. D. A. M. Spallicci et al. "Cosmology and photon frequency shift induced by the Standard-Model Extension". In: *The European Physical Journal C* 81 (2021), p. 4. DOI: 10.1140/epjc/s10052-020-08703-3. eprint: arXiv2011.12608[astro-ph.CO].

[35] A. D. A. M. Spallicci, G. Sarracino, and S. Capozziello. "Investigating dark energy by electromagnetic frequency shifts". In: *The European Physical Journal Plus* 137.2 (2022), p. 2. DOI: 10.1140/epjp/s13360-022-02450-y. URL: https://doi.org/10.1140/epjp/s13360-022-02450-y.

[36] D. Scolnic et al. "The Pantheon+ Analysis: The Full Data Set and Light-curve Release". In: *The Astrophysical Journal* 938.2 (2022), p. 113. DOI: 10.3847/1538-4357/ac8b7a. URL: https://doi.org/10.3847/1538-4357/ac8b7a.

[37] L. de Broglie. "Rayonnement noir et quanta de lumière". In: *J. Phys. et Radium* 3 (1922), p. 422. DOI: 10.1051/jphysrad:01922003011042200.

[38] A. Proca. "Sur les équations fondamentales des particules élémentaires". In: *Comptes Rendus Hebd. Séances Acad. Sc. Paris* 202 (1936), p. 1490. DOI: ark:/12148/bpt6k3154f.

[39] J. A. Helayël-Neto and A. D. A. M. Spallicci. "Frequency variation for *in vacuo* photon propagation in the Standard-Model Extension". In: *The European Physical Journal C* 79 (2019), p. 590. DOI: 1140/epjc/s10052-019-7105-9. URL: https://doi.org/10.1140/epjc/s10052-019-7105-9.

[40] M. Born and L. Infeld. "Foundations of the new field theory". In: *Proceedings of the Royal Society of London A* 144 (1934), p. 425. DOI: 10.1098/rspa.1934.0059.

[41] W. Heisenberg and H. Euler. "Folgerungen aus der Diracschen Theorie des Positrons". In: *Zeitschrift fur Physik* 98 (1936), p. 714. DOI: 10.1007/BF01343663.

[42] S. A. Fuselier et al. "Magnetospheric Multiscale Science mission profile and operations". In: *Space Science Reviews* 199 (2016), p. 77. DOI: 10.1007/s11214-014-0087-x. URL: https://link.springer.com/article/10.1007/s11214-014-0087-x.

[43] M. W. Dunlop et al. "Analysis of multipoint magnetometer data". In: *Advances in Space Research* 8 (1988), p. 273. DOI: 10.1016/0273-1177(88)90141-X.

[44] M. Benetti, S. Capozziello, and G. Lambiase. "Updating constraints on f(T) teleparallel cosmology and the consistency with big bang nucleosynthesis". In: *Monthly Notices of the Royal Astronomical Society* 500.2 (2021), pp. 1795–1805. DOI: 10.1093/mnras/staa3368. URL: https://doi.org/10.1093/mnras/staa3368.

[45] A.A. Starobinsky. "Spectrum of relict gravitational radiation and the early state of the universe". In: *Journal of Experimental and Theoretical Physics Letters* 30 (1979), pp. 682–685.

[46] S. Capozziello and M. Funaro. *Introduzione alla relativitá generale. Con applicazioni all'astrofisica relativistica e alla cosmologia*. Liguori, Napoli, 2006.

[47] R. Kippenhahn, A. Weigert, and A. Weiss. *Stellar Structure and Evolution*. Springer, Berlino, 2012.

[48] R. Farinelli et al. "Numerical solutions of the modified Lane-Emden equation in f(R)-gravity". In: *Monthly Notices of the Royal Astronomical Society* 440.3 (2014), pp. 2894–2900. DOI: 10.1093/mnras/stu423. URL: https://doi.org/10.1093/mnras/stu423.

[49] S. Capozziello et al. "Hydrostatic equilibrium and stellar structure in f(R)-gravity". In: *Physical Review D* 83.6 (2011), p. 064004. DOI: 10.1103/physrevd.83.064004. URL: https://doi.org/10.1103/physrevd.83.064004.

[50] P. A. Crowther et al. "The R136 star cluster dissected with Hubble Space Telescope/STIS. I. Far-ultraviolet spectroscopic census and the origin of He ii λ1640 in young star clusters". In: *Monthly Notices of the Royal Astronomical Society* 458.1 (2016), pp. 624–659. DOI: 10.1093/mnras/stw273. URL: https://doi.org/10.1093/mnras/stw273.

[51] H. Zinnecker and H. W. Yorke. "Toward Understanding Massive Star Formation". In: *Annual Review of Astronomy and Astrophysics* 85 (2007), pp. 481–563. DOI: 10.1146/annurev.astro.44.051905.092549. URL: https://doi.org/10.1146/annurev.astro.44.051905.092549.

[52] S. Capozziello et al. "Jeans analysis of self-gravitating systems in f(R)-gravity". In: *Physical Review D* 85.4 (2012), p. 044022. DOI: 10.1103/physrevd.85.044022. URL: https://doi.org/10.1103/physrevd.85.044022.

[53] G. Sarracino, A. D. A. M. Spallicci, and S. Capozziello. "Investigating dark energy by electromagnetic frequency shifts II: the Pantheon+ sample". In: *The European Physical Journal Plus* 137.12 (2022), p. 1386. DOI: 10.1140/epjp/s13360-022-03595-6. URL: https://doi.org/10.1140/epjp/s13360-022-03595-6.

[54] A. D. A. M. Spallicci et al. "Testing the Ampère-Maxwell law on the photon mass and Lorentz-Poincaré symmetry violation with MMS multi-spacecraft data". In: (2023). DOI: 10.48550/ARXIV.2205.02487. URL: https://arxiv.org/abs/2205.02487.

[55] E. N. Parker. "Dynamics of the interplanetary gas and magnetic fields". In: *The Astrophysical Journal* 128 (1958), p. 664.

[56] A. Einstein. "On the electrodynamics of moving bodies." In: *Annalen der Physik* 322.10 (1905), pp. 891–921.

[57] E. Shrodinger. *Space-Time structure*. Cambridge University Press, Cambridge, 1950.

[58] H. P. Robertson. "Kinematics and World-Structure." In: *Astrophysical Journal* 82 (1935), p. 284.

[59] H. P. Robertson. "Kinematics and World-Structure II." In: *Astrophysical Journal* 83 (1936), p. 187.

[60] H. P. Robertson. "Kinematics and World-Structure III." In: *Astrophysical Journal* 83 (1936), p. 257.

[61] A. Friedmann. "Uber die Krummung des Raumes." In: *Zeitschrift fur Physik* 10 (1922), pp. 377–386.

[62] D. W. Hogg. "Distance measures in cosmology". In: (1999). DOI: 10.48550/arXiv.astro-ph/9905116. URL: https://arxiv.org/abs/astro-ph/9905116.

[63] R. J. Nemiroff and B. Patla. "Adventures in Friedmann cosmology: A detailed expansion of the cosmological Friedmann equations". In: *American Journal of Physics* 76.3 (2008), pp. 265–276. DOI: 10.1119/1.2830536. URL: http://dx.doi.org/10.1119/1.2830536.

[64] F. Zwicky. "Die Rotverschiebung von extragalaktischen Nebeln." In: *Helvetica Physica Acta* 6 (1933), pp. 110–127.

[65] H. W. Babcock. “The rotation of the Andromeda Nebula.” In: *Lick Observatory bulletin* 498 (1939), pp. 41–51. DOI: 10.5479/ADS/bib/1939LicOB.19.41B.

[66] V. C. Rubin and V. K. Ford. “Rotation of the Andromeda Nebula from a Spectroscopic Survey of Emission Regions.” In: *Astrophysical Journal* 159 (1970), p. 379. DOI: 10.1086/150317.

[67] A. Einstein. “Kosmologische Betrachtungen zur allgemeinen Relativitätstheorie.” In: *Sitzungsberichte der Königlich Preußischen Akademie der Wissenschaften* (1917), pp. 142–152.

[68] M. M. Phillips. “The Absolute Magnitudes of Type IA Supernovae.” In: *Astrophysical Journal Letters* 413 (1993), p. L105. DOI: 10.1086/186970.

[69] D. Kasen and S. E. Woosley. “On the Origin of the Type Ia Supernova Width-Luminosity Relation”. In: *The Astrophysical Journal* 656.2 (2007), pp. 661–665. DOI: 10.1086/510375. URL: http://dx.doi.org/10.1086/510375.

[70] P. de Bernardis et al. “A Flat universe from high resolution maps of the cosmic microwave background radiation”. In: *Nature* 404 (2000), pp. 955–959. DOI: 10.1038/35010035. URL: https://doi.org/10.1038/35010035.

[71] R. Stompor et al. “Cosmological implications of the MAXIMA-I high resolution cosmic microwave background anisotropy measurement”. In: *The Astrophysical journal* 561.1 (2001), pp. 7–10. DOI: 10.1086/324438. URL: https://doi.org/10.1086/324438.

[72] L. Verde, R. Jimenez, and S. Feeney. “The importance of local measurements for cosmology”. In: *Physics of the Dark Universe* 2.2 (2013), pp. 65–71. DOI: 10.1016/j.dark.2013.04.003. URL: https://arxiv.org/abs/1303.5341.

[73] X. Luri et al. “Gaia Data Release 2”. In: *Astronomy & Astrophysics* 616 (2018), A9. DOI: 10.1051/0004-6361/201832964. URL: http://dx.doi.org/10.1051/0004-6361/201832964.

[74] M. Marconi, I. Musella, and G. Fiorentino. “Cepheid Pulsation Models at Varying Metallicity and Δ Y/ΔZ”. In: *The Astrophysical Journal* 632.1 (2005), pp. 590–610. DOI: 10.1086/432790. URL: http://dx.doi.org/10.1086/432790.

[75] M. Salaris and S. Cassisi. “The "tip" of the red giant branch as a distance indicator: results from evolutionary models”. In: *Monthly Notices of the Royal Astronomical Society* 289.2 (1997), pp. 406–414. DOI: 10.1093/mnras/289.2.406. URL: http://dx.doi.org/10.1093/mnras/289.2.406.

[76] S. Alam et al. “Completed SDSS-IV extended Baryon Oscillation Spectroscopic Survey: Cosmological implications from two decades of spectroscopic surveys at the Apache Point Observatory”. In: *Phys. Rev. D* 103 (2021), p. 083553. DOI: 10.1103/physrevd.103.083533. URL: https://doi.org/10.1103/physrevd.103.083533.

[77] A. Heavens. “Weak lensing: dark matter, dark energy and dark gravity”. In: *Nucl. Phys. Proc. Suppl.* 194 (2009), p. 76. DOI: 10.1016/j.nuclphysbps.2009.07.005. URL: https://doi.org/10.1016/j.nuclphysbps.2009.07.005.

[78] D. Huterer. “Weak lensing, dark matter and dark energy”. In: *Gen. Rel. Grav.* 42 (2010), p. 2177. DOI: 10.1007/s10714-010-1051-z. URL: https://doi.org/10.1007/s10714-010-1051-z.

[79] B. P. Abbott et al. “GW170817: Observation of Gravitational Waves from a Binary Neutron Star Inspiral”. In: *Physical Review Letters* 119.16 (2017), p. 161101. DOI: 10.1103/physrevlett.119.161101. URL: http://dx.doi.org/10.1103/PhysRevLett.119.161101.

[80] E. Di Valentino et al. “Snowmass2021 - Letter of interest cosmology intertwined I: Perspectives for the next decade”. In: *Astroparticle Physics* 131 (2021), p. 102606. DOI: 10.1016/j.astropartphys.2021.102606. URL: http://dx.doi.org/10.1016/j.astropartphys.2021.102606.

[81] E. Di Valentino et al. “Snowmass2021 - Letter of interest cosmology intertwined II: The hubble constant tension”. In: *Astroparticle Physics* 131 (2021), p. 102605. DOI: 10.1016/j.astropartphys.2021.102605. URL: http://dx.doi.org/10.1016/j.astropartphys.2021.102605.

[82] E. Di Valentino et al. “Cosmology intertwined III: fσ8 and S8”. In: *Astroparticle Physics* 131 (2021), p. 102604. DOI: 10.1016/j.astropartphys.2021.102604. URL: http://dx.doi.org/10.1016/j.astropartphys.2021.102604.

[83] E. Di Valentino et al. “Snowmass2021 - Letter of interest cosmology intertwined IV: The age of the universe and its curvature”. In: *Astroparticle Physics* 131 (2021), p. 102607. DOI: 10.1016/j.astropartphys.2021.102607.

URL: http://dx.doi.org/10.1016/j.astropartphys.2021.102607.

[84] L. Witten. *Gravitation an Introduction to Current Research.* John Wiley and Sons, Hoboken, 1962.

[85] C. DeWitt-Morette and J. A. Wheeler. *Battelle rencontres; 1967 lectures in mathematics and physics.* New York; Benjamin, 1968.

[86] C. Dewitt and B. Dewitt. *Relativity, Groups and Topology, 1963 (Les Houches Lectures) Relativite, Groupes et Topologie*. Gordon and Breach, New York, 1964.

[87] T. Bringmann, C. Kiefer, and D. Polarski. "Primordial black holes from inflationary models with and without broken scale invariance". In: *Physical Review D* 65.2 (2001), pp. 1–15. DOI: 10.1103/PhysRevD.65.024008. URL: https://doi.org/10.1103/physrevd.65.024008.

[88] P.M. Okouma, Y. Fantaye, and B.A. Bassett. "How flat is our Universe really?" In: *Physics Letters B* 719.1–3 (2013), pp. 1–4. DOI: 10.1016/j.physletb.2012.12.070. URL: http://dx.doi.org/10.1016/j.physletb.2012.12.070.

[89] E. Di Valentino, A. Melchiorri, and J. Silk. "Planck evidence for a closed Universe and a possible crisis for cosmology". In: *Nature Astronomy* 4.2 (2019), pp. 196–203. DOI: 10.1038/s41550-019-0906-9. URL: http://dx.doi.org/10.1038/s41550-019-0906-9.

[90] A. Rajantie. "Magnetic monopoles in field theory and cosmology". In: *Philosophical Transactions of the Royal Society A: Mathematical, Physical and Engineering Sciences* 370.1981 (2012), pp. 5705–5717. DOI: 10.1098/rsta.2011.0394. URL: http://dx.doi.org/10.1098/rsta.2011.0394.

[91] S. Capozziello and V. Faraoni. *Beyond Einstein Gravity; a survey of Gravitational Theories for Cosmology and Astrophisics*. Fundamental theories of physics. Springer, Berlino, 2011.

[92] L. M Sokolowski. "Metric gravity theories and cosmology: I. Physical interpretation and viability". In: *Classical and Quantum Gravity* 24.13 (2007), pp. 3391–3411. DOI: 10.1088/0264-9381/24/13/015. URL: http://dx.doi.org/10.1088/0264-9381/24/13/015.

[93] L. M Sokolowski. “Metric gravity theories and cosmology: II. Stability of a ground state in f(R) theories”. In: *Classical and Quantum Gravity* 24.14 (2007), pp. 3713–3734. DOI: 10.1088/0264-9381/24/14/011. URL: http://dx.doi.org/10.1088/0264-9381/24/14/011.

[94] A. H. Guth, David I. Kaiser, and Yasunori Nomura. “Inflationary paradigm after Planck 2013”. In: *Physics Letters B* 733 (2014), pp. 112–119. DOI: 10.1016/j.physletb.2014.03.020. URL: http://dx.doi.org/10.1016/j.physletb.2014.03.020.

[95] S Gottlober, H -J Schmidt, and A A Starobinsky. “Sixth-order gravity and conformal transformations”. In: *Classical and Quantum Gravity* 7.5 (1990). DOI: 10.1088/0264-9381/7/5/018.

[96] L. Amendola et al. “Generalized sixth-order gravity and inflation”. In: *Classical and Quantum Gravity.* 10.5 (1993). DOI: 10.1088/0264-9381/10/5/001.

[97] A. H Guth. “Inflationary universe: A possible solution to the horizon and flatness problems”. In: *Physics Letters D* 23 (1981), pp. 347–356. DOI: 10.1103/PhysRevD.23.347.

[98] L. Amendola et al. “Coupling first order phase transitions to curvature squared inflation”. In: *Physical Review D* 45.2 (1992), pp. 417–425. DOI: 10.1103/PhysRevD.45.417.

[99] H. E. S. Velten, R. F. vom Marttens, and W. Zimdahl. “Aspects of the cosmological "coincidence problem"”. In: *The European Physical Journal C* 74.11 (2014). DOI: 10.1140/epjc/s10052-014-3160-4. URL: http://dx.doi.org/10.1140/epjc/s10052-014-3160-4.

[100] P. J. E. Peebles and B. Ratra. “Cosmology with a Time-Variable Cosmological “Constant””. In: *Astrophysical Journal Letters* 325 (1988), p. L17. DOI: 10.1086/185100.

[101] B. Ratra and P. J. E. Peebles. “Cosmological consequences of a rolling homogeneous scalar field”. In: *Physical Review D* 37 (1988), pp. 3406–3427. DOI: 10.1103/PhysRevD.37.3406.

[102] E. J. Copeland, M. Sami, and S. Tsujikawa. “Dynamics Of Dark Energy”. In: *International Journal of Modern Physics D* 15.11 (2006), pp. 1753–1935. DOI: 10.1142/S021827180600942X.

[103] E. Piedipalumbo et al. “A matter-dominated cosmological model with variable G and Λ and its confrontation with observational data”. In: *General Relativity and Gravitation* 44.10 (2012), pp. 2477–2501. DOI: 10.1007/s10714-012-1409-5. URL: http://dx.doi.org/10.1007/s10714-012-1409-5.

[104] S.A. Bonometto, M. Mezzetti, and R. Mainini. “Strongly coupled dark energy with warm dark matter vs. LCDM”. In: *Journal of Cosmology and Astroparticle Physics* 2017.10 (2017), pp. 011–011. DOI: 10.1088/1475-7516/2017/10/011. URL: http://dx.doi.org/10.1088/1475-7516/2017/10/011.

[105] S. Nojiri and S. D. Odintsov. “Modified f(R)gravity consistent with realistic cosmology: From a matter dominated epoch to a dark energy universe”. In: *Physical Review D* 74.8 (2006), p. 086005. DOI: 10.1103/physrevd.74.086005. URL: https://doi.org/10.1103/physrevd.74.086005.

[106] A. Lue, R. Scoccimarro, and G. Starkman. “Differentiating between modified gravity and dark energy”. In: *Physical Review D* 69.15 (2004), p. 044005. DOI: 10.1103/physrevd.69.044005. URL: https://doi.org/10.1103/physrevd.69.044005.

[107] S. Capozziello and F. Bajardi. “Nonlocal gravity cosmology: An overview”. In: *International Journal of Modern Physics D* 31.06 (2021). DOI: 10.1142/s0218271822300099. URL: https://doi.org/10.1142/0218271822300099.

[108] S. Capozziello et al. “Matching torsion Lambda - term with observations”. In: *International Journal of Modern Physics D* 12.3 (2003), pp. 381–394. DOI: 10.1142/S0218271803003074. URL: https://doi.org/10.1142/s0218271803003074.

[109] B. Li and J. D. Barrow. “Cosmology of f(R) gravity in the metric variational approach”. In: *Physical Review D* 75.8 (2007), p. 104047. DOI: 10.1103/PhysRevD.75.084010. URL: https://doi.org/10.1103/physrevd.76.104047.

[110] A. G. Riess et al. “Large Magellanic Cloud Cepheid Standards Provide a 1% Foundation for the Determination of the Hubble Constant and Stronger Evidence for Physics beyond ΛCDM”. In: *The Astrophysical Journal* 876.1 (2019), p. 85. DOI: 10.3847/1538-4357/ab1422. URL: https://doi.org/10.3847/1538-4357/ab1422.

[111] S. Dhawan, S. W. Jha, and B. Leibundgut. "Measuring the Hubble constant with Type Ia supernovae as near-infrared standard candles". In: *Astronomy & Astrophysics* 609 (2018), A72. DOI: 10.1051/0004-6361/201731501. URL: https://doi.org/10.1051/0004-6361/201731501.

[112] L. Verde, T. Treu, and A. G. Riess. "Tensions between the early and late Universe". In: *Nature Astronomy* 3.10 (2019), pp. 891–895. DOI: 10.1038/s41550-019-0902-0. URL: https://doi.org/10.1038/s41550-019-0902-0.

[113] A. G. Riess. "The expansion of the Universe is faster than expected". In: *Nature Reviews Physics* 2.1 (2019), pp. 10–12. DOI: 10.1038/s42254-019-0137-0. URL: https://doi.org/10.1038/s42254-019-0137-0.

[114] E. Di Valentino et al. "In the realm of the Hubble tension-a review of solutions". In: *Classical and Quantum Gravity* 38.15 (2021), p. 153001. DOI: 10.1088/1361-6382/ac086d. URL: https://doi.org/10.1088/1361-6382/ac086d.

[115] A. G. Riess et al. "Cosmic Distances Calibrated to 1% Precision with Gaia EDR3 Parallaxes and Hubble Space Telescope Photometry of 75 Milky Way Cepheids Confirm Tension with ΛCDM". In: *The Astrophysical Journal Letters* 908.1 (2021), p. L6. DOI: 10.3847/2041-8213/abdbaf. URL: https://doi.org/10.3847/2041-8213/abdbaf.

[116] S. Capozziello, P. K S Dunsby, and O. Luongo. "Model-independent reconstruction of cosmological accelerated-decelerated phase". In: *Monthly Notices of the Royal Astronomical Society* 509.4 (2021), pp. 5399–5415. DOI: 10.1093/mnras/stab3187. URL: https://doi.org/10.1093/mnras/stab3187.

[117] G. Bargiacchi et al. "Cosmography by orthogonalized logarithmic polynomials". In: *Astronomy & Astrophysics* 649 (2021), A65. DOI: 10.1051/0004-6361/202140386. URL: https://doi.org/10.1051/0004-6361/202140386.

[118] R. Arjona and S. Nesseris. "What can machine learning tell us about the background expansion of the Universe?" In: *Physical Review D* 101.12 (2020), p. 123525. DOI: 10.1103/physrevd.101.123525. URL: https://doi.org/10.1103/physrevd.101.123525.

[119] M. Moresco et al. “Unveiling the Universe with Emerging Cosmological Probes”. In: *Living Reviews in Relativity* 25.1 (2022). DOI: 10.1007/s41114-022-00040-z. URL: https://doi.org/10.1007/s41114-022-00040-z.

[120] The LIGO Scientific Collaboration et al. “Constraints on the cosmic expansion history from GWTC-3”. In: (2021). DOI: 10.48550/ARXIV.2111.03604. URL: https://arxiv.org/abs/2111.03604.

[121] A. Palmese et al. “A standard siren measurement of the Hubble constant using gravitational wave events from the first three LIGO/Virgo observing runs and the DESI Legacy Survey”. In: *The Astrophysical Journal* 943.1 (2023), p. 56. DOI: 10.3847/1538-4357/aca6e3. URL: https://iopscience.iop.org/article/10.3847/1538-4357/aca6e3.

[122] A. Challinor. “CMB anisotropy science: a review”. In: *Proceedings of the International Astronomical Union* 8.S288 (2012).
, pp. 42–52. DOI: 10.1017/s1743921312016663. URL: https://doi.org/10.1017/s1743921312016663.

[123] S. Carloni et al. “Non minimally coupled condensate cosmologies: matching observational data with phase space”. In: *Journal of Cosmology and Astroparticle Physics* 2019.09 (2019), pp. 014–014. DOI: 10.1088/1475-7516/2019/09/014. URL: https://doi.org/10.1088/1475-7516/2019/09/014.

[124] D. Psaltis. “Probes and Tests of Strong-Field Gravity with Observations in the Electromagnetic Spectrum”. In: *Living Reviews in Relativity* 11.9 (2008). DOI: 10.12942/lrr-2008-9. URL: https://doi.org/10.12942/lrr-2008-9.

[125] B. P. Abbott et al. “GW170817: Observation of Gravitational Waves from a Binary Neutron Star Inspiral”. In: *Physical Review Letters* 119.16 (2017), p. 161101. DOI: 10.1103/physrevlett.119.161101. URL: https://doi.org/10.1103/physrevlett.119.161101.

[126] C. M. Will. *The Confrontation between General Relativity and Experiment*. Springer, Berlino, 2006.

[127] J. R. Oppenheimer and H. Snyder. “On Continued Gravitational Contraction”. In: *Physical Review letters* 56.5 (1939), pp. 455–459.

[128] R. Abbott et al. "Properties and Astrophysical Implications of the 150 $M_\odot$ Binary Black Hole Merger GW190521". In: *The Astrophysical Journal* 900.1 (2020), p. L13. DOI: 10.3847/2041-8213/aba493. URL: https://doi.org/10.3847/2041-8213/aba493.

[129] N.-B. Zhang and B.-A. Li. "Implications of the Mass $M = 2.17^{+0.11}_{-0.10} M_\odot$ of PSR J0740+6620 on the Equation of State of Super-dense Neutron-rich Nuclear Matter". In: *The Astrophysical Journal* 879.2 (2019), p. 99. DOI: 10.3847/1538-4357/ab24cb. URL: https://doi.org/10.3847/1538-4357/ab24cb.

[130] A. Wojnar. "White dwarf stars in modified gravity". In: *International Journal of Geometric Methods in Modern Physics* 18.supp01 (2021), p. 2140006. DOI: 10.1142/s0219887821400065. URL: https://doi.org/10.1142/s0219887821400065.

[131] A. V. Astashenok, S. Capozziello, and S. D. Odintsov. "Extreme neutron stars from Extended Theories of Gravity". In: *Journal of Cosmology and Astroparticle Physics* 2015.01 (2015), pp. 001–001. DOI: 10.1088/1475-7516/2015/01/001. URL: https://doi.org/10.1088/1475-7516/2015/01/001.

[132] A.V. Astashenok et al. "Causal limit of neutron star maximum mass in f(R) gravity in view of GW190814". In: *Physics Letters B* 816 (2021), p. 136222. DOI: 10.1016/j.physletb.2021.136222. URL: https://doi.org/10.1016/j.physletb.2021.136222.

[133] S. Capozziello et al. "Mass-radius relation for neutron stars in $f(R)$ gravity". In: *Physical Review D* 93.2 (2016), p. 023501. DOI: 10.1103/physrevd.93.023501. URL: https://doi.org/10.1103/physrevd.93.023501.

[134] G. J. Olmo, D. Rubiera-Garcia, and A. Wojnar. "Stellar structure models in modified theories of gravity: Lessons and challenges". In: *Physics Reports* 876 (2020), pp. 1–75. DOI: 10.1016/j.physrep.2020.07.001. URL: https://doi.org/10.1016/j.physrep.2020.07.001.

[135] Sarah A. Brands et al. "The R136 star cluster dissected with Hubble Space Telescope/STIS. III. The most massive stars and their clumped winds". In: *Astronomy & Astrophysics* 663 (2022), A36. DOI: 10.1051/0004-6361/202142742. URL: https://doi.org/10.1051/0004-6361/202142742.

[136] S.-W. Wu et al. “The massive stellar population of W49: A spectroscopic survey”. In: *Astronomy & Astrophysics* 589 (2016), A16. DOI: 10.1051/0004-6361/201527823. URL: https://doi.org/10.1051/0004-6361/201527823.

[137] D. F. Figer. “An upper limit to the masses of stars”. In: *Nature* 434.7030 (2005), pp. 192–194. DOI: 10.1038/nature03293. URL: https://doi.org/10.1038/nature03293.

[138] A. Wojnar. “Polytropic stars in Palatini gravity”. In: *The European Physical Journal C* 79.1 (2019). DOI: 10.1140/epjc/s10052-019-6555-4. URL: https://doi.org/10.1140/epjc/s10052-019-6555-4.

[139] J. Sakstein. “Stellar oscillations in modified gravity”. In: *Physical Review D* 88.12 (2013), p. 124013. DOI: 10.1103/physrevd.88.124013. URL: https://doi.org/10.1103/physrevd.88.124013.

[140] B. Jain, V. Vikram, and J. Sakstein. “Astrophysical tests of modified gravity: constraints from distance indicators in the nearby Universe”. In: *The Astrophysical Journal* 779.1 (2013), p. 39. DOI: 10.1088/0004-637x/779/1/39. URL: https://doi.org/10.1088/0004-637x/779/1/39.

[141] M. De Laurentis, I. De Martino, and R. Lazkoz. “Modified gravity revealed along geodesic tracks”. In: *The European Physical Journal C* 78.11 (2018). DOI: 10.1140/epjc/s10052-018-6401-0. URL: https://doi.org/10.1140/epjc/s10052-018-6401-0.

[142] D. Borka et al. “Estimating the Parameters of Extended Gravity Theories with the Schwarzschild Precession of S2 Star”. In: *Universe* 7.11 (2021), p. 407. DOI: 10.3390/universe7110407. URL: https://doi.org/10.3390/universe7110407.

[143] A. D’Addio. “S-star dynamics through a Yukawa-like gravitational potential”. In: *Physics of the Dark Universe* 33 (2021). DOI: 10.1016/j.dark.2021.100871.

[144] A. D’Addio et al. “Orbits in bootstrapped Newtonian gravity”. In: *Physical Review D* 105.10 (2022), p. 104010. DOI: 10.1103/physrevd.105.104010. URL: https://doi.org/10.1103/physrevd.105.104010.

[145] F. B. Bianco et al. “Multi-color Optical and Near-infrared Light Curves of 64 Stripped-envelope Core-Collapse Supernovae”. In: *The Astrophysical Journal Supplement Series* 213.2 (2014), p. 19. DOI: 10.1088/0067-0049/213/2/19. URL: https://doi.org/10.1088/0067-0049/213/2/19.

[146] H. B. Perets et al. “A faint type of supernova from a white dwarf with a helium-rich companion”. In: *Nature* 465.7296 (2010), pp. 322–325. DOI: 10.1038/nature09056. URL: https://doi.org/10.1038/nature09056.

[147] W. Hillebrandt and J. C. Niemeyer. “Type Ia Supernova Explosion Models”. In: *Annual Review of Astronomy and Astrophysics* 38.1 (2000), pp. 191–230. DOI: 10.1146/annurev.astro.38.1.191. URL: https://doi.org/10.1146/annurev.astro.38.1.191.

[148] D. Maoz, F. Mannucci, and G. Nelemans. “Observational Clues to the Progenitors of Type Ia Supernovae”. In: *Annual Review of Astronomy and Astrophysics* 52.1 (2014), pp. 107–170. DOI: 10.1146/annurev-astro-082812-141031. URL: https://doi.org/10.1146/annurev-astro-082812-141031.

[149] K. Nomoto, F.-K. Thielemann, and K. Yokoi. “Accreting white dwarf models for type I supern. III. Carbon deflagration supernovae.” In: *Astrophysical Journal* 286 (1984), pp. 644–658. DOI: 10.1086/162639.

[150] S. A. Colgate and C. McKee. “Early Supernova Luminosity.” In: *Astrophysical Journal* 157 (1969), p. 623. DOI: 10.1086/150102.

[151] S. M. Carroll. “The Cosmological Constant”. In: *Living Reviews in Relativity* 4.1, 1 (2001), p. 1. DOI: 10.12942/lrr-2001-1. URL: https://doi.org/10.12942/lrr-2001-1.

[152] A. V. Filippenko et al. “The Peculiar Type IA SN 1991T: Detonation of a White Dwarf?” In: *Astrophysical Journal Letters* 384 (1992), p. L15. DOI: 10.1086/186252.

[153] A. V. Filippenko et al. “The Subluminous, Spectroscopically Peculiar Type 1a Supernova 1991bg in the Elliptical Galaxy NGC 4374”. In: *Astrophysical Journal* 104 (1992), p. 1543. DOI: 10.1086/116339.

[154] A. M. Khokhlov. “Delayed detonation model for type IA supernovae”. In: *Astronomy and Astrophysics* 245.1 (1991), pp. 114–128.

[155] S. Perlmutter et al. “Cosmology From Type IA Supernovae: Measurements, Calibration Techniques, and Implications”. In: *American Astronomical Society Meeting Abstracts*. Vol. 191. American Astronomical Society Meeting Abstracts. 1997, 85.04, p. 85.04. arXiv: astro-ph/9812473 [astro-ph].

[156] X. Meng, Y. Gao, and Z. Han. "SNe Ia as a cosmological probe". In: *International Journal of Modern Physics D* 24.14 (2015), p. 1530029. DOI: 10.1142/s0218271815300293. URL: https://doi.org/10.1142/s0218271815300293.

[157] M. Hamuy et al. "The Absolute Luminosities of the Calan/Tololo Type IA Supernovae". In: *The Astronomical Journal* 112 (1996), p. 2391. DOI: 10.1086/118190. URL: https://doi.org/10.1086/118190.

[158] A. G. Riess et al. "BVRI Light Curves for 22 Type Ia Supernovae". In: *The Astronomical Journal* 117.2 (1999), pp. 707–724. DOI: 10.1086/300738. URL: https://doi.org/10.1086/300738.

[159] S. Jha et al. "UBVRI Light Curves of 44 Type Ia Supernovae". In: *The Astronomical Journal* 131.1 (2006), pp. 527–554. DOI: 10.1086/497989. URL: https://doi.org/10.1086/497989.

[160] M. Hicken et al. "Improved Dark Energy Constraints from 100 New CfA Supernova Type Ia Light Curves". In: *The Astrophysical Journal* 700.2 (2009), pp. 1097–1140. DOI: 10.1088/0004-637x/700/2/1097. URL: https://doi.org/10.1088/0004-637x/700/2/1097.

[161] M. Hicken et al. "CfA3: 185 Type Ia Supernova Light Curves from the CfA". In: *The Astrophysical Journal* 700.1 (2009), pp. 331–357. DOI: 10.1088/0004-637x/700/1/331. URL: https://doi.org/10.1088/0004-637x/700/1/331.

[162] M. Hicken et al. "CfA4: Light Curves for 94 Type Ia Supernovae". In: *The Astrophysical Journal Supplement Series* 200.2 (2012), p. 12. DOI: 10.1088/0067-0049/200/2/12. URL: https://doi.org/10.1088/0067-0049/200/2/12.

[163] C. Contreras et al. "The Carnegie Supernova Project: First Photometry Data Release of Low-Redshift Type Ia Supernovae". In: *The Astronomical Journal* 139.2 (2010), pp. 519–539. DOI: 10.1088/0004-6256/139/2/519. URL: https://doi.org/10.1088/0004-6256/139/2/519.

[164] M.Ganeshalingam, W. Li, and A. V. Filippenko. "Constraints on dark energy with the LOSS SN Ia sample". In: *Monthly Notices of the Royal Astronomical Society* 433.3 (2013), pp. 2240–2258. DOI: 10.1093/mnras/stt893. URL: https://doi.org/10.1093/mnras/stt893.

[165] G. Narayan et al. “Light Curves of 213 Type Ia Supernovae from the ESSENCE Survey”. In: *The Astrophysical Journal Supplement Series* 224.1 (2016), p. 3. DOI: 10.3847/0067-0049/224/1/3. URL: https://doi.org/10.3847/0067-0049/224/1/3.

[166] M. Sullivan et al. “SNLS3: Constraints on Dark Energy Combining the Supernova Legacy Survey Three-year Data with Other Probes”. In: *The Astrophysical Journal* 737.2 (2011), p. 102. DOI: 10.1088/0004-637x/737/2/102. URL: https://doi.org/10.1088/0004-637x/737/2/102.

[167] R. Kessler et al. “First-year Sloan Digital Sky Survey-II (SDSS-II) Supernova Results: Hubble Diagram and Cosmological Parameters”. In: *The Astrophysical Journal Supplement Series* 185.1 (2009), pp. 32–84. DOI: 10.1088/0067-0049/185/1/32. URL: https://doi.org/10.1088/0067-0049/185/1/32.

[168] A. Rest et al. “Cosmological Constraints from Measurements of Type Ia Supernovae discovered during the first 1.5 years of the Pan-STARRS1 Survey”. In: *The Astrophysical Journal* 795.1 (2014), p. 44. DOI: 10.1088/0004-637x/795/1/44. URL: https://doi.org/10.1088/0004-637x/795/1/44.

[169] N. Suzuki et al. “The Hubble Space Telescope Cluster Supernova Survey: V. Improving the Dark Energy Constraints Above z>1 and Building an Early-Type-Hosted Supernova Sample”. In: *The Astrophysical Journal* 746.1 (2012), p. 85. DOI: 10.1088/0004-637x/746/1/85. URL: https://doi.org/10.1088/0004-637x/746/1/85.

[170] A. G. Riess et al. “New Hubble Space Telescope Discoveries of Type Ia Supernovae at z $\geq$ 1: Narrowing Constraints on the Early Behavior of Dark Energy”. In: *The Astrophysical Journal* 659.1 (2007), pp. 98–121. DOI: 10.1086/510378. URL: https://doi.org/10.1086/510378.

[171] S. A. Rodney et al. “Type Ia Supernova Rate Measurements to Redshift 2.5 from CANDELS : Searching for Prompt Explosions in the Early Universe”. In: *The Astronomical Journal* 148.1 (2014), p. 13. DOI: 10.1088/0004-6256/148/1/13. URL: https://doi.org/10.1088/0004-6256/148/1/13.

[172] O. Graur et al. “Type-Ia Supernova Rates to Redshift 2.4 from CLASH: The Cluster Lensing And Supernova Survey with Hubble”. In: *The Astrophysical Journal* 783.1 (2014), p. 28. DOI: 10.1088/0004-637x/783/1/28. URL: https://doi.org/10.1088/0004-637x/783/1/28.

[173] D. Brout et al. “The Pantheon+ Analysis: Cosmological Constraints”. In: *The Astrophysical Journal* 938.2 (2022), p. 110. DOI: 10.3847/1538-4357/ac8e04. URL: https://doi.org/10.3847/1538-4357/ac8e04.

[174] N. Gehrels et al. “The Swift Gamma-Ray Burst Mission”. In: *The Astrophysical Journal* 611.2 (2004), pp. 1005–1020. DOI: 10.1086/422091. URL: https://doi.org/10.1063/1.1810924.

[175] E. P. Mazets et al. “Catalog of cosmic gamma-ray bursts from the KONUS experiment data”. In: *Astrophysics and Space Science* 80.1 (1981), pp. 3–83. DOI: 10.1007/BF00649140.

[176] C. Kouveliotou et al. “Identification of Two Classes of Gamma-Ray Bursts”. In: *Astrophysical Journal Letters* 413 (1993), p. L101. DOI: 10.1086/186969.

[177] C. A. Meegan et al. “Spatial distribution of γ-ray bursts observed by BATSE”. In: *Nature* 355.6356 (1992), pp. 143–145. DOI: 10.1038/355143a0.

[178] D. Band et al. “BATSE Observations of Gamma-Ray Burst Spectra. I. Spectral Diversity”. In: *Astrophysical Journal* 413 (1993), p. 281. DOI: 10.1086/172995.

[179] M. S. Briggs et al. “Observations of GRB 990123 by the Compton Gamma Ray Observatory”. In: *The Astrophysical Journal* 524.1 (1999), pp. 82–91. DOI: 10.1086/307808. URL: https://doi.org/10.1086/307808.

[180] E. Troja et al. “Swift Observations of GRB 070110: An Extraordinary X-Ray Afterglow Powered by the Central Engine”. In: *The Astrophysical Journal* 665.1 (2007), pp. 599–607. DOI: 10.1086/519450. URL: https://doi.org/10.1086/519450.

[181] A. Nicuesa Guelbenzu et al. “GRB 090426: Discovery of a jet break in a short burst afterglow”. In: *Astronomy & Astrophysics* 531 (2011), p. L6. DOI: 10.1051/0004-6361/201116657. URL: https://doi.org/10.1051/0004-6361/201116657.

[182] A. Panaitescu et al. “Evidence for chromatic X-ray light-curve breaks in Swift gamma-ray burst afterglows and their theoretical implications”. In: *Monthly Notices of the Royal Astronomical Society* 369.4 (2006), pp. 2059–2064. DOI: 10.1111/j.1365-2966.2006.10453.x. URL: https://doi.org/10.1111/j.1365-2966.2006.10453.x.

[183] E. Troja et al. “The X-ray counterpart to the gravitational-wave event GW170817”. In: *Nature* 551.7678 (2017), pp. 71–74. DOI: 10.1038/nature24290. URL: https://doi.org/10.1038/nature24290.

[184] B. D. Metzger et al. “Electromagnetic counterparts of compact object mergers powered by the radioactive decay of r-process nuclei”. In: *Monthly Notices of the Royal Astronomical Society* 406.4 (2010), pp. 2650–2662. DOI: 10.1111/j.1365-2966.2010.16864.x. URL: https://doi.org/10.1111/j.1365-2966.2010.16864.x.

[185] J. S. Bloom et al. “The unusual afterglow of the γ-ray burst of 26 March 1998 as evidence for a supernova connection”. In: *Nature* 401.6752 (1999), pp. 453–456. DOI: 10.1038/46744. URL: https://doi.org/10.1038/46744.

[186] B. Zhang et al. “Physical Processes Shaping Gamma-Ray Burst X-Ray Afterglow Light Curves: Theoretical Implications from the Swift X-Ray Telescope Observations”. In: *The Astrophysical Journal* 642.1 (2006), pp. 354–370. DOI: 10.1086/500723. URL: https://doi.org/10.1086/500723.

[187] R. Willingale et al. “Testing the Standard Fireball Model of Gamma-Ray Bursts Using Late X-Ray Afterglows Measured by Swift”. In: *The Astrophysical Journal* 662.2 (2007), pp. 1093–1110. DOI: 10.1086/517989. URL: https://doi.org/10.1086/517989.

[188] N. Lyons et al. “Can X-ray emission powered by a spinning-down magnetar explain some gamma-ray burst light-curve features?” In: *Monthly Notices of the Royal Astronomical Society* 402.2 (2010), pp. 705–712. DOI: 10.1111/j.1365-2966.2009.15538.x. URL: https://doi.org/10.1111/j.1365-2966.2009.15538.x.

[189] R. Narayan, B. Paczynski, and T. Piran. “Gamma-ray bursts as the death throes of massive binary stars”. In: *The Astrophysical Journal* 395 (1992), p. L83. DOI: 10.1086/186493. URL: https://doi.org/10.1086/186493.

[190] S. E. Woosley. “Gamma-Ray Bursts from Stellar Mass Accretion Disks around Black Holes”. In: *The Astrophysical Journal* 405 (1993), p. 273. DOI: 10.1086/172359.

[191] B. Zhang et al. “Discerning the Physical Origins of Cosmological Gamma-ray Bursts Based on Multiple Observational Criteria: The Cases of z = 6.7 GRB 080913, z = 8.2 GRB 090423, and Some Short/Hard GRBs”. In: *The Astrophysical Journal* 703.2 (2009), pp. 1696–1724. DOI: 10.1088/0004-637x/703/2/1696. URL: https://doi.org/10.1088/0004-637x/703/2/1696.

[192] Z. G. Dai and T. Lu. "Gamma-Ray Bursts and Afterglows from Rotating Strange Stars and Neutron Stars". In: *Physical Review Letters* 81.20 (1998), pp. 4301–4304. DOI: 10.1103/physrevlett.81.4301. URL: https://doi.org/10.1103/physrevlett.81.4301.

[193] R. A. Chevalier and Z.-Y. Li. "Wind Interaction Models for Gamma-Ray Burst Afterglows: The Case for Two Types of Progenitors". In: *The Astrophysical Journal* 536.1 (2000), pp. 195–212. DOI: 10.1086/308914. URL: https://doi.org/10.1086/308914.

[194] T. Liu et al. "Comparison of Gravitational Waves from Central Engines of Gamma-Ray Bursts: Neutrino-dominated Accretion Flows, Blandford-Znajek Mechanisms, and Millisecond Magnetars". In: *The Astrophysical Journal* 850.1 (2017), p. 30. DOI: 10.3847/1538-4357/aa92c4. URL: https://doi.org/10.3847/1538-4357/aa92c4.

[195] G. Stratta et al. "On the Magnetar Origin of the GRBs Presenting X-Ray Afterglow Plateaus". In: *The Astrophysical Journal* 869.2 (2018), p. 155. DOI: 10.3847/1538-4357/aadd8f. URL: https://doi.org/10.3847/1538-4357/aadd8f.

[196] B. Gendre et al. "The Ultra-long Gamma-Ray Burst 111209A: The Collapse of a Blue Supergiant?" In: *The Astrophysical Journal* 766.1 (2013), p. 30. DOI: 10.1088/0004-637x/766/1/30. URL: https://doi.org/10.1088/0004-637x/766/1/30.

[197] L. Piro et al. "A hot cocoon in the ultralong GRB 130925A: hints of a PopIII-like progenitor in a low density wind environment". In: *The Astrophysical Journal* 790.2 (2014), p. L15. DOI: 10.1088/2041-8205/790/2/l15. URL: https://doi.org/10.1088/2041-8205/790/2/l15.

[198] J. P. Norris, N. Gehrels, and J. D. Scargle. "Threshold for Extended Emission in Short Gamma-Ray Bursts". In: *The Astrophysical Journal* 717.1 (2010), pp. 411–419. DOI: 10.1088/0004-637x/717/1/411. URL: https://doi.org/10.1088/0004-637x/717/1/411.

[199] L. Amati et al. "Intrinsic spectra and energetics of BeppoSAX Gamma-Ray Bursts with known redshifts". In: *Astronomy & Astrophysics* 390.1 (2002), pp. 81–89. DOI: 10.1051/0004-6361:20020722. URL: https://doi.org/10.1051/0004-6361:20020722.

[200] L. Amati. "The Ep,i-Eiso correlation in gamma-ray bursts: updated observational status, re-analysis and main implications". In: *Monthly Notices of the Royal Astronomical Society* 372.1 (2006), pp. 233–245. DOI: 10.1111/j.1365-2966.2006.10840.x. URL: https://doi.org/10.1111/j.1365-2966.2006.10840.x.

[201] L. Amati et al. "Addressing the circularity problem in the Ep-Eiso correlation of gamma-ray bursts". In: *Monthly Notices of the Royal Astronomical Society: Letters* 486.1 (2019), pp. L46–L51. DOI: 10.1093/mnrasl/slz056. URL: https://doi.org/10.1093/mnrasl/slz056.

[202] E. Nakar and T. Piran. "Outliers to the peak energy-isotropic energy relation in gamma-ray bursts". In: *Monthly Notices of the Royal Astronomical Society: Letters* 360.1 (2005), pp. L73–L76. DOI: 10.1111/j.1745-3933.2005.00049.x. URL: https://doi.org/10.1111/j.1745-3933.2005.00049.x.

[203] G. Ghirlanda et al. "The Epeak-Eiso plane of long gamma-ray bursts and selection effects". In: *Monthly Notices of the Royal Astronomical Society* 387.1 (2008), pp. 319–330. DOI: 10.1111/j.1365-2966.2008.13232.x. URL: https://doi.org/10.1111/j.1365-2966.2008.13232.x.

[204] D. M. Wei and W. H. Gao. "Are there cosmological evolution trends on gamma-ray burst features?" In: *Monthly Notices of the Royal Astronomical Society* 345.3 (2003), pp. 743–746. DOI: 10.1046/j.1365-8711.2003.06971.x. URL: https://doi.org/10.1046/j.1365-8711.2003.06971.x.

[205] D. Yonetoku et al. "Gamma-Ray Burst Formation Rate Inferred from the Spectral Peak Energy-Peak Luminosity Relation". In: *The Astrophysical Journal* 609.2 (2004), pp. 935–951. DOI: 10.1086/421285. URL: https://doi.org/10.1086/421285.

[206] G. Ghirlanda et al. "Short versus long gamma-ray bursts: spectra, energetics, and luminosities". In: *Astronomy & Astrophysics* 496.3 (2009), pp. 585–595. DOI: 10.1051/0004-6361/200811209. URL: https://doi.org/10.1051/0004-6361/200811209.

[207] G. Ghirlanda, G. Ghisellini, and D. Lazzati. "The Collimation-corrected Gamma-Ray Burst Energies Correlate with the Peak Energy of Their νF_ν Spectrum". In: *The Astrophysical Journal* 616.1 (2004), pp. 331–338. DOI: 10.1086/424913. URL: https://doi.org/10.1086/424913.

[208] E. Liang and B. Zhang. "Model-independent Multivariable Gamma-Ray Burst Luminosity Indicator and Its Possible Cosmological Implications". In: *The Astrophysical Journal* 633.2 (2005), pp. 611–623. DOI: 10.1086/491594. URL: https://doi.org/10.1086/491594.

[209] C. Firmani et al. "Discovery of a tight correlation among the prompt emission properties of long gamma-ray bursts". In: *Monthly Notices of the Royal Astronomical Society* 370.1 (2006), pp. 185–197. DOI: 10.1111/j.1365-2966.2006.10445.x. URL: https://doi.org/10.1111/j.1365-2966.2006.10445.x.

[210] D. A. Frail et al. "Beaming in Gamma-Ray Bursts: Evidence for a Standard Energy Reservoir". In: *The Astrophysical Journal* 562.1 (2001), pp. L55–L58. DOI: 10.1086/338119. URL: https://doi.org/10.1086/338119.

[211] J. P. Norris, G. F. Marani, and J. T. Bonnell. "Connection between Energy-dependent Lags and Peak Luminosity in Gamma-Ray Bursts". In: *The Astrophysical Journal* 534.1 (2000), pp. 248–257. DOI: 10.1086/308725. URL: https://doi.org/10.1086/308725.

[212] D. E. Reichart et al. "A Possible Cepheid-like Luminosity Estimator for the Long Gamma-Ray Bursts". In: *The Astrophysical Journal* 552.1 (2001), pp. 57–71. DOI: 10.1086/320434. URL: https://doi.org/10.1086/320434.

[213] V. F. Cardone, S. Capozziello, and M. G. Dainotti. "An updated gamma-ray bursts Hubble diagram". In: *Monthly Notices of the Royal Astronomical Society* 400.2 (2009), pp. 775–790. DOI: 10.1111/j.1365-2966.2009.15456.x. URL: https://doi.org/10.1111/j.1365-2966.2009.15456.x.

[214] V. F. Cardone et al. "Constraining cosmological parameters by gamma-ray burst X-ray afterglow light curves". In: *Monthly Notices of the Royal Astronomical Society* 408.2 (2010), pp. 1181–1186. DOI: 10.1111/j.1365-2966.2010.17197.x. URL: https://doi.org/10.1111/j.1365-2966.2010.17197.x.

[215] M. G. Dainotti et al. "Determination of the intrinsic Luminosity Time Correlation in the X-ray Afterglows of GRBs". In: *The Astrophysical Journal* 774.2 (2013), p. 157. DOI: 10.1088/0004-637x/774/2/157. URL: https://doi.org/10.1088/0004-637x/774/2/157.

[216] M. G. Dainotti, V. F. Cardone, and S. Capozziello. "A time-luminosity correlation for γ-ray bursts in the X-rays". In: *Monthly Notices of the Royal Astronomical Society: Letters* 391.1 (2008), pp. L79–L83. DOI: 10.1111/j.1745-3933.

2008.00560.x. URL: https://doi.org/10.1111/j.1745-3933.2008.00560.x.

[217] M. G. Dainotti, M. Ostrowski, and R. Willingale. "Towards a standard gamma-ray burst: tight correlations between the prompt and the afterglow plateau phase emission". In: *Monthly Notices of the Royal Astronomical Society* 418.4 (2011), pp. 2202–2206. DOI: 10.1111/j.1365-2966.2011.19433.x. URL: https://doi.org/10.1111/j.1365-2966.2011.19433.x.

[218] M. Dainotti et al. "Luminosity-time and luminosity-luminosity correlations for GRB prompt and afterglow plateau emissions". In: *Monthly Notices of the Royal Astronomical Society* 451.4 (2015), pp. 3898–3908. DOI: 10.1093/mnras/stv1229. URL: https://doi.org/10.1093/mnras/stv1229.

[219] J. K. Cannizzo and N. Gehrels. "A New Paradigm for Gamma Ray Bursts: Long Term Accretion Rate Modulation by an External Accretion Disk". In: *The Astrophysical Journal* 700.2 (2009), pp. 1047–1058. DOI: 10.1088/0004-637x/700/2/1047. URL: https://doi.org/10.1088/0004-637x/700/2/1047.

[220] A. Rowlinson et al. "Signatures of magnetar central engines in short GRB light curves". In: *Monthly Notices of the Royal Astronomical Society* 430.2 (2013), pp. 1061–1087. DOI: 10.1093/mnras/sts683. URL: https://doi.org/10.1093/mnras/sts683.

[221] A. Rowlinson et al. "Constraining properties of GRB magnetar central engines using the observed plateau luminosity and duration correlation". In: *Monthly Notices of the Royal Astronomical Society* 443.2 (2014), pp. 1779–1787. DOI: 10.1093/mnras/stu1277. URL: https://doi.org/10.1093/mnras/stu1277.

[222] H. J. van Eerten. "Gamma-ray burst afterglow plateau break time-luminosity correlations favour thick shell models over thin shell models". In: *Monthly Notices of the Royal Astronomical Society* 445.3 (2014), pp. 2414–2423. DOI: 10.1093/mnras/stu1921. URL: https://doi.org/10.1093/mnras/stu1921.

[223] P. Beniamini et al. "X-ray plateaus in gamma-ray bursts' light curves from jets viewed slightly off-axis". In: *Monthly Notices of the Royal Astronomical Society* 492.2 (2020), pp. 2847–2857. DOI: 10.1093/mnras/staa070. URL: https://doi.org/10.1093/mnras/staa070.

[224] M. G. Dainotti et al. “The Optical Luminosity-Time Correlation for More than 100 Gamma-Ray Burst Afterglows”. In: *The Astrophysical Journal Letters* 905.2 (2020), p. L26. DOI: 10.3847/2041-8213/abcda9. URL: https://doi.org/10.3847/2041-8213/abcda9.

[225] S. R. Oates et al. “Exploring the canonical behaviour of long gamma-ray bursts using an intrinsic multiwavelength afterglow correlation”. In: *Monthly Notices of the Royal Astronomical Society* 453.4 (2015), pp. 4122–4136. DOI: 10.1093/mnras/stv1956. URL: https://doi.org/10.1093/mnras/stv1956.

[226] M. G. Dainotti et al. “A fundamental plane for long gamma-ray bursts with X-ray plateaus”. In: *The Astrophysical Journal* 825.2 (2016), p. L20. DOI: 10.3847/2041-8205/825/2/l20. URL: https://doi.org/10.3847/2041-8205/825/2/l20.

[227] M. G. Dainotti et al. “On the Existence of the Plateau Emission in High-energy Gamma-Ray Burst Light Curves Observed by Fermi-LAT”. In: *The Astrophysical Journal Supplement Series* 255.1 (2021), p. 13. DOI: 10.3847/1538-4365/abfe17. URL: https://doi.org/10.3847/1538-4365/abfe17.

[228] M. G. Dainotti et al. “Closure relations during the plateau emission of Swift GRBs and the fundamental plane”. In: *Publications of the Astronomical Society of Japan* 73.4 (2021), pp. 970–1000. DOI: 10.1093/pasj/psab057. URL: https://doi.org/10.1093/pasj/psab057.

[229] G. P. Srinivasaragavan et al. “On the Investigation of the Closure Relations for Gamma-Ray Bursts Observed by Swift in the Post-plateau Phase and the GRB Fundamental Plane”. In: *The Astrophysical Journal* 903.1 (2020), p. 18. DOI: 10.3847/1538-4357/abb702. URL: https://doi.org/10.3847/1538-4357/abb702.

[230] I. Contopoulos and A. Spitkovsky. “Revised Pulsar Spin-down”. In: *The Astrophysical Journal* 643.2 (2006), pp. 1139–1145. DOI: 10.1086/501161. URL: https://doi.org/10.1086/501161.

[231] J. Hjorth and J. S. Bloom. “The Gamma-Ray Burst - Supernova Connection”. In: (2011). DOI: 10.48550/ARXIV.1104.2274. URL: https://arxiv.org/abs/1104.2274.

[232] L. Xiao and B. E. Schaefer. “Estimating Redshifts for Long Gamma-Ray Bursts”. In: *The Astrophysical Journal* 707.1 (2009), pp. 387–403. DOI: 10.1088/0004-637X/707/1/387. URL: https://doi.org/10.1088/0004-637x/707/1/387.

[233] Y. Avni. "Energy spectra of X-ray clusters of galaxies." In: *The Astrophysical Journal* 210 (1976), pp. 642–646. DOI: 10.1086/154870.

[234] T. Sakamoto et al. "The Second Swift Burst Alert Telescope Gamma-Ray Burst Catalog". In: *The Astrophysical Journal Supplement Series* 195.1 (2011), p. 2. DOI: 10.1088/0067-0049/195/1/2. URL: https://doi.org/10.1088/0067-0049/195/1/2.

[235] E. M. Levesque et al. "GRB 090426: the environment of a rest-frame 0.35-s gamma-ray burst at a redshift of 2.609". In: *Monthly Notices of the Royal Astronomical Society* 401.2 (2010), pp. 963–972. DOI: 10.1111/j.1365-2966.2009.15733.x. URL: https://doi.org/10.1111/j.1365-2966.2009.15733.x.

[236] B. Gendre et al. "Can we quickly flag ultra-long gamma-ray bursts?" In: *Monthly Notices of the Royal Astronomical Society* 486.2 (2019), pp. 2471–2476. DOI: 10.1093/mnras/stz1036. URL: https://doi.org/10.1093/mnras/stz1036.

[237] L. Li et al. "Constraining the Type of Central Engine of GRBs with Swift Data". In: *The Astrophysical Journal Supplement Series* 236.2 (2018), p. 26. DOI: 10.3847/1538-4365/aabaf3. URL: https://doi.org/10.3847/1538-4365/aabaf3.

[238] D. A. Coulter et al. "Swope Supernova Survey 2017a (SSS17a), the optical counterpart to a gravitational wave source". In: *Science* 358.6370 (2017), pp. 1556–1558. DOI: 10.1126/science.aap9811. URL: https://doi.org/10.1126/science.aap9811.

[239] B. D. Metzger and E. Berger. "What is the Most Promising Electromagnetic Counterpart of a Neutron Star Binary Merger?" In: *The Astrophysical Journal* 746.1 (2012), p. 48. DOI: 10.1088/0004-637x/746/1/48. URL: https://doi.org/10.1088/0004-637x/746/1/48.

[240] H. Gao et al. "GRB 080503 late afterglow re-brightening: signature of a magnetar powered merger-nova". In: *The Astrophysical Journal* 807.2 (2015), p. 163. DOI: 10.1088/0004-637x/807/2/163. URL: https://doi.org/10.1088/0004-637x/807/2/163.

[241] H. Gao et al. "Searching for Magnetar-powered Merger-novae from Short GRBS". In: *The Astrophysical Journal* 837.1 (2017), p. 50. DOI: 10.3847/1538-4357/aa5be3. URL: https://doi.org/10.3847/1538-4357/aa5be3.

[242] A Rossi et al. “A comparison between short GRB afterglows and kilonova AT2017-gfo: shedding light on kilonovae properties”. In: *Monthly Notices of the Royal Astronomical Society* 493.3 (2020), pp. 3379–3397. DOI: 10.1093/mnras/staa479. URL: https://doi.org/10.1093/mnras/staa479.

[243] B. P. Gompertz et al. “The Diversity of Kilonova Emission in Short Gamma-Ray Bursts”. In: *The Astrophysical Journal* 860.1 (2018), p. 62. DOI: 10.3847/1538-4357/aac206. URL: https://doi.org/10.3847/1538-4357/aac206.

[244] J. S. Bloom, D. A. Frail, and R. Sari. “The Prompt Energy Release of Gamma-Ray Bursts using a Cosmological k-Correction”. In: *The Astronomical Journal* 121.6 (2001), pp. 2879–2888. DOI: 10.1086/321093. URL: https://doi.org/10.1086/321093.

[245] J. Torrado and A. Lewis. “Cobaya: code for Bayesian analysis of hierarchical physical models”. In: *Journal of Cosmology and Astroparticle Physics* 05 (2021), p. 057. DOI: 10.1088/1475-7516/2021/05/057. URL: https://doi.org/10.1088/1475-7516/2021/05/057.

[246] B.-B. Zhang et al. “How Long does a Burst Burst?” In: *The Astrophysical Journal* 787.1 (2014), p. 66. DOI: 10.1088/0004-637x/787/1/66. URL: https://doi.org/10.1088/0004-637x/787/1/66.

[247] B. D. Metzger. “Kilonovae”. In: *Living Reviews in Relativity* 20.1 (2017). DOI: 10.1007/s41114-017-0006-z. URL: https://doi.org/10.1007/s41114-017-0006-z.

[248] A. S. G. Robotham and D. Obreschkow. “Hyper-Fit: Fitting Linear Models to Multidimensional Data with Multivariate Gaussian Uncertainties”. In: *Publications of the Astronomical Society of Australia* 32 (2015). DOI: 10.1017/pasa.2015.33. URL: https://doi.org/10.1017/pasa.2015.33.

[249] J. R. Bond and G. Efstathiou. “The statistics of cosmic background radiation fluctuations”. In: *Monthly Notices of the Royal Astronomical Society* 226 (1987), pp. 655–687. DOI: 10.1093/mnras/226.3.655.

[250] D. J. Eisenstein and W. Hu. “Baryonic Features in the Matter Transfer Function”. In: *The Astrophysical Journal* 496.2 (1998), pp. 605–614. DOI: 10.1086/305424. URL: https://doi.org/10.1086/305424.

[251] S. Bashinsky and E. Bertschinger. "Position-Space Description of the Cosmic Microwave Background and Its Temperature Correlation Function". In: *Physical Review Letters* 87.8 (2001), p. 081301. DOI: 10.1103/physrevlett.87.081301. URL: https://doi.org/10.1103/physrevlett.87.081301.

[252] B. A. Bassett and R. Hlozek. "Baryon Acoustic Oscillations". In: (2009). DOI: 10.48550/ARXIV.0910.5224. URL: https://arxiv.org/abs/0910.5224.

[253] K. S. Dawson et al. "The Baryon Oscillation Spectroscopic Survey of SDSS-III". In: *The Astronomical Journal* 145.1 (2013), p. 10. DOI: 10.1088/0004-6256/145/1/10. URL: https://doi.org/10.1088/0004-6256/145/1/10.

[254] D. J. Eisenstein et al. "SDSS-III: Massive Spectroscopic Surveys of the Distant Universe, the Milky Way Galaxy, and Extra-Solar Planetary Systems". In: *The Astronomical Journal* 142.3 (2011), p. 72. DOI: 10.1088/0004-6256/142/3/72. URL: https://doi.org/10.1088/0004-6256/142/3/72.

[255] K. S. Dawson et al. "The SDSS-IV extended Baryon Oscillation Spectroscopic Survey: Overview and Early Data". In: *The Astronomical Journal* 151.2 (2016), p. 44. DOI: 10.3847/0004-6256/151/2/44. URL: https://doi.org/10.3847/0004-6256/151/2/44.

[256] Michael R. B. et al. "Sloan Digital Sky Survey IV: Mapping the Milky Way, Nearby Galaxies, and the Distant Universe". In: *The Astrophysical Journal* 154.1, 28 (2017), p. 28. DOI: 10.3847/1538-3881/aa7567. arXiv: 1703.00052 [astro-ph.GA].

[257] F. Beutler et al. "The 6dF Galaxy Survey: baryon acoustic oscillations and the local Hubble constant". In: *Monthly Notices of the Royal Astronomical Society* 416.4 (2011), pp. 3017–3032. DOI: 10.1111/j.1365-2966.2011.19250.x. URL: https://doi.org/10.1111/j.1365-2966.2011.19250.x.

[258] C. Blake et al. "The WiggleZ Dark Energy Survey: joint measurements of the expansion and growth history at z<1". In: *Monthly Notices of the Royal Astronomical Society* 425.1 (2012), pp. 405–414. DOI: 10.1111/j.1365-2966.2012.21473.x. URL: https://doi.org/10.1111/j.1365-2966.2012.21473.x.

[259] G. S. Sharov. "Observational constraints on cosmological models with Chaplygin gas and quadratic equation of state". In: *Journal of Cosmology and Astroparticle Physics* 2016.06 (2016), pp. 023–023. DOI: 10.1088/1475-7516/2016/06/023. URL: https://doi.org/10.1088/1475-7516/2016/06/023.

[260] G. S. Sharov and V. O. Vasiliev. "How predictions of cosmological models depend on Hubble parameter data sets". In: *Mathematical Modelling and Geometry* 6.1 (2018). DOI: 10.26456/mmg/2018-611. URL: https://doi.org/10.26456/mmg/2018-611.

[261] A. J. Ross et al. "The clustering of the SDSS DR7 main Galaxy sample - I. A 4 per cent distance measure at z=0.15". In: *Monthly Notices of the Royal Astronomical Society* 449.1 (2015), pp. 835–847. DOI: 10.1093/mnras/stv154. URL: https://doi.org/10.1093/mnras/stv154.

[262] H. du Mas des Bourboux et al. "The Completed SDSS-IV Extended Baryon Oscillation Spectroscopic Survey: Baryon Acoustic Oscillations with Lyα Forests". In: *The Astrophysical Journal* 901.2 (2020), p. 153. DOI: 10.3847/1538-4357/abb085. URL: https://doi.org/10.3847/1538-4357/abb085.

[263] M. G. Dainotti et al. "On the Hubble Constant Tension in the SNe Ia Pantheon Sample". In: *The Astrophysical Journal* 912.2 (2021), p. 150. DOI: 10.3847/1538-4357/abeb73. URL: https://doi.org/10.3847/1538-4357/abeb73.

[264] J. Guy et al. "The Supernova Legacy Survey 3-year sample: Type Ia supernovae photometric distances and cosmological constraints". In: *Astronomy & Astrophysics* 523 (2010), A7. DOI: 10.1051/0004-6361/201014468. URL: https://doi.org/10.1051/0004-6361/201014468.

[265] N. Chotard et al. "The reddening law of type Ia supernovae: separating intrinsic variability from dust using equivalent widths". In: *Astronomy & Astrophysics* 529 (2011), p. L4. DOI: 10.1051/0004-6361/201116723. URL: https://doi.org/10.1051/0004-6361/201116723.

[266] W. D. Kenworthy, D. Scolnic, and A. Riess. "The local perspective on the Hubble tension: local structure does not impact measurement of the Hubble constant". In: *Astrophys. J.* 875 (2019), p. 145. DOI: 10.3847/1538-4357/ab0ebf. URL: https://doi.org/10.3847/1538-4357/ab0ebf.

[267] E. Aubourg et al. “Cosmological implications of baryon acoustic oscillation measurements”. In: *Physical Review D* 92.12 (2015), p. 123516. DOI: 10.1103/physrevd.92.123516. URL: https://doi.org/10.1103/physrevd.92.123516.

[268] B. E. Schaefer. “Gamma-Ray Burst Hubble Diagram to z=4.5”. In: *The Astrophysical Journal* 583.2 (2003), pp. L67–L70. DOI: 10.1086/368104. URL: https://doi.org/10.1086/368104.

[269] J. S. Bloom, D. A. Frail, and S. R. Kulkarni. “Gamma-Ray Burst Energetics and the Gamma-Ray Burst Hubble Diagram: Promises and Limitations”. In: *The Astrophysical Journal* 594.2 (2003), pp. 674–683. DOI: 10.1086/377125. URL: https://doi.org/10.1086/377125.

[270] Z. G. Dai, E. W. Liang, and D. Xu. “Constraining Ω_M and Dark Energy with Gamma-Ray Bursts”. In: *The Astrophysical Journal* 612.2 (2004), pp. L101–L104. DOI: 10.1086/424694. URL: https://doi.org/10.1086/424694.

[271] G. Ghirlanda et al. “Gamma-Ray Bursts: New Rulers to Measure the Universe”. In: *The Astrophysical Journal* 613.1 (2004), pp. L13–L16. DOI: 10.1086/424915. URL: https://doi.org/10.1086/424915.

[272] D. Xu, Z. G. Dai, and E. W. Liang. “Can Gamma-Ray Bursts Be Used to Measure Cosmology? A Further Analysis”. In: *The Astrophysical Journal* 633.2 (2005), pp. 603–610. DOI: 10.1086/466509. URL: https://doi.org/10.1086/466509.

[273] M. Demianski et al. “Cosmology with gamma-ray bursts I. The Hubble diagram through the calibrated $E_{p,i} - E_{iso}$ correlation”. In: *Astronomy & Astrophysics* 598 (2017), A112. DOI: 10.1051/0004-6361/201628909. URL: https://doi.org/10.1051/0004-6361/201628909.

[274] N. Khadka and B. Ratra. “Constraints on cosmological parameters from gamma-ray burst peak photon energy and bolometric fluence measurements and other data”. In: *Monthly Notices of the Royal Astronomical Society* 499.1 (2020), pp. 391–403. DOI: 10.1093/mnras/staa2779. URL: https://doi.org/10.1093/mnras/staa2779.

[275] N. Khadka et al. “Do gamma-ray burst measurements provide a useful test of cosmological models?” In: *Journal of Cosmology and Astroparticle Physics* 2021.9, 042 (2021), p. 042. DOI: 10.1088/1475-7516/2021/09/042. URL: https://doi.org/10.1088/1475-7516/2021/09/042.

[276] M. G. Dainotti et al. "Determination of the Intrinsic Luminosity Time Correlation in the X-Ray Afterglows of Gamma-Ray Bursts". In: *The Astrophysical Journal* 774.2, 157 (2013), p. 157. DOI: 10.1088/0004-637X/774/2/157. URL: https://doi.org/10.1088/0004-637x/774/2/157.

[277] S. Postnikov et al. "Nonparametric Study of the Evolution of the Cosmological Equation of State with SNeIa, BAO, and High-redshift GRBs". In: *The Astrophysical Journal* 783.2, 126 (2014), p. 126. DOI: 10.1088/0004-637X/783/2/126. URL: https://doi.org/10.1088/0004-637x/783/2/126.

[278] F. Y. Wang et al. "Standardized Long Gamma-Ray Bursts as a Cosmic Distance Indicator". In: *The Astrophysical Journal* 924.2 (2022), p. 97. DOI: 10.3847/1538-4357/ac3755. URL: https://doi.org/10.3847/1538-4357/ac3755.

[279] J. P. Hu, F. Y. Wang, and Z. G. Dai. "Measuring cosmological parameters with a luminosity-time correlation of gamma-ray bursts". In: *Monthly Notices of the Royal Astronomical Society* 507.1 (2021), pp. 730–742. DOI: 10.1093/mnras/stab2180. URL: https://doi.org/10.1093/mnras/stab2180.

[280] S. Cao, N. Khadka, and B. Ratra. "Standardizing Dainotti-correlated gamma-ray bursts, and using them with standardized Amati-correlated gamma-ray bursts to constrain cosmological model parameters". In: *Monthly Notices of the Royal Astronomical Society* 510.2 (2022), pp. 2928–2947. DOI: 10.1093/mnras/stab3559. URL: https://doi.org/10.1093/mnras/stab3559.

[281] S. Cao, M. G. Dainotti, and B. Ratra. "Standardizing Platinum Dainotti-correlated gamma-ray bursts, and using them with standardized Amati-correlated gamma-ray bursts to constrain cosmological model parameters". In: *Monthly Notices of the Royal Astronomical Society* 512.1 (2022), pp. 439–454. DOI: 10.1093/mnras/stac517. URL: https://doi.org/10.1093/mnras/stac517.

[282] Shu-Kun Si et al. "The Three-parameter Correlations About the Optical Plateaus of Gamma-Ray Bursts". In: *The Astrophysical Journal* 863.1, 50 (2018), p. 50. DOI: 10.3847/1538-4357/aad08a. URL: https://doi.org/10.3847/1538-4357/aad08a.

[283] M. G. Dainotti et al. "The Optical Two- and Three-dimensional Fundamental Plane Correlations for Nearly 180 Gamma-Ray Burst Afterglows with Swift/UVOT, RATIR, and the Subaru Telescope". In: *The Astrophysical Journal Supplement Series* 261.2 (2022), p. 25. DOI: 10.3847/1538-4365/ac7c64. URL: https://doi.org/10.3847/1538-4365/ac7c64.

[284] D. Foreman-Mackey et al. “emcee: The MCMC Hammer”. In: *Publications of the Astronomical Society of the Pacific* 125.925 (2013), pp. 306–312. DOI: 10.1086/670067. URL: https://doi.org/10.1086/670067.

[285] M. G. Dainotti et al. “Gamma-ray Bursts as distance indicators through a machine learning approach”. In: *arXiv e-prints* (2019). DOI: 10.48550/ARXIV.1907.05074. URL: https://arxiv.org/abs/1907.05074.

[286] J. Wei et al. “The Deep and Transient Universe in the SVOM Era: New Challenges and Opportunities - Scientific prospects of the SVOM mission”. In: *arXiv e-prints* (2016). DOI: 10.48550/ARXIV.1610.06892. URL: https://arxiv.org/abs/1610.06892.

[287] L. Amati et al. “The THESEUS space mission concept: science case, design and expected performances”. In: *Advances in Space Research* 62.1 (2018), pp. 191–244. DOI: 10.1016/j.asr.2018.03.010. URL: https://doi.org/10.1016/j.asr.2018.03.010.

[288] B. Cordier et al. “The SVOM mission, a pathfinder for THESEUS.” In: *Mem. Società Astronomica Italiana* 89 (2018), p. 266. URL: https://arxiv.org/abs/1802.01681.

[289] S. E. Gralla, A. I. Harte, and R. M. Wald. “Rigorous derivation of electromagnetic self-force”. In: *Physical Review D* 80.2 (2009), p. 024031. DOI: 10.1103/physrevd.80.024031. URL: https://doi.org/10.1103/physrevd.80.024031.

[290] P. Di Bari. “On the origin of matter in the universe”. In: *Progress in Particle and Nuclear Physics* 122 (2022), p. 103913. DOI: 10.1016/j.ppnp.2021.103913. URL: https://doi.org/10.1016/j.ppnp.2021.103913.

[291] R. N. Mohapatra and G. Senjanovic. “Neutrino mass and spontaneous parity nonconservation”. In: *Physical Review Letters* 44 (1980), p. 912. DOI: 10.1103/PhysRevLett.44.912.

[292] J. A. Formaggio, A. L. C. de Gouvêa, and R. G. Hamish Robertson. “Direct measurements of neutrino mass”. In: *Physics Reports* 914 (2021), p. 1. DOI: 10.1016/j.physrep.2021.02.002. URL: https://doi.org/10.1016/j.physrep.2021.02.002.

[293] L. de Broglie. “Ondes et quanta”. In: *Comptes Rendus Hebd. Séances Acad. Sci. Paris* 177 (1923), p. 507. DOI: ark:/12148/bpt6k3130n.

[294] L. de Broglie. *Recherches sur la théorie des quanta*. Doctorate thesis (Dir. P. Langevin) Université de Paris, Sorbonne. Paris: Masson & C^{ie}, 1924.

[295] L. de Broglie. *Nouvelles Recherches sur la Lumière*. Vol. 411. Actualités Scientifiques et Industrielles. Paris: Hermann & C^ie, 1936.

[296] A. Proca. "Sur les photons et les particules charge pure". In: *Comptes Rendus Hebd. Séances Acad. Sc. Paris* 203 (1936), p. 709. DOI: ark:/12148/bpt6k3155r.

[297] A. S. Goldhaber and M. M. Nieto. "Photon and graviton mass limits". In: *Reviews of Modern Physics* 82 (2010), p. 939. DOI: 10.1103/RevModPhys.82.939. URL: https://doi.org/10.1103/revmodphys.82.939.

[298] D. Colladay and V. A. Kostelecký. "CPT violation and the Standard Model". In: *Physical Review D* 55.11 (1997), p. 6760. DOI: 10.1103/PhysRevD.55.6760. URL: https://doi.org/10.1103/physrevd.55.6760.

[299] D. Colladay and V. A. Kostelecký. "Lorentz-violating extension of the Standard Model". In: *Physical Review D* 58.11 (1998). DOI: 10.1103/PhysRevD.58.116002. URL: https://doi.org/10.1103/physrevd.58.116002.

[300] L. Bonetti et al. "Effective photon mass from Super and Lorentz symmetry breaking". In: *Physics Letters B* 764 (2017), p. 203. DOI: 10.1016/j.physletb.2016.11.023. URL: https://doi.org/10.1016/j.physletb.2016.11.023.

[301] L. Bonetti et al. "Photon sector analysis of Super and Lorentz symmetry breaking: effective photon mass, bi-refringence and dissipation". In: *The European Physical Journal C* 78 (2018), p. 811. DOI: 10.1140/epjc/s10052-018-6247-5. URL: https://doi.org/10.1140/epjc/s10052-018-6247-5.

[302] M. Born and L. Infeld. "On the quantization of the new field equations. I". In: *Proceedings of the Royal Society of London A* 147 (1934), p. 522.

[303] E. S. Fradkin and A. A. Tseytlin. "Non-linear electrodynamics from quantized strings". In: *Physics Letters B* 163.1-4 (1985), pp. 123–130. DOI: 10.1016/0370-2693(85)90205-9.

[304] S. M. Carroll, G. B. Field, and R. Jackiw. "Limits on a Lorentz- and parity-violating modification of electrodynamics". In: *Physical Review D* 41 (1990), p. 1231. DOI: 10.1103/PhysRevD.41.1231.

[305] J. B. Oke and J. E. Gunn. "Secondary standard stars for absolute spectrophotometry". In: *The Astrophysical Journal* 266 (1983), p. 713. DOI: 10.1086/160817.

[306] V. A. Kostelecký and S. Samuel. "Spontaneous breaking of Lorentz symmetry in string theory". In: *Physical Review D* 39 (1989), p. 683. DOI: 10.1103/PhysRevD.39.683.

[307] A. Einstein and W. de Sitter. "On the relation between the expansion and the mean density of the universe". In: *Proc. Nat. Ac. of Sci. USA* 18 (1932), p. 213. DOI: 10.1073/pnas.18.3.213.

[308] S. Perlmutter et al. "Measurements of the cosmological parameters Ω and Λ from the first seven Supernovae at z$\geq$ 0.35". In: *The Astrophyisical Journal* 483 (1997), p. 565. DOI: 10.1086/304265. URL: https://doi.org/10.1086/304265.

[309] P. A. Oesch et al. "A remarkably luminous galaxy at z=11.1 measured with Hubble Space Telescope Grism Spectroscopy". In: *The Astrophyisical Journal* 819 (2016), p. 129. DOI: 10.3847/0004-637X/819/2/129. URL: https://doi.org/10.3847/0004-637x/819/2/129.

[310] G. Goldhaber et al. "Timescale stretch parameterization of type Ia Supernova B-B and light curves". In: *The Astrophysical Journal* 558 (2001), p. 359. DOI: 10.1086/322460. URL: https://doi.org/10.1086/322460.

[311] S. Blondin et al. "Time dilation in Type Ia Supernova spectra at high redshift". In: *The Astrophysical Journal* 682 (2008), p. 724. DOI: 10.1086/589568. URL: https://doi.org/10.1086/589568.

[312] F. Zwicky. "On the red shift of spectral lines through interstellar space". In: *Proc. Nat. Ac. Sci. USA* 15 (1929), p. 773. DOI: 10.1073/pnas.15.10.773.

[313] M. López-Corredoira. "Tests and problems of the Standard Model in cosmology". In: *Foundations of Physics* 47 (2017), p. 711. DOI: 10.1007/s10701-017-0073-8. URL: https://doi.org/10.1007/s10701-017-0073-8.

[314] M. López-Corredoira. "Peaks in the CMBR power spectrum II: physical interpretation for any cosmological scenario". In: *International Journal of Modern Physics D* 22 (2013), p. 1350032. DOI: 10.1142/S0218271813500326. URL: https://doi.org/10.1142/s0218271813500326.

[315] P. Astier and R. Pain. "Observational evidence of the accelerated expansion of the universe". In: *Comptes rendus - Physique* 13 (2012), p. 521. DOI: 10.1016/j.crhy.2012.04.009. URL: https://doi.org/10.1016/j.crhy.2012.04.009.

[316] S. Capozziello, M. Benetti, and A. D. A. M. Spallicci. "Addressing the cosmological H_0 tension by the Heisenberg uncertainty". In: *Foundations of Physics* 50 (2020), p. 893. DOI: 10.1007/s10701-020-00356-2. URL: https://doi.org/10.1007/s10701-020-00356-2.

[317] A. D. A. M. Spallicci, M. Benetti, and S. Capozziello. "Heisenberg principle at cosmological scales". In: *Foundations of Physics* 52 (2022), p. 23. DOI: 10.1007/s10701-021-00531-z. URL: https://doi.org/10.1007/s10701-021-00531-z.

[318] E. R. Williams, J. E. Faller, and H. A. Hill. "New experimental test of Coulomb's law: A laboratory upper limit on the photon rest mass". In: *Physical Review Letters* 26 (1971), p. 721. DOI: 10.1103/PhysRevLett.26.721.

[319] L.-C. Tu, J. Luo, and G. T. Gillies. "The mass of the photon". In: *Reports on Progress in Physics* 68.1 (2005), pp. 77–130. DOI: 10.1088/0034-4885/68/1/R02.

[320] L. Bonetti et al. "Photon mass limits from fast radio bursts". In: *Physics Letters B* 757 (2016), p. 548. DOI: 0.1016/j.physletb.2016.04.035. URL: https://doi.org/10.1016/j.physletb.2016.04.035.

[321] L. Bonetti et al. "FRB 121102 casts new light on the photon mass". In: *Physics Letters B* 768 (2017), p. 326. DOI: 10.1016/j.physletb.2017.03.014. URL: https://doi.org/10.1016/j.physletb.2017.03.014.

[322] H. Wang, X. Miao, and L. Shao. "Bounding the photon mass with cosmological propagation of fast radio bursts". In: *Physics Letters B* 820 (2021), p. 136596. DOI: 10.1016/j.physletb.2021.136596. URL: https://doi.org/10.1016/j.physletb.2021.136596.

[323] M. J. Bentum, L. Bonetti, and A. D. A. M. Spallicci. "Dispersion by pulsars, magnetars, fast radio bursts and massive electromagnetism at very low radio frequencies". In: *Advances in Space Research* 59 (2017), p. 736. DOI: 10.1016/j.asr.2016.10.018. URL: https://doi.org/10.1016/j.asr.2016.10.018.

[324] D. J. Bartlett et al. "Constraints on quantum gravity and the photon mass from gamma ray bursts". In: *Physical Review D* 104 (2021), p. 103516. DOI: 10.1103/PhysRevD.104.103516. URL: https://doi.org/10.1103/physrevd.104.103516.

[325] D. D. Ryutov. "The role of finite photon mass in magnetohydrodynamics of space plasmas". In: *Plasma Physics and Controlled Fusion* 39 (1997), A73. DOI: 10.1088/0741-3335/39/5A/008.

[326] D. D. Ryutov. "Using plasma physics to weigh the photon". In: *Plasma Physics and Controlled Fusion* 49 (2007), B429. DOI: 10.1088/0741-3335/49/12B/S40.

[327] A. Retinò, A. D. A. M. Spallicci, and A. Vaivads. "Solar wind test of the de Broglie-Proca massive photon with Cluster multi-spacecraft data". In: *Astroparticle Physics* 82 (2016), p. 49. DOI: 10.1016/j.astropartphys.2016.05.006. URL: https://doi.org/10.1016/j.astropartphys.2016.05.006.

[328] E. Adelberger, G. Dvali, and A. Gruzinov. "Photon-mass bound destroyed by vortices". In: *Physical Review Letters* 98 (2007), p. 010402. DOI: 10.1103/PhysRevLett.98.010402. URL: https://doi.org/10.1103/physrevlett.98.131104.

[329] G. V. Chibisov. "Astrophysical upper limits on the photon rest mass". In: *Soviet Physics Uspekhi* 19 (1976). [Uspekhi Fizicheskikh Nauk, 119 (1976) 591], p. 624.

[330] Y. Yamaguchi. "A composite theory of elementary particles". In: *Progress of Theoretical Physics Supplements* 11 (1959), p. 1.

[331] A. Barnes and J. D. Scargle. "Improved upper limit on the photon rest mass". In: *Physical Review Letters* 35 (1975), p. 1117. DOI: 10.1103/PhysRevLett.35.1117.

[332] R. Lakes. "Experimental limits on the photon mass and cosmic magnetic vector potential". In: *Physical Review Letters* 80 (1998), p. 1826. DOI: 10.1103/PhysRevLett.80.1826.

[333] J. Luo et al. "New experimental limit on the photon rest mass with a rotating torsion balance". In: *Physical Review Letters* 90 (2003). Reply, 91, 149102 (2003), p. 081801. DOI: 10.1103/PhysRevLett.90.081801-Reply10.1103/PhysRevLett.91.149102.

[334] L.-C. Tu et al. "Test of U(1)local gauge invariance in Proca electrodynamics". In: *Physics Letters A.* 352 (2006), p. 267. DOI: 10.1016/j.physleta.2005.12.017.

[335] P. A. Franken and G. W. Ampulski. "Photon Rest Mass". In: *Physical Review Letters* 26 (1971), p. 115. DOI: 10.1103/PhysRevLett.26.115.

[336] M. Füllekrug. "Probing the speed of light with radio waves at extremely low frequencies". In: *Physical Review Letters* 93 (2004), p. 043901. DOI: 10.1103/PhysRevLett.93.043901.

[337] L. Davis jr., A. S. Goldhaber, and M. N. Nieto. "Limit on the photon mass deduced from Pioneer-10 observations of Jupiter's magnetic field". In: *Physical Review Letters* 35 (1975), p. 1402. DOI: 10.1103/PhysRevLett.35.1402.

[338] E. Fischbach et al. "New geomagnetic limits on the photon mass and on long-range forces coexisting with electromagnetism". In: *Physical Review Letters* 73 (1994), p. 514. DOI: 10.1103/PhysRevLett.73.514.

[339] A. S. Goldhaber and M. M. Nieto. "New geomagnetic limit on the mass of the photon". In: *Physical Review Letters* 21 (1968), p. 567. DOI: 10.1103/PhysRevLett.21.567.

[340] J. V. Hollweg. "Improved limit on photon rest mass". In: *Physical Review Letters* 32 (1974), p. 961. DOI: 10.1103/PhysRevLett.32.961. eprint: arXiv:1006.4907[gr-qc].

[341] Y. M. P. Gomes and P. C. Malta. "Laboratory-based limits on the Carroll-Field-Jackiw Lorentz violating electroynamics". In: *Physical Review D* 94 (2016), p. 025 031. DOI: 10.1103/PhysRevD.94.025031. URL: https://doi.org/10.1103/physrevd.94.025031.

[342] V. A. Kostelecký and N. Russell. "Data tables for Lorentz and CPT violation". In: *Reviews of Modern Physics* 83 (2011), p. 11. DOI: 10.1103/RevModPhys.83.11. URL: https://doi.org/10.1103/revmodphys.83.11.

[343] C. Pollock et al. "Fast plasma investigation for magnetospheric multiscale". In: *Space Science Reviews* 199 (2016), p. 331. DOI: 10.1007/s11214-016-0245-4. URL: https://link.springer.com/article/10.1007/s11214-016-0245-4.

[344] C. T. Russell et al. "The Magnetospheric Multiscale Magnetometers". In: *Space Science Reviews* 199 (2016), p. 189. DOI: 10.1007/s11214-014-0057-3. URL: https://link.springer.com/article/10.1007/s11214-014-0057-3.

[345] V. Génot et al. "Automated Multi-Dataset Analysis (AMDA): An on-line database and analysis tool for heliospheric and planetary plasma data". In: *Planetary and Space Science* 201 (2021), p. 105214. DOI: 10.1016/j.pss.2021.105214. URL: https://www.sciencedirect.com/science/article/pii/S0032063321000532?via%5C%3Dihub.

[346] D. J. Gershman et al. “The calculation of moment uncertainties from velocity distribution functions with random errors”. In: *Journal of Geophysical Research: Space Physics* 120 (2015), p. 6633. DOI: 10.1002/2014JA020775. URL: https://agupubs.onlinelibrary.wiley.com/doi/full/10.1002/2014JA020775.

[347] D. J. Gershman et al. “Systematic uncertainties in plasma parameters reported by the Fast Plasma Investigation on NASA’s Magnetospheric Multiscale Mission”. In: *Journal of Geophysical Research: Space Physics* 124 (2019), p. 10345. DOI: 10.1029/2019JA026980. URL: https://agupubs.onlinelibrary.wiley.com/doi/10.1029/2019JA026980.

[348] M. W. Dunlop et al. “Four-point Cluster application of magnetic field analysis tools: the curlometer”. In: *Journal of Geophysical Research: Space Physics* 107 (2002), p. 1384. DOI: 10.1029/2001JA005088. URL: https://agupubs.onlinelibrary.wiley.com/doi/full/10.1029/2001JA005088.

[349] G. Chanteur and F. Mottez. “Geometrical tools for Cluster data analysis”. In: *Spatio-Temporal Analysis for Resolving plasma Turbulence (START)*. Vol. ESA WPP-47. 31 January-5 February 1993 Aussois. Noordwijk: European Space Agency, 1993, p. 341.

[350] R. B. Torbert et al. “The FIELDS instrument suite on MMS: scientific objectives, measurements, and data products”. In: *Space Science Reviews* 199 (2016), p. 105. DOI: 10.1007/s11214-014-0109-8. URL: https://link.springer.com/article/10.1007/s11214-014-0109-8.

[351] D. Kelbel et al. “Relative navigation algorithms for the phase 1 of the MMS formation”. https://ntrs.nasa.gov/citations/20040084078. 2003.

[352] M. W. Dunlop et al. “Multipoint analysis of electric currents in geospace using the curlometer technique”. In: *Electric Currents in Geospace and Beyond*. Ed. by A. Keiling, O. Marghitu, and M. Wheatland. Vol. 235. Geophysical Monograph Series. Hoboken: John Wiley & Sons, 2018, p. 67. ISBN: 9781119324492. DOI: 10.1002/9781119324522.ch4.

[353] A. C. Barrie et al. “Characterizing spacecraft potential effects on measured particle trajectories”. In: *Physics of Plasmas* 26 (2019), p. 103504. DOI: 10.1063/1.5119344. URL: https://aip.scitation.org/doi/10.1063/1.5119344.

[354] J. W. Bieber, P. A. Evenson, and W. H. Matthaeus. "Magnetic helicity of the Parker field". In: *The Astrophysical Journal* 315 (1987), p. 700. DOI: 10.1086/165171.

[355] S. Capozziello, A. Stabile, and A. Troisi. "The Newtonian limit of F(R) Gravity". In: *Physical Review D* 76.10 (2007), p. 104019. DOI: 10.1103/physrevd.76.104019. URL: https://doi.org/10.1103/physrevd.76.104019.

[356] S. Capozziello and A. Stabile. "The Weak Field Limit of Fourth Order Gravity". In: (2010). DOI: 10.48550/ARXIV.1009.3441. URL: https://arxiv.org/abs/1009.3441.

[357] M. De Laurentis, I. De Martino, and R. Lazkoz. "Analysis of the Yukawa gravitational potential in $f(R)$ gravity. II. Relativistic periastron advance". In: *Physical Review D* 97.10 (2018), p. 104068. DOI: 10.1103/physrevd.97.104068. URL: https://doi.org/10.1103/physrevd.97.104068.

[358] B. W. Carrol and D. A. Ostlie. *An Introduction to Modern Astrophysics (2nd Edition)*. Pearson, Londra, 2006.

[359] A. Stabile. "The Post-Newtonian Limit of f(R)-gravity in the Harmonic Gauge". In: *Physical Review D* 82.6 (2010), p. 124026. DOI: 10.1103/physrevd.82.124026. URL: https://doi.org/10.1103/physrevd.82.124026.

[360] Z. Eker et al. "Main-Sequence Effective Temperatures from a Revised Mass-Luminosity Relation Based on Accurate Properties". In: *The Astronomical Journal* 149.4 (2015), p. 131. DOI: 10.1088/0004-6256/149/4/131. URL: https://doi.org/10.1088/0004-6256/149/4/131.

[361] M. I. Ivanov. "On Nonlinear Radial Adiabatic Pulsations of Polytropes". In: (2014). DOI: 10.48550/ARXIV.1402.3804. URL: https://arxiv.org/abs/1402.3804.

[362] M. A. Seeds and D. Backman. *Foundations of Astronomy*. Cengage Learning, Boston, 2018.

[363] I. Soszyński et al. "Additional Galactic Cepheids from the OGLE Survey". In: *Acta Astronomica* 70.2 (2020), pp. 101–119. DOI: 10.32023/0001-5237/70.2.2. URL: https://doi.org/10.32023/0001-5237/70.2.2.

[364] N. R.Evans et al. "Binary Cepheids: separations and mass rations in $5M_{\odot}$ binaries". In: *The Astronomical Journal* 146.4 (2013), p. 93. DOI: 10.1088/0004-6256/146/4/93. URL: https://doi.org/10.1088/0004-6256/146/4/93.

[365] T. E. Nordgren et al. "Stellar Angular Diameters of Late-Type Giants and Supergiants Measured with the Navy Prototype Optical Interferometer". In: *The Astrophysical Journal* 118.6 (1999), pp. 3032–3038. DOI: 10.1086/301114.

[366] M. Marconi et al. "The Eclipsing Binary Cepheid OGLE-LMC-CEP-0227 in the Large Magellanic Cloud: pulsation modelling of light and radial velocity curves". In: *The Astrophysical Journal* 768.1 (2013), p. L6. DOI: 10.1088/2041-8205/768/1/l6. URL: https://doi.org/10.1088/2041-8205/768/1/l6.

[367] M. Marconi et al. "On a new theoretical framework for RR Lyrae stars I: the metallicity dependence". In: *The Astrophysical Journal* 808.1 (2015), p. 50. DOI: 10.1088/0004-637x/808/1/50. URL: https://doi.org/10.1088/0004-637x/808/1/50.

[368] G. De Somma et al. "An Extended Theoretical Scenario for Classical Cepheids. I. Modeling Galactic Cepheids in the Gaia Photometric System". In: *The Astrophysical Journal Supplement Series* 247.1 (2020), p. 30. DOI: 10.3847/1538-4365/ab7204. URL: https://doi.org/10.3847/1538-4365/ab7204.

[369] S. D. Odintsov, D. Sáez-Chillón Gómez, and G. S. Sharov. "Is exponential gravity a viable description for the whole cosmological history?" In: *The European Physical Journal C* 77.12 (2017). DOI: 10.1140/epjc/s10052-017-5419-z. URL: https://doi.org/10.1140/epjc/s10052-017-5419-z.

[370] L. Yang et al. "Observational constraints on exponential gravity". In: *Physical Review D* 82.10 (2010), p. 103515. DOI: 10.1103/physrevd.82.103515. URL: https://doi.org/10.1103/physrevd.82.103515.

[371] Y. Chen et al. "Constraints on the exponential $f(R)$ model from latest Hubble parameter measurements". In: *Physical Review D* 91.4 (2015), p. 044019. DOI: 10.1103/physrevd.91.044019. URL: https://doi.org/10.1103/physrevd.91.044019.

[372] E. N. Saridakis et al., eds. *Modified gravity and cosmology: an update by the CANTATA network*. Cham: Springer Nature Switzerland, 2021. ISBN: 978-3-030-83714-3. eprint: arXiv:2105.12582[gr-qc].

Ringraziamenti

Gli anni del dottorato sono stati decisamente quelli in cui sono cresciuto di più, soprattutto dal punto di vista professionale, affrontando sfide che non avevo mai vissuto prima, superando nuove difficoltà e ottenendo risultati soddisfacenti. E' stato un percorso travagliato e pieno di sorprese, che, in retrospettiva, probabilmente non cambierei, data l'enorme crescita umana e professionale che ha comportato.

Ringrazio, prima di tutto, i miei due relatori, profs. Salvatore Capozziello e Alessandro Spallicci, che mi hanno seguito ed aiutato nel corso degli anni del mio dottorato, permettendomi di raggiungere notevoli traguardi professionali e non solo.

Ringrazio, inoltre, tutte le persone con cui ho collaborato in questi anni, come la professoressa Maria Giovanna Dainotti ed il collega Pasquale Feola. Queste collaborazioni mi hanno permesso di scoprire situazioni e mondi che prima non conoscevo, e che hanno contribuito sicuramente a rendermi una persona piú completa, sia come astrofisico che come uomo.

Ringrazio la mia famiglia, che mi ha supportato in questi anni, aiutandomi nei momenti piú difficili e gioiendo in quelli piú felici.

Ringrazio i miei amici, con cui condivido i ricordi piú cari.

Grazie.